Tampere University

JARKKO KIILAKOSKI

Damage Tolerance of Thermally Sprayed Oxide Coatings

Tampere University Dissertations 229

Tampere University Dissertations 229

JARKKO KIILAKOSKI

Damage Tolerance of Thermally Sprayed Oxide Coatings

ACADEMIC DISSERTATION
To be presented, with the permission of
the Faculty of Engineering and Natural Sciences
of Tampere University,
for public discussion in auditorium K1702
of the Konetalo building, Korkeakoulunkatu 6, Tampere,
on 27 March 2020, at 12 o'clock.

ACADEMIC DISSERTATION
Tampere University, Faculty of Engineering and Natural Sciences
Finland

Responsible supervisor and Custos	Prof. Petri Vuoristo Tampere University Finland	
Supervisor	Dr. Heli Koivuluoto Tampere University Finland	
Pre-examiners	Prof. Christopher C. Berndt Swinburne University of Technology Australia	Dr. Alain Denoirjean Université de Limoges France
Opponents	Prof. Christopher C. Berndt Swinburne University of Technology Australia	Prof. Jari Koskinen Aalto University Finland

The originality of this thesis has been checked using the Turnitin OriginalityCheck service.

Cover design: Roihu Inc.

ISBN 978-952-03-1504-7 (print)
ISBN 978-952-03-1505-4 (pdf)
ISSN 2489-9860 (print)
ISSN 2490-0028 (pdf)
http://urn.fi/URN:ISBN:978-952-03-1505-4

PunaMusta Oy – Yliopistopaino
Tampere 2020

PREFACE

This work was carried out in the Laboratory of Materials Science and Environmental Engineering of the Faculty of Engineering and Natural Sciences at Tampere University (formerly Tampere University of Technology) during the years 2014-2019. The work was funded by the HYBRIDS Research Programme of DIMECC in the years 2014-2016 and by the graduate school of the President of Tampere University of Technology and "Ductile & Damage Tolerant Ceramic Coatings"-project of Business Finland in the years 2016-2018. Support in finishing the thesis during the year 2019 from the foundation of K.F and Maria Dunderberg is gratefully acknowledged.

I was introduced to the idea of pursuing a doctorate by the collaboration between my then-supervisor at Metso Paper Inc., M.Sc. Ville Eronen, and my thesis supervisor Prof. Petri Vuoristo. Together they were able to persuade me into taking on this task and seeing the value in a post-graduate degree. I am grateful to them both. During the thesis, I was lucky enough to have been able to travel to many conferences of our field and meet and network with academia and industry alike. Through these experiences I am grateful to have had such good collaboration with great co-authors in all my articles. I would like to thank Dr. Matti Lindroos and Dr. Marian Apostol for assisting me in performing high-impact experiments and Dr. Jouni Puranen for coming to me with the idea of combining a solution precursor with powder in-situ during thermal spray. Jouni also helped shape and refine my scientific thinking during our collaboration. I am extremely thankful for the collaboration I was able to do with our colleagues in foreign research institutes. Dr. Radek Musalek and Dr. Frantisek Lukac were very welcoming and helpful during my visit to the Institute of Plasma Physics in Prague, Czech Republic. Dr. Sophie Costil and Dr. Cécile Langlade helped accommodate and instruct me during my visit to Université de Technologie de Belfort-Montbéliard in Sevenans, France. I am deeply grateful for the time I got to spent with Prof. Shrikant Joshi when he visited us in Tampere. I was lucky enough to

pick his brain for nearly a month on the topics of liquid feedstock spraying, thermal spraying and life after a doctoral degree.
I would like to thank my supervisor Professor Petri Vuoristo for his gentle guidance and patience throughout this long process. A lot of wisdom and history was dug out during deep conversations on the subject of thermally sprayed ceramic coatings. My thesis instructor, Dr. Heli Koivuluoto, deserves my earnest gratitude for her guidance and firm belief in my abilities when self-doubt tried to raise its head. My colleagues, room-mates, brothers(and sister)-in-arms: M.Sc. Ville Matikainen, M.Sc. Davide Fantozzi and M.Sc Henna Niemelä-Anttonen... We formed a bond during our struggles that has turned into true friendship even as our paths have deviated. I would like to thank the Surface Engineering group M.Sc. Tommi Varis, Dr. Jussi Laurila, Dr. Jari Tuominen and the staff of the laboratory, especially Mr. Mikko Kylmälahti and Mr. Anssi Metsähonkala for depositing the coatings, M.Sc. Jarmo Laakso and Dr. Mari Honkanen for helping with the materials characterization and the many research assistants our group was lucky to have over the years.
I am grateful to have had the understanding of my family and friends. My beloved Léna, who has been supporting me throughout and taken the burden of running the family life, especially during the last few months. And especially my daughters, Maïlis and Noémi, who do not understand any of this yet, but who have been the biggest motivation to see this work through. Your smiles have relieved my mind whenever I needed it most.

Jarkko Kiilakoski

14.11.2019
Rognonas, France

ABSTRACT

Thermally sprayed ceramic coatings are utilized in various applications in industries, such as paper- and process, aerospace and energy production. The requirements for the coatings vary from wear resistance and chemical stability to functional properties, such as low surface energy or thermal conductivity. Oxide coatings, such as yttria-stabilized zirconium oxide, aluminum oxide, titanium oxide and chromium oxide are commonly deposited by thermal spray processes using an atmospheric plasma, a high-velocity oxy-fuel or a flame spray torch.

The biggest drawback of the oxide coatings is their susceptibility to catastrophic failure from sudden, unexpected impacts, consequently leading to the functional failure of the component. The possibility of such impacts is omnipresent in most applications where ceramic coatings are used, which makes the topic attractive to a wide range of industries. This property of the coatings — named damage tolerance for the purposes of this thesis — additionally limits the number of possible applications. Therefore, any improvement in damage tolerance could open doors to various new technologies. Multiple workarounds have been attempted in improving the damage tolerance of ceramic coatings, such as metallic additions, oxide mixtures and nano-structured coatings, but so far increases in performance have been modest or have deteriorated other beneficial functions of the coating.

Furthermore, there lies a challenge in accurate and repeatable measurement of the damage tolerance. Current methodology includes testing in laboratory scale, giving information on the nature of the material and coating, and application-based testing, where the obtained information is not widely applicable in other conditions.

In this study, the primary focus was to evaluate different methods of measuring the damage tolerance of thermally sprayed ceramic coatings. Damage tolerance was divided in two distinguishable properties: crack propagation resistance and resistance to low-energy impacts. The former is akin to fracture toughness, but aims to give

a more transferable result. Measurement methods of crack propagation resistance evaluated include four-point bending with acoustic emission instrumentation and high-energy impacts from spherical projectiles with crack path tracing. These methods provided insights into the effect of microstructure on the toughness of the coating. Interlamellar cohesion was shown to be the weakest link of toughness in that the weak interfaces provide the path of least resistance for crack propagation. Additionally, denser HVOF coatings proved more brittle than their plasma-sprayed counterparts as they did not have stress-relieving zones from pre-cracked areas.

The low-energy impact approach is slightly more application-oriented, aiming to emulate impact damage conditions in real-life environments. The methods used to measure it are micro-impact fatigue, where a small indenter is repeatedly impacted on the surface with high frequency, and cavitation erosion, where a vast number of impacts from collapsing bubbles create a statistical approach to measuring coating cohesion in the micrometer scale. The results of these tests correlated well with the concept of damage-tolerance as they measured the properties of the coating in a more general level. Since these methods rely on small impacts, hardness of the coating was a determining factor of damage-tolerance until the energy of the impact rose past a coating-specific threshold. Above this value, the coatings either failed catastrophically, or showed a more gradual failure propagation. The latter of these behaviors is highly preferred, as it gives time to react before the component fails in real conditions.

The secondary focus was to create ceramic coatings with increased damage tolerance through novel spray processes, as measured by the screened testing methods. The spray methods were suspension HVOF-spraying and solution-precursor -powder hybrid HVOF spraying. The suspension sprayed Cr_2O_3-coatings provided improvements in damage tolerance with similar or improved levels of wear resistance and hardness. The hybrid-spraying of Al_2O_3 powder and a zirconium acetate based precursor proved to still require further optimization of the spray process, as unmolten agglomerates of precursor-derived nanoparticles rather weakened the coating, instead of improving the cohesion. Nonetheless, promising potential is foreseen for the hybrid-spraying in the future due to its ability to tailor the coating composition rather seamlessly.

TIIVISTELMÄ

Termisesti ruiskutettuja keraamipinnoitteita käytetään useissa sovelluksissa eri teollisuudenaloilla, kuten paperi- ja prosessiteollisuudessa, avaruus- ja ilmailuteollisuudessa, sekä energiantuotannossa. Pinnoitteille asetetut vaatimukset vaihtelevat kulumisen ja korroosion kestosta funktionaalisiin ominaisuuksiin, kuten alhaiseen pintaenergiaan tai lämmönjohtavuuteen. Oksidipinnoitteet, kuten yttriastabiloitu zirkoniumoksidi, alumiinioksidi, titaanioksidi ja kromioksidi muodostetaan yleisesti termisen ruiskutuksen prosesseilla käyttäen atmosfääristä plasmaa, suurnopeusliekkiruiskutusta tai perinteistä liekkiruiskutusta.

Oksidipinnoitteiden suurin varjopuoli on niiden alttius katastrofaaliseen murtumiseen yhtäkkisestä, odottamattomasta iskusta johtuen. Tämänkaltaisten iskujen mahdollisuus on jatkuvasti läsnä useimmissa sovelluksissa, missä keraamisia pinnoitteita käytetään, minkä vuoksi aihe herättää kiinnostusta laajassa skaalassa teollisuuden aloja. Lisäksi tämä pinnoitteiden ominaisuus — tässä työssä nimetty vauriosietoisuudeksi — rajaa mahdollisten sovelluskohteiden määrää. Tämän vuoksi pienikin parannus vauriosietoisuudessa voi avata ovia uusille teknologioille. Useita keinoja keraamipinnoitteiden vauriosietoisuuden parantamiseksi on kokeiltu, kuten metallin lisäystä pinnoitteeseen, oksidisekoituksia ja nanorakenteisia pinnoitteita, mutta toistaiseksi parannukset suorituskyvyssä ovat olleet varsin nimellisiä, tai ovat heikentäneet pinnoitteen muita hyödyllisiä ominaisuuksia.

Lisäksi vauriosietoisuuden mittaaminen tarkasti ja toistettavasti on haastavaa. Nykymenetelmiin kuuluu laboratoriomittakaavan kokeet, jotka antavat tietoa materiaalin ja pinnoitteen luonteesta, sekä sovelluspainotteiset kokeet, joista saatu tieto ei ole laajasti hyödynnettävissä muissa ympäristöissä.

Tämän tutkimuksen pääpaino oli arvioida eri menetelmiä termisesti ruiskutettujen keraamipinnoitteiden vauriosietoisuuden mittaamiseksi. Vauriosietoisuus jaettiin kahteen selkeästi toisistaan eroavaan ominaisuuteen: särön etenemisen vastustuskykyyn

ja matalaenergisten iskujen vastustuskykyyn. Näistä edellinen on lähellä murtositkeyden määritelmää, mutta tähtää tuottamaan laajemmin sovellettavia tuloksia. Särön etenemisen vastustuskyvyn mittausmenetelmiin luetaan nelipistetaivutus akustisella emissiolla instrumentoituna ja suuren energia iskut särön polun tutkimisella. Nämä menetelmät antavat tietoa mikrorakenteen vaikutuksesta pinnoitteen sitkeyteen. Lamellienvälinen koheesio paljastui sitkeyden kannalta heikoimmaksi lenkiksi, sillä heikko rajapinta luo helpoimman etenemisreitin särölle. Edelleen kokeet paljastivat, että tiiviimmät HVOF-pinnoitteet käyttäytyivät hauraammin kuin plasmaruiskutetut vastinparinsa, sillä niissä ei ollut esisäröytyneitä alueita, jotka voisivat vapauttaa pinnoitteeseen muodostuneita jännitystiloja.

Matalaenergisten iskujen vastustuskyky on hieman enemmän sovelluslähtöinen tähdäten mukailemaan iskumaista vauriota tosielämän tilanteissa. Sen mittausmenetelmiin taas luetaan väsyttäminen mikrokoon iskuilla, joissa pieni painin iskeytyy pintaan toistuvasti korkealla taajuudella, sekä kavitaatioeroosio, jossa valtava määrä luhistuvista kuplista johtuvia iskeymiä tuottavat tilastollisen lähestymistavan mikrometriluokan pinnoitteen koheesion mittaamiseen. Näiden testien tulokset korreloivat hyvin vauriosietoisuuden käsitteen kanssa, sillä ne mittasivat pinnoitteen ominaisuuksia yleisemmällä tasolla. Koska nämä mittaustavat hyödyntävät pieniä iskuja, pinnoitteen kovuus oli vauriosietoisuuden kannalta määräävä tekijä, kunnes iskujen energia ylitti tietyn raja-arvon. Tätä rajaa suurempienergiset iskut johtivat joko pinnoitteen katastrofaaliseen vaurioitumiseen tai vaiheittaiseen vaurion etenemiseen. Näistä jälkimmäinen on vahvasti suositumpi, sillä silloin tosielämän tilanteissa jää aikaa reagoida ennen komponentin tuhoutumista.

Toissijainen painopiste oli parannetun vauriosietoisuuden keraamipinnoitteiden valmistaminen uusia ruiskutusprosesseja käyttäen. Tämän toteamiseksi käytetään ensimmäisessä vaiheessa arvioituja mittausmenetelmiä. Käytetyt ruiskutusmenetelmät olivat suspensiosuurnopeusliekkiruiskutus ja nestemäisen prekursorin ja jauheen syöttäminen samanaikaisesti nk. hybridisuurnopeusliekkiruiskutuksessa. Suspensioruiskutetut kromioksidipinnoitteet osoittivat parannuksia vauriosietoisuudessa säilyttäen tai parantaen kulumisenkestoaan ja kovuuttaan. Alumiinioksidijauheen ja zirkoniumasetaattiliuoksen hybridiruiskutus paljasti tarpeen ruiskutusprosessin lisäoptimoinnille, sillä sulamattomat, prekursorista peräisin olevat nanopartikkeliagglomeraatit heikensivät pinnoiterakennetta koheesion parantamisen sijaan. Tästä huolimatta, pinnoitteen saumattoman räätälöinnin lupaava potentiaali kannustaa

tutkimaan myös hybridiruiskutusta tulevaisuudessa.

CONTENTS

ABBREVIATIONS

AE	acoustic emission
Al	aluminum
Al_2O_3	aluminum oxide, alumina
AlO(OH)	aluminum hydroxide oxide, aluminum oxyhydroxide
APS	Atmospheric plasma spray
Ar	argon
BSE	back-scattered electron
CaO	calcium oxide, calcia
Co	cobalt
Cr	chromium
Cr_2O_3	chromium oxide, chromia
Cu	copper
D-Gun	detonation gun
D.C. plasma spray	direct current plasma spray
Fe	iron
Fe_2O_3	iron (III) oxide, hematite
H_2	hydrogen
He	helium
HV	Vickers hardness
HVAF	High-Velocity Air-Fuel spray
HVOF	High-Velocity Oxy-Fuel spray

HVPI	High-Velocity Particle Impactor
Hybrid-HVOF	Hybrid high-velocity oxy-fuel spray (simultaneous feeding of solution precursor and powder)
La_2O_3	lanthanum oxide, lanthana
MDE	mean depth of erosion
$MgAl_2O_4$	magnesium aluminate
MgO	magnesium oxide, magnesia
Mn	manganese
N_2	nitrogen
Ni	nickel
$Ni(NO_2)_2$	nickel (II) nitrate
NiO	nickel oxide
PSZ	partially stabilized zirconia
S-HVOF	Suspension high-Velocity Oxy-Fuel spray
SEM	Scanning electron microscope
SER	steady erosion rate
SiC	silicon carbide
SiO_2	silicon (di)oxide, silica
slpm	standard liters per minute
SPPS	solution precursor plasma spray
SPS	suspension plasma spray
T_m	melting temperature
TBC	thermal barrier coating
Ti	titanium
TiO_2	titanium (di)oxide, titania
V	vanadium
WC	tungsten carbide
WSP	water-stabilized plasma

XRD	X-ray diffraction
Y_2O_3	yttrium oxide, yttria
YAG	yttrium aluminum garnet, $Y_3Al_5O_12$
YSZ	yttria stabilized zirconia
ZrO_2	zirconium (di)oxide, zirconia

ORIGINAL PUBLICATIONS

Publication I J. Kiilakoski, R. Musalek, F. Lukac, H. Koivuluoto and P. Vuoristo. Evaluating the toughness of APS and HVOF-sprayed Al_2O_3-ZrO_2-coatings by in-situ- and macroscopic bending. *Journal of the European Ceramic Society* 38.4 (2018), 1908–1918. DOI: 10.1016/j.jeurceramsoc.2017.11.056.

Publication II J. Kiilakoski, J. Puranen, E. Heinonen, H. Koivuluoto and P. Vuoristo. Characterization of Powder-Precursor HVOF-Sprayed Al_2O_3-YSZ/ZrO_2 Coatings. *Journal of Thermal Spray Technology* 28.1 (2018), 98–107. DOI: 10.1007/s11666-018-0816-x.

Publication III J. Kiilakoski, M. Lindroos, M. Apostol, H. Koivuluoto, V.-T. Kuokkala and P. Vuoristo. Characterization of High-Velocity Single Particle Impacts on Plasma-Sprayed Ceramic Coatings. *Journal of Thermal Spray Technology* 25.6 (2016), 1127–1137. DOI: 10.1007/s11666-016-0428-2.

Publication IV J. Kiilakoski, C. Langlade, H. Koivuluoto and P. Vuoristo. Characterizing the micro-impact fatigue behavior of APS and HVOF-sprayed ceramic coatings. *Surface and Coatings Technology* 371 (2018), 245–254. DOI: 10.1016/j.surfcoat.2018.10.097.

Publication V J. Kiilakoski, R. Trache, S. Björklund, S. Joshi and P. Vuoristo. Process Parameter Impact on Suspension-HVOF-Sprayed Cr_2O_3 Coatings. *Journal of Thermal Spray Technology* (2019), 1–12. DOI: 10.1007/s11666-019-00940-7.

Author's contribution

Publication I

The author deposited the coatings together with laboratory staff, developed the four-point bending test procedure and performed the experiment, planned the in-situ experiment together R. Musalek and performed the experiment, conducted the characterization of the powders and coatings and performed the signal analysis. The author wrote the first draft of the article and revised it based on the comments of the co-authors.

Publication II

The author planned the spray process with J. Puranen, deposited the coatings together with laboratory staff, planned the test procedure and characterization of the coatings and supervised mechanical and cavitation erosion testing of the coatings. The author wrote the first draft of the article and revised it based on the comments of the co-authors.

Publication III

The author deposited the coatings together with laboratory staff, planned the high-velocity impact experiment together with M. Lindroos and M. Apostol, conducted the characterization of the powders, coatings and impact sites and analysed the results together with the co-authors. The author wrote the first draft of the article and revised it together with the co-authors.

Publication IV

The author deposited the coatings together with laboratory staff, planned the micro-impact fatigue test together with C. Langlade and performed the experiment, conducted the characterization of the coatings and impact sites and supervised the cavitation erosion experiment. The author wrote the first draft of the article and revised it based on the comments of the co-authors.

Publication V

The author planned the parameter screening with S. Joshi and R. Trache, deposited the coatings together with laboratory staff, conducted the characterization of the

coatings and performed mechanical and cavitation erosion testing of the coatings. The author wrote the first draft of the article and revised it based on the comments of the co-authors.

1 INTRODUCTION

Surface engineering has been a key technology in increasing the lifetime and performance of engineering components. This has been made possible by improvements in resistance to wear and corrosion of the components, among other added functionalities. Thermal spraying is a surface engineering method that is often the choice when thick coatings on large components are required. [1, 2] In thermal spraying, a coating of tens of micrometers up to some millimeters is deposited by propelling molten or semi-molten material on to a substrate, where it then flattens and solidifies forming a coating. [2] Various materials can be deposited: metals, ceramics, cermets, polymers and mixtures of them. The feedstock can be in the form of powders, wires, cored wires, ceramic cords or rods, suspensions or solution precursors. Various processes can be used in thermal spraying that can differ significantly, most importantly in the way the thermal and kinetic energy are produced; in the case of ceramics typically by electric discharge or combustion of gases.

The global thermal spray market is expected to grow to 14.99 B$ by 2025 at a rate of 6.7 %. The main product areas are aerospace (32.3 % in 2017) and industrial gas turbines and corrosion resistant coatings for the oil and gas industry. [3] Thermal spraying in the Finnish industry is concentrated on the following industries: pulp and paper, aero-engine repair, process industry (valves), power generation and mechanical engineering. Of these, the pulp and paper industry is the largest by volume, with applications like creping and doctor blades, drying and yankee cylinders and center and calender rolls, where hard metal and ceramic coatings are used along with metallic bond coats mainly for wear- and corrosion protection. The used processes comprise virtually all common processes from Atmospheric Plasma Spray (APS), High-Velocity Oxy-Fuel spray (HVOF), wire arc to flame spray. [4] Thermally sprayed ceramic coatings are most commonly deposited by plasma spraying due to the high energy required to melt the feedstock. [2] The biggest drawback of this method is the poros-

ity of the coating. This results in hindered performance in applications requiring liquid- or gas-tightness or resistance to mechanical stresses. Novel spraying methods, such as HVOF spraying of powder feedstock, high velocity spraying of suspensions (S-HVOF) and solution precursor spraying are in early industrial or research stages and are viewed as feasible ways to deposit a dense ceramic coating with advanced properties, such as high density, hardness and wear resistance or non-lamellar, fine microstructure with enhanced toughness. [5, 6]

1.1 Background

The history of ceramic materials goes back millennia. They have always presented a resistance to high temperatures and a stability in various corrosive media. More recently, advanced engineering ceramic have increased the hardness and chemical inertness to enable their use in various applications, such as electrical conductors or insulators, permanent magnets, optical fibers, wear resistant coatings or thermally insulating tiles in space shuttles. The wide range of properties is a direct result of the chemistry and structure of the material. [7]
On the other hand, ceramic materials are known to be brittle, due to their inability to resist crack growth through plastic deformation, which leads to sudden failure through the rapid propagation of the crack. [8] The investigation of fracture mechanics in ceramics began in the mid-1960s, when the effect of microstructure and flaws in the material on its strength could be separated. Soon after, attempts to increase the toughness in ceramics began. Interest in enhancing the properties of ceramics escalated with the discovery of toughened zirconia ceramics, and the realization of the potential of materials design on properties of ceramics. Research on the toughness of ceramics was boosted by the discovery of the indentation technique. It was soon found that the strength of tougher materials after indentation varied significantly less as a function of load after indentation than for brittle materials. That is, their mechanical properties are not affected as much by the presence of cracks. Toughening principles in ceramics are based on the premise that a growing flaw induces greater strength — or fracture toughness — in the material, a property named resistance curve behavior. [9]
The challenge of brittleness in thermally sprayed ceramic coatings is even more com-

plex, as the great amount of defects in the coating act as initiation points for cracking under stress. [10] Effort has been placed in improving the quality of the coating for the whole existence of thermal spraying, but so far few attempts to quantify the damage tolerance of ceramic coatings have been made. For traditional ceramics, some studies have been performed to assess the ductility of different ceramics and thin ceramic coatings [11, 12] but no successful procedure to create new materials that would improve this characteristic for thermally sprayed coatings has been established. The brittleness of ceramic coatings can result in them being discarded in many possible applications, especially ones that include constant impacts or thermal shocks. This gives rise to the necessity for improvement of the coatings toughness, which can be accomplished by tailoring the feedstock material and developing the deposition process.

Methods of improving the fracture toughness of traditional ceramics has been the focus for decades through various methods involving the absorption of strain energy released by cracking. The improvement of toughness leads to the hindrance of crack propagation and formation, which are key components in improving damage tolerance. [9] Many of the toughening methods have been attempted also for thermally sprayed ceramic coatings through

- nanostructures [13, 14]
- metallic additives [15–17]
- oxide-carbide mixtures [18]
- multilayer structures [19]

The determination of damage tolerance of the coatings is typically based on toughness measurements, such as

- qualitative estimation of
  - wear tracks [19–21]
  - indentations [13, 17, 22]
- quantitative results of
  - fracture toughness [23, 24]
  - elastic modulus [25, 26]

None of the methods above are straightforward in terms of determining the strain tolerance of a coating. Qualitative analysis is quite subjective and it can detect modes of failure, not the differences in the propensity for the behavior between similar coatings. The two quantitative methods mentioned are widely used and thought of as a standard in the field. [10] Fracture toughness is an indication of the ability of the coating to

suppress the propagation of a pre-existing flaw. It is often measured by propagating a crack by indentation with a known load, and measuring the distance the crack travels. Elastic modulus is a measure of the coatings stiffness — its resistance to deformation — and it is often measured by depth-sensing instrumented indentation techniques. [10] However, they have underlying assumptions that lower their credibility. There are many formulas used for the measuring of fracture toughness from which to choose from and the measurement itself can be tedious for ceramic coatings that are anisotropic, and in many cases, heterogeneous. This often leads to difficulties in measuring the crack length when the crack is not straight or it doesn't exist in a certain direction at all. In measuring the elastic modulus, a load small enough needs to be used to avoid cracking of the coating which typically leads to the use of nanoindentation inside a scanning electron microscope (SEM) for ceramic coatings, utilizing the Oliver-Pharr method and depth-sensing indentation. However, the recorded values are local intra-splat values and discard the effect of voids, pores and pre-existing cracks and, thus, can not be up-scaled to represent the performance of the whole coating. An additional presumption comes from Poisson's ratio, which is required for elastic modulus calculations but is very challenging to measure from thermally sprayed coatings due to the unique, parameter-dependent, lamellar microstructure. [10] As an example, values of 0.2-0.3 are commonly used for the coatings, but experimental measurements have yielded values between 0.04-0.2 [27] and 0.15 [28], representing a potential error of 500 %. In the end, these types of errors are transferred to the final values through the formula used to calculate the elastic modulus.

Clearly, while a plethora of information can be obtained with current methods as it pertains to general toughness and elastic properties of the coatings, each method comes with presumptions or restrictions that cast some degree of doubt to the applicability of the result. Therefore there is a need to explore the gap between these methods and the damage tolerance of a coating in a more practical sense.

The concept of damage tolerance for the purpose of this work means the statistical reliability of the coating system in an environment where unpredictable and sudden impacts can occur at any moment and the component must be able to continue functioning nonetheless. The inception for the study came purely from practical industrial needs of key components in paper machines, waste-to-energy boilers and metallurgical processes.

1.2 Aim

The intention of the thesis is to bring clarity to the topic of damage tolerance in ceramic coatings, its measurement methods, factors influencing it, and new processes and microstructural tailoring to improve it. While various efforts have been put forth in order to improve damage tolerance, these attempts have been narrow: aimed at one application or one coating and have either settled for laboratory-scale test methods for toughness or have been too focused on a truly application-based test scheme. Thus, the primary goal of this work is to evaluate suitability of different testing methods for damage tolerance, divided in two components: crack-propagation resistance and impact resistance. The second goal of the thesis is to improve the damage tolerance by producing advanced coatings by utilizing novel material combinations and thermal spray methods.

The thesis is a compilation study. The theoretical framework is presented in chapters 2–4, the experimental methodology in chapter 5, the most important results and findings in chapter 6 and the conclusions in chapter 7.The scientific findings are presented in detail in the five original publications appended to this thesis.

1.3 Research questions

This work aims to answer the following research questions:

1. What is damage tolerance in a thermally sprayed ceramic coating and how to evaluate it?
    - Which coating characteristics factor into improving damage tolerance?
    - What is the usefulness of different experimental methods in determining damage tolerance?
2. How to improve the damage tolerance of a thermally sprayed ceramic coating?
    - Which routes in feedstock modification and process selection are beneficial in improving damage tolerance?

Table 1.1 lists the corresponding publications and chapters in this dissertation wherein the above research questions are discussed.

Table 1.1 Research questions

Research questions	1	2
Theme	Measuring damage tolerance	Improving damage tolerance
Publications	I & III & IV	II & V
Chapter	6.1 - 6.3	6.4

2 THERMAL SPRAYING OF CERAMICS

Thermal spraying was discovered in 1909 when the Swiss inventor Dr. Max Ulrich Schoop first applied for a patent for the process called "metal spray" [29]. In the process, a low-melting metal — such as lead or tin — was melted in a modified oxy-acetylene torch and propelled to a surface by pressurized air, forming a coating. [30] Vast amounts of development has occurred during the century since its discovery: today, thermal spraying is a widely used method in depositing thick (tens of micrometers up to some millimetres) coating of essentially any material on a plethora of underlying substrate materials. In modern thermal spraying, the coating material is fed in the form of powder, rod, wire, or — more recently — liquid in to a flame or plume where it is melted fully, partially or merely softened, and propelled towards the substrate by a gas stream. [31] Regardless of the choice of feedstock medium, the result in-flight is discrete particles of various sizes. In this chapter, the formation of a ceramic coating by thermal spraying is step-wise described, with examples of commonly used spray methods. Finally, properties of thermally sprayed ceramic coatings are presented.

2.1 From particles to a coating

The performance of a thermally sprayed coating in a given condition is the direct results of the history of the material forming it. The milestones in the life of an individual particle are essentially feedstock manufacturing, phenomena and interactions during thermal spraying and the deposition and cooling down of the coating. In this section the steps during thermal spraying, in-flight interactions and coating formation are examined more closely.

2.1.1 In-flight interactions of particles

One of the defining parameters during thermal spray processing is the particle size and mass, which leads to different melting degrees not only due to the difference in energy required but, in the case of radial feedstock injection, different penetration depths of the particles in to the spray jet/plasma plume causing a plethora of particle time-temperature histories. [32] The velocity and temperature of the particle are strongly dependent on the size of the particles [33], due to varying dwell-times of the particles in the flame or plasma [34]. The stages the particle goes through are heating of the solid phase, melting, heating of the liquid phase and evaporation. [32] In practice, for the material to be sprayable, the difference between the melting and vaporization temperatures should be at least 300 °C to allow for a reasonable deposition efficiency. [35] The limitations in powder manufacturing methods practically make it impossible to obtain a single particle size, but rather always lead to a distribution of particle sizes. The particle size distribution is characterized by descriptive statistics, such as mean particle diameter or cumulative diameter up to 10 or 90 %, for instance. [2] Since the deposition parameters are optimized for the average size of particles, smaller particles are overheated and larger particles are not heated sufficiently. [32] This, in turn, leads to a heterogeneous coating structure with various phases, unmelted particles and scales of details. [2]

2.1.2 Coating formation

The most important process parameters that control the interaction between the particle and substrate are the particle velocity (specifically the normal component), temperature and diameter of the particle. [35] An illustration of a typical thermal spray process and coating is presented in Figure 2.1. Additionally, the shape and topography of the substrate or already deposited layers play an especially important role. [35] The surface is often roughened prior to spraying to improve adhesion, typically by grit blasting. [36] When a splat impacts the surface, the particle cool-down happens rapidly (up to 10^6 K/s). [30] A single splat flattens in its malleable state in under 5 μs and solidifies in 0.8-10 μs. The splat has a columnar structure with a range of grain sizes typically between 50 and 200 nm. A second molten particle impacts on top of the first splat and repeats the cycle in 10-100 μs and a

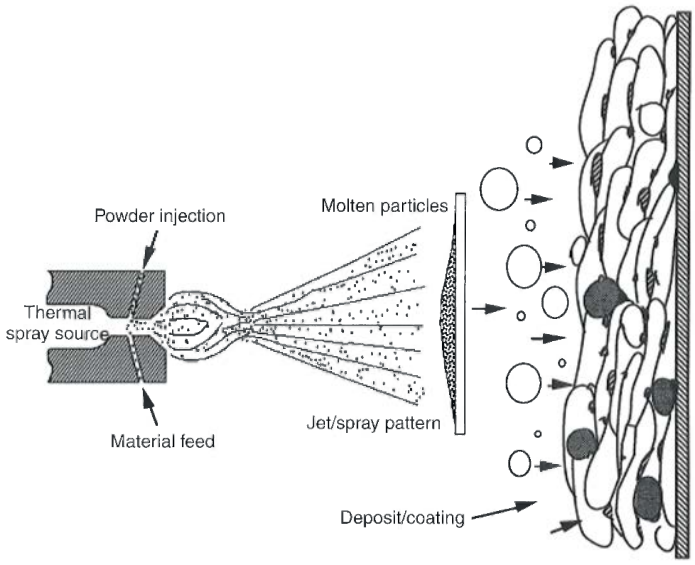

Figure 2.1 A typical thermal spray process and the formation of a coating. [30]

layer of multiple splats is formed in under 10 ms. [35] The contact between the substrate and splat is determined to a large degree by the substrate topography and temperature. Low temperature and high roughness of the substrate promote splashing of the particle, whereas preheating of the substrate along with a smooth topography promote a uniform, lenticular shape with high bonding. [32] Cold substrates often have condensed water on the surface, which vaporizes with the molten material deposited, causing splashing and poor adhesion in the outer rim of the splat. [37, 38] A compromise in roughness has to be reached due to the fact that an important bonding mechanism between the coating and substrate comes from mechanical anchoring, which, in turn, is promoted by high substrate roughness. [39] The phenomenon is further complicated by changes in the substrate, such as local melting caused by an impact of a molten particle with a much higher melting temperature (as is the case with oxides). This also leads to splashing and promotes a "flower structure". [39, 40] SEM-images of a splashed, "flower-like" particle and a lenticular one are presented in Figure 2.2.

The crystal structure in the coating rises from the solidification of individual splats. In a single splat, the nucleation from the liquid phase starts from the contact point with the substrate where the formed grains are equiaxed towards the substrate, to the direction of the flow of heat. At the top section of the splat the grains are more

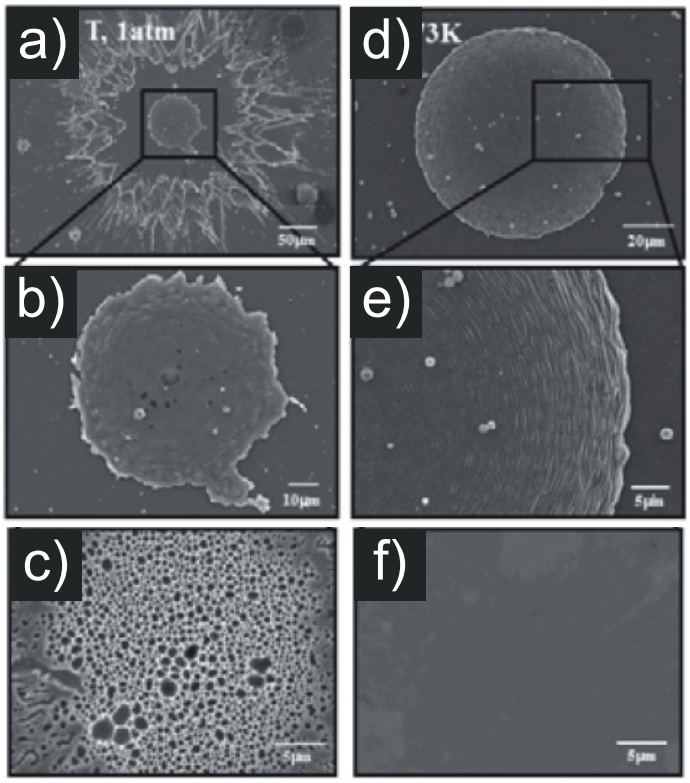

Figure 2.2 SEM-images from Cu-splats deposited at room temperature (a-c) and at 500 °C (d-f). The top surface of the splats are presented in a),b),d) and e), and the bottom surface in c) and f). Modified from [37].

randomly oriented, since the heat conduction is slower through the recently solidified lower part of the splat. [41] An illustration of the heat and liquid flows in a recently impacted splat is presented in Figure 2.3. If the formed phase is metastable, it can be retained to room temperature due to the rapid cooling, as is usually the case with aluminum oxide (Al_2O_3) -coatings, for example, where coatings consist mainly of the metastable γ-Al_2O_3. [42] The impacting of consecutive splats on top of each other eventually forms layers of 5-40 μm thickness during one pass of the spray [31], which on consecutive passes of the spray form the coating. The coating properties are heavily influenced by the thermal history of the sprayed particle from melting to resolidifying, as well as their consequent pile-up. The defects generated at this stage are impossible to remove later. [1, 2] Detrimental defects, such as oxidation, porosity and unmelted particles derive from in-flight oxidation of the particle, poor

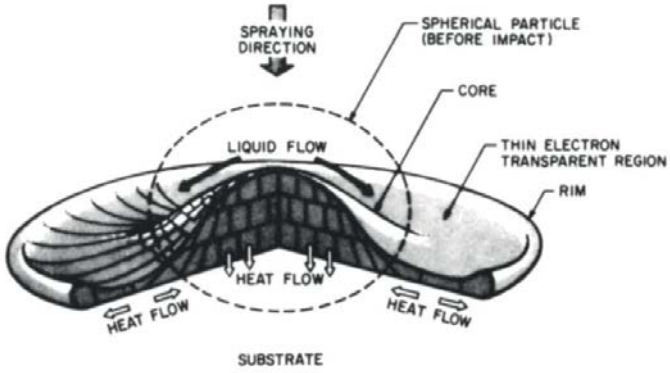

Figure 2.3 A diagram of a particle after impacting onto a flat surface depicting the direction of heat and liquid flows inside the particle [41]

conformity of the molten particle into the topography of the previous layer of coating and poor in-flight melting of the particle, respectively. [36] Other common defects are delamination, spalling and residue grits from the surface preparation by grit-blasting and cracking from the rapid cool-down and mismatch of coefficient of expansion of the coating and substrate. [1, 10]

2.2 Spray processes

Thermal spray processes can be categorized by the type of energy utilized in creating the coating: electric discharge energy (plasma spraying, arc spraying), combustion energy (flame spraying, high-velocity oxy-/air-fuel spraying) and kinetic energy (cold spraying). [1, 10] The choice of process is made based on the material to be sprayed and the required coating properties that, by extension, dictate the needed microstructure. Generally, higher melting materials require either a plasma or gases with high flame temperatures, while dense structures typically require higher particle velocities. Gas temperatures and velocities for various thermal spray processes are presented in a chart in Figure 2.4.

2.2.1 Atmospheric plasma spraying

In atmospheric plasma spraying, the energy source used to melt the feedstock material is a thermal plasma created by ionizing plasma-forming gases with direct current

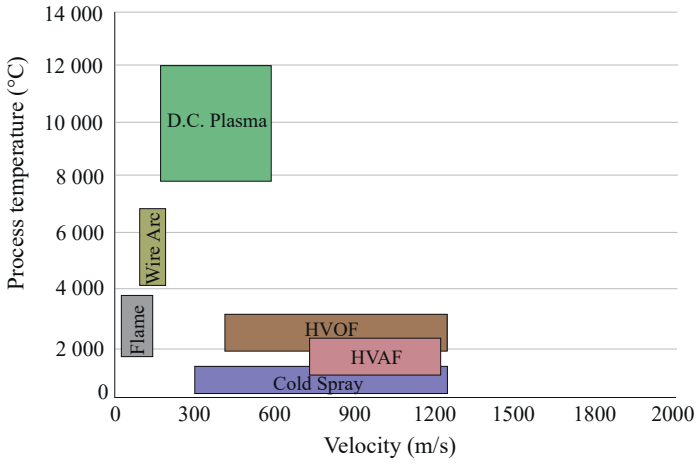

Figure 2.4 Gas temperatures and velocities obtained with different thermal spray systems. HVOF = High-velocity oxy-fuel, HVAF = High-velocity air-fuel, Flame = Flame spray, D.C. Plasma = direct current plasma spray. Modified from [1, 31] and [34]

.

or a radio frequency discharge. Commonly used gases are argon (Ar), helium (He), nitrogen (N_2) and hydrogen (H_2), which are often used in a combination of two or three gases. A primary heavy gas (Ar, N_2) is used for the flow and particle entrapment while a secondary gas (He or H_2) is used to increase the heat transfer through an increase in gas enthalpy. [31] The diatomic gases — N_2 and H_2 — are first dissociated before ionizing, allowing them to produce more energy into the plasma during recombination of the gas atoms. [1, 35, 43] Plasma spraying can be performed in vacuum, low-pressure, or atmospheric conditions. Of these, atmospheric plasma spraying is by far the most economical and the most conventional. Plasma spraying is the preferred method to deposit coatings of high melting-point ceramic materials due the high plasma temperatures of up to 15000 °C [30]. The combination of gases also affect the melting power due to different enthalpies, e.g., an Ar plasma temperature has to be slightly over 10700 °C to melt a tungsten particle, while in Ar-H_2 a temperature close to 8700 °C will suffice. [44] This occurs due to the addition of dissociation enthalpy of diatomic gases to the ionization enthalpy of all gases leading to higher melting energy at lower temperatures. [45]

Most plasma spray systems consist of a rod-type tungsten cathode and a copper anode. The plasma-forming gases flow through them and an electric discharge between them ionizes the gases. Typical gas velocity with nozzle exit diameters between 6 and 8

mm is 500-2600 m/s and power of the plasma is 20-80 kW leading to a high melting degree and typical particle velocities of 100-300 m/s. [31] A schematic of a typical DC plasma torch is presented in Figure 2.5. The powder is usually fed into the plasma

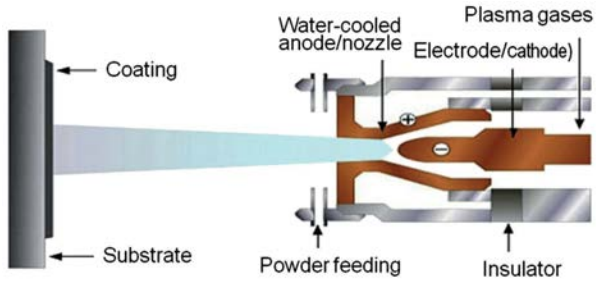

Figure 2.5 A schematic of a typical DC plasma spray torch with radial powder injection. [1]

radially in most equipment using an inert carrier gas, typically Ar or N_2. It is critical to adjust the carrier gas flow so that the powder is injected in to the center of the plasma plume; particles need to have enough momentum to penetrate the plasma but not pierce it. The majority of the powder is naturally desired in the center of the plume where the temperature and the gas velocity are the highest. [46] The benefit of radial feeding is its simple design leading to low cost and the deficit is the difficulty of feeding the powder to the center of the plume. Additional challenges arise from utilizing powders with different densities, particle size distributions etc. Commonly used torches are the F4, Sinplex and Triplex from Oerlikon Surface Solutions (Pfäffikon, Switzerland), 100HE from Progressive Surface (Grand Rapids, MI, USA) and ProPlasma from Saint Gobain Coating Solutions (Avignon, France). A coaxial feed is possible in some torch designs that utilize a three-cathode setup, such as the Axial III from Northwest Mettech Corp. (Surrey, BC, Canada). This enables feeding all of the feedstock powder directly in the center of the plume, improving the deposition efficiency and rate. [1]. Additionally, the three-cathode setup, which is also used in the "Triplex" torch [47], increases the lifetimes of the electrode due to less wear and promotes uniform coating quality due to diminished arc voltage fluctuation. [31] Furthermore, ternary gas mixtures can be used with the HE100 and Axial III, increasing the available power levels to 105 and 120 kW, respectively compared to ca. 40 kW for the single cathode, binary gas torches. [38]

2.2.2 High-velocity oxy-fuel spraying (HVOF)

High-velocity oxy-fuel spraying utilizes a continuous flow of a gaseous or liquid hydrocarbon and oxygen or air to create the required energy for the melting and transporting the feedstock. The gases are injected in to a combustion chamber, where they combust creating a supersonic jet that exits through an accelerating nozzle to exit the torch. The feedstock is usually injected into the combustion chamber axially to maximize the dwell-time and, thus, the melting of the particle, although radial injection in to the throat of the nozzle is also utilized. Combustion gases commonly used in HVOF-processes are H_2, ethene, propane, propene, kerosene and acetylene. [30, 48] Flame temperatures of the most common gases are presented in Table 2.1. In practice, ceramics are sprayed with acetylene or ethene, which have sufficiently high maximum flame temperatures of 3160 °C and 2924 °C [49], respectively. However, some low-melting ceramics, such as titanium oxide (TiO_2), can also be sprayed with H_2 or propane. Typical systems used with ceramic feedstock are HVOF-torches that allow sufficiently low velocities to maximize the melting capacity of the torch, such as the TopGun (GTV GmbH, Luckenbach, Germany) or the HV2000 (Praxair, Danbury, CT, USA). More conventional systems with higher velocities, like the Diamond Jet Hybrid from Oerlikon Surface Solutions AG (Pfäffikon, Switzerland) can be utilized with the lower melting ceramics, when dwell-time is less critical. A schematic of an HVOF-torch is presented in Figure 2.6.

Table 2.1 Maximum flame temperatures of fuel gases and a liquid fuel commonly used in HVOF-spraying. Reproduced from [49].

Fuel	Maximum flame temperature [°C]
Propane	2828
Propylene	2896
Hydrogen	2856
Ethylene	2924
Acetylene	3160
Kerosene	ca. 2900

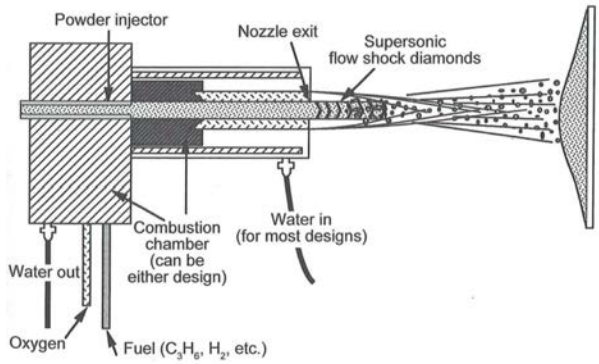

Figure 2.6 A schematic of a typical HVOF-system with its typical features: Fuel and oxygen inlets, mixing block and combustion chamber, powder injector (often axial) and water cooling. [30]

2.3 Properties of thermally sprayed oxide coatings

The majority of thermally sprayed ceramics are oxides, due to non-oxide ceramics being very sensitive to oxidation and decomposition during spraying. [31] Some common oxides used in thermal spraying are chromium oxide (Cr_2O_3), Al_2O_3, zirconium oxide (ZrO_2) and TiO_2. [1] Although oxides withstand the melting and re-solidifying well, most oxide-coatings have a different phase composition than the feedstock (notable exceptions being magnesium aluminate, $MgAl_2O_4$, and Cr_2O_3). [50] Oxide materials are characterized by the predominantly ionic bond between a metal and oxygen, leading to high melting points due to the high bond strengths. [7, 8] Well-documented beneficial properties of thermal spray oxides are low thermal conductivity, stability at high temperatures, wear resistance, electric insulation and corrosion resistance. [51] However, due to their high stability and melting point, restrictions and challenges in thermal spraying regarding the equipment and feedstock emerge. In the following, typical characteristics of spraying some oxides — and properties thereof — are described.

2.3.1 Characteristic properties of oxide coatings

Thermally sprayed ceramic coatings are used in various applications due to many of them having multifunctionality. Properties such as wear and corrosion resistance combined with electrical or thermal properties are not uncommon. [52] Yet, the

coatings always have inherent drawbacks in comparison with the same materials in bulk, which necessitate exploration.

2.3.1.1 Mechanical properties

The lamellar structure described in section 2.1.2 leads to anisotropic mechanical properties for the coatings and, thus, the properties vary significantly in the parallel and perpendicular directions from the substrate. [10] Additionally, the pores and cracks inherent in the coating structure further reduce the mechanical properties of the coatings. [53] In practice, a bond coat is often applied on to the substrate prior to the deposition of the ceramic coating. This reduces the thermal mismatch between the substrate and the coating, improves adhesion of the ceramic and can act as a corrosion barrier to prevent degradation of the substrate. The addition of a bond coat increases the complexity of the system, making a sandwich-like structure and evidently influencing the mechanical properties of the ceramic coating by altering the deformation mechanism of the splats. [10]
An important characteristic of thermal spray coatings that influences the mechanical properties vastly, is residual stresses generated during the spray process. Residual stresses arise from three parts

i. **Quenching stresses** from the cooling and shrinking of a splat after deposition. [54]

ii. **Peening stresses** from impacts from incoming particles onto the substrate or underlying coating layers. This is mainly pronounced with high-velocity processes and when the impacting particles are not fully molten. [55]

iii. **Differential thermal contraction stresses** from differing coefficients of thermal expansion between the coating material and the substrate. [54]

The final stress state of the coating is a result of all three, and can change within the coating structure, as presented in Figure 2.7. The stresses can play in favor of hardness and wear resistance if they are compressive, but can also hinder the same properties when excessive tensile stresses exist.

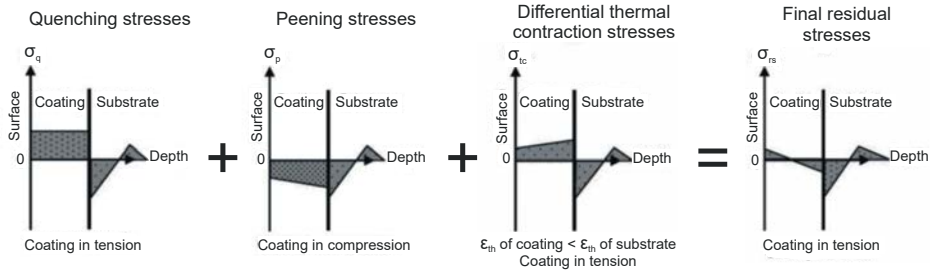

Figure 2.7 A schematic representation of the accumulation of stresses leading to the final stress state in a ceramic coating. Modified from [10] based on [56]

Thermally sprayed ceramic coatings typically exhibit tensile residual stresses, due to their inability to deform by peening and a large component of quenching stress. The stresses can however be slightly compressive close to the surface as presented in Figure 2.7 due to the thermal mismatch between the coating and the substrate. [57] Thermally sprayed ceramic coatings are typically among the hardest along with carbide coatings, but the variation is wide: From ca. 600 HV_{300} for yttria-stabilized zirconia (YSZ) to ca. 1200 HV_{300} for Cr_2O_3. [2] However, the structure of the coating has in many cases a more significant effect on hardness than the material, and therefore the spray process and process parameter selection are elemental. [58]
Wear resistance in general is favored by high hardness, which makes ceramic coatings attractive in wearing applications. However, wear is a system property, where coatings structure — cohesion and density — and residual stresses play a key role. [2] Therefore a direct correlation from hardness to wear cannot be established in thermally sprayed coatings.

2.3.1.2 Chemical properties

While oxide materials are stable in atmospheric conditions, they can be subject to chemical attack in other environments. As metals are easily oxidized in the presence of excess oxygen, so are oxides subject to reducing back to metals in a sufficiently reducing atmosphere or oxidizing to a higher oxide if such a phase exists. [8] Ceramic coatings — such as Al_2O_3 or Cr_2O_3 — are a viable option against chemical degradation in high temperatures, especially in steam environments. [59] Due to their chemical resistance, ceramic coatings are used as a protective coating, where no discontinuity is allowed. The tiniest crevice would inescapably lead to rapid pitting corrosion of the

(usually) less-noble metal substrate. [39] The through-porosity of the coatings often lead to the necessity of using a protective bond-coat, as often the interface suffers from intense local corrosion, leading to delamination of the coating. [60]

2.3.2 Chromium oxide (Cr_2O_3)

Thermally sprayed chromium oxide coatings are some of the most used due their high density, hardness and wear resistance, particularly against sliding wear. They are also insoluble in acids, alkalis and alcohol. Cr_2O_3 has a melting point of 2435 C. [31] Cr_2O_3 can be sprayed with APS, HVOF, detonation gun (D-Gun) or flame spray, but due to its high melting point APS is the conventional choice. The coatings can have very high hardnesses of up to 1900-2000 HV_{5N} [36], and wear resistance among the highest in the family of oxide coatings especially in sliding wear applications, where Cr_2O_3 can even be considered as a replacement for HVOF cermets. [61] Cr_2O_3 is an excellent choice of coating material especially when corrosion resistance is wanted in addition to the wear resistance: it shows mainly inert reactions with most alkalis and acids. [59, 62]

Chromium oxide has a clear green color in its stoichiometric Cr_2O_3-form. Typically, however, the spray powders are black, with a sub-stoichiometric compound of Cr_2O_{3-x} ($x \approx 0.01$). The coatings are usually black due to reduction occurring in spraying, especially in plasma-spraying, leading to a reduction in corrosion resistance and the occurrence of pure metallic chromium. [63, 64] The biggest drawback with thermally sprayed Cr_2O_3-coatings is their tendency to vaporize and form gaseous oxide and hydroxide compounds during spraying according to Equations 2.1 and 2.2 [65–67]

$$Cr_2O_{3(s)} + \frac{3}{2}O_{2(g)} = 2CrO_{3(g)} \tag{2.1}$$

in a dry atmosphere, or

$$Cr_2O_{3(s)} + 2H_2O_{(g)} + \frac{3}{2}O_{2(g)} = 2CrO_2(OH)_{2(g)} \tag{2.2}$$

in a wet atmosphere. This not only lowers the deposition efficiency, but also leads to an incoherent structure where resolidified Cr_2O_3 can be found in the splat borders. Additionally, the high melting point leads to high quenching stresses during cooling of the splat, which are relaxed by microcracking of the coating. [68] Cr_2O_3 is often

mixed with small amounts of TiO_2 or Al_2O_3 in order to lower the melting point, reduce oxygen loss during spraying and increase the sprayability by reducing the tendency to vaporize. [63, 69, 70] The alloying leads to a one-phase structure with low amounts of TiO_2 (Al_2O_3 and Cr_2O_3 are fully miscible), and usually lowers the hardness and wear resistance in relation to the amount of the alloying constituent. Furthermore, the hydrogen containing atmosphere in conventional APS processes can lead to a reduction of Cr_2O_3 to Cr, CrO and Cr_3O_4. [64, 71] Plasma-sprayed chromium oxide coatings are used in movable parts in water pumps and seals, printing/anilox rolls, protective coatings for steel rollers for ore classification. [62]

2.3.3 Aluminum oxide (Al_2O_3)

Aluminum oxide in its stable form is corundum (α-Al_2O_3), has a melting point of 2050 °C, good mechanical properties and high chemical stability. [52] Thermally sprayed Al_2O_3 coatings are typically sprayed by APS, flame spray, D-Gun or HVOF, with the first two producing a typical lamellar microstructure and the last two a finer, denser structure due to the possibility to use finer feedstock. Hardnesses range from 800 HV to 1200 HV. [52] Al_2O_3 coatings are susceptible to corrosion in acidic and basic solutions due to the predominant amount of the metastable γ-phase in comparison to the more stable α-phase. [72–74] Al_2O_3 coatings are used in, e.g., sink rolls in the steel industry, electrical insulators, decorative coatings, furnace linings and pump seals. [1, 75] To circumvent the impairing effect of γ-Al_2O_3, alloying of the feedstock powder with Cr_2O_3 has been shown to lead to a retention of the α-phase of up to 100 % retention with Cr_2O_3 amounts upwards of 20 wt.%. [76] Another way of stabilization is the use of suspension feedstock with suitable parameters, that has been shown to lead to high α content. [77] A special mixture of Al_2O_3-13TiO_2 has been developed to increase the deposition rate, toughness, corrosion- and wear resistance of alumina coatings, while keeping the beneficial properties of hardness and sprayability. [78] This is realized by the lowering of the feedstock melting temperature towards the eutectic formation temperature of the liquid phase at 1840 °C leading to a denser microstructure. [52]

2.3.4 Titanium oxide (TiO_2)

Titanium oxide is a fascinating material due to the ability of titanium dioxide to readily lose oxygen and form suboxides with planar stacking faults (so called Magnéli phases). [79] Thermally sprayed coatings containing typically a mixture of substoichiometric titania, where the oxide vacancies are distributed heterogeneously, leading to different properties depending on the configuration. [80] The amount of oxygen can also change as a function of temperature either during the spraying or in service, leading to (typically undesired) changes in the coating properties. The challenge of obtaining a desired phase structure when processing titania, either in powder manufacturing or during thermal spraying can be envisaged from the Ti-O phase diagram presented in Figure 2.8. Some sought after properties of titania include photocatalysis [81], high electrical conductivity of the substoichiometric Magnéli phases [82], and good tribological properties of the rutile [83] phase of TiO_2. TiO_2 is sprayed by flame spray, APS or HVOF from rod, powder or liquid, and it being one of the easiest oxides to spray due to its low melting point. [80] The hardnesses of titania coatings are in the order of 730-800 HV depending on the spray method. [2] Despite the lower hardness the higher toughness allows the wear resistance to be close to that of most other oxides. [84, 85]

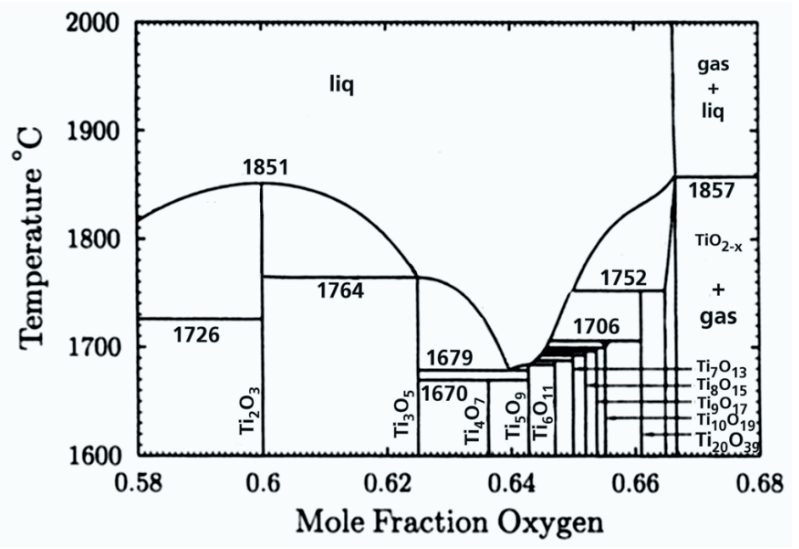

Figure 2.8 The Ti-O phase diagram in the composition range between Ti_2O_3 and TiO_2. [79]

2.3.5 Zirconium oxide (ZrO_2)

Zirconium oxide is a very refractory ceramic with a melting point of 2716 °C and it can exist in three phases: monoclinic (m), tetragonal (t) and cubic (c). The transformation between the phases is temperature dependent; in room temperature monoclinic is the stable form which transforms into tetragonal with increasing temperature by 1170 °C, after which the t-structure transforms into cubic zirconia starting at about 2370 °C. [86] All the transformations are martensitic, i.e., diffusionless, athermal (transformation over a range of temperatures instead of a specific temperature) and involving a shape deformation. [87] The shape deformation is important, since it includes a volume change. For example, when cooling (as in the case of cooling down of a thermally sprayed coating) ZrO_2 the volume increase is approx. $c \longrightarrow t$: 2.31 % and $t \longrightarrow m$: 4.5 %. [86] This phenomenon leads to a deterioration of mechanical properties of the coating, but the created porosity through the crack network can be utilized to the benefit of thermal insulation as is the case in thermal barrier coatings (TBC). [88] To diminish the volume change the zirconia can be alloyed with lower valence oxides, such as CaO, MgO, La_2O_3 and Y_2O_3 to stabilize the c and t lattice structures in room temperature. This occurs by the replacement of the Zr^{4+} ions by the dopant ions and the consequent vacancies in the structure to keep the neutral charge. [89, 90] Achieving partial stabilization of the zirconia by optimizing the amount of the dopant is sometimes favored in traditional ceramics in order to achieve a crack-arresting behavior. This occurs by a metastable t'-phase transforming into m-phase in the presence of a crack leading to an increase in volume and an ensuing arresting of the crack. [91] An illustration of this phenomenon is presented in Figure 2.9. However, the usefulness of the crack-arresting behavior is dubious in thermal spray coatings, where the microstructural cohesion is already a critical factor and the pre-existing pores and cracks can accommodate deformation, thus diminishing the size of the zone of influence of the phase change. [57]

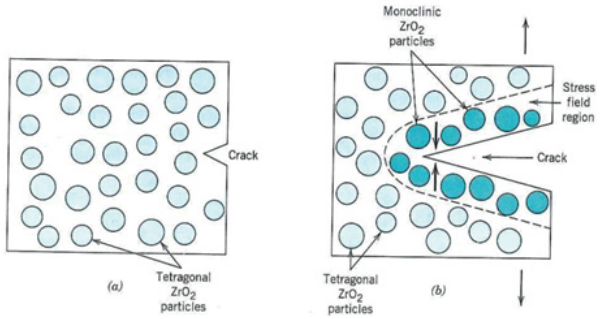

Figure 2.9 Schematic demonstration of transformation toughening. a) A crack prior to inducement of the ZrO_2 particle phase transformation. b) Crack arrestment due to the stress-induced phase transformation. [91]

ZrO_2 is usually sprayed from powder, sometimes also suspension or solution, with a plasma-spray system due to the high melting point [92] and in practice, it has one important application as a thermal spray coating: thermal barrier coating (TBC) in gas turbines aerospace and energy production industries. [59] Their market accounts for 60 % of the total thermal spray market [93] Other uses are as solid ionic conductors and corrosion-resistant coatings in lambda probes of combustion engines. [59]

2.3.6 Aluminum oxide-zirconium oxide (Al_2O_3-ZrO_2)

Zirconia toughened alumina presents a special case of an alloy due to its large scale use in traditional ceramics. [94, 95] While ZrO_2 has a high melting point, the eutectic mixture of Al_2O_3-42,5ZrO_2 has a lower melting point than even alumina [96], leading to good sprayability of the material. The abrasion wear resistance of the coatings has been reported to increase when compared to pure alumina, in some cases even dramatically, while the hardness remains comparable. [97, 98] The aspiration is that the addition of zirconia would toughen the alumina coating, as it does in traditional ceramics [99], but this theory in coatings is unproven and debated, due to the incohesiveness and high amount of defects in the nature of thermally-sprayed coatings. [42] This leads to an inability to relieve stresses from a large volume of coating by a simple phase-change. The Al_2O_3-ZrO_2 coatings are sprayed by APS or HVOF and the hardnesses are in the order of 800-1100 HV. [97, 100] The wear resistance has, in some cases, been very high; even comparable to Cr_2O_3-coatings.

[98]

2.3.7 Other oxides

Magnesium aluminate has been studied as a coating for electrical insulation. [101, 102] The addition of MgO into Al_2O_3 increases electrical resistivity and gas permeability of the coatings compared to pure alumina coatings. An issue is the hydrophilic nature of the coatings which decreases the insulation manifold in higher humidities. Another application is in lambda-sensors in combustion engines. [1]

Mullite and Zircon are compounds of Al_2O_3 or ZrO_2 and SiO_2, respectively. These coatings have low coefficients of thermal expansion making them useful in high temperature applications. [103] Indeed both can be used in heat-exchanger tubes to protect silicon-based ceramics against the alkali salts and water vapor. [103, 104] Other application for mullite are cooling liners in combustion chambers of gas turbines [105], additives in TBCs [106] and components requiring electrical resistivity [107]. Zircon can be potentially used as a TBC or instead of PSZ especially when producing self-standing components, although it readily decomposes to its constituents, ZrO_2 and glassy silica. [108] It is possible to recombine the coating back to zircon. [109]

YAG (yttrium aluminum garnet) has the composition of $Y_3Al_5O_{12}$ can be used as a thin coating to measure surface temperatures by spraying undoped [110] or doped either with dysprosium [111] or europium [112] with solution precursor plasma spray (SPPS). The doping leads to photo-luminescent properties. Another promising future use of YAG is as a binder for silicon carbide (SiC) to create extremely hard SiC-containing coating. This is possible by surrounding the SiC particles by YAG to prevent oxidation of the SiC. [113] Additionally, YAG does not react with SiC. [114]

3 DAMAGE TOLERANCE IN THERMALLY SPRAYED CERAMIC COATINGS

Damage tolerance is a multi-dimensional system property of a coating. The term tolerance, indicates a type of reliability, which is indeed accurate for ceramic coatings where a single microscopic flaw can produce a catastrophic failure of the whole component. The flaw can be pre-existing or produced, for example, by an unexpected impact. The property that is nowadays understood as damage tolerance is a combination of wear resistance, corrosion protection, fatigue resistance and adhesion to the substrate. These properties are a product of the following processing effects: Residual stresses, feedstock alteration during spraying, microstructure of the coating and properties of the substrate. [115] The description of damage tolerance is illustrated in Figure 3.1. Since a majority of applications for thermal spray coatings have some form of impact, erosion or contact wear [116], it is of importance to assess these properties and how to improve them for ceramic coatings.

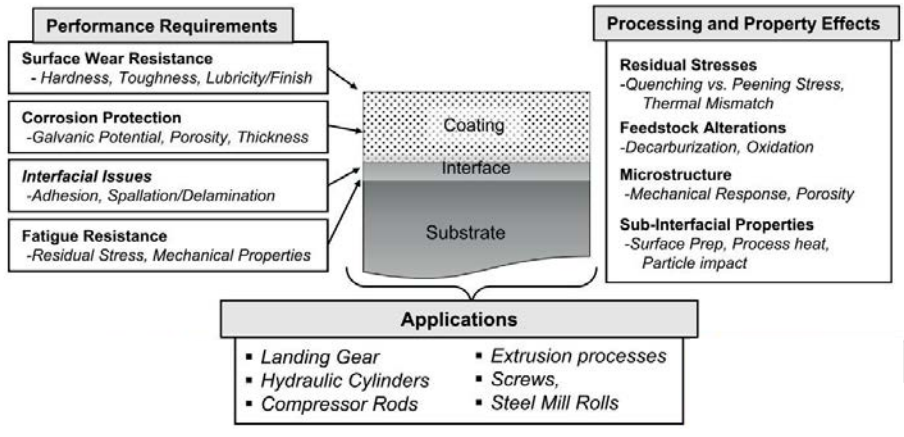

Figure 3.1 Performance and processing considerations in producing damage tolerant coatings. [115]

It is currently understood that the hardness of a brittle thermally sprayed coating is a poor indicator of its wear resistance, in experimental set-ups and in real life. Rather, fracture toughness has shown a stronger correlation to wear properties. [117, 118] Additionally, based on the characteristics of ceramic coatings that they are intrinsically more apt to resist chemical attacks than sharp mechanical impacts (as described in section 2.3.1), prioritizing wear resistance to corrosion resistance is agreeable.
The typical mechanism of wear for ceramics is brittle fracture with almost no prior plastic deformation. The phenomenon includes crack initiation and propagation perpendicular to the applied load. The crack propagation in crystalline solids, such as ceramics, occurs usually through the grains and along planes of high atomic density. [2, 91] Once the crack reaches a critical size, determined by the fracture toughness of the coating, the component fails. [8, 9, 119] An illustration of this is shown in 3.2. Damage tolerance in traditional ceramics is understood as a measure of load between the onset of first cracking and final failure [120], allowing time to replace a component before an abrupt process stoppage, for example. Increasing this means essentially giving more time to notice the impeding failure before a costly breakdown, while not compromising on the other required properties, such as corrosion resistance or low porosity. For thermally sprayed ceramic coatings, additional issues arise from

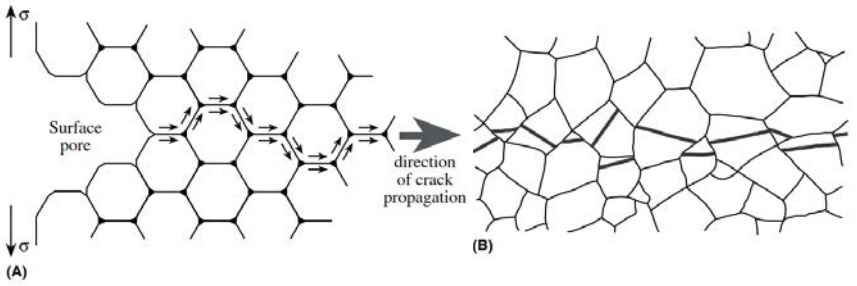

Figure 3.2 Illustrations of a) intergranular cracking and b) transgranular cracking. [7]

the defects in the coating structure (described in detail in 2.1.2). They have shown significantly lower fracture toughness values in the in-plane direction compared to out-of-plane direction. [121] This is a direct result of the anisotropy of the lamellar structure. Pores, pre-existing cracks from thermal mismatches, interlamellar interfaces and un-/semi-melted particles all have to be considered when attempting to toughen coatings. [2] Some coating defects and properties can be detrimental to toughness, such as pores and poor cohesion between lamellae [122], while others

might be considered useful. These include poorly melted particles [13], pre-existing microcracks [9] and residual stresses [123]. In general, high density and homogeneity (or at least homogeneous distribution of dispersions) are desirable for coatings to optimize their structural integrity and thus mechanical properties.
The damage tolerance investigation in the scope of this thesis can be divided in two components as stated in 1.2: crack propagation resistance and impact resistance. The division is two dimensional — resulting from the discussion above, increasing damage tolerance means, in other words, to hinder crack propagation in the coating without compromising other properties. While these results are an indication of potential for the system, there is a need for practical validity of the results: when considering different applications and the environments that ceramic coatings must endure, often the situations where ceramic coatings fail mechanically are caused by either small repeated impacts or isolated higher energy impacts. Therefore it is essential to have sense of the applicability of the results to real-life conditions. In other words, crack propagation resistance is though of as a material/coating property, while impact resistance is a system property.

3.1 Improving the damage tolerance of thermally sprayed ceramic coatings

Significant improvement in the crack propagation resistance or fracture toughness and impact resistance of thermally sprayed coatings have been reported by optimizing the coating architecture through novel processing routes. These routes include the addition of a metallic constituent to the feedstock, use of nanostructured powder feedstock or the use of suspension feedstock.

3.1.1 Influence of metallic additions

A logical path to increase damage tolerance is through increasing the toughness of the coating system by adding an already tough material as a constituent in the coating. Metals make for an obvious choice, while care has to be taken to preserve the beneficial characteristic properties of a ceramic coating. Advances in ceramic-metallic coatings are presented in this section.

Aluminum additions have been used in powder feedstock of iron oxide (Fe_2O_3) [22] and Fe_2O_3 / Cr_2O_3 [124] to achieve reactive plasma spraying of the thermite system. The resulting structures composed of $FeAl_2O_4$, Fe, AlFe, Al_2O_3 and Cr. The wear volume in abrasion decreased from 0.78 mm^3 to 0.55 mm^3 with the addition of Cr_2O_3, both significantly less than a reference coating Al_2O_3 (2.31 mm^3). The $Al/Fe_2O_3/Cr_2O_3$-coating had more numerous hard Cr particles, which lead to higher crack propagation resistance and was believed to attribute to the lower abrasion wear. Al was also added to conventional Al_2O_3 powder to obtain a coating with lower hardness, but 22 % higher fracture toughness, higher bending strength via three-point bending of free-standing coatings, and adhesion to substrate. [125, 126]

Ceramic composite powders containing Ni and NiO alloyed with Al_2O_3 have been synthesized from AlO(OH) and $Ni(NO_3)_2$. [26] These coatings where compared with the pure Al_2O_3 constituent, along with other ceramic-ceramic composites. In the study, improvement in fracture toughness was achieved with both the Ni and NiO -additions, but the variation of the results was very large, indicating inhomogeneous coating quality. The metallic addition did not enable reaching the toughness values of Al_2O_3-ZrO_2, Cr_2O_3, or Cr_2O_3-ZrO_2 in the same comparison. Additionally, the wear resistance was subpar and the hardness lower. The beneficial effect in crack length reduction from a Vickers indentation on the metallic Ni-addition was seen with 5 % or more Ni, while 2 % did not yet show an improvement. However, the hardness and wear resistance were already with 2 % Ni. [127]

It is known that the corrosion and wear properties of porous ceramic coatings can be improved drastically by sealing as a post-treatment. [128, 129] One method of sealing is with a metallic addition, for example Mn-alloys in liquid form [130] or by electrodeposition of Ni [16] or Cu [20]. Clear improvements have been found with these metals in Vickers hardness (10 %, [16, 20]), erosion rate (<50 %, [16, 20]) and fracture toughness (>2x, [130]). Additionally, scratch tests have been performed on some samples that showed brittle fracture on the unsealed ceramic coating versus plastic deformation on the Cu-sealed coating, Figure 3.3. An observation can be made on the issue of scale; a larger particle size of the feedstock material typically leads to a coarser microstructure, where the sealing provided a more significant improvement than with finer feedstock and finer microstructure. [16, 20]

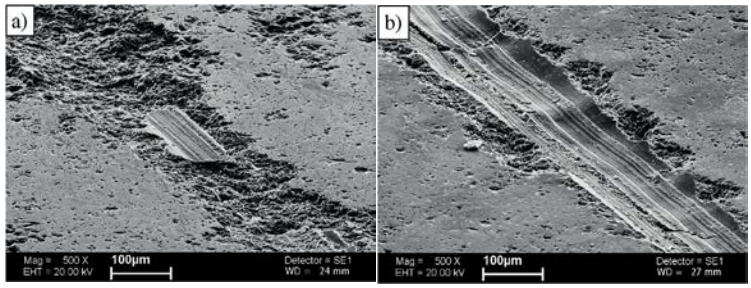

Figure 3.3 Single scratches on a) an unsealed Al_2O_3 coating showing predominantly brittle fracture and b) a Cu-sealed Al_2O_3 coating showing predominantly plastic deformation highlighting the effect of a metallic addition in a thermally sprayed ceramic coating. SEM-images. [20]

3.1.2 Nanostructured coatings

Nanostructured materials have drawn wide interest in the research community due to the Hall-Petch empirical formula that suggests improving mechanical properties with decreasing grain size. In theory, decreasing the crystal grain size to < 100 nm can lead to superplasticity (elongation of 100-1000 % before fracture), but so far this phenomenon has not been proven in temperatures under $0.5T_m$ [131, 132]. Recently, some research has shown amorphous nanometric films of alumina to present viscous flow in room temperature. [133]

3.1.2.1 Nanostructured coatings from powder feedstock

The influence of nanostructured powder feedstock on the properties of thermally sprayed ceramic coatings has been studied widely. In most cases the feedstock has been manufactured by agglomerating and sintering (A&S) nanosized primary particles and sprayed by HVOF instead of plasma spray to avoid fusing of the nanoparticles during melting in a plasma plume. [5, 134] Coating optimization regarding the characteristics mentioned in the beginning of the chapter is made possible with powder manufacturing by agglomeration and sintering. [5, 135, 136] Compositions, such as Al_2O_3-$13TiO_2$ [137], TiO_2 [13, 138] and Cr_2O_3-$25TiO_2$ [137], have been studied. Improvement in wear resistance of HVOF-sprayed nanostructured A&S Al_2O_3-$13TiO_2$ was found when compared to its fused and crushed counterpart. The distribution of phases in the coating is vastly more homogeneous, stemming from the better mixing of the nanosized constituents in the powder particles. The larger and

softer TiO_2 lamellae were more prone to wear, acting as the "weak-link" and leading to pull-out of the alumina-regions. [137] Similarly, wear resistance was improved for the A&S TiO_2-coating, due to better melting of the surface of the particles leading to better interlamellar cohesion and consequently better wear resistance. [17]
A similar observation was made by Lima et al. [13] when comparing HVOF-sprayed TiO_2-coatings from fused & crushed (F&C) and A&S powders. The biggest discovery was the bimodal and isotropic nature of the coating from nanostructured feedstock. The bimodality is caused by the A&S-particles being 'semi-molten' during deposition, leading to sufficient melting of the surface to deposit, but retaining the nanostructured nature inside the particle. The nanostructured zones acted as crack arresters (an example presented in Figure 3.4) leading to an improvement in crack propagation resistance from a Vickers indent of 65 %, even though the hardness was slightly lowered. Additionally, the wear volume in abrasion and bond strength were improved.

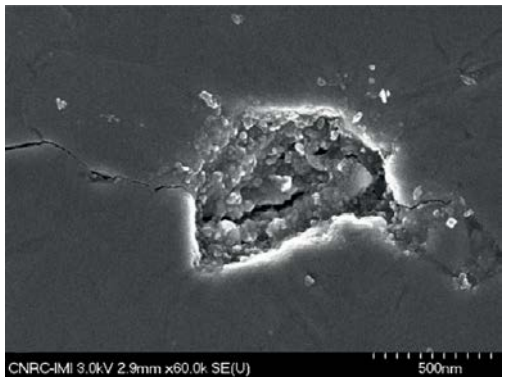

Figure 3.4 A Vickers indentation crack arrested by an embedded nanostructured zone in a coating. [13]

Various other studies have been published in this topic, usually comparing APS and HVOF sprayed Al_2O_3-13TiO_2 and/or TiO_2 coatings from F&C and A&S (nanostructured) powders. In many [138–141], the conclusion is that the partially molten A&S particles lead to embedded nanostructured zones in the coating that arrest cracks and lead to improved mechanical properties. The bond strength improvement seems to derive from the partially-melted regions to steel having a higher adhesion with steel than the fully-melted regions. [142] The reason for this was deemed to be unclear for the moment.

3.1.2.2 Nanostructured coatings from liquid feedstock

Utilising a liquid instead of a gas as the carrier of feedstock creates many possibilities of microstructure tailoring. The two common processes utilize either suspensions (ceramic particles suspended in liquid) or solutions (dissolved chemicals leading to an in-situ reaction during deposition). [5] Since the primary particle-size can be small (nanometer scale) without prior agglomeration, it is reasonably facile to obtain a nanostructured coating — albeit with these techniques a myriad of challenges related to the spray process arise, as well. [5] Most of the common oxides used in thermal spraying have been also sprayed and investigated in suspension or solution spraying for which particle sizes of 10-500 nm are commercially available.
Typically the coatings produced from suspension feedstock have at least comparable and usually superior wear and corrosion properties when compared to coatings from similar powder feedstock. [143, 144] This results from complete melting of the nanoparticles during spraying leading to very thin lamellae with a smaller crystal size than is obtainable with conventional methods. The rate of cooling can be fast enough to promote homogeneous cooling rather than heterogeneous common in traditional methods, leading to the absence of columnar crystals altogether (see Figure 3.5) [5, 145]. Consequently, with the reduction of the scale of lamellae, also the average pore size and — thus — amount of porosity is smaller. [143]

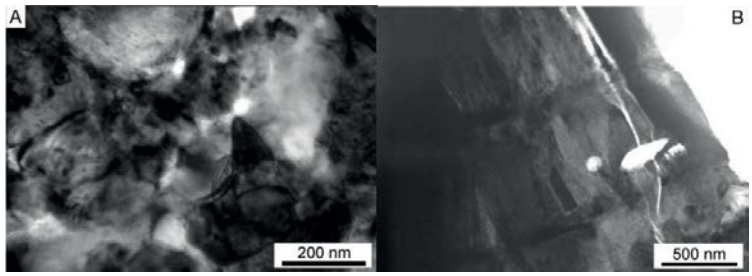

Figure 3.5 TEM micrographs showing the difference in grain-size and type between suspension-sprayed and HVOF-sprayed TiO_2. a) S-HVOF coating with disordered equiaxed grains of <200 nm b) HVOF coating with columnar crystals. [145]

The crack propagation resistance (i.e. toughness) has been found to be higher for S-HVOF-sprayed than suspension plasma sprayed (SPS) Al_2O_3-40ZrO_2 coatings. [14] The cause for this was determined to be finely dispersed unmolten tetragonal and

monoclinic ZrO_2 particles in a matrix of Al_2O_3 and Al_2O_3-ZrO_2 acting as crack arresters, analogous to the discussion in the previous section 3.1.2.1. Toughness was found to correspond well with erosion resistance, but not abrasion resistance. The lower melting power of S-HVOF additionally led to a higher retention of t-ZrO_2 and α-Al_2O_3 than SPS, stemming from unmelted particles, in addition to nearly 50 % of amorphous phase. Micrographs of the cross-sections of the SPS and S-HVOF sprayed coatings are presented in Figure 3.6.

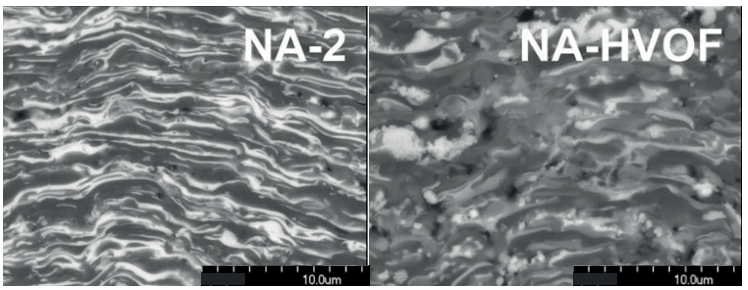

Figure 3.6 Cross sectional micrographs of an SPS coating from nanometric feedstock (NA-2, left), showing distinct lamellar structure and an S-HVOF-sprayed coating from the same nanometric feedstock (NA-HVOF, right), showing a complex lamellar structure containing amorphous Al_2O_3-ZrO_2 pseudo-alloyed and embedded unmelted clusters of submicron zirconia particles. Modified from [14]

Fracture toughness has been shown [95] to increase from 2 $MPam^{1/2}$ to 4 $MPam^{1/2}$ between APS Al_2O_3 and SPS Al_2O_3, with an additional leap to 8.5 $MPam^{1/2}$ for simultaneous feeding of Al_2O_3 and YSZ suspensions. The improvement is attributed to a higher amount of α-Al_2O_3 in the more dense SPS-coating, which has been shown to lead to higher fracture toughness over α-Al_2O_3 in S-HVOF-coatings [146]. The high contribution of YSZ to the toughness of the coating led to the vast increase for the mixed suspension coating. The utilisation of suspensions lowered the friction coefficient and in the case of Al_2O_3-YSZ a reduction of wear rate by an order of magnitude, while hardness was higher in the APS-coating. Solution precursor-spraying has led to very fine nanostructures in the coating due to the in-situ reaction in the flame. For example, Al_2O_3-ZrO_2 [147], Al_2O_3 [148], TiO_2 [149] have been successfully processed into coatings from precursors. Since the coating is formed from nanoparticles synthesized in the plasma or flame, the deposition rate of the coating is often low — e.g. around 0.5 μm/pass. So far mechanical properties have not been in

the focus of research for these coatings since they are still in the exploratory stage of the technology.

4 DETERMINING THE DAMAGE TOLERANCE OF A THERMALLY SPRAYED CERAMIC COATING

The first step in optimizing a coating for damage tolerance is to develop valid methods to measure and evaluate the required properties. Measurement of toughness of thermally sprayed ceramic coatings has some issues due to their brittleness; most methods of measurement, such as a tensile test, are developed for metallic materials, while others, such as the four-point-bending test, are mainly used for bulk ceramics. The relatively low thickness of thermally sprayed coatings makes it often difficult to produce self-standing samples and, thus, requires them to be assessed on top of the substrate, which has to be accounted for when selecting experiments for the coatings. This eliminates many methods such as the aforementioned traditional tensile test, where load-displacement data would be heavily impacted by the properties of the substrate. Impacting experiments have been developed for ceramic coatings in numbers, but the challenge lies in obtaining some that give pertinent, quantifiable information especially in the view of restricting catastrophic failure. Various types of indentation and impact-related results and hypotheses related to determining toughness in ceramics and ceramic coatings are presented.

4.1 Crack propagation resistance

The measurement of crack-propagation resistance requires the generation of a flaw or a crack, and the observation of the growth of the flaw until failure. The crack is usually induced either by inducing a tensile stress mode to the coating by bending or by indenting with a sharp object. These two cases are individually examined in the

following sections.

4.1.1 Bending experiments

Four-point bending tests for coatings in order to determine toughness have been widely performed. Measuring the acoustic emission (AE) signals gives a proven tool to determine the starting of subsurface cracking and it has been found to give useful information when combined with four-point bending of metallic- [123], ceramic- [150–153] and hard metal coatings [154, 155] or tensile testing of ceramic coatings [156]. In the experiment, a tensile stress is induced to a coating on a substrate by bending. The AE-sensor (or sensors) is usually attached on the uncoated side of the substrate [123] or on the bending jig [151] mechanically, by spreading silicon grease on the substrate surface to improve contact. Most frequently investigated outputs are threshold-passing signal counts and peak amplitude, which essentially means counting the number of cracking events and the "severity" of the individual cracks, respectively. An illustration of a test setup is presented in Figure 4.1.

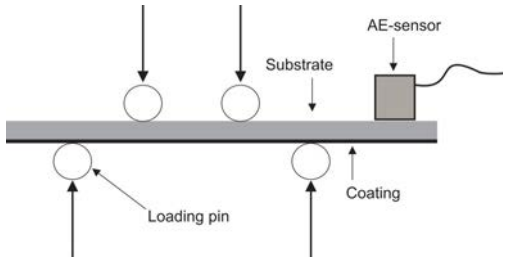

Figure 4.1 A schematic of the experimental setup of the four-point bending. [Publication I]

When using multiple sensors it is also possible to locate the positions of the cracks. [150] The strain of the coating can be measured with strain gauges [123, 150] or it can be calculated according to beam theory from the displacement data of the universal testing machine where the AE-signal is fitted to indicate the onset of cracking (Figure 4.2) [151, 154]. The signals obtainable from acoustic emission include signal counts, peak amplitude and its rise time, ringdown counts and the energy of the wave. [123, 150–152, 154] In ceramic coatings, catastrophic failure can be differentiated from a more gradual microcracking by assessing the normalized AE intensity versus strain or deflection. [153] Residual stresses play an essential role in interpreting the results

of the test and they should be counted for in the test. [123] The experiment has been

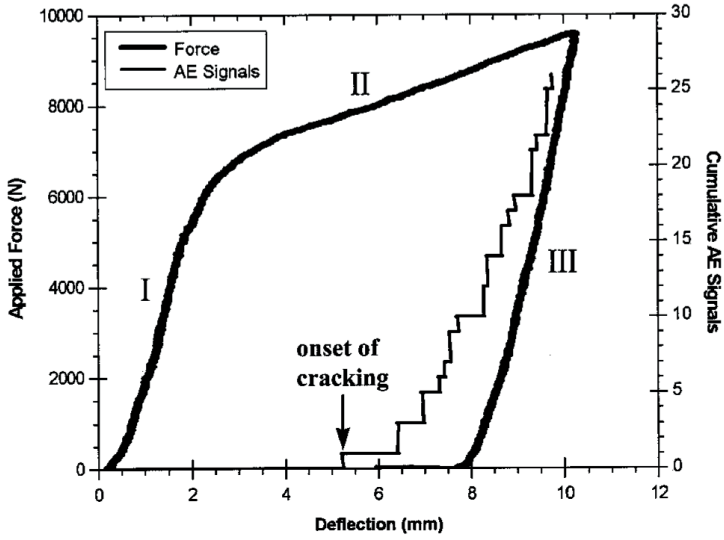

Figure 4.2 AE-measurement data fitted in the same graph with the results from the bending test. Area I is elastic- and area II is plastic deformation. Area III is the removal of external load. [123]

found to be very repeatable, as 56 repetitions performed by Cox [154] resulted in a variation of 7.3 % in hard metal coatings. Additionally she found no correlation between strain-to-fracture with hardness and a high correlation with residual stress using multivariate correlation.

The most critical issue in measuring acoustic emission is elimination of sources of noise that can lead to false positives in the signal processing. For example Yao et al. [156] determined the characteristic frequencies for cracking of TBC coatings in a tensile test as follows: random signal from the substrate at 140 kHz, a vertical crack in the coating at 220-250 kHz and cracking in the coating/substrate-interface or delamination at 80-100 kHz, clearly indicating the potential of AE to distinguish between different types of failure. Typically noise is recorded in the lower end of the spectrum of acoustic emission. In the experiments found in the literature, the noise value has usually been measured by running the test for the substrate and determining a threshold value for the signal. [123, 151] Signals that surpass this value must hence originate from the coating. A graph of the strength of an AE-signal as a function of strain is presented in Figure 4.3, illustrating the small background noise of a substrate and the acoustic noise exceeding the threshold. The point where the acoustic signal surpasses the threshold value of the substrate, can be indicated as strain-

to-fracture, i.e., the moment of failure of the coating. Bending of a thermally sprayed

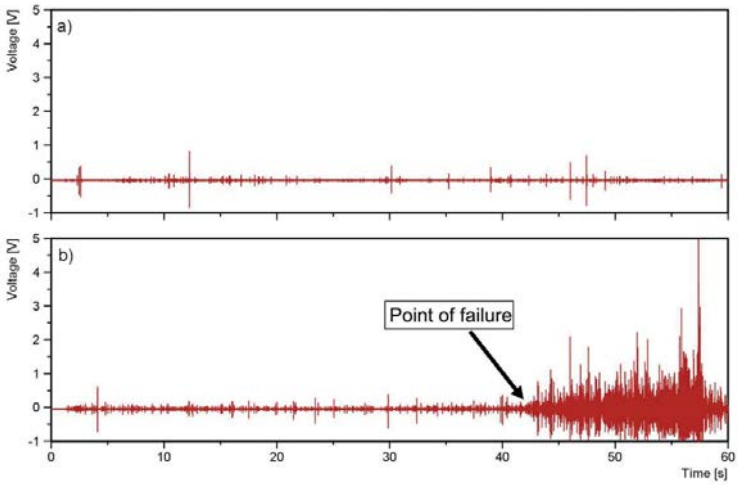

Figure 4.3 Graphs of the AE-signal vs. time of a) an uncoated and b) a sample coated with a ceramic during four-point- bending. [Publication I]

self-standing alumina coating has been examined in-situ in an SEM by Mušálek et al. [157], proving the feasibility of providing additional fractographic information on the cracking behavior of the coatings. Intrasplat cracking, intersplat decohesion, splat sliding, interlinking of pores and pore compaction were found as the phenomena occuring during tensile straining of the coating. Smith et al. [121] prepared self-standing coating samples in the parallel and perpendicular direction to the substrate, and found that the flexural strength in three-point bending was ca. 30 % smaller in the perpendicular direction.

4.1.2 Indentation techniques

Indentation by a diamond indenter is one of the most used measures of fracture toughness, i.e., crack propagation resistance. [10] Intersplat cohesion has been found to be a key factor in the coatings ability to resist crack propagation [158], while indenting the top surface tends to be linked to material property and indenting the cross-section is more indicative of the lamella cohesion [159]. Similarly, crack tortuosity (the total length of a crack compared to the distance between its end-points, i.e., "curviness of pathway") has been shown to be higher in the perpendicular than parallel directions, when a cross-section of a ceramic coating is indented. [121] This is proportional to

crack propagation resistance and shows that in the parallel direction the crack can propagate reasonably unscathed.

Mušálek et al. [160] studied spherical indentation on thermally sprayed Al_2O_3-coatings and found cracking, closing of existing cracks, debonding and sliding at splat interfaces, indicating the possibility of a behavior analogous to quasi-plasticity. Indentation hardness provides a numeric value of the coating cohesion. However, especially in thermally sprayed ceramic coatings it is vital to have a reliability estimate for the coating due to the existing flaws potentially acting as weakest links. Microhardness in combination with Weibull modulus can be use to find a more detailed response of the coating to fracturing, and has been shown to provide a useful classification method. [161] The effect of load on indentation hardness was investigated by Lima et al. [6] for HVOF-sprayed TiO_2 coatings. They noticed a transition that was deemed to represent the junction between micro- and macrohardness. Rather than looking at the hardness number directly, they were comparing the change in the Weibull distribution of the hardness values. They discovered that after an indentation volume of 500 μm^3 (macrohardness region), the amount of defects under the indent becomes constant and in larger loads than that the hardness value and the Weibull modulus are relatively constant. This means that with lighter loads the local heterogeneity of the coating affects the hardness and thus would imply the existence of a similar transition point for these coatings than what was discovered by Quinn et al. [162] for bulk ceramics. They determined an aptly named "brittleness" term consisting of hardness, elastic modulus and fracture toughness and found that increasing load leads to change in the response of the material to the indenter. This leads to a hypothesis that being able to increase the Weibull modulus would increase reliability and predictability of the coating behavior, like Lima et al. [6] achieved for their coatings when compared with traditional plasma-sprayed coatings, due partly to non-lamellar uniform microstructure, which agrees with the above speculation on lamella cohesion being one of the limiting factors of crack propagation resistance.

An interesting observation made in traditional ceramics is that when the ceramic is fatigued with a spherical indenter, the failure evolution starts with a "brittle" cone-crack followed by "quasi-plastic" radial cracking. [163] The quasi-plasticity stems from dissipative slipping at shear faults, such as weak particle/matrix interfaces. [164] The result is deformation in lieu of catastrophic brittle fracture, which is typically the more desirable outcome in practice. Lee et al. [165] found that higher toughness of a

thin film led to suppression of cone-cracking with less strength degradation and these coatings give the prospect of an "early warning" prior to failure due to substantial distributed and detectable damage prior to failure.

4.2 Impact resistance

Different domains can be distinguished within impact resistance in order to approach the phenomenon: the shape of the impacting object and the velocity of the impact. For the intent of this work, the main focus will be placed on spherical impacting objects, since the aim is to not crack the coating, which is often the case for ceramics impacted by sharp objects. First, spherical indenting will be reviewed on traditional ceramics and coatings, followed by erosion and impact studies on them.
One of the common impacting experiments, albeit typically used to measure wear resistance, is erosion. It is well known that the erosion modes of ductile and brittle materials differ fundamentally. Ductile materials erode by plastic deformation mechanisms, while brittle materials develop micro-cracks that lead to median- and lateral cracking in the macroscale and subsequent chipping of material. The angle for maximum erosive wear in ductile materials is 15-30° and for brittle materials 90° [2, 166] However, some brittle materials have been found [166] to behave similarly to ductile materials in certain types of erosion; the maximum erosive wear in these cases happens in the same range as for ductile materials, at about 30°. This is achieved with decreasing the size of the impinging particles and it is connected to the “ductile-brittle transition” of ceramics that changes the wear mechanism fundamentally. This is of fundamental interest since it drops the erosion rate dramatically. Hence ceramic components might be used in erosive applications where the impingement angle is low but erosive particles are small as well. The mechanism for the erosion wear has been suggested to be similar to that of scribing, where the average pressure and threshold loads for median and lateral cracking are dependent on the wearing particle’s geometry, which is opposite to that of indentation. [166] Tests have been made comparing the effect of scribing with the face of a particle leading and with the edge leading, as shown in Figure 4.4. Sparks and Hutchings [167] eroded a glass ceramic with angular and rounded silica particles and glass ballotini of sizes 125–150 μm. The authors noticed a sharp transition in the wear rate with the rounded silica particles at 30° impact angle at a velocity of about 50 ms^{-1} in their experiments. Above the transition

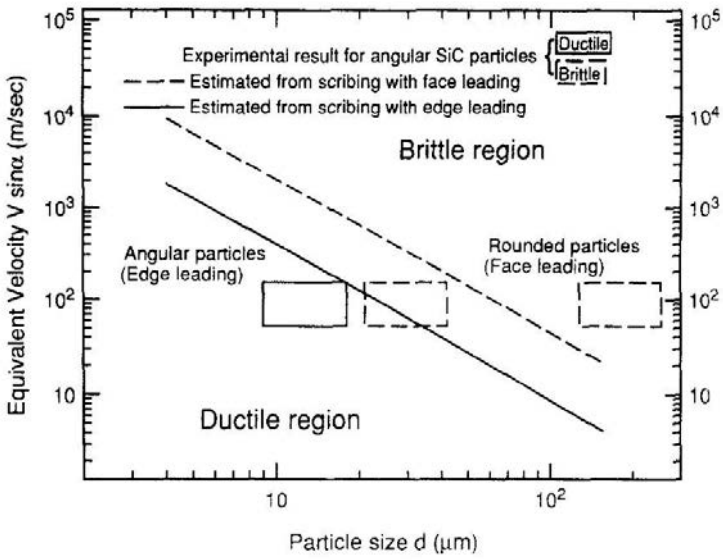

Figure 4.4 Approximate predictions for the velocity and particle size at which the brittle-ductile transition occurs in glass. The two cases considered are indenters with edge leading or face leading. [166]

(rounded particles with high velocities and angular particles with all velocities) they noticed wear to occur by lateral fracture and flaking. Below the transition velocity with rounded particles they deemed wear to occur by material removal via small fragments after accumulated plastic strain and fracture. A third type of wear they determined was by the glass ballotini at 90° and above 87 ms^{-1}, where wear occurred by fine-scale fracture with much less plastic deformation. This behavior was named elastic fatigue wear. The results of Finnie [166] and Sparks and Hutchings [167] suggest that it might be possible to rank the ductility of brittle materials based by their behavior in different erosion conditions by varying the size, shape, velocity and impact angle of the particles.

A micro-impact fatigue equipment has been used in various works, for example by Ledrappier et al. [168], to test the behaviour of thin films under repeated impacts in the millimeter scale. By varying the impact conditions, progressive damage evolution could be observed, starting with buckling followed by blistering/spalling followed by film failure from a delaminated surface. Micro-impact in an even smaller micrometer scale can be evaluated by cavitation erosion. Matikainen et al.[21] were able to identify factors affecting the erosion rate of ceramic thermally sprayed coatings as

the cohesion and resistance to brittle fracture of the coatings. This property could be improved by inducing a quasi-plastic behavior into the coating, similarly to what Mušálek et al. [160] and Lima et al. [6] discussed for indentations.

5 MATERIALS AND METHODS

This chapter summarizes the experimental setups used in the original research articles of this thesis. It presents the feedstock materials and spray processes used to produce the coatings, as well as the coating characterization methods. Emphasis is placed on the unique measurement methods used for evaluating the damage tolerance of ceramic coatings.

5.1 Feedstock & coating deposition

In this study, commercially available powders were deposited by an HVOF-process (TopGun, GTV Gmbh, Luckenbach, Germany) and an atmospheric plasma spray process (A-3000S 4/2 system and F4 torch, Oerlikon Metco AG, Winterthur, Switzerland) with a Plasma Technik A-3000S 4/2 plasma spray system. Additionally, the aforementioned HVOF-process was used to deposit a commercial suspension as well as a solution-precursor/powder mixture, both fed with a liquid feeder made in-house, that was equipped with a closed-loop mass-flow meter to stabilize the liquid flow rate and either a pressure vessel or a diaphragm pump feeding mechanism. Additionally, an injection setup of the powder into the liquid for the "Hybrid"-spraying was made in-house based on the model of Björklund et al. [169]. The feedstock materials and spray processes are presented in Table 5.1. The detailed process parameters can be found in the original publications appended to this thesis.

Table 5.1 Coatings studied in this work. Powders manufactured by fusing and crushing unless otherwise indicated.

Material	Manufacturer	Commercial name	Size distribution (μm)	Spray process
Cr_2O_3	H.C. Starck	Amperit 704.001	-45+22	APS
TiO_2	H.C. Starck	Amperit 782.1	-45+22	
Al_2O_3-40ZrO_2	Ceram	-	-51+20	
Al_2O_3-42.5ZrO_2	Millidyne	A104	-41+10(*	
Al_2O_3	H.C. Starck	Amperit 740.001	-45+22	
Cr_2O_3	Saint-Gobain	2022	-15+5	HVOF
Cr_2O_3-3TiO_2	Millidyne	C103	-30+10(*	
Cr_2O_3-5TiO_2	Millidyne	-	-25+8(*	
Al_2O_3	H.C. Starck	Amperit 740.008	-20+5	
Al_2O_3-40ZrO_2	Ceram	-	-25+5	
Al_2O_3-42.5ZrO_2	Millidyne	A104	-27+10(*	
Al_2O_3-20YSZ Al_2O_3-40YSZ Al_2O_3-40ZrO_2	H.C.Starck - Sigma-Aldrich	Amperit 740.008 - Experimental	-20+5 (powder)/"nano" (solution)	Hybrid-HVOF
Cr_2O_3	Treibacher AG	Auercoat	-8+0,4	S-HVOF

(* Powder manufactured by agglomerating and sintering.

5.2 Materials characterization

The microstructure of the coatings and the feedstock were studied from polished cross-sections or morphological samples with Scanning Electron Microscopes (SEM) (Philips XL30/Helios Nanolab 600, FEI, Hillsboro, Oregon, United States or EVO 15/ULTRAplus/Crossbeam 540, Zeiss GmbH, Jena, Germany). The phase compositions of some coatings and powders were studied by X-ray diffraction (Cu-Kα radiation) (D8 Discover XRD, Bruker, Karlsruhe, Germany or Empyrean, Malvern PANalytical, Malvern, United Kingdom). The microhardness of the coatings was measured from ten indentations on the coating cross-section using a Vickers hardness tester (MMT-X7, Matsuzawa Co., Ltd., Akita, Japan), in most cases with a load of 300 gf ($HV_{0.3}$) with the exception of two thin S-HVOF coatings that were tested with a load of 50 gf.

5.3 Evaluation methods for damage tolerance

In this section, equipment and experiment used for the specific purpose of evaluating the damage tolerance of the coatings are presented.

5.3.1 High-velocity particle impactor

The damage tolerance of plasma-sprayed Cr_2O_3 and TiO_2 was tested with the high-velocity particle impactor (HVPI) to shed light on the cracking behavior and crack propagation of ceramic coatings under high-strain rate high-stress impacts in Publication III. The high-velocity particle impactor utilizes a computer controlled pressure air reservoir to accelerate a projectile through a smooth bore barrel towards the substrate that can be positioned to the desired angle between 10° and 90°. The velocity of the projectile is measured with a ballistic chronograph placed in front of the sample, and a high-speed camera (Memrecam fx K5, nac Image Technology, Simi Valley, CA, USA) was used to calculate the exit velocities of the projectiles after the impact. A schematic of the impactor is presented in Figure 5.1 The projectiles in this study were

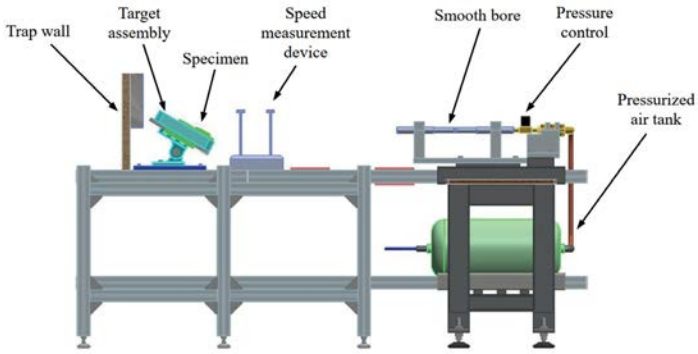

Figure 5.1 A schematic of the high-velocity particle impactor. [170]

steel balls of diameters 5 and 9 mm, and the incident velocities were around 47 and 35 m/s, respectively. The energy dissipated in the coating-substrate system could be calculated from deducting the kinetic energy of the projectile after the incident from its kinetic energy before the incident following Equation 5.1

$$E_d = E_{inci} - E_{refl} = \frac{1}{2} m_p (v_{inci} - v_{exit})^2, \tag{5.1}$$

where v_{inci} is the incident velocity, E_{inci} is the incident kinetic energy, v_{exit} is the exit velocity and E_{refl} is the kinetic energy of the reflected projectile. The experimental data can be found in Table 5.2. The surfaces and cross-sections of the impact scars were examined by SEM (Philips XL30, FEI, Hillsboro, Oregon, United States).

Table 5.2 Parameters for the HVPI-experiment

APS coating	Impact angle [°]	Projectile diameter [mm]	Projectile mass [g]	Projectile incident velocity [m/s]
Cr_2O_3	15	9	2.9	34.7±0.5
		5	0.51	48.0±0.0
	30	9	2.9	34.3±0.5
		5	0.51	47.3±0.5
TiO_2	15	9	2.9	35.0±0.0
		5	0.51	47.7±0.5
	30	9	2.9	35.0±0.0
		5	0.51	47.3±0.5

5.3.2 Instrumented four-point-bending

Instrumented four-point bending was utilized to asses the crack propagation resistance of the ceramic coatings in tensile stress in Publication I. A universal testing machine (Instron 8800, Norwood, MA, USA) was utilized with a 100 kN load cell and a four point bending jig. The coatings were placed in tension with the span of the inner support pins being 45 mm and the outer support pins 110 mm. Acoustic emission monitoring was used to record cracking events with a piezoelectric sensor (8313, Brüel & Kjær, Nærum, Denmark) placed on the uncoated side of the substrate. A schematic of the test procedure is presented in Figure 5.2. The resonance frequency of the sensor was 200 kHz and it was attached to a data acquisition unit (input module 9223 in cDAQ9174, National Instruments, Austin, TX, USA) via a pre-amplifier (2637, Brüel & Kjær, Nærum, Denmark). The sampling frequency was 1 MHz and the data was analysed with a signal processing software (DIAdem, National Instruments, Austin, TX, USA). The samples were bent with a constant speed of 10 mm/min until a displacement of 10 mm. This led to a 14±0.5 mm displacement at the middle of the

samples. The acoustic energy E_{AE} emitted during bending was calculated according to the Equation 5.2 [171]

$$E_{AE} = \frac{1}{R}\int_{t_1}^{t_2} V(t)^2 dt, \tag{5.2}$$

where R is the electrical resistance of the pre-amplifier (10 kΩ is chosen per convention) and V is the amplitude of the signal. A threshold value of energy was calculated by bending two uncoated samples and the total acoustic energy emitted was averaged. When a coated sample reached the threshold, a "strain-to-fracture" was obtained using beam theory according to Equation 5.3

$$\epsilon[\%] = \frac{436Dh}{L^2}, \tag{5.3}$$

where D is the displacement at mid-span, h is the thickness of the sample and L is the distance of the outer pins.

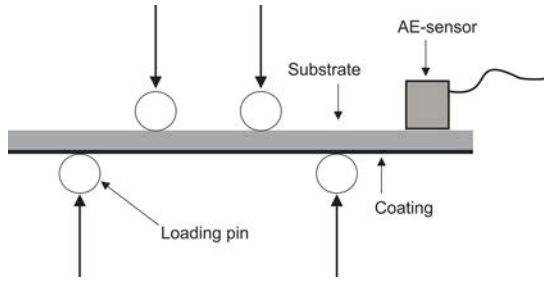

Figure 5.2 A schematic of the experimental setup of the four-point bending. [Publication I]

5.3.3 In-situ three-point bending

Additional insight on crack propagation in the coatings was aimed to be obtained from in-situ analysis of stepwise bending in Publication I. The in-situ bending was performed inside a low vacuum in a scanning electron microscope (SEM) EVO MA 15 (Carl Zeiss AG, Oberkochen, Germany) with a Microtest 200 N tensile tester (Deben UK Ltd., Suffolk, United Kingdom) at the Institute of Plasma Physics (Prague, Czech Republic). The outer span of the three-point bending setup was 23 mm, and BSE imaging was used to record the event. The samples were cut from as-sprayed

samples and ground and polished from the face of the cross-section with a standard metallographic procedure with the final polishing done with colloidal silica (OP-S). The dimensions of the samples were ca. 1.5 x 1.5 x 30 mm. The thickness of the coating remained at 0.3-0.35 mm. The samples were loaded in tension and a displacement rate of 0.1 mm/min was used. The bending was interrupted periodically to document the evolution of failure in the coating by a high-resolution image. Three samples were tested for each coating to increase reliability.

5.3.4 Micro-impact fatigue

The micro-impact fatigue properties of ceramic coatings was tested in Publication IV with an in-house made apparatus at Université de Technologie de Belfort-Montbéliard (Sevenans, France). The schematic is presented in Figure 5.3 and a detailed description of the device is available in [168, 172, 173]. The device uses an electromagnet to accelerate an indenter towards the coated surface with a predetermined frequency, in our case 10 Hz. The load induced through the sample is measured by a load sensor from the substrate side of the sample and the velocity of the indenter is measured optically. The indenter was a 2 mm diameter ZrO_2 ball, and the initial distance between the indenter and sample was 0.7 mm. In the experiment both the excitation time (acceleration) of the indenter and the number of repetitions was varied. The sample surfaces were ground and polished before the test. The impact energies ranged from 0.7 to 5 mJ and the impact craters were examined with an optical microscope and an optical profilometer (Infinitefocus G5, Alicona Imaging GmbH, Raaba, Austria). Raman spectroscopy was performed on APS and HVOF sprayed pure Cr_2O_3 coatings

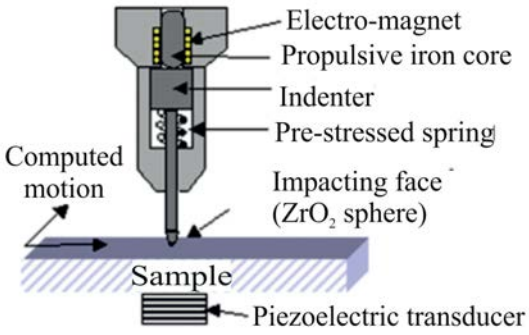

Figure 5.3 A schematic presentation of the micro-impact fatigue test apparatus. Modified from [168]

and impact debris with a Raman microspectrometer (XPlora+, Horiba, Kyoto, Japan) at Université de Technologie de Belfort-Montbéliard (Sevenans, France). A green laser wavelength of 532 nm was used for all tests. Several objectives (x10, x50 and x100) were used and the nominal laser power of 25 mW has been reduced from 100 to 0.1% to study the thermal sensibility of the various samples. Each analysis lasted from 30 to 180 seconds and several acquisitions were accumulated to reduce the signal/noise ratio. Considering the theoretical optical properties of Cr_2O_3 crystals, the theoretical penetration depth was estimated to be 350 nm.

5.3.5 Cavitation erosion

Cavitation erosion was utilized in publications I, II, IV and IV as an indication of the cohesion of the coatings as the cavitation erosion resistance is typically proportional with good cohesion. [21, 100, 174, 175] The experiment was performed with an ultrasonic transducer (VCX-750, Sonics & Materials Inc, Newtown, CT, USA) according to the standard for indirect cavitation erosion ASTM G32-10. The vibrating tip of the transducer was made of Ti-6Al-4V. The samples were cleaned in an ultrasonic bath with ethanol prior to weighings that were conducted periodically during the experiment. In publications I and IV the samples were ground flat up to a 3 μm diamond finish using a standard metallographic procedure but were later tested as-sprayed, as this was found not to provide any significant difference in the case of ceramic coatings. The total duration of the test was 90 minutes, and the samples were weighed at 15, 30, 60 and 90 minutes. The mean depth of erosion (MDE) was calculated from Equation 5.4

$$MDE[\frac{\mu m}{min}] = \frac{1000[\frac{\mu m}{mm}] * SER[\frac{mm^3}{h}]}{60[\frac{min}{h}] * A[mm^2]}, \tag{5.4}$$

where SER (steady erosion rate) is the volume loss of the sample during the last hour of testing to remove the effects of surface roughness and bubble incubation stage and to lend credibility into the long term cavitation resistance of the coating. A is the surface area of the vibrating tip. For volume loss calculations the coatings were presumed fully dense for simplicity. Cavitation erosion resistance was calculated as the reciprocal of MDE.

6 RESULTS AND DISCUSSION

The main results from publications I-V are presented in this chapter. The results are divided in three sections. Section 6.1 discusses the effect of the material selection and microstructure of the coatings on the impact resistance component of damage tolerance. Section 6.2 presents the main finding on the evaluation of crack propagation resistance on the Cr_2O_3, TiO_2 and Al_2O_3 -based coatings. Section 6.3 presents a compilation of the results of cavitation erosion leading to a discussion on the factors affecting the cohesive strength of ceramic coatings.

6.1 Impact resistance of ceramic coatings

The impact resistance of ceramic coatings was measured with repeating small energy impacts in Publication IV and high-energy single impacts in Publication III. The microscope images of craters from the micro-impact fatigue experiment with constant repetitions and varying acceleration times are presented in Figure 6.1. With the shortest excitation time (0.7 ms, cumulative energy ca. 1.3 J), very slight indents were formed — if any — depending on the coating. When increasing the acceleration, for most coatings the damage accretion was gradual as seen from the enlargement of the impact sites all the way until the highest excitation time of 1.1 ms (ca. 4.5-5 J). A stark contradiction to this general behavior was evidenced in HVOF-sprayed Cr_2O_3-based coatings that seemed to resist the impact well in lower energies, but with higher energies failed catastrophically. The effect of the thermal history is evidently crucial in order to minimize the residual compressive stresses [176, 177]. These stresses can on one hand be beneficial for hardness and wear resistance in milder conditions but on the other, can cause catastrophic failure when impact energies rise above a critical level. In the literature, compressive stresses are usually deemed beneficial to tensile fatigue [178–180] but clearly the combination of compression, tension and shear

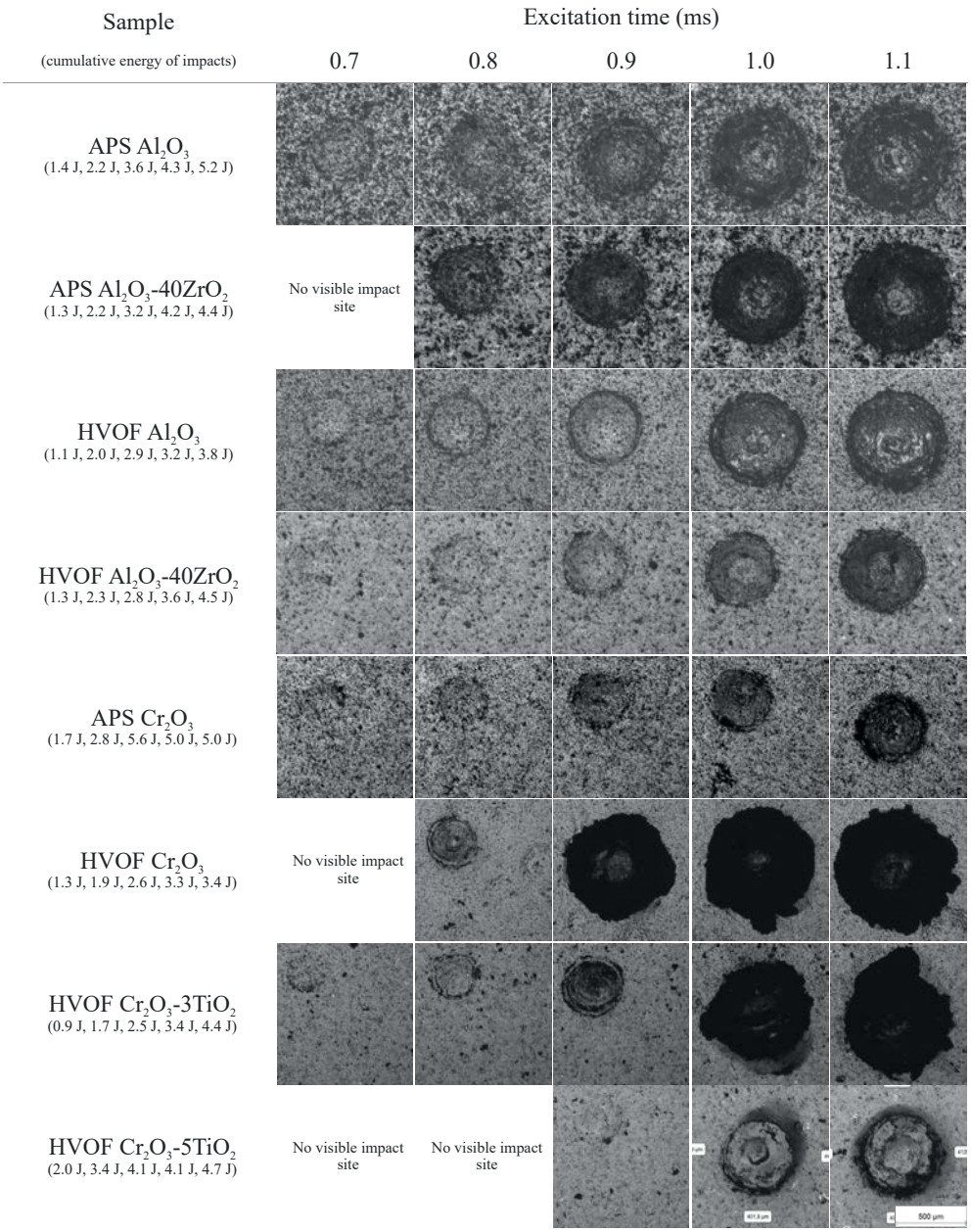

Figure 6.1 Micro-impact fatigue craters on ceramic coatings with varying impact energies and fixed repetitions [Publication IV].

complicate the situation in terms of clearly distinguishing the beneficial properties of the coating against micro-impact fatigue.

In order to quantify the damage accretion, the coating failures were determined from the incremental increase in crater volumes. This practice was adapted from a phenomena seen in traditional ceramics, where the strength of the ceramic suddenly collapses as a function of either load or number of cycles [163, 181]. In the case of coatings, measuring the strength evolution is not straightforward, and therefore crater volume was used. Further examination was conducted by keeping the respective excitation times of failure for each coating constant, but varying the impact repetitions from 100 to 800. The resulting impact craters are presented in Figure 6.2. All coatings displayed a visible crater already with 100 repetitions and for most the damage accretion was gradual like in the initial experiment. Once again the HVOF-sprayed Cr_2O_3-based coatings were the exception, by failing catastrophically when their endurance limit was reached.

The volumes of the craters were measured and the incremental change in volume was was again used as a measure of the point of failure. The failure could only be determined to take place within the range of repetitions with a specific impact energy, and therefore the endurance of the coatings is presented as a range of cumulative energy (energy of impact times number of impacts). The results are presented in Figure 6.3. What can be deducted from the results is that the choice of coating material does not influence the impact fatigue resistance directly. However, the material affects the choice of spray parameters, which lead to higher residual stresses especially with high melting materials, such as Cr_2O_3, that are released under fatigue and lead to coating failure. Also the addition of a second phase is beneficial, which can be deducted from comparing APS Al_2O_3 and Al_2O_3-40ZrO_2, since in this case the lower melting temperature of the alloy is not required. Therefore adding another phase to the coating can be doubly beneficial: to present a discontinuity in the microstructure to act as a crack deflector, and in some cases lower the melting temperature along with other benefits in the sprayability of the material.

The behavior of a critical threshold found with micro-impact fatigue was identical to what was seen in Publication III when comparing APS-sprayed TiO_2 and Cr_2O_3 coatings under higher energy single impacts; with smaller impact energies the Cr_2O_3-coating was relatively unabashed, while a relatively higher increase in dissipated energy as well as crater cracking was observed with the harshest impact conditions. The behavior was more predictable for TiO_2 in that the gradual damage accretion was witnessed. The behavior is similar to what was found in a study by Takeuchi et

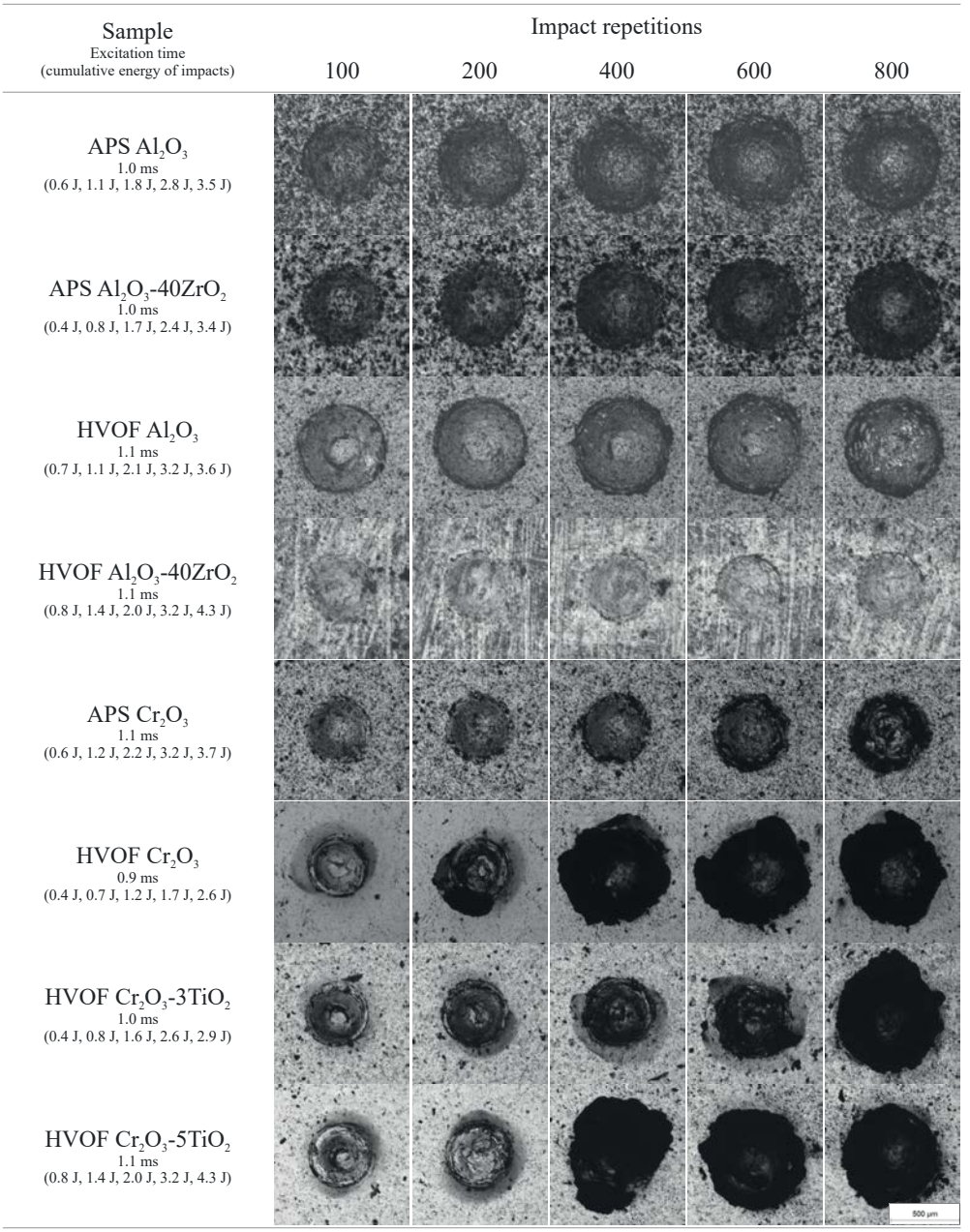

Figure 6.2 Micro-impact fatigue craters on ceramic coatings with varying repetitions and fixed impact energies [Publication IV].

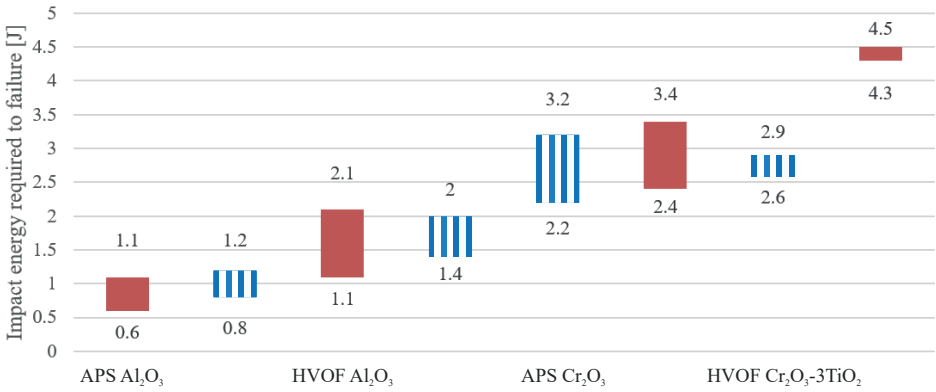

	HVOF Cr_2O_3		HVOF Cr_2O_3-5TiO_2		APS Al_2O_3-40ZrO_2		HVOF Al_2O_3-40ZrO_2	
Excit. Time (ms)	1	0.9	1.1	1.1	1.1	1	1	1.1
Repetititons	200	400	400	400	600	800	800	1000

Figure 6.3 The cumulative impact energies required for failure. Red bars indicate Al_2O_3-based samples and blue striped bars Cr_2O_3-based samples. In the table the excitation time and repetitions to failure are given [Publication IV].

al. [182], where a plasma-sprayed TiO_2-coating had superior resistance compared to a Cr_2O_3-coating in a drop test of a steel ball. Similarly they found that in high impact angles, TiO_2 out performs Cr_2O_3 in particle erosion resistance. To supplement the above, Sparks et al. [167] found a sever increase in the wear rate of glass ceramics as a function of increasing impact angle or particle velocity, i.e., energy. The impact craters of the high-velocity impacts with different used angles and projectiles on TiO_2 and Cr_2O_3 -coatings are presented in Figure 6.4.

6.1.1 Effect of residual stresses on impact resistance

To verify the existence and influence of residual stresses Raman analyses were performed for two samples having different behaviours and presumably different residual stresses: APS and HVOF Cr_2O_3. The spectra of an unimpacted coating was compared to that of the impact debris, with the hypotheses that on the impact site the potential stresses would have been released. As Cr_2O_3 coatings and debris are temperature

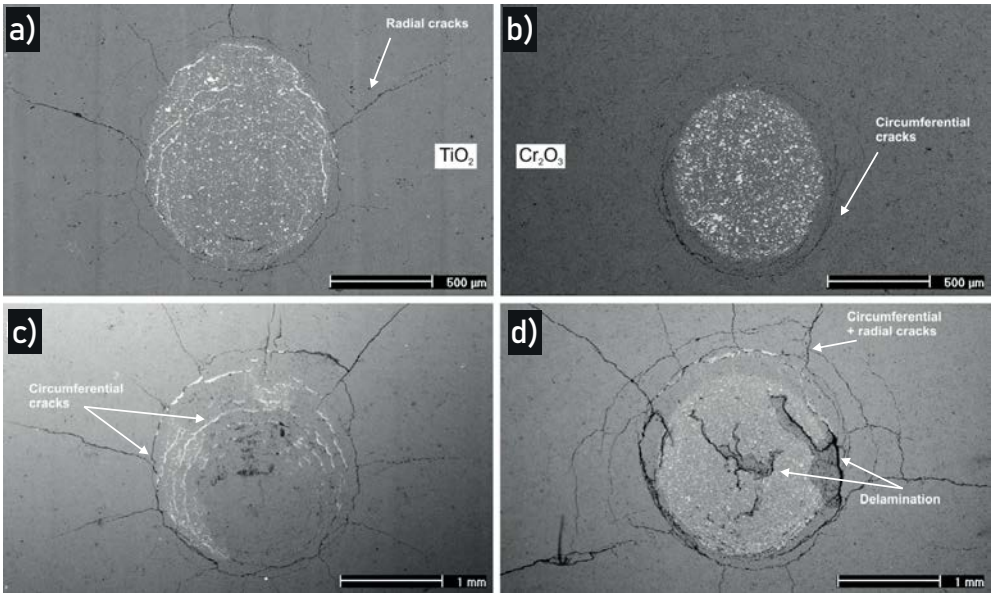

Figure 6.4 Surface of the impact craters: (a) TiO_2, 5 mm, 15°; (b) Cr_2O_3, 5 mm, 15°; (c) TiO_2, 9 mm, 30°; and (d) Cr_2O_3, 9 mm, 30°. SEM BSE (backscattered electron) images [Publication III].

sensitive, specific care has been taken in order to get the comparable values of the peak position. Particularly, the Raman peaks observed from the impact debris are significantly shifted and broadened with increasing laser power or acquisition duration. To control and minimize these effects, numerous analyses has been done on both coatings and debris under various conditions to identify optimal operating conditions and to avoid any thermal effect. Each value and standard deviation presented in the following has been calculated from more than 25 points. All the Raman spectra present the characteristic Raman peaks of Cr_2O_3 crystals at 300, 360, 555, 610 and 660 cm^{-1}. The main band at 555 cm^{-1} that has the highest intensity and better definition has been used for comparison. It has been fitted using the Origin software using a Lorentz model. Figure 6.5 illustrates the shift in the main Raman peak observed on the APS coating due to the release of residual stresses.

For APS coatings the observed shift appears to be slightly positive indicating tensile stresses. However, considering the standard deviation and the spectrometer resolution, extreme caution has to be taken in interpreting the result. For HVOF coatings the shift is negative indicating the presence of compression stresses. The shift-stress relationship established by Mougin et al. [183] enables us to estimate the residual stresses present in the two coatings. Table 6.1 summarizes the results for both APS

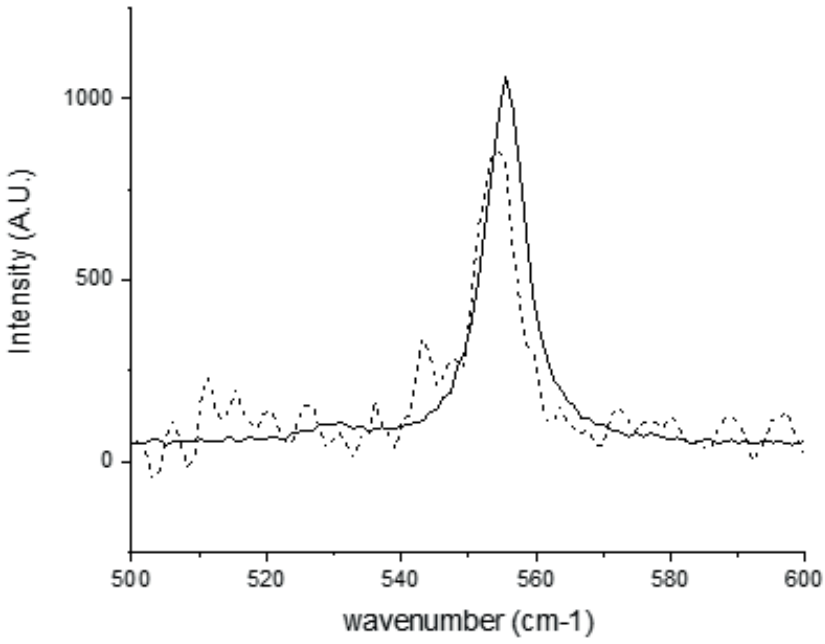

Figure 6.5 Main Raman peak position for coating (black line) and debris (dash line with x10 intensity) obtained on Cr_2O_3 APS coating.

and HVOF coatings. The stress values should not be literally interpreted, but rather in comparison with each other. Residual stress measurements in thermally-sprayed coatings are a many, each of them with their own intricacies and assumptions making them directly incomparable. However, the clearly much higher compressive stresses in the HVOF-coating support the theory hypothesized in Publication IV, that high compressive stresses are beneficial for damage tolerance with small loads, but can be catastrophic with higher loads.

Table 6.1 Peak shifts, standard deviations and estimated stresses obtained on APS and HVOF Cr_2O_3 samples

Coating	Peak shift $[cm^{-1}]$	Standard deviation $[cm^{-1}]$	Estimated residual stress [MPa]
APS Cr_2O_3	+1	±0.5	$< \pm 300$
HVOF Cr_2O_3	-2.5	±0.5	-750 ± 150

6.2 Crack propagation resistance

Crack propagation resistance was investigated by in-situ and four-point bending in Publication I and by tracing a propagating crack of the HVPI-experiment in Publication III. Cross-sections of in-situ bending of APS and HVOF-sprayed Al_2O_3-ZrO_2 coatings are presented in Figure 6.6. All coatings behaved in a similar fashion: several short cracks appeared at the point of maximum strain where critical flexural strain could be calculated. When the strain increased, a crack would penetrate the coating and continue at the coating/substrate interface leading to delamination of the coating. The phenomenon is incredibly fast and hard to detect, since the difference in the degree of bending between the left and right sides of Figure 6.6 is only about 0.3%. The penetration would generally happen with only one crack right on top of the central support pin, since its opening would lead to strain relief large enough to close the other cracks. Any deflection of the cracks by discontinuities in the structure were absent at this scale, which leads to believe additions of other phases play an insignificant role as a toughening mechanism in coatings as it pertains to crack deflections; there exists a sufficient multitude of vulnerable sites for the crack to propagate.
The results is in contrast to the findings of Lima et al. [13], where cracks were successfully arrested by nanostructured zone in coatings sprayed from A&S particles. In their case, however, the indenting load was constant and the crack had a finite amount of energy. In in-situ bending, the experiment was controlled by strain; more load was applied in each step of the experiment. Therefore detecting such crack arresting behaviour would have required stopping the experiment at an optimal time and finding an arrested crack. In the macroscopic behavior in the test, the arresting by nanostructured zones was not found to be essential.
Differences were also seen on the distribution of the vertical cracks: in HVOF coatings the cracks were generated at roughly half of the distance to APS coatings. That, combined with about 20 % higher flexural strain, would indicate that the coarser microstructure of the APS coatings can distribute stresses in a larger area than the finer structure of the HVOF coatings. This behavior corresponds well to findings by Mušálek et al. [184], when they compared the behavior of HVOF and water-stabilized plasma (WSP) -sprayed Al_2O_3 coatings under four-point bending. The WSP coating from coarser feedstock and the resulting microstructure had decreased stiffness which led to an increased strain-to-fracture.

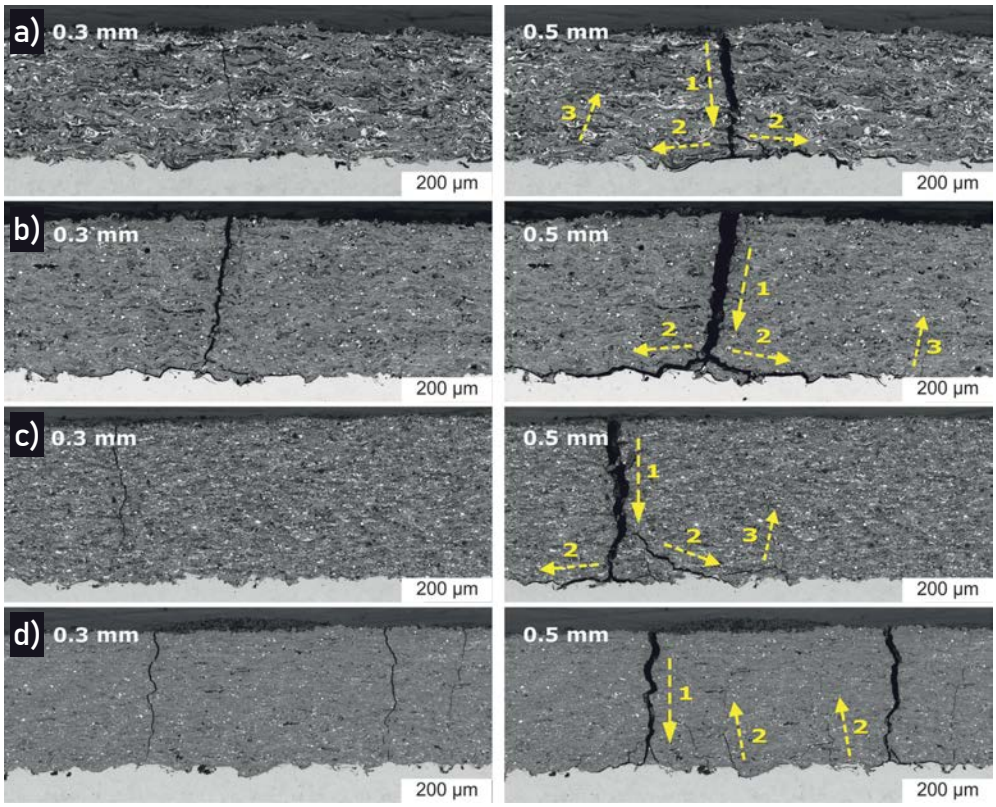

Figure 6.6 Failure evolution during in-situ observation of the three-point bending of APS a) F&C, b) A&S and HVOF c) F&C, d) A&S sprayed Al_2O_3-40ZrO_2 coatings. Displacement of the central support 0.3 mm (left) and 0.5 mm (right). Arrows show the direction and propagation of the cracks. Numbers denote the order of appearance of cracks. [Publication I].

The same phenomenon was evidenced in four-point bending which was utilized to evaluate the strain tolerance in a more macroscopic, statistical manner. While by average the APS coatings had a higher critical strain, also the scatter in the results was immense, especially with agglomerated and sintered powders. The lower critical strain and higher variation of the A&S powders can be explained by the larger amount of nanostructured and/or amorphous phases in the coating. The differences in the cracking behavior can be examined from a power density spectra comparison of the acoustic noise of the coatings during bending, Figure 6.7. A&S coatings (both APS and HVOF) produce higher frequency elastic waves during bending than fused and crushed coatings: the most intense threshold bins are at 200-225 kHz vs. 175-200 kHz,

respectively. This implies that the crack propagation is more violent or abrupt in A&S coatings, which is indicative of a slightly more brittle behavior. F&C coatings on the other hand are able to slow down or deflect the crack propagation, either due to more available slip planes of the polycrystalline coating or crack deflection by secondary phases (which could not be determine with in-situ bending). Additionally, both HVOF-coatings produced more signals then APS-coatings in the frequency range 100-150 kHz. Analogously to the above consideration, the conclusion to be drawn here is that the APS coatings have fewer but stronger intersplat connections that crack more forcefully, while the HVOF-coatings include areas of poorer bonding, unmelted particles and other crack deflectors that slow down the crack propagation. The same trail of thought has been utilized by Driver et al. [185], who found the opening of pre-existing cracks to produce less acoustic noise than well-molten structures in bending HVOF-sprayed WC-17Co coatings. Additionally, Ma et al. [150] attributed lower frequency noise to a slip in the coating or coating/substrate-interface and higher frequency noise to a local fracture of a weak area.

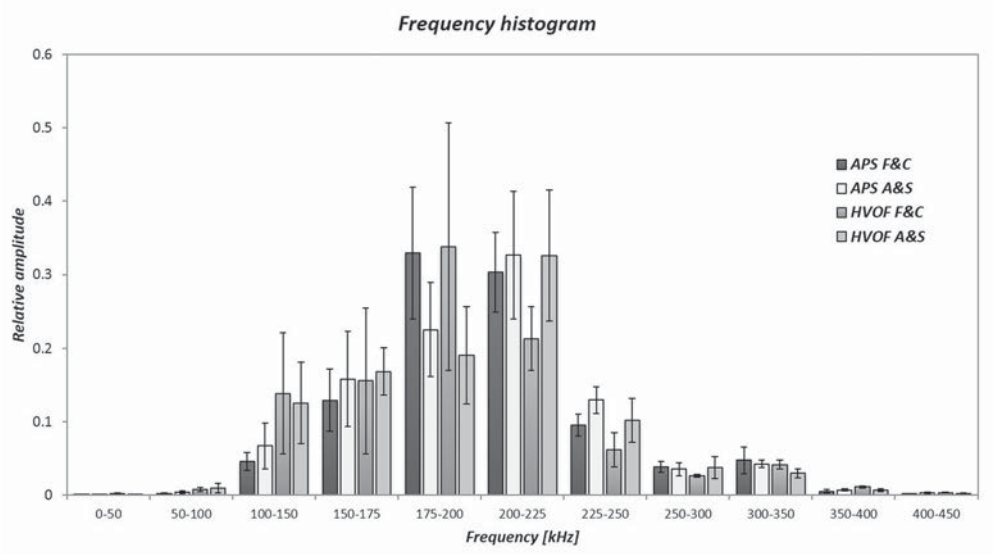

Figure 6.7 A normalized histogram of the average power density spectra of the coating samples describing differences in the characteristic frequencies [Publication I].

The HVPI experiment revealed large-scale cohesive failure under the crater of the Cr_2O_3, which was not the case with TiO_2. The crater cross-sections are presented in Figure 6.8. The coating thickness with TiO_2 was significantly smaller, leading to

the maximum Hertzian stresses to be rather at the substrate interface or within the substrate, but regardless somewhat more violent failure within the coating would be expected. Regardless, when following the crack path further from the crater (towards the direction of the impact) where only the interfacial crack exists, a deflection from the substrate-coating interface into the interlayer region of the coating can be evidenced in the Cr_2O_3. This indicates the importance of a cohesive microstructure since the same behavior is not seen in TiO_2 and follows the conclusion of Westergård et al. [152] who noted that cracking under erosion tended to follow a path of interlinking weak sites in plasma-sprayed ceramic coating. The reason for the structural weakness in Cr_2O_3 can be attributed to the well documented tendency of Cr_2O_3 to vaporize and condensate during spraying on the sample, typically ending up as dust-like particles between the spray passes. Micrographs of the cross-sections of as-sprayed APS Cr_2O_3 and TiO_2 are presented in Figure 6.9 highlighting the difference in inter-splat cohesion between the coatings.

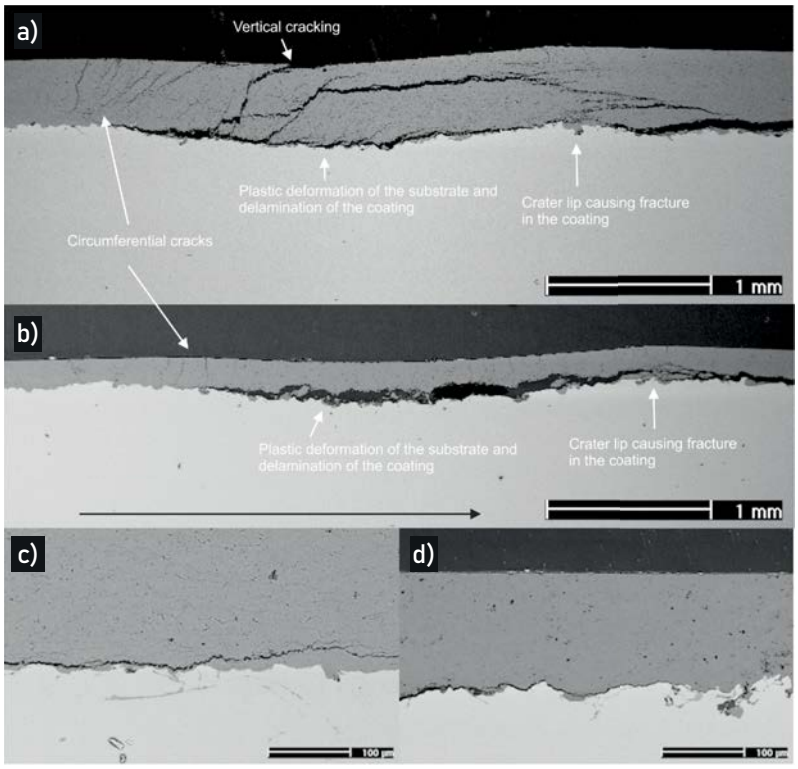

Figure 6.8 SEM-images of the cross-sections of the impact craters created by the 9-mm projectile at a 30° angle in (a, c) Cr_2O_3-coating and (b, d) TiO_2-coating. Impact direction in all images is left-to-right as also shown by the arrow [Publication III].

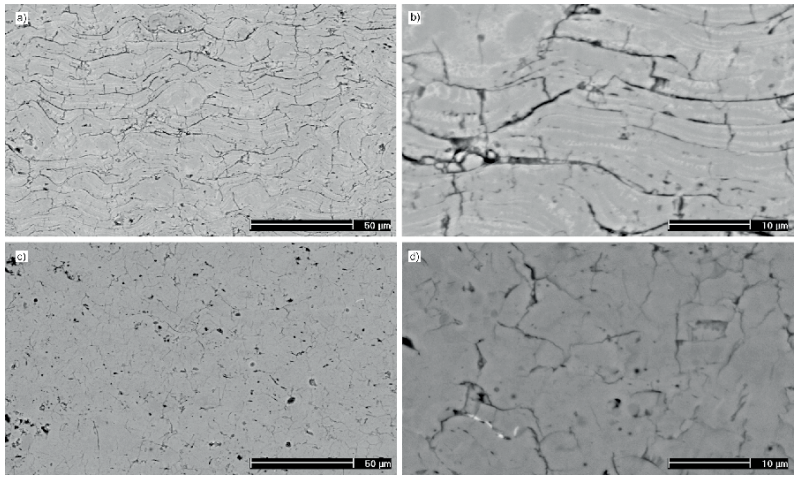

Figure 6.9 SEM-images of the cross-sections of as-sprayed APS (a, b) Cr_2O_3-coating and (c, d) TiO_2-coating. [Publication III].

6.3 Cohesive strength of ceramic coatings

The third component of damage tolerance was studied extensively in various publications by cavitation erosion. Erickson et al. [186] determined large particle erosion to be a good measure of cohesion for plasma-sprayed coatings. With the introduction of new processes leading to a reduction in scale of the microstructure, it is necessary to utilize methods with smaller impact sites to reliably determine the cohesion. The compiled results from Publications I-II and IV-V are presented in Table 6.2. Within the conventional spray processes, HVOF coatings clearly outperform their APS counterparts. This can be explained by the main erosion mechanism being the drilling effect of the cavitating bubbles, the nucleation of which increases drastically in likelihood in the presence of cavities of >10 μm. [187] A micrograph of a cavitated surface of an HVOF-sprayed Cr_2O_3-coating highlighting the selective nucleation is presented in Figure 6.10. The comparison between APS and HVOF-sprayed Al_2O_3-40ZrO_2 has been studied by the author [100] and craters of up to 200 μm in diameter were found. It is therefore speculated that the larger size of the feedstock for APS-coatings leads to not only larger splat size but also larger defects, such as voids, which are preferable nucleation sites for the bubbles. Additionally, the cavitation resistance seems to improve by increasing cohesion in the case of lower melting alloys (Al_2O_3-40ZrO_2 vs. Al_2O_3) for both spray systems. Another factor for good cavitation resistance is coating hardness, as is the case for HVOF Cr_2O_3. This could be analogous to the behaviour seen with micro-impact fatigue, where the high hardness of Cr_2O_3 was able to deter damage with small loads. Since hardness can be a factor with lighter loads, good performance in these experiments should not be interpreted directly as good cohesion.

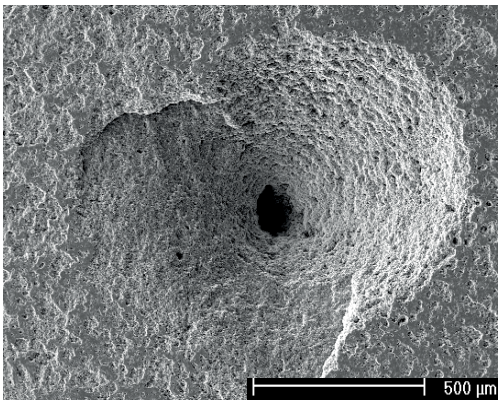

Figure 6.10 SEM-image of the surface of an HVOF-sprayed Cr_2O_3-coating after cavitation erosion highlighting the drilling effect generated by the preferential nucleation of the cavitation bubbles in pre-existing cavities.

Table 6.2 Cavitation erosion resistance and hardness values for various coatings in this study.

Spray Process	Material	Cavitation resistance [min/μm]	Hardness [$HV_{0.3}$]	Publication
APS	Al_2O_3	0.5	813±78	IV
	Al_2O_3-40ZrO_2	2.0	796±59	
	Cr_2O_3	0.4	1176±118	
HVOF	Al_2O_3 (1	5.3	1045±49	IV
	Al_2O_3 (2	7.8	1090±105	II
	Al_2O_3-40ZrO_2	9.3	917±48	IV
	Cr_2O_3	11.7	1443±118	
	Cr_2O_3-3TiO_2	8.5	1484±86	
	Cr_2O_3-5TiO_2	9.3	1602±70	
Hybrid	Al_2O_3-20YSZ	3.5	1032±128	II
	Al_2O_3-40YSZ	1.1	869±68	
	Al_2O_3-40ZrO_2	1.1	823±113	
S-HVOF	Cr_2O_3	19.7	1351±47	V

(1 Standoff distance=150 mm (2 Standoff distance=100 mm

6.4 Novel methods for improving the damage tolerance of ceramic coatings

In this section are presented new way to modify the coating architecture of thermally sprayed ceramic coatings in order to achieve damage tolerance. Cavitation erosion was used as the first method of cohesion evaluation in these trials.

6.4.1 Hybrid powder-solution precursor spraying to improve the cohesion of Al_2O_3-YSZ/ZrO_2 coatings

Hybrid-sprayed Al_2O_3-YSZ/ZrO_2 coatings were produced by utilizing a new type of injector to reliably inject a mixture of powder and a liquid precursor into the flame of the HVOF-torch. The hypothesis was to achieve a "gluing" effect of nanosized YSZ/ZrO_2 particles sintering with the neighboring Al_2O_3 splats in low temperatures due to a significant reduction in particle size [188]. However, the particles ended up as poorly bonded clusters in the structure, acting as weak sites easily removed by cavitation erosion. The feed-rate of the liquid precursor was seemingly too high and the atomization insufficient, since the clusters were not homogeneously distributed in the structure as seen in Figure 6.11a. A similar phenomenon occurred previously when Murray et al. [95] utilized a commercial YSZ suspension with Al_2O_3-powder plasma spray hybrid (Figure 6.11b).

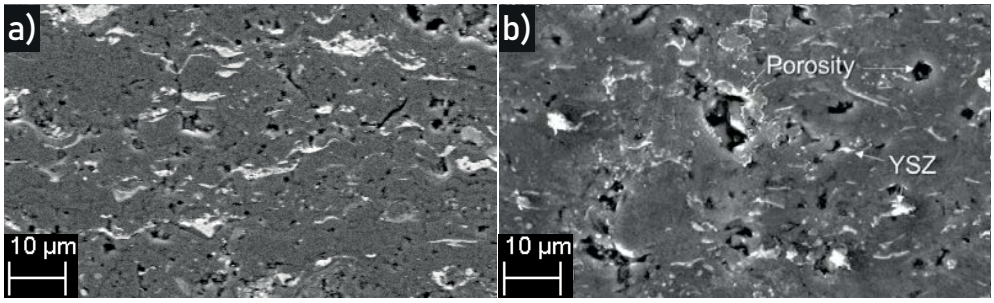

Figure 6.11 SEM-images of the cross-sections of hybrid-sprayed Al_2O_3-20YSZ coatings. a) HVOF-sprayed using liquid precursor used in this study and b) plasma-sprayed using a commercial YSZ suspension, modified from [95].

They speculated that the nanosized YSZ preferentially infiltrated the large pores

created between the relatively coarse Al_2O_3-splats, leading to the cluster formation. In their study a mixture of two suspensions with the same compositions was also deposited, and the YSZ distribution was clearly more homogeneous. Regardless of the similar structure achieved, Murray et al. [95] were able to achieve vast improvements in both fracture toughness and wear rate in comparison with a conventional plasma-sprayed Al_2O_3-coating. Obviously, tweaking of the process parameters will be necessary with hybrid HVOF spraying of liquid precursor and powder to achieve the required momentum and melting of the nanoparticles. As seen in Table 6.2, the HVOF-sprayed Al_2O_3 matrix was strong enough to withstand erosion better than APS coatings, once again underlining the importance of defect size. Additionally, the effect of the potential of the transformation toughening of ZrO_2 was investigate by comparing stabilized and unstabilized ZrO_2, but due to the cluster formation no conclusions on this subject could be drawn from the experiment.

6.4.2 Suspension HVOF spraying of Cr_2O_3

The S-HVOF spraying of Cr_2O_3 was carried out through a thorough parameter screening, including spray distance, suspension feed rate, combustion gas flow, air flow through a cooling nozzle and the pressure of an air curtain. The spray distance was varied between 80 and 110 mm with 10 mm increments, the suspension feed was around 50 and 25 g/min, combustion gas flow high/low, the air flow through a cooling nozzle was 0, 400 and 600 slpm and the air curtain pressure was 0, 0.2, 0.4 and 0.7 MPa.

Longer spray distances produced a seemingly flawless coating that was lacking in hardness, while using a short spray distance led to a hard coating but with a lot of defects, presumably from excessive heat load to the substrate. Regardless, the route of removing defects from a promising coating seemed less tedious than improving poor cohesion, and shorter spray distances were chosen. By utilizing the air nozzles and an air curtain the heat load was reduced enough and the surface cleaned enough to improve the microstructure manifold, as can be seen from Figure 6.12, where the evolution of the microstructure along with increasing air flow and pressure is presented in the form of SEM micrographs. A reduction in suspension feed or an increase in combustion gas flow did not produce beneficial results and their branches

of investigation were discarded at this time.
Finally, the optimal combination of parameters from the study are:

- Spray distance 90 mm
- Suspension feed rate 50 g/min
- Combustion gas flows - Ethene 88 slpm, Oxygen 213 slpm
- Air cooling nozzles air flow 400 slpm
- Air curtain pressure 0.4 MPa

With this combination of parameters, the S-HVOF-sprayed Cr_2O_3 coating proved to be very resistant to cavitation erosion, establishing an apparent link between splat size, microstructural integrity and cavitation resistance. Similarly, Toma et al. [189] found denser microstructure and higher hardness for S-HVOF sprayed Cr_2O_3 and Cr_2O_3-15TiO_2 coatings when compared with traditional methods utilizing powder feedstock. In Publication V, it was shown that clearing the residual inter-layer debris from the coating by utilizing auxiliary air cleaning methods had a direct - and within a certain frame, linear - impact on the cavitation erosion resistance.

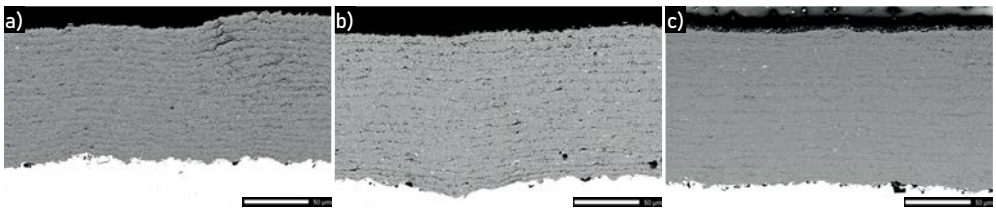

Figure 6.12 SEM-images of the cross-sections of S-HVOF-sprayed Cr_2O_3 coatings with a spray distance of 90 mm and a) no auxiliary air cooling or air curtain, b) 400 slpm air cooling and no air curtain, c) 400 slpm air cooling and 0.4 MPa air curtain. Modified from [Publication V].

7 CONCLUSIONS

Investigating and improving the damage tolerance of ceramic coatings has been a perpetual goal for the thermal spray community for decades. New developments in process technologies and materials engineering give rise to attempts at improving this property. In this work the initial investigation was placed on comparing and evaluating different new testing methods for damage tolerance, namely high-velocity single impacts, bending test and micro-impact fatigue. Afterwards, latest developments in thermal spray processes utilizing suspension and a combination of liquid precursor with powder were used with the intention of preparing a ceramic coating with improved damage tolerance.

7.1 Scientific contribution

The research questions placed in chapter 1 are discussed below.

i. **What is damage tolerance in a thermally sprayed ceramic coating and how to evaluate it?**

   Damage tolerance of a ceramic coating is thought to consist of two components: impact resistance and strain tolerance (or toughness), which are dictated by the mechanical strength and fracture behavior of the coating. While in practice damage tolerance and impact resistance are more or less interchangeable for ceramic coatings, in order to improve impact resistance the coating must be able to deform to some degree. Ergo, toughness is the second beneficial component. The biggest difficulties in measuring either property stem from the thinness of the coating relative to the coating-substrate system and of the coating heterogeneity. Therefore, traditional methods, such as single-edge notched beam

or indentation fracture toughness are of limited use. To this end, both impact resistance and toughness measurements require either modern in-situ monitoring or meticulous scrutinizing of the results with advanced microscopy. In the following the tests are shortly examined based on their potential and use.

The high-velocity single impact provided information on the cracking behavior of the coating from a carefully polished cross-section. Its main benefit, however, is to evaluate the ballistic response of a coating-substrate -system; something thin ceramic coatings are clearly not made for. Additionally, the sample preparation procedure to obtain the cross-section is very laborious in view of the amount of useful information obtained. The impact was simply too harsh for the coating, even efforts were made to have as little energy input to the coating as the experiment allowed.

The micro-impact fatigue experiment was the next iteration of impact-resistance testing, and it already showed promise. The impact-resistance of the coatings was very fast and straightforward to test, making the test ideal for quick screening of coatings for applications requiring damage tolerance. This could be realized either in a large study requiring quick pass/fail -type of screening or in manufacturing for quality control. Promisingly, the coatings performance in this test had no correlation with either hardness or cavitation resistance, opening a window to a new property clearly closest to an event that could be described as damage occurring in a component. However, as it pertains to material/coating development, the information acquired from the test is somewhat limited and efforts were made to make an arbitrary threshold of when the coating is considered damaged. This distinction could obviously be refined when more test data could be collected and different behaviors of coatings observed.

Toughness testing of the coatings was performed by four-point-bending with acoustic emission -monitoring. The monitoring was absolutely essential since the coating failure was gradual and indistinguishable from the load-displacement curve. The acoustic emission signal includes a great deal of data that one could spend a lot of time to go through and find the most interesting nuances. The downfall of the experiment comes from the same source, as it can be a tedious task to compare signals with different coatings and deciding how failure is defined. Once this distinction is made the comparison becomes very straight-

forward and one of the few ways where the tensile strain tolerance of ceramic coatings can be measured.

In-situ three-point bending was used inside an SEM to supplement the information from the four-point bending test. The point of failure could be determined most accurately by this method, although some insecurity is left as to the scalability of the result. Since three-point bending produces the maximum strain in one point in the coatings, it does not account for the heterogeneity of the coating. Therefore the defects that exist in most coatings would most likely not be in the zone of maximum tension. The test does, however, give valuable insight into the formation and propagation of a crack in the coating and could be very useful in the development and evaluation of coatings with the intention of introducing crack arresters and deflectors into the microstructure.

Cavitation erosion is one of the simplest ways to evaluate the coating cohesion. The result is mass loss during erosion, and the mechanism of particle detachment can be evaluated retrospectively by different characterization methods. The procedure is analogous to wear testing methods, but the environment of cavitation erosion can be controlled very precisely, and the scale of the test places heavy emphasis on the splat-to-splat adhesion of the coating, i.e. cohesion. This is thought to be a measure of microstructural integrity essential for damage tolerance. Limitations of the test come from the practical arrangements requiring a testing time up to some hours.

To summarize an answer to the research question, there is no one method of measuring a system property, such as damage tolerance; rather, the choice of method depends on the definition of damage tolerance required for the current application. In the authors view, the most widely useful experiment is the micro-impact fatigue test with its practical applicability combined with the possibility of retrospective analysis. If the component where the coating is being designed for is not susceptible to impact damage but rather gradual tensile stresses through, e.g., thermal cycling, one could veer towards a combination of a bending test and cavitation erosion.

ii. **How to improve the damage tolerance of a thermally sprayed ceramic coating?**

Three routes of microstructure modifications were evaluated with the intention

of obtaining a higher damage tolerance for thermally sprayed ceramic coatings: addition of a secondary phase in traditional ceramic powders, addition of a nanosized secondary phase by injecting a liquid precursor into the spray process and reduction of the feedstock particle size by utilizing a suspension feedstock. The decision made at the onset of the project was that the wear and corrosion resistance of the ceramic should not be compromised, as they are the key properties that differentiate ceramics from other coating materials. Therefore, metallic additions that potentially deteriorate the chemical stability were ruled out and as dense a coating structure as possible was pursued. This eliminated pre-cracked structures that are apparently resistant to crack propagation, but whose wear resistance is compromised.

Addition of a secondary phase in traditional feedstock proved to be generally beneficial. In the case of Cr_2O_3 the wear resistance suffered slightly with the addition of TiO_2, but the more efficient deposition due to a lower melting point reduced the thermal load on the component to the point that the impact resistance of the coating improved, likely due to milder residual stresses. Addition of ZrO_2 to Al_2O_3 lowered the coating hardness but increased both cavitation resistance and micro-impact fatigue property significantly, likely due to a homogeneous distribution of the secondary phase providing crack deflection in the coating and also to the eutectic composition lowering the melting point of the coating, providing higher cohesion.

A novel hybrid injector was utilized to inject a mixture of powder and liquid precursor in to a flame to produce a bimodal coating structure: micron-sized Al_2O_3 matrix with clusters of nanosized YSZ/ZrO_2. The hypothesis was that since sintering temperature lowers when particle size is significantly reduced, the YSZ/ZrO_2 could diffuse from the interface into the outer regions of the Al_2O_3 splats, acting as a "glue" to improve cohesion of the coating. The coatings were successfully deposited, but the desired beneficial effect was not achieved. The clusters of nanoparticles were too large and unevenly distributed, leading to disjointed regions of the coating that weakened the structure. There were significant reduction in the cohesion and hardness of the coatings when compared to an Al_2O_3 coating sprayed with an identical setup.

Regardless, the hybrid method of spraying has promising potential in seamless mixing of two constituents, either two ceramics or metal-matrix composites

with ceramic particulates. Tailoring of coating properties can be foreseen to be relatively facile with this method and new functionalities can be brought to the surface, as long as the process parameters are carefully optimized to provide even distribution of the nanoparticles in the structure.
Suspension spraying of a commercially available Cr_2O_3 was performed by S-HVOF. Promising results from suspension plasma spraying led to the desire to investigate the plausibility of producing a viable coating by a lower temperature method. After careful parameter optimization, astonishing improvements in the coating structure and cavitation resistance was achieved, when compared to HVOF-sprayed Cr_2O_3. Essentially identical deposition efficiency was achieved with vastly lower fuel gas consumption and flame temperature, leading to a dense and homogeneous structure. The necessity of cleaning of the by auxiliary air nozzles and/or an air curtain surface between spray passes became evident, as the debris between coating layers was gradually removed, which also translated to near-linear improvement in cavitation erosion resistance as a function of the strength of cleaning utilized.

7.2 Suggestions for future research

In this work, a wide variety of testing methods and material options were studied in order to increase the damage tolerance of the ceramic coatings. The logical following steps are to narrow down the selection to fewer options to focus on more profoundly. Regarding material development, while hybrid spraying with solutions and powder offers a near-unlimited range of possibilities, it would behoove us to rather utilize suspensions in hybrid spraying due to the higher deposition efficiency and lower cost attainable. This approach has already been proven feasible for SPS and to continue this development with S-HVOF with current, high-quality suspensions would expand the processing window of the technique to lower particle temperatures and higher speeds. It could provide a more refined and dense structure for coatings of select materials, for which the HVOF would have sufficient melting capacity.
Suspension spraying by itself has already proven immense potential and applicability. The following steps with S-HVOF would be to further optimize the feeding in to the combustion chamber. Practical applications are hindered by the total instability of the process, stemming from clogging of the nozzle from variations in the trajectory of

the suspension in the chamber/nozzle. Further, spray parameters are to be optimized to find optimal melting for each feedstock separately. Unfortunately, the feed of the suspension to the torch is interlinked with its back pressure (which changes with spray parameters), making independent optimization studies ineffective. The matrix of parameters requires great amount of time and effort, but nonetheless it is a worthy endeavor.

Damage tolerance continues to provide challenges in its characterization. While promising methods have been assessed in this thesis and in the literature, there is still no clear-cut option for an easy, accurate, reliable and repeatable method. To supply for the need of the industry, a micro-impact -type of test equipment should be utilized and developed more to the need of coatings and specifically for low-energy impacts since it showed the most promise being fast and most correlating with the term "damage tolerance". Its optimization means even smaller indenters and a more adjustable impact energy (as opposed to acceleration time) which could be done, e.g., by a loopback from velocity measurement. An interesting observation in this thesis was the change in recorded load from the load sensor under the sample when the coating failed. This theory is worth exploring with a more narrow test series of just one coating with many test conditions and repetitions.

REFERENCES

[1] P. Vuoristo. Thermal spray coating processing. *Comprehensive Materials Processing Volume 4: Films and Coatings: Technology and Recent Development*. Ed. by S. Hashmi. First Edit. Vol. 4. Elsevier Ltd, Oxford, UK, 2014, 229–276. ISBN: 9780080965321. DOI: 10.1016/B978-0-08-096532-1.00407-6.

[2] L. Pawlowski. *The Science and Engineering of Thermal Spray Coatings*. 2nd ed. West Sussex, England: John Wiley & Sons, 2008, 656. ISBN: 978-0-471-49049-4. DOI: 10.1002/9780470754085.

[3] *Thermal Spray Coatings Market Size, Share & Trends Analysis Report By Product, By Technology (Cold, Flame, Plasma, HVOF, Electric Arc), By Application, By Region, And Segment Forecasts, 2019–2025*. Tech. rep. Grand View Research, Inc., 2019, 230. URL: https://www.giiresearch.com/report/grvi614708-thermal-spray-coatings-market-size-share-trends.html.

[4] P. Vuoristo and P. Nylén. Industrial and Research Activities in Thermal Spray Technology in the Nordic Region of Europe. *Journal of Thermal Spray Technology* 16.4 (Oct. 2007), 466–471. DOI: 10.1007/s11666-007-9136-2.

[5] P. Fauchais, G. Montavon, R. S. Lima and B. R. Marple. Engineering a new class of thermal spray nano-based microstructures from agglomerated nanostructured particles, suspensions and solutions: An invited review. *Journal of Physics D: Applied Physics* 44.9 (Mar. 2011), 53. DOI: 10.1088/0022-3727/44/9/093001.

[6] R. Lima and B. Marple. High Weibull Modulus HVOF Titania Coatings. *Journal of Thermal Spray Technology* 12.2 (2003), 240–249. DOI: 10.1361/105996303770348357.

[7] C. B. Carter and M. G. Norton. *Ceramic materials: Science and engineering*. 2013, 1–766. DOI: 10.1007/978-1-4614-3523-5.

[8] M. W. Barsoum. *Fundamentals Of Ceramics*. Ed. by B. Cantor and M. J. Goringe. 2nd. London: IOP Publishing, 2002, 624. ISBN: 0750309024.

[9] A. Evans. Perspective on the Development of High-Toughness Ceramics. *Journal of the American Ceramic society* 73.2 (1990), 187–206. DOI: 10.1111/j.1151-2916.1990.tb06493.x.

[10] A. S. M. Ang and C. C. Berndt. A review of testing methods for thermal spray coatings. *International Materials Reviews* 59.4 (May 2014), 179–223. DOI: 10.1179/1743280414Y.0000000029.

[11] B. R. Lawn, N. P. Padture, H. Cai and F. Guiberteau. Making ceramics "ductile". *Science* 263.5150 (1994), 1114–1116. DOI: 10.1126/science.263.5150.1114.

[12] Y. X. Wang and S. Zhang. Toward hard yet tough ceramic coatings. *Surface and Coatings Technology* 258 (Nov. 2014), 1–16. DOI: 10.1016/j.surfcoat.2014.07.007.

[13] R. S. Lima and B. R. Marple. Enhanced ductility in thermally sprayed titania coating synthesized using a nanostructured feedstock. *Materials Science and Engineering A* 395.1-2 (2005), 269–280. DOI: 10.1016/j.msea.2004.12.039.

[14] J. Oberste Berghaus, J.-G. Legoux, C. Moreau, F. Tarasi and T. Chráska. Mechanical and Thermal Transport Properties of Suspension Thermal-Sprayed Alumina-Zirconia Composite Coatings. *Journal of Thermal Spray Technology* 17.1 (Dec. 2007), 91–104. DOI: 10.1007/s11666-007-9146-0.

[15] G. Taillon, F. Pougoum, S. Lavigne, L. Ton-That, R. Schulz, E. Bousser, S. Savoie, L. Martinu and J.-E. Klemberg-Sapieha. Cavitation erosion mechanisms in stainless steels and in composite metal–ceramic HVOF coatings. *Wear* 364-365 (2016), 201–210. DOI: 10.1016/j.wear.2016.07.015.

[16] R. Westergård and S. Hogmark. Sealing to improve the wear properties of plasma sprayed alumina by electro-deposited Ni. *Wear* 256.11-12 (June 2004), 1153–1162. DOI: 10.1016/j.wear.2003.07.005.

[17] E. Turunen, T. Varis, T. E. Gustafsson, J. Keskinen, T. Fält and S. P. Hannula. Parameter optimization of HVOF sprayed nanostructured alumina and alumina-nickel composite coatings. *Surface and Coatings Technology* 200.16-17 (2006), 4987–4994. DOI: 10.1016/j.surfcoat.2005.05.018.

[18] A. Förg, A. Myrell, A. Killinger and R. Gadow. Suspension and coating characterization of high velocity suspension flame sprayed (HVSFS) mixed titanium oxide–titanium carbide coatings. *Surface and Coatings Technology* 371 (Aug. 2019), 90–96. DOI: 10.1016/j.surfcoat.2018.08.085.

[19] V. Cannillo, L. Lusvarghi, C. Siligardi and A. Sola. Characterization of glass-alumina functionally graded coatings obtained by plasma spraying. *Journal of the European Ceramic Society* 27.4 (Jan. 2007), 1935–1943. DOI: 10.1016/j.jeurceramsoc.2006.05.105.

[20] R. Westergård, S. Hogmark and P. Vuoristo. Tribological properties of sprayed alumina coatings sealed by electro-deposition of Cu. *Wear* 256.11-12 (June 2004), 1163–1175. DOI: 10.1016/j.wear.2003.07.004.

[21] V. Matikainen, K. Niemi, H. Koivuluoto and P. Vuoristo. Abrasion, Erosion and Cavitation Erosion Wear Properties of Thermally Sprayed Alumina Based Coatings. *Coatings* 4.1 (Jan. 2014), 18–36. DOI: 10.3390/coatings4010018.

[22] D. Yan, Y. Dong, Y. Yang, L. Wang, X. Chen, J. He and J. Zhang. Microstructure Characterization of the $FeAl_2O_4$-Based Nanostructured Composite Coating Synthesized by Plasma Spraying Fe_2O_3/Al Powders. *Journal of Thermal Spray Technology* 20.6 (July 2011), 1269–1277. DOI: 10.1007/s11666-011-9673-6.

[23] G. Bolelli, L. Lusvarghi, T. Manfredini, F. Pighetti Mantini, R. Polini, E. Turunen, T. Varis and S.-P. Hannula. Comparison between plasma- and HVOF-sprayed ceramic coatings. Part I : microstructure and mechanical properties. *International Journal of Surface Science and Engineering* 1.1 (2007), 38–61.

[24] T. Varis, J. Knuuttila, T. Suhonen, U. Kanerva, J. Silvonen, J. Leivo and E. Turunen. Improving the properties of HVOF- sprayed Cr_2O_3 by nanocomposite powders. *Thermal Spray 2008: Crossing Borders*. Ed. by B. Marple, M. Hyland, Y.-C. Lau, C.-J. Li, R. Lima and G. Montavon. Maastricht, The Netherlands: Springer, 2008, 8–11.

[25] G. Bolelli, J. Rauch, V. Cannillo, A. Killinger, L. Lusvarghi and R. Gadow. Microstructural and Tribological Investigation of High-Velocity Suspension Flame Sprayed (HVSFS) Al_2O_3 Coatings. *Journal of Thermal Spray Technology* 18.1 (2009), 35–49. DOI: 10.1007/s11666-008-9279-9.

[26] E. Turunen, T. Varis, J. Keskinen, T. Fält and S. P. Hannula. Improved Mechanical Properties by Nanoreinforced Ceramic Composite HVOF Coatings. *Advances in Science and Technology* 45.3 (2006), 1240–1245. DOI: 10.4028/www.scientific.net/AST.45.1240.

[27] S. R. Choi, D. Zhu and R. A. Miller. Mechanical Properties/Database of Plasma-Sprayed ZrO_2-8wt% Y_2O_3 Thermal Barrier Coatings. *International Journal of Applied Ceramic Technology* 1.4 (2004), 330–342. DOI: 10.1111/j.1744-7402.2004.tb00184.x.

[28] W.-Z. Wang, C.-J. Li and Y.-Y. Wang. Effect of Spray Distance on the Mechanical Properties of Plasma Sprayed Ni-45Cr Coatings. *Materials Transactions* 47.7 (2006), 1643–1648. DOI: 10.2320/matertrans.47.1643.

[29] S. Siegmann and C. Abert. 100 years of thermal spray: About the inventor Max Ulrich Schoop. *Surface and Coatings Technology* 220 (Apr. 2013), 3–13. DOI: 10.1016/j.surfcoat.2012.10.034.

[30] J. R. Davis. *ASM Handbook, Volume 5A: Thermal Spray Technology*. Ed. by R. C. J. Tucker. Materials Park, OH, USA: ASM International, 2013, 412. ISBN: 978-1-61503-996-8.

[31] P. L. Fauchais, J. V. R. Heberlein and M. I. Boulos. *Thermal Spray Fundamentals: From Powder to Part*. New York: Springer Science+Business Media, 2014, 1566. ISBN: 9780387689913.

[32] M. Vardelle, A. Vardelle and K.-i. Li. Coating generation: vaporization of particles in plasma spraying and splat formation. *Pure & Applied Chemistry* 68.5 (1996), 1093–1099.

[33] M. Li and P. D. Christofides. Computational study of particle in-flight behavior in the HVOF thermal spray process. *Chemical Engineering Science* 61.19 (Oct. 2006), 6540–6552. DOI: 10.1016/j.ces.2006.05.050.

[34] M. Oksa, E. Turunen, T. Suhonen, T. Varis and S.-P. Hannula. Optimization and Characterization of High Velocity Oxy-fuel Sprayed Coatings: Techniques, Materials, and Applications. *Coatings* 1 (2011), 17–52. DOI: 10.3390/coatings1010017.

[35] P. Fauchais. Understanding plasma spraying. *Journal of Physics D: Applied Physics* 37.9 (May 2004), R86–R108. DOI: 10.1088/0022-3727/37/9/R02.

[36] P. L. Fauchais, J. V. Heberlein and M. I. Boulos. Overview of Thermal Spray. *Thermal Spray Fundamentals: From Powder to Part*. New York: Springer Science+Business Media, 2014. Chap. 2, 17–72. DOI: 10.1007/978-0-387-68991-3_2.

[37] M. Fukumoto, K. Yang, S. Yoshida, D. Mano, M. Yamada and T. Yasui. Flattening Mechanism of Thermal Sprayed Particles. *Thermal Spray 2012: Proceedings of the International Thermal Spray Conference, Air, Land, Water, and the Human Body: Thermal Spray Science and Applications*. Ed. by B. Marple, A. Agarwal, F.-L. Toma, M. M. Hyland, Y.-C. Lau, C.-J. Li, R. S. Lima and A. McDonald. Houston, TX, USA: Springer, 2012, 718–723. ISBN: 9781632666796.

[38] P. Fauchais, M. Vardelle and S. Goutier. Latest Researches Advances of Plasma Spraying: From Splat to Coating Formation. *Journal of Thermal Spray Technology* 25.8 (2016), 1534–1553. DOI: 10.1007/s11666-016-0435-3. URL: http://link.springer.com/10.1007/s11666-016-0435-3.

[39] P. L. Fauchais, J. V. Heberlein and M. I. Boulos. Coating Characterizations. *Thermal Spray Fundamentals: From Powder to Part*. New York: Springer Science+Business Media, 2014. Chap. 15, 1113–1250.

[40] C.-J. Li, C.-X. Li, G.-J. Yang and Y.-Y. Wang. Examination of Substrate Surface Melting-Induced Splashing During Splat Formation in Plasma Spraying. *Journal of Thermal Spray Technology* 15.4 (Dec. 2006), 717–724. DOI: 10.1361/105996306X146947.

[41] S. Safai and H. Herman. Microstructural investigation of plasma-sprayed aluminum coatings. *Thin Solid Films* 45.2 (1977), 295–307. DOI: 10.1016/0040-6090(77)90263-2.

[42] R. McPherson. A review of microstructure and properties of plasma sprayed ceramic coatings. *Surface and Coatings Technology* 39-40 (1989), 173–181. DOI: 10.1016/0257-8972(89)90052-2.

[43] A. Vardelle, C. Moreau, N. J. Themelis and C. Chazelas. A Perspective on Plasma Spray Technology. *Plasma Chemistry and Plasma Processing* 35.3 (2014), 491–509. DOI: 10.1007/s11090-014-9600-y.

[44] P. L. Fauchais, J. V. Heberlein and M. I. Boulos. Gas Flow–Particle Interaction. *Thermal Spray Fundamentals: From Powder to Part*. New York: Springer Science+Business Media, 2014. Chap. 4, 113–226. DOI: 10.1007/978-0-387-68991-3_4.

[45] M. I. Boulos, P. Fauchais and E. Pfender. Thermodynamic Properties. *Thermal Plasmas - Fundamentals and Applications*. 1st ed. Boston, MA: Springer US, 1994. Chap. 6, 213–264. ISBN: 978-1-4899-1337-1. DOI: 10.1007/978-1-4899-1337-1_6. URL: http://link.springer.com/10.1007/978-1-4899-1337-1%7B%5C_%7D6.

[46] M. Jadidi, A. Vardelle, A. Dolatabadi and C. Moreau. Heat Transfer in Suspension Plasma Spraying. *Handbook of Thermal Science and Engineering*. Ed. by F. A. Kulacki. Springer International Publishing, 2017, 1–44. DOI: 10.1007/978-3-319-32003-8_30-1.

[47] J. Zierhut, P. Haslbeck, K. D. Landes, G. Barbezat, M. Muller and M. Schutz. TRIPLEX - An innovative three-cathode plasma torch. *Proceedings of the International Thermal Spray Conference*. Ed. by C. Coddet. Vol. 2. Nice, France: ASM International, 1998, 1375–1379.

[48] P. L. Fauchais, J. V. Heberlein and M. I. Boulos. Fundamentals of Combustion and Thermal Plasma. *Thermal Spray Fundamentals: From Powder to Part*. New York: Springer Science+Business Media, 2014. Chap. 3, 73–112. DOI: 10.1007/978-0-387-68991-3_3.

[49] H. Kreye, F. Gärtner, A. Kirsten and R. Schwetzke. High-velocity Oxy-fuel Flame Spraying State of the Art, Prospects and Alternatives. *5. Colloquium on High Velocity Flame Spraying*. Erding, Germany: Gemeinschaft Thermisches Spritzen e.V. (GTS), 2000, 5.

[50] N. N. Ault. Characteristics of Refractory Oxide Coatings Produced by Flame-Spraying. *Journal of the American Ceramic Society* 40.3 (1957), 69–74. DOI: 10.1111/j.1151-2916.1957.tb12578.x.

[51] S. Elbel. Ceramic Thermal Spray: Realized Benefits Leading to Expansive Growth. *Spraytime* 26 (Apr. 2019), 4–7.

[52] L.-M. Berger. Tribology of Thermally Sprayed Coatings in the Al_2O_3-Cr_2O_3-TiO_2 System. *Thermal Sprayed Coatings and their Tribological Performances*. Ed. by M. Roy and J. Paulo Davim. IGI Global, 2015. Chap. 8, 227–267. DOI: 10.4018/978-1-4666-7489-9.ch008.

[53] S. H. Leigh and C. C. Berndt. Modelling of elastic constants of plasma spray deposits with ellipsoid-shaped voids. *Acta Materialia* 47.5 (Mar. 1999), 1575–1586. DOI: 10.1016/S1359-6454(99)00019-1.

[54] T. W. Clyne and S. C. Gill. Residual Stresses in Thermal Spray Coatings and Their Effect on Interfacial Adhesion: A Review of Recent Work. *Journal of Thermal Spray Technology* 5.4 (1996), 401–418. DOI: 10.1007/BF02645271.

[55] J. Matejicek and S. Sampath. Intrinsic residual stresses in single splats produced by thermal spray processes. *Acta Materialia* 49.11 (June 2001), 1993–1999. DOI: 10.1016/S1359-6454(01)00099-4.

[56] J. Pina, A. Dias and J. L. Lebrun. Study by X-ray diffraction and mechanical analysis of the residual stress generation during thermal spraying. *Materials Science and Engineering A* 347.1-2 (2003), 21–31. DOI: 10.1016/S0921-5093(02)00580-4.

[57] G. Bolelli, L. Lusvarghi, T. Varis, E. Turunen, M. Leoni, P. Scardi, C. L. Azanza-Ricardo and M. Barletta. Residual stresses in HVOF-sprayed ceramic coatings. *Surface and Coatings Technology* 202.19 (2008), 4810–4819. DOI: 10.1016/j.surfcoat.2008.04.066.

[58] O. Sarikaya. Effect of some parameters on microstructure and hardness of alumina coatings prepared by the air plasma spraying process. *Surface and Coatings Technology* 190.2 (2005), 388–393. DOI: 10.1016/j.surfcoat.2004.02.007.

[59] R. B. Heimann. Applications of plasma-sprayed ceramic coatings. *Key Engineering Materials* 122-124 (1996), 399–442. DOI: 10.4028/www.scientific.net/KEM.122-124.399.

[60] D. Fantozzi, J. Kiilakoski, H. Koivuluoto, P. Vuoristo, M. Uusitalo, G. Bolelli, V. Testa and L. Lusvarghi. High temperature corrosion properties of thermally sprayed ceramic oxide coatings. *Proceedings of the International Thermal Spray Conference*. Ed. by F. Azarmi, K. Balani, T. Eden, T. Hussain, Y.-C. Lau, H. Li

and K. Shinoda. Vol. 2018-May. Orlando, FL, USA: ASM International, 2018, 501–507. ISBN: 9781510880405.

[61] G. Bolelli, V. Cannillo, L. Lusvarghi and T. Manfredini. Wear behaviour of thermally sprayed ceramic oxide coatings. *Wear* 261.11-12 (Dec. 2006), 1298–1315. DOI: 10.1016/j.wear.2006.03.023.

[62] H. G. Schütz, T. Gøβmann, D. Støver, H. P. Buchkremer and D. Jäger. Manufacture and properties of plasma sprayed Cr_2O_3. *Materials and Manufacturing Processes* 6.4 (1991), 649–669. DOI: 10.1080/10426919108934795.

[63] H. Eschnauer. Hard material powders and hard alloy powders for plasma surface coating. *Thin Solid Films* 73.1 (1980), 1–17. DOI: 10.1016/0040-6090(80)90323-5.

[64] L. Pawlowski. Technology of thermally sprayed anilox rolls: State of art, problems, and perspectives. *Journal of Thermal Spray Technology* 5.3 (1996), 317–334. DOI: 10.1007/BF02645884.

[65] D. Caplan and M. Cohen. The Volatilization of Chromium Oxide. *Journal of The Electrochemical Society* 108.5 (1961), 438–442. DOI: 10.1149/1.2428106.

[66] G. R. Holcomb. Calculation of reactive-evaporation rates of chromia. *Oxidation of Metals* 69.3-4 (2008), 163–180. DOI: 10.1007/s11085-008-9091-4.

[67] N. Jacobson, D. Myers, E. Opila and E. Copland. Interactions of water vapor with oxides at elevated temperatures. *Journal of Physics and Chemistry of Solids* 66.2-4 (2005), 471–478. DOI: 10.1016/j.jpcs.2004.06.044.

[68] S. Kuroda and T. Clyne. The quenching stress in thermally sprayed coatings. *Thin Solid Films* 200.1 (May 1991), 49–66. DOI: 10.1016/0040-6090(91)90029-W.

[69] L.-M. Berger, F.-L. Toma, S. Scheitz, R. Trache and T. Börner. Thermisch gespritzte Schichten im System Al_2O_3-Cr_2O_3-TiO_2 - ein Update. *Materialwissenschaft und Werkstofftechnik* 45.6 (2014), 465–475. DOI: 10.1002/mawe.201400260.

[70] S. H. Yu and H. Wallar. *Chromia Spray Powders*. 2006.

[71] M. Vippola, J. Vuorinen, P. Vuoristo, T. Lepistö and T. Mäntylä. Thermal analysis of plasma sprayed oxide coatings sealed with aluminium phosphate. *Journal of the European Ceramic Society* 22.12 (2002), 1937–1946. DOI: 10.1016/S0955-2219(01)00522-2.

[72] R. McPherson. On the formation of thermally sprayed alumina coatings. *Journal of Materials Science* 15.12 (1980), 3141–3149. DOI: 10.1007/BF00550387.

[73] E. Leivo, M. Vippola, P. Sorsa, P. Vuoristo and T. Mäntylä. Wear and corrosion properties of plasma sprayed Al_2O_3 and Cr_2O_3 coatings sealed by aluminum phosphates. *Journal of Thermal Spray Technology* 6.2 (1997), 205–210. DOI: 10.1007/s11666-997-0014-8.

[74] M. Herrmann, F. L. Toma, L. M. Berger, G. Kaiser and C. C. Stahr. Comparative study of the corrosion resistance of thermally sprayed ceramic coatings and their bulk ceramic counterparts. *Journal of the European Ceramic Society* 34.2 (2014), 493–504. DOI: 10.1016/j.jeurceramsoc.2013.08.033.

[75] *Aluminum Oxide Thermal Spray Powders*. 2019. URL: https://www.oerlikon.com/ecomaXL/files/metco/oerlikon%7B%5C_%7DDSMTS-0005.6%7B%5C_%7DAl2O3.pdf&download=1 (visited on 07/20/2019).

[76] P. Chráska, J. Dubsky, K. Neufuss and J. Písacka. Alumina-base plasma-sprayed materials part I: Phase stability of alumina and alumina-chromia. *Journal of Thermal Spray Technology* 6.3 (1997), 320–326. DOI: 10.1007/s11666-997-0066-9.

[77] F.-L. Toma, L.-M. Berger, C. C. Stahr, T. Naumann and S. Langner. *Thermally sprayed Al_2O_3 layers having a high content of corundum without any property-reducing additives, and method for the production thereof*. Dec. 2009. URL: https://patents.google.com/patent/US8318261.

[78] *Aluminum Oxide 13 % Titanium Dioxide Powders*. 2019. URL: https://www.oerlikon.com/ecomaXL/files/metco/oerlikon%7B%5C_%7DDSMTS-0084.3%7B%5C_%7DAl2O3%7B%5C_%7D13TiO2.pdf&download=1 (visited on 08/11/2019).

[79] L. M. Berger. Titanium oxide - new opportunities for an established coating material. *Thermal Spray 2004: Advances in Technology and Application: Proceedings of the International Thermal Spray Conference, 10-12 May, 2004, Osaka, Japan*. Osaka, Japan: ASM International, 2004, 934–945. ISBN: 1615031014.

[80] M. Buchmann and R. Gadow. Mechanical and Tribological Characterization of APS and HVOF Sprayed TiO_2 Coatings on Light Metals. *Thermal Spray 2001: New Surfaces for A New Millennium*. Ed. by C. Berndt, K. A. Khor and E. Lugscheider. Singapore, Singapore: ASM International, 2001, 1003–1008.

[81] A. Fujishima, T. N. Rao and D. A. Tryk. Titanium dioxide photocatalysis. *Journal of Photochemistry and Photobiology C: Photochemistry Reviews* 1.1 (June 2000), 1–21. DOI: 10.1016/S1389-5567(00)00002-2.

[82] H. Gruber and E. Krautz. Magnetoresistance and conductivity in the binary system titanium–oxygen. II. Semiconductive Titanium Oxides. *physica status solidi (a)* 75.2 (1983), 511–518. DOI: 10.1002/pssa.2210750222.

[83] M. N. Gardos. Magnéli phases of anion-deficient rutile as lubricious oxides. Part I. Tribological behavior of single-crystal and polycrystalline rutile (Ti_nO_{2n-1}). *Tribology Letters* 8.2/3 (2000), 65–78. DOI: 10.1002/andp.200410099.

[84] P. Vuoristo, A. Määttä, T. Mäntylä, L.-M. Berger and S. Thiele. Properties of ceramic coatings prepared by HVOF and plasma spraying of titanium suboxide powders. *Proceedings of the International Thermal Spray Conference 2002*. Ed. by E. Lugscheider and C. Berndt. Essen, Germany: DVS Deutscher Verband für Schweissen, 2002, 488–493.

[85] K. Niemi. Abrasion wear characteristics of thermally sprayed alumina based coatings. Doctoral Thesis, Publication 820. Tampere: Tampere Univesity of Technology, 2009.

[86] J. R. Kelly and I. Denry. Stabilized zirconia as a structural ceramic: An overview. *Dental Materials* 24.3 (2008), 289–298. DOI: 10.1016/j.dental.2007.05.005.

[87] A. G. Evans and A. H. Heuer. REVIEW—Transformation Toughening in Ceramics: Martensitic Transformations in Crack-Tip Stress Fields. *Journal of the American Ceramic Society* 63.5-6 (1980), 241–248. DOI: 10.1111/j.1151-2916.1980.tb10712.x.

[88] R. A. Miller. Thermal barrier coatings for aircraft engines: History and directions. *Journal of Thermal Spray Technology* 6.1 (1997), 35–42. DOI: 10.1007/BF02646310.

[89] J. P. Goff, W. Hayes, S. Hull, M. T. Hutchings and K. N. Clausen. Defect structure of yttria-stabilized zirconia and its influence on the ionic conductivity at elevated temperatures. *Physical Review B* 59.22 (1999), 14202–14219. DOI: 10.1103/PhysRevB.59.14202.

[90] R. C. Garvie and P. S. Nicholson. Structure and Thermomechanical Properties of Partially Stabilized Zirconia in the CaO-ZrO_2 System. *Journal of the American Ceramic Society* 55.3 (1972), 152–157. DOI: 10.1111/j.1151-2916.1972.tb11241.x.

[91] W. D. Callister. *Materials Science and Engineering: An Introduction*. 6th ed. New York: John Wiley & Sons, 2002, 848. ISBN: 978-0-470-41997-7. arXiv: arXiv:1011.1669v3.

[92] D. Tejero-Martin, M. Rezvani Rad, A. McDonald and T. Hussain. Beyond Traditional Coatings: A Review on Thermal-Sprayed Functional and Smart Coatings. *Journal of Thermal Spray Technology* 28.4 (2019), 598–644. DOI: 10.1007/s11666-019-00857-1.

[93] M. R. Dorfman and A. Sharma. Challenges and Strategies for Growth of Thermal Spray Markets: The Six-Pillar Plan. *Journal of Thermal Spray Technology* 22.5 (Mar. 2013), 559–563. DOI: 10.1007/s11666-013-9906-y.

[94] J. J. Swab. *Role of Oxide Additives in Stabilizing Zirconia for Coating Applications*. Tech. rep. ARL-TR-2591. Aberdeen, MD, USA: Army Research Laboratory, 2001, 42.

[95] J. W. Murray, A. Leva, S. Joshi and T. Hussain. Microstructure and wear behaviour of powder and suspension hybrid Al_2O_3–YSZ coatings. *Ceramics International* 44.7 (Feb. 2018), 8498–8504. DOI: 10.1016/j.ceramint.2018.02.048.

[96] S. M. Lakiza and L. M. Lopato. Stable and Metastable Phase Relations in the System Alumina-Zirconia-Yttria. *Journal of the American Ceramic Society* 80.4 (2005), 893–902. DOI: 10.1111/j.1151-2916.1997.tb02919.x.

[97] K. Niemi, P. Vuoristo and T. Mäntylä. Properties of alumina-based coatings deposited by plasma spray and detonation gun spray processes. *Journal of Thermal Spray Technology* 3.2 (1994), 199–203. DOI: 10.1007/BF02648279.

[98] G. Barbezat, A. R. Nicol and A. Sickinger. Abrasion, erosion and scuffing resistance of carbide and oxide ceramic thermal sprayed coatings for different applications. *Wear* 162-164 (1993), 529–537. DOI: 10.1016/0043-1648(93)90538-W.

[99] J. Chevalier, A. H. De Aza, G. Fantozzi, M. Schehl and R. Torrecillas. Extending the lifetime of ceramic orthopaedic implants. *Advanced Materials* 12.21 (2000), 1619–1621. DOI: 10.1002/1521-4095(200011)12:21<1619::AID-ADMA1619>3.0.CO;2-O.

[100] J. Kiilakoski, F. Lukac, H. Koivuluoto and P. Vuoristo. Cavitation wear characteristics of Al_2O_3-ZrO_2 -ceramic coatings deposited by APS and HVOF -processes. *Proceedings of the ITSC 2017*. Düsseldorf, Germany: DVS Media GmbH, Düsseldorf, Germany, 2017, 928–933.

[101] M. Niittymaki, I. Rytoluoto, K. Lahti, J. Metsajoki and T. Suhonen. Role of microstructure in dielectric properties of thermally sprayed ceramic coatings. *Proceedings of the 2016 IEEE International Conference on Dielectrics, ICD 2016*. Vol. 2. IEEE, July 2016, 1102–1105. DOI: 10.1109/ICD.2016.7547811.

[102] H. Filmer, J. Hochstrasser, A. Nicoll and S. Rangaswamy. Plasma spray deposition of alumina-based ceramic coatings. *American Ceramic Society Bulletin* 69.12 (1990), 1955–1958.

[103] D. P. Butt, J. J. Mecholsky, M. van Roode and J. R. Price. Effects of Plasma-Sprayed Ceramic Coatings on the Strength Distribution of Silicon Carbide Materials. *Journal of the American Ceramic Society* 73.9 (1990), 2690–2696. DOI: 10.1111/j.1151-2916.1990.tb06747.x.

[104] K. N. Lee. Contamination effects on interfacial porosity during cyclic oxidation of mullite-coated silicon carbide. *Journal of the American Ceramic Society* 81.12 (1998), 3329–3332. DOI: 10.1111/j.1151-2916.1998.tb02777.x.

[105] U. Steinhauser, W. Braue, J. Göring, B. Kanka and H. Schneider. A new concept for thermal protection of all-mullite composites in combustion chambers. *Journal of the European Ceramic Society* 20.5 (2000), 651–658. DOI: 10.1016/S0955-2219(99)00265-4.

[106] E. Withey, C. Petorak, R. Trice, G. Dickinson and T. Taylor. Design of 7wt.% Y_2O_3–ZrO_2/mullite plasma-sprayed composite coatings for increased creep resistance. *Journal of the European Ceramic Society* 27.16 (2007), 4675–4683. DOI: 10.1016/j.jeurceramsoc.2007.02.214.

[107] P. Ctibor, J. Sedláček, K. Neufuss, J. Dubský and P. Chráska. Dielectric properties of plasma-sprayed silicates. *Ceramics International* 31.2 (2005), 315–321. DOI: 10.1016/j.ceramint.2004.05.022.

[108] P. Chráska, K. Neufuss and H. Herman. Plasma spraying of zircon. *Journal of Thermal Spray Technology* 6.4 (1997), 445–448. DOI: 10.1007/s11666-997-0029-1.

[109] S. Schelz, F. Enguehard, N. Caron, D. Plessis, B. Minot, F. Guillet, J.-L. Longuet, N. Teneze and E. Bruneton. Recombination of silica and zirconia into zircon by means of laser treatment of plasma-sprayed coatings. *Journal of Materials Science* 43.6 (Mar. 2008), 1948–1957. DOI: 10.1007/s10853-007-2406-z.

[110] B. G. Ravi, S. Sampath, R. Gambino, P. S. Devi and J. B. Parise. Plasma spray synthesis from precursors: Progress, issues, and considerations. *Journal of Thermal Spray Technology* 15.4 (2006), 701–707. DOI: 10.1361/105996306X147117.

[111] D. Chen, E. H. Jordan, M. W. Renfro and M. Gell. Dy:YAG phosphor coating using the solution precursor plasma spray process. *Journal of the American Ceramic Society* 92.1 (2009), 268–271. DOI: 10.1111/j.1551-2916.2008.02846.x.

[112] P. S. Devi, J. Margolis, J. B. Parise, C. P. Grey, S. Sampath, H. Herman and H. D. Gafney. Single-step deposition of Eu-doped Y_2O_3 phosphor coatings through a precursor plasma spraying technique. *J. Mater. Res.* 17.11 (2002), 2771–2774. DOI: 10.1063/1.5100392.

[113] F. Mubarok and N. Espallargas. Suspension Plasma Spraying of Sub-micron Silicon Carbide Composite Coatings. *Journal of Thermal Spray Technology* 24.5 (2015), 817–825. DOI: 10.1007/s11666-015-0242-2.

[114] L. Gao, H. Wang, H. Kawaoka, T. Sekino and K. Niihara. Fabrication of YAG–SiC nanocomposites by spark plasma sintering. *Journal of the European Ceramic Society* 22.5 (2002), 785–789. DOI: 10.1016/S0955-2219(01)00368-5.

[115] A. Vackel, G. Dwivedi and S. Sampath. Structurally Integrated, Damage-Tolerant, Thermal Spray Coatings. *Jom* 67.7 (2015), 1540–1553. DOI: 10.1007/s11837-015-1400-1.

[116] G. M. Smith, M. Resnick, K. Flynn, G. Dwivedi and S. Sampath. Nature inspired, multi-functional, damage tolerant thermal spray coatings. *Surface and Coatings Technology* 297 (2016), 43–50. DOI: 10.1016/j.surfcoat.2016.04.047.

[117] S. Usmani, S. Sampath, D. L. Houck and D. Lee. Effect of carbide grain size on the sliding and abrasive wear behavior of thermally sprayed WC-Co coatings. *Tribology Transactions* 40.3 (1997), 470–478. DOI: 10.1080/10402009708983682.

[118] I. Hutchings, P. Shipway, I. Hutchings and P. Shipway. Wear by hard particles. *Tribology*. Ed. by I. Hutchings and P. Shipway. 2nd ed. Butterworth-Heinemann, 2017. Chap. 6, 165–236. ISBN: 978-0-08-100910-9. DOI: 10.1016/B978-0-08-100910-9.00006-4.

[119] B. R. Lawn. Fracture and deformation in brittle solids: A perspective on the issue of scale. *Journal of Materials Research* 19.01 (Mar. 2004), 22–29. DOI: 10.1557/jmr.2004.19.1.22.

[120] B. R. Lawn, Y. Deng, P. Miranda, A. Pajares, H. Chai and D. K. Kim. Overview: damage in brittle layer structures from concentrated loads. *Journal of Materials Research* 17 (12 2002), 3019–3036. DOI: 10.1557/JMR.2002.0440.

[121] G. M. Smith, M. Resnick, B. Kjellman, J. Wigren, G. Dwivedi and S. Sampath. Orientation-dependent mechanical and thermal properties of plasma-sprayed ceramics. *Journal of the American Ceramic Society* 101.6 (2018), 2471–2481. DOI: 10.1111/jace.15405.

[122] R. McPherson and B. V. Shafer. Interlamellar contact within plasma-sprayed coatings. *Thin Solid Films* 97.3 (1982), 201–204. DOI: 10.1016/0040-6090(82)90453-9.

[123] J. Voyer and H. Kreye. Determination of cracking resistance of thermal spray coatings during four-point bend testing using an acoustic emission technique. *Journal of thermal spray technology* 12.3 (2003), 416–426. DOI: 10.1361/105996303770348285.

[124] L. Wang, D. Yan, Y. Yang, Y. Dong, X. Chen and J. Zhang. Structure and properties of nanostructured ceramic matrix composite coatings prepared in-situ by reactive plasma spraying micro-sized Al–Fe_2O_3–Cr_2O_3 powders. *Ceramics International* 40.5 (June 2014), 6481–6486. DOI: 10.1016/j.ceramint.2013.11.100.

[125] Z. Yin, S. Tao, X. Zhou and C. Ding. Preparation and characterization of plasma-sprayed Al/Al_2O_3 composite coating. *Materials Science and Engineering: A* 480.1-2 (May 2008), 580–584. DOI: 10.1016/j.msea.2007.07.009.

[126] Z. Yin, S. Tao, X. Zhou and C. Ding. Microstructure and mechanical properties of Al_2O_3–Al composite coatings deposited by plasma spraying. *Applied Surface Science* 254.6 (Jan. 2008), 1636–1643. DOI: 10.1016/j.apsusc.2007.07.135.

[127] S. P. Hannula, E. Turunen, J. Keskinen, T. Varis, T. Fält, T. E. Gustafsson and R. Nowak. Development of Nanostructured Al_2O_3-Ni HVOF Coatings. *Key Engineering Materials* 317-318 (2009), 539–544. DOI: 10.4028/www.scientific.net/kem.317-318.539.

[128] J. Knuuttila, P. Sorsa and T. Mäntylä. Sealing of thermal spray coatings by impregnation. *Journal of Thermal Spray Technology* 8.6 (1999), 249–257. DOI: 10.1007/s11666-999-0002-2.

[129] S. Ahmaniemi, J. Tuominen, P. Vuoristo and T. Mäntylä. Sealing Procedures for Thick Thermal Barrier Coatings. *Journal of Thermal Spray Technology* 11.3 (2002), 320–332. DOI: 10.1361/105996302770348718.

[130] A. Ohmori, Z. Zhou, K. Inoue, K. Murakami and T. Sasaki. Penetration treatment of plasma-sprayed ZrO_2 coating by liquid Mn alloys. *Journal of Thermal Spray Technology* 5.2 (1996), 134–138. DOI: 10.1007/BF02646426.

[131] L. Yulin and P. K. Liaw. The mechanical properties of nanostructured materials. *JOM* 53.3 (Mar. 2001), 31–35. DOI: 10.1007/s11837-001-0177-6.

[132] A. J. Winnubst, M. M. Boutz, Y. J. He, A. J. Burggraaf and H. Verweij. Plasticity of nanocrystalline zirconia ceramics and composites. *Ceramics International* 23.3 (Jan. 1997), 215–221. DOI: 10.1016/S0272-8842(96)00028-4.

[133] E. Frankberg. *Plastic Deformation of Amorphous Aluminium Oxide: Flow of Inorganic Glass at Room Temperature*. English. Tampere University of Technology, Mar. 2018. ISBN: 978-952-15-4102-5.

[134] L. Pawlowski. Properties Of Coatings. *The Science and Engineering of Thermal Spray Coatings*. 2nd ed. West Sussex, England: John Wiley & Sons, 2008. Chap. 8, 383–541.

[135] N. Keller, G. Bertrand, B. Comas and C. Coddet. On the Tailoring of Spray Dried Thermal Spray Powders. *Proceedings of the International Thermal Spray Conference*. Ed. by C. Berndt, K. Khor and E. Lugscheider. ASM International, 2001, 285–290.

[136] R. Lima and B. Marple. Thermal spray coatings engineered from nanostructured ceramic agglomerated powders for structural, thermal barrier and biomedical applications: a review. *Journal of Thermal Spray Technology* 16.1 (Mar. 2007), 40–63. DOI: 10.1007/s11666-006-9010-7.

[137] T. Varis, J. Knuuttila, E. Turunen, J. Leivo, J. Silvonen and M. Oksa. Improved protection properties by using nanostructured ceramic powders for HVOF coatings. *Journal of Thermal Spray Technology* 16.4 (Oct. 2007), 524–532. DOI: 10.1007/s11666-007-9072-1.

[138] R. Lima and B. Marple. Superior Performance of High-Velocity Oxyfuel-Sprayed Nanostructured TiO_2 in Comparison to Air Plasma-Sprayed Conventional Al_2O_3-13TiO_2. *Journal of Thermal Spray Technology* 14.3 (Sept. 2005), 397–404. DOI: 10.1361/105996305X59413.

[139] R. S. Lima and B. Marple. From APS to HVOF spraying of conventional and nanostructured titania feedstock powders: A study on the enhancement of the mechanical properties. *Surface and Coatings Technology* 200.11 (Mar. 2006), 3428–3437. DOI: 10.1016/j.surfcoat.2004.10.137.

[140] H. Luo, D. Goberman, L. Shaw and M. Gell. Indentation fracture behavior of plasma-sprayed nanostructured Al_2O_3-13wt.%TiO_2 coatings. *Materials Science and Engineering A* 346.1-2 (Apr. 2003), 237–245. DOI: 10.1016/S0921-5093(02)00523-3.

[141] M. Gell, E. H. Jordan, Y. H. Sohn, D. Goberman, L. Shaw and T. D. Xiao. Development and implementation of plasma sprayed nanostructured ceramic coatings. *Surface and Coatings Technology* 146-147 (Sept. 2001), 48–54. DOI: 10.1016/S0257-8972(01)01470-0. URL: https://www.sciencedirect.com/science/article/pii/S0257897201014700.

[142] P. Bansal, N. P. Padture and A. Vasiliev. Improved interfacial mechanical properties of Al_2O_3-13wt%TiO_2 plasma-sprayed coatings derived from nanocrystalline powders. *Acta Materialia* 51.10 (June 2003), 2959–2970. DOI: 10.1016/S1359-6454(03)00109-5.

[143] G. Bolelli, V. Cannillo, L. Lusvarghi, I. Modena, J. Rauch, A. Killinger, R. Gadow and D. Stuttgart. Comparison between APS , HVOF and high-velocity suspension flame spraying (HVSFS) - deposited Al_2O_3 coatings. *Thermal Spray 2008: Crossing Borders, on CD-ROM*. Ed. by E. Lugscheider. Maastricht, The Netherlands: DVS-Verlag GmbH, Düsseldorf, Germany, 2008, 657–662.

[144] G. Bolelli, V. Cannillo and R. Gadow. Properties of High Velocity Suspension Flame Sprayed (HVSFS) TiO_2 coatings. *Surface and Coatings Technology* 203 (2009), 1722–1732. DOI: 10.1016/j.surfcoat.2010.05.011.

[145] G. Bolelli, V. Cannillo, L. Lusvarghi and R. Gadow. Deposition of TiO_2 Coatings: Comparison Between High Velocity Suspension Flame Spraying (HVSFS), Atmospheric Plasma Spraying and HVOF-spraying. *Thermal Spray 2009: Expanding Thermal Spray Performance to New Markets and Applications*. Ed. by B. Marple, M. Hyland, Y.-C. Lau, C.-J. Li, R. Lima and G. Montavon. May 4-7, 2009 (Las Vegas, Nevada): Springer, 2010, 207–212. DOI: 10.1361/cp2009itsc0207.

[146] J. W. Murray, A. S. Ang, Z. Pala, E. C. Shaw and T. Hussain. Suspension High Velocity Oxy-Fuel (SHVOF)-Sprayed Alumina Coatings: Microstructure, Nanoindentation and Wear. *Journal of Thermal Spray Technology* 25.8 (Dec. 2016), 1700–1710. DOI: 10.1007/s11666-016-0462-0.

[147] D. Chen, E. H. Jordan and M. Gell. Solution precursor high-velocity oxy-fuel spray ceramic coatings. *Journal of the European Ceramic Society* 29.16 (Dec. 2009), 3349–3353. DOI: 10.1016/j.jeurceramsoc.2009.07.010.

[148] G. Sivakumar, R. O. Dusane and S. V. Joshi. A novel approach to process phase pure α-Al_2O_3 coatings by solution precursor plasma spraying. *Journal of the European Ceramic Society* 33.13-14 (2013), 2823–2829. DOI: 10.1016/j.jeurceramsoc.2013.05.005.

[149] D. Chen, E. H. Jordan and M. Gell. Porous TiO_2 coating using the solution precursor plasma spray process. *Surface and Coatings Technology* 202.24 (Aug. 2008), 6113–6119. DOI: 10.1016/j.surfcoat.2008.07.017.

[150] X. Ma, S. Cho and M. Takemoto. Acoustic emission source analysis of plasma sprayed thermal barrier coatings during four-point bend tests. *Surface and Coatings Technology* 139.1 (May 2001), 55–62. DOI: 10.1016/S0257-8972(01)00995-1.

[151] C.-K. Lin, C. C. Berndt, S.-H. Leigh and K. Murakami. Acoustic Emission Studies of Alumina-13% Titania Free-Standing Forms during Four-Point Bend Tests. *Journal of the American Ceramic Society* 80.9 (2005), 2382–2394. DOI: 10.1111/j.1151-2916.1997.tb03130.x.

[152] R. Westergård, N. Axén, U. Wiklund and S. Hogmark. An evaluation of plasma sprayed ceramic coatings by erosion, abrasion and bend testing. *Wear* 246.1-2 (Nov. 2000), 12–19. DOI: 10.1016/S0043-1648(00)00506-8.

[153] C. C. Berndt, C. K. Lin and S. H. Leigh. Characterization of Cracking within Thermal Spray Deposits by an Acoustic Emission Method-Extended Abstract. *Journal of Thermal Spray Technology* 7.3 (Sept. 1998), 334–336. DOI: 10.1361/105996398770350800.

[154] L. C. Cox. The four-point bend test as a tool for coating characterization. *Surface and Coatings Technology* 36.3-4 (Dec. 1988), 807–815. DOI: 10.1016/0257-8972(88)90021-7.

[155] E. Mayrhofer, L. Janka, W. P. Mayr, J. Norpoth, M. R. Ripoll and M. Gröschl. Cracking resistance of Cr_3C_2–NiCr and WC–Cr_3C_2–Ni thermally sprayed coatings under tensile bending stress. *Surface and Coatings Technology* 281 (2015), 169–175. DOI: 10.1016/j.surfcoat.2015.09.002.

[156] W. Yao, C. Dai, W. Mao, C. Lu, L. Yang and Y. Zhou. Acoustic emission analysis on tensile failure of air plasma-sprayed thermal barrier coatings. *Surface and Coatings Technology* 206.18 (May 2012), 3803–3807. DOI: 10.1016/j.surfcoat.2012.03.050.

[157] R. Mušálek, O. Kovářík and J. Matějíček. In-situ observation of crack propagation in thermally sprayed coatings. *Surface and Coatings Technology* 205.7 (2010), 1807–1811. DOI: 10.1016/j.surfcoat.2010.03.064.

[158] H. Brantner, R. Pippan and W. Prantl. Local and Global Fracture Toughness of a Flame Sprayed Molybdenum Coating. *Journal of Thermal Spray Technology* 12.December (2003), 560–571. DOI: 10.1361/105996303772082314.

[159] T. Varis, T. Suhonen, A. Ghabchi, A. Valarezo, S. Sampath, X. Liu and S. P. Hannula. Formation mechanisms, structure, and properties of HVOF-sprayed WC-CoCr coatings: An approach toward process maps. *Journal of Thermal Spray Technology* 23.6 (2014), 1009–1018. DOI: 10.1007/s11666-014-0110-5.

[160] R. Musalek, J. Matejicek, M. Vilemova and O. Kovarik. Non-Linear Mechanical Behavior of Plasma Sprayed Alumina Under Mechanical and Thermal Loading. *Journal of Thermal Spray Technology* 19.1-2 (Jan. 2010), 422–428. DOI: 10.1007/s11666-009-9362-x.

[161] C. K. Lin and C. C. Berndt. Statistical analysis of microhardness variations in thermal spray coatings. *Journal of Materials Science* 30.1 (1995), 111–117. DOI: 10.1007/BF00352139.

[162] J. B. Quinn and G. D. G. Quinn. Indentation brittleness of ceramics: a fresh approach. *Journal of Materials Science* 2 (1997), 4331–4346. DOI: 10.1023/A:1018671823059.

[163] D. K. Kim, Y. G. Jung, I. M. Peterson and B. R. Lawn. Cyclic fatigue of intrinsically brittle ceramics in contact with spheres. *Acta Materialia* 47.18 (Dec. 1999), 4711–4725. DOI: 10.1016/S1359-6454(99)00246-3.

[164] Y. Xie and H. Hawthorne. Wear mechanism of plasma-sprayed alumina coating in sliding contacts with harder asperities. *Wear* 225-229 (Apr. 1999), 90–103. DOI: 10.1016/S0043-1648(98)00351-2.

[165] S. K. Lee, S. Wuttiphan and B. R. Lawn. Role of Microstructure in Hertzian Contact Damage in Silicon Nitride : *J. Am. Ceram. Soc.* 80.9 (1997), 2367–2381. DOI: 10.1111/j.1151-2916.1997.tb03129.x.

[166] I. Finnie. Some reflections on the past and future of erosion. *Wear* 186-187 (July 1995), 1–10. DOI: 10.1016/0043-1648(95)07188-1.

[167] A. Sparks and I. Hutchings. Transitions in the erosive wear behaviour of a glass ceramic. *Wear* 149.1-2 (Sept. 1991), 99–110. DOI: 10.1016/0043-1648(91)90367-4.

[168] F. Ledrappier, C. Langlade, Y. Gachon and B. Vannes. Blistering and spalling of thin hard coatings submitted to repeated impacts. *Surface and Coatings Technology* 202.9 (Feb. 2008), 1789–1796. DOI: 10.1016/j.surfcoat.2007.07.107.

[169] S. Björklund, S. Goel and S. Joshi. Function-dependent coating architectures by hybrid powder-suspension plasma spraying: Injector design, processing and concept validation. *Materials and Design* 142 (2018), 56–65. DOI: 10.1016/j.matdes.2018.01.002.

[170] M. Apostol, V. Kuokkala, A. Laukkanen, K. Holmberg, R. Waudby and M. Lindroos. High velocity particle impactor–modelling and experimental verification of impact wear tests. *Proceedings of 5th World Tribology Congress WTC 2013*. Turin, Italy, 2013, 2–5.

[171] M. Löhr, D. Spaltmann, S. Binkowski, E. Santner and M. Woydt. In situ Acoustic Emission for wear life detection of DLC coatings during slip-rolling friction. *Wear* 260.4-5 (Feb. 2006), 469–478. DOI: 10.1016/j.wear.2005.03.009.

[172] A. C. Sekkal, C. Langlade and A. B. Vannes. A micro/macro impact test at controlled energy for erosion and phase-transformation simulation. *Tribology Letters* 15.3 (2003), 263–274. DOI: 10.1023/A:1024996621189.

[173] G. Kermouche and C. Langlade. Mechanical nano-structuration of a C45 steel under repeated normal impacts. *IOP Conference Series: Materials Science and Engineering*. Vol. 63. Aug. 2014, 012019. DOI: 10.1088/1757-899X/63/1/012019.

[174] V. Matikainen, S. Rubio Peregrina, N. Ojala, H. Koivuluoto, J. Schubert, S. Houdková and P. Vuoristo. Erosion wear performance of WC-10Co4Cr and Cr_3C_2-25NiCr coatings sprayed with high-velocity thermal spray processes. *Surface and Coatings Technology* 370 (July 2019), 196–212. DOI: 10.1016/j.surfcoat.2019.04.067. URL: https://www.sciencedirect.com/science/article/pii/S025789721930444X.

[175] A. Milanti, H. Koivuluoto, P. Vuoristo, G. Bolelli, F. Bozza and L. Lusvarghi. Microstructural Characteristics and Tribological Behavior of HVOF-Sprayed Novel Fe-Based Alloy Coatings. *Coatings* 4.1 (Jan. 2014), 98–120. DOI: 10.3390/coatings4010098. URL: http://www.mdpi.com/2079-6412/4/1/98/.

[176] J. Matejicek, S. Sampath and J. Dubsky. X-ray residual stress measurement in metallic and ceramic plasma sprayed coatings. *Journal of thermal spray technology* 7.4 (1998), 489–496.

[177] G. Bolelli, V. Cannillo, R. Gadow, A. Killinger, L. Lusvarghi, T. Manfredini and P. Müller. Properties of Al_2O_3 coatings by High Velocity Suspension Flame Spraying (HVSFS): Effects of injection systems and torch design. *Surface and Coatings Technology* 270 (Mar. 2015), 175–189. DOI: 10.1016/j.surfcoat.2015.03.005.

[178] R. T. McGrann, D. J. Greving, J. R. Shadley, E. F. Rybicki, B. E. Bodger and D. A. Somerville. The Effect of Residual Stress in HVOF Tungsten Carbide Coatings on the Fatigue Life in Bending of Thermal Spray Coated Aluminum. *Journal of Thermal Spray Technology* 7.4 (Dec. 1998), 546–552. DOI: 10.1361/105996398770350774.

[179] A. Ibrahim, R. Lima, C. Berndt and B. Marple. Fatigue and mechanical properties of nanostructured and conventional titania (TiO_2) thermal spray coatings. *Surface and Coatings Technology* 201.16-17 (May 2007), 7589–7596. DOI: 10.1016/j.surfcoat.2007.02.025.

[180] A. Vackel and S. Sampath. Fatigue behavior of thermal sprayed WC-CoCr-steel systems: Role of process and deposition parameters. *Surface and Coatings Technology* 315 (Apr. 2017), 408–416. DOI: 10.1016/j.surfcoat.2017.02.062.

[181] J. H. Kim, S. Lee, K. S. Lee and D. K. Kim. The effect of grain boundary phase on contact damage resistance of alumina ceramics. *Journal of Materials Science* 39.23 (2004), 7023–7030. DOI: 10.1023/B:JMSC.0000047547.09325.3d.

[182] J. Takeuchi, H. Nakahira and J. Nagai. Physical properties of some oxide coatings by low pressure plasma spraying. *2nd Plasma Technik Symposium, Vol. 2*. Ed. by S. Blum-Sandmeier, H. Eschnauer, P. Huber and A. Nicoll. Wohlen, Switzerland: Plasma Technik AG, 1991, 141–151.

[183] J. Mougin, T. Le Bihan and G. Lucazeau. High-pressure study of Cr_2O_3 obtained by high-temperature oxidation by X-ray diffraction and Raman spectroscopy. *Journal of Physics and Chemistry of Solids* 62.3 (Mar. 2001), 553–563. DOI: 10.1016/S0022-3697(00)00215-8.

[184] R. Mušálek, J. Matějíček, V. Pejchal, E. Mari, a. Valarezo and S. Sampath. Influence of Pores and Cracks Morphology on Mechanical Behavior of Thermally Sprayed Ceramics. *Proceedings of the 2010 International Thermal Spray Conference* Singapore, (2010), 723–728.

[185] L. C. Driver, P. H. Shipway and D. G. Mccartney. Acoustic Emission as a Tool for Characterising HVOF-Sprayed WC-Co Coatings. *Thermal Spray 2003: Advancing the Science & Applying the Technology*. Ed. by B. Marple and C. Moreau. Orlando, USA: ASM, 2003, 801–807.

[186] L. Erickson, R. Westergård, U. Wiklund, N. Axén, H. Hawthorne and S. Hogmark. Cohesion in plasma-sprayed coatings — a comparison between evaluation methods. *Wear* 214.1 (Jan. 1998), 30–37. DOI: 10.1016/S0043-1648(97)00216-0.

[187] C. E. Brennen. *Cavitation and Bubble Dynamics*. 1st ed. Vol. 44. New York: Oxford University Press Inc, 1995, 282. ISBN: 0195094093.

[188] W. Rhodes. Agglomerate and Particle Size Effects on Sintering Yttria-Stabilized Zirconia. *Journal of the American Ceramic Society* 64.1 (1981), 19–22. DOI: 10.1111/j.1151-2916.1981.tb09552.x.

[189] F. L. Toma, A. Potthoff and M. Barbosa. Microstructural Characteristics and Performances of Cr_2O_3 and Cr_2O_3-15%TiO_2 S-HVOF Coatings Obtained from Water-Based Suspensions. *Journal of Thermal Spray Technology* 27.3 (Jan. 2018), 344–357. DOI: 10.1007/s11666-018-0687-1.

PUBLICATIONS

PUBLICATION

I

Evaluating the toughness of APS and HVOF-sprayed Al_2O_3-ZrO_2-coatings by in-situ- and macroscopic bending

J. Kiilakoski, R. Musalek, F. Lukac, H. Koivuluoto and P. Vuoristo

Journal of the European Ceramic Society 38.4 (2018), 1908–1918
DOI: 10.1016/j.jeurceramsoc.2017.11.056

Journal of the European Ceramic Society 38 (2018) 1908–1918

Contents lists available at ScienceDirect

Journal of the European Ceramic Society

journal homepage: www.elsevier.com/locate/jeurceramsoc

Original Article

Evaluating the toughness of APS and HVOF-sprayed Al_2O_3-ZrO_2-coatings by in-situ- and macroscopic bending

J. Kiilakoski[a,*], R. Musalek[b], F. Lukac[b], H. Koivuluoto[a], P. Vuoristo[a]

[a] Laboratory of Materials Science, Tampere University of Technology, Korkeakoulunkatu 6, 33720 Tampere, Finland
[b] Department of Materials Engineering, Institute of Plasma Physics CAS, v.v.i, Za Slovankou 3, Prague ,18200, Czech Republic

ARTICLE INFO

Keywords:
Thermal spray
Al_2O_3-ZrO_2
Toughening
Fracture
Mechanical testing

ABSTRACT

Thermally-sprayed ceramic coatings are commonly used in applications where high wear and corrosion resistance are essential. However, their inherently low toughness and resistance to impacts often limit their use. In bulk ceramics, the toughening effect of ZrO_2 has been successfully implemented in different compositions of Al_2O_3-ZrO_2. Successful toughening leads to increased wear resistance and higher reliability. In this study, APS- and HVOF-sprayed Al_2O_3-40ZrO_2 coatings were characterized with SEM and XRD techniques. The toughness of the coatings was evaluated by measuring their strain tolerance with in-situ (SEM) three-point-bending and macroscopic four-point bending with acoustic emission instrumentation. The APS-coatings had a higher strain-to-fracture but failed abruptly. In HVOF-coatings, the cracking commenced earlier but proceeded slower with more crack deflections. The observed behaviour is likely to derive from the coarser microstructure of the APS-coatings, which allows strain distribution in a larger area unlike the finer structure with a lesser melting degree of the HVOF-coatings.

1. Introduction

Thermal spraying is widely used in creating thick protective or functional coatings on substrates of various materials. The coating is formed by melting the feedstock –typically powder or wire – and propelling the droplets onto a surface where they impinge and solidify. Thermally sprayed ceramic coatings are often used in thermal barrier coatings (TBC), where stabilized ZrO_2 is the most common material. Other oxides, such as Al_2O_3, Cr_2O_3, TiO_2 are used in tribological applications requiring both wear and corrosion resistance. Examples of such applications are center press rolls of paper machines, process valves, mechanical seals etc. [1,2] Ceramic coatings have traditionally been sprayed with atmospheric plasma spray (APS) but recently, high-velocity oxy-fuel (HVOF) systems have been successfully used to produce dense, applicable and innovative coatings. [3] The main drawback of ceramic coatings has been their brittleness [4]. Therefore, increasing their fracture toughness without increasing the amount of defects in the structure is of great interest.

In the research of bulk ceramics, ZrO_2 has been long known to exhibit high toughness [5], owing to both its ability to toughen due to the transformation from tetragonal to monoclinic phase as well as ferroelastic domain switching in the tetragonal phase. [6] A side effect of this phase change is a large volume increase which usually deteriorates the coating integrity. However, this can be countered by stabilizing the ZrO_2 to either non-transformable tetragonal or cubic phases with additions of stabilizing oxides, such as MgO or Y_2O_3 as is already widely utilized in top-coats of thermal barrier coatings, where the coatings resistance to catastrophic failure is critical due to immense cyclic thermo-mechanical loading. [1,7] Adjusting the amount of stabilizer allows for differing degrees of transformability, leading to the so-called partially stabilized zirconias (PSZ). [8]

Aluminium oxide is used in thermal spraying due to its low cost and ability to achieve sufficient mechanical and electric properties [9]. Efforts to incorporate the toughening effect of ZrO_2 into the Al_2O_3 coatings have been made recently [10–13]. Research on bulk ceramics has shown that already small additions of ZrO_2 to Al_2O_3 may result in improvements in fracture toughness compared to pure Al_2O_3 [14–16]. For example, Chevalier et al. [14] have obtained a higher toughness for Al_2O_3-10ZrO_2 (5.9 MPa√m) than either pure Al_2O_3 (4.2 MPa√m) or pure ZrO_2 (5.5 MPa√m).

It is known, that during the coating deposition the fast cooling of Al_2O_3-ZrO_2 readily leads to the formation of an amorphous phase [10,17], which Oberste Berghaus et al. [10] have found to reduce the mechanical strength and wear resistance of the coatings. On the other hand, in their study they also found that unlike in the case of APS spraying, the employment of HVOF-spraying lead to the retention of

* Corresponding author.
E-mail address: jarkko.kiilakoski@tut.fi (J. Kiilakoski).

https://doi.org/10.1016/j.jeurceramsoc.2017.11.056
Received 1 June 2017; Received in revised form 22 November 2017; Accepted 25 November 2017
Available online 02 December 2017

small ZrO_2 particles in a matrix of Al_2O_3-ZrO_2, which in turn improved the crack propagation resistance of the coating by over 30%. In various studies, Chen et al. utilized APS [11], suspension plasma spray (SPS) [11,12], and solution precursor high-velocity oxy-fuel spray (SPHVOF) [13] to deposit Al_2O_3-ZrO_2 –coatings. They were able to achieve an amorphous and nanocrystalline structure with high amounts of α-Al_2O_3 and t-ZrO_2.

It is a common practice to measure the toughness of thermally sprayed ceramic coatings by indentation measurements or four-point bend tests. [18] The drawback of using these tests is the required knowledge of elastic moduli and/or Poisson's ratio of the coating, which have their own difficulties of determining. Additionally, measuring values from only the coating in the four-point bending can prove difficult when testing a coated sample and not a free-standing coating. The addition of acoustic emission to the four-point bending experiment allows for further interpretation of the cracking behaviour of a coating. This method has proven to be both repeatable [19] and informative [20–22]. Additional information has also been found from the traditional fracture toughness indentation test with the addition of acoustic emission instrumentation [23]. The understanding of these properties combined with wear testing of the coatings could lead to wholesome understanding of the damage tolerance of ceramic coatings, including resistance to macro- and micro-scale wear.

In the current study, Al_2O_3-ZrO_2 coatings deposited with both APS and HVOF from two different feedstocks have been studied. The coatings were characterized by scanning electron microscopy (SEM) and X-ray diffraction, and their fracture characteristics were evaluated by four-point bending with acoustic emission (AE) monitoring and in-situ three-point bending in the SEM. The aim is to compare these novel toughness testing methods and to determine the applicability of the AE-instrumented four-point bending as a fast, robust way to determine coating toughness reliably. The effects of powder morphology and spray process on the coating properties are evaluated based on the results.

2. Experimental procedures

2.1. Materials and coating manufacturing

The coatings were prepared from two different feedstocks, a fused & crushed (F&C) powder (Ceram GmbH, Germany) and an agglomerated & sintered (A&S) powder (MilliDyne Oy, Finland). The latter was manufactured to the precise eutectic composition of the Al_2O_3-ZrO_2 –system [24]. For the two spray methods, appropriate powder size distributions were used. The APS samples were sprayed using Oerlikon Metco F4MB atmospheric plasma spray system. The HVOF samples were sprayed with TopGun (GTV Verschleißschutz GmbH, Germany) with ethene as the fuel gas. The coatings were deposited on AISI 5120 low carbon steel plates which were grit-blasted with alumina (grit 36) before spraying. The samples for four-point bending were grit-blasted on both sides prior to spraying and their size was 180 × 25 × 5 mm. The deposition parameters are listed in Table 1.

Table 1
Spray parameters for the coating deposition.

Sample name Process	APS F&C APS	APS A&S	HVOF F&C HVOF	HVOF A&S
Material Chemical Composition [wt.%]	Al_2O_3-40ZrO_2	Al_2O_3-42.5ZrO_2	Al_2O_3-40ZrO_2	Al_2O_3-42.5ZrO_2
Powder Manufacturer	Ceram	MilliDyne	Ceram	MilliDyne
Powder Size [Microns]	−51 + 20	−41 + 10	−30 + 10	−27 + 10
Current [A]	610		–	
Voltage [V]	70		–	
Power [kW]	42.7		–	
C_2H_4 [slpm]	–		90	
O_2 [slpm]	–		257	
Ar [slpm]	41		–	
H_2 [slpm]	13		–	
Standoff distance [mm]	140		150	
Relative surface speed [m/min]	87		179	
Offset [mm/pass]	7		2.9	
Passes [number]	36	48	36	30
Coating thickness [μm]	300	350	330	300

2.2. Microstructural and mechanical characterization

The powders and coatings were characterized by scanning electron microscopy and energy dispersive spectroscopy (SEM + EDS, Zeiss Evo 15, Zeiss GmbH, Germany and Philips XL30, FEI, Eindhoven, The Netherlands). X-ray diffraction with quantitative Rietveld refinement phase analysis [25] of the feedstock powders and coatings was performed by TOPAS v5 software on data acquired by D8 Discover XRD [26] (Bruker, Karlsruhe, Cu-Kα radiation of wavelength 1.5406 Å, Germany). The microhardness of the coatings was measured from ten indentations using a Vickers hardness tester (MMT-X7, Matsuzawa, Japan) and a load of 300 gf ($HV_{0.3}$). The coating porosities were estimated from six cross-sectional SEM micrographs using back-scattered electron (BSE) imaging mode and three different magnifications (1000x, 3000 x and 5000x), two images per each magnification.

2.3. Four-point bending with acoustic emission instrumentation

A universal testing machine (Instron 8800, Norwood, MA, USA) was utilized with a 100 kN load cell and a four-point bending jig. In the jig, the inner span of the support pins was 45 mm and for the outer pins 110 mm. The samples were tested with the coating in tension facing downwards and a piezoelectric sensor (8313, Bruel & Kjær, Denmark) with a resonance frequency of 200 kHz was attached to the substrate side of the sample to detect the elastic waves initiated by coating failure. A schematic presentation of the experimental setup is presented in Fig. 1. Four samples of each coating were tested. The AE-sensor was attached via a preamplifier (2637, Bruel & Kjær, Denmark) to a data acquisition unit (NI cDAQ9174 and NI9223, National Instruments, USA) that was connected to a computer. The sampling frequency was 1 MHz. The acquired data was analysed with the DIAdem-software (National Instruments, USA).

The samples were bent with a speed of 10 mm/min, until the central support displacement of 10 mm was reached. This led to a displacement of 14.0 ± 0.5 mm at mid-span of the samples. The acoustic energy E_{AE} emitted during bending was calculated according to Eq. (1) [27]

$$E_{AE} = \frac{1}{R}\int_{t_1}^{t_2} V(t)^2 dt \quad (1)$$

where R is the electrical resistance of the preamplifier (10 kΩ is chosen per convention) and V is the amplitude of the signal. Two uncoated

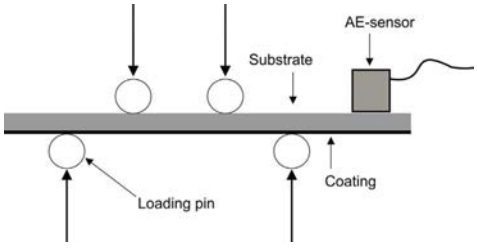

Fig. 1. A schematic of the experimental setup of the four-point bending.

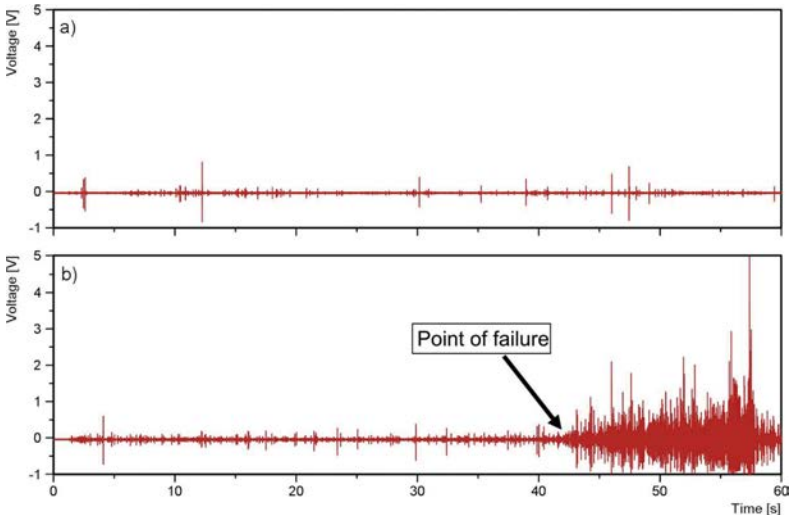

Fig. 2. Graphs of the AE-signal vs. time of a) uncoated and b) coated sample during four-point-bending.

samples were also bent and the total energy averaged. This value was kept as a reference threshold value for the bend tests; when the total acoustic energy of a coated sample surpasses this threshold value, the strain is marked as "strain-to-fracture". The surface strain value is calculated from the displacement using beam theory according to Eq. (2) [28]

$$\varepsilon[\%] = \frac{436Dh}{L^2}, \tag{2}$$

where D is displacement at mid-span in mm, h is the thickness of the sample and L is the distance of the outer pins. Graphs of a raw AE-signal vs. time for an uncoated and coated sample are illustrated in Fig. 2.

2.4. In-situ three-point bending

In-situ three-point bending was carried out in low vacuum mode in SEM microscope EVO MA 15 (Carl Zeiss SMT, Germany) equipped with Microtest 200 N tensile tester (Deben, UK). BSE imaging was used in order to obtain desired phase contrast. Three-point bending setup with outer support span of 23 mm was used. Samples for testing were cut from the as-sprayed samples with a metallographic precision saw and ground in order to remove any material possibly damaged during cutting and assure proper geometry of the samples and planarity of the cuts. Substrate was thinned by grinding in order to decrease stiffness of the samples. Cross-section to be observed was polished using a standard materialographic procedure up to an oxide polishing stage using colloidal silica (OP-S). Dimensions of the final beams were approximately 1.5 × 1.5 × 30 mm (width × thickness × length), with the thickness of the coating remaining as sprayed, i.e. 0.3–0.35 mm and the thickness of the substrate being 1.15–1.2 mm. Samples were loaded with the coating in tension, displacement rate of central support of 0.1 mm/min and interrupted "stepwise" loading mode [29], i.e., at predefined displacements, loading was stopped and the ongoing materials failure was documented with acquisition of high-resolution image. From the time-

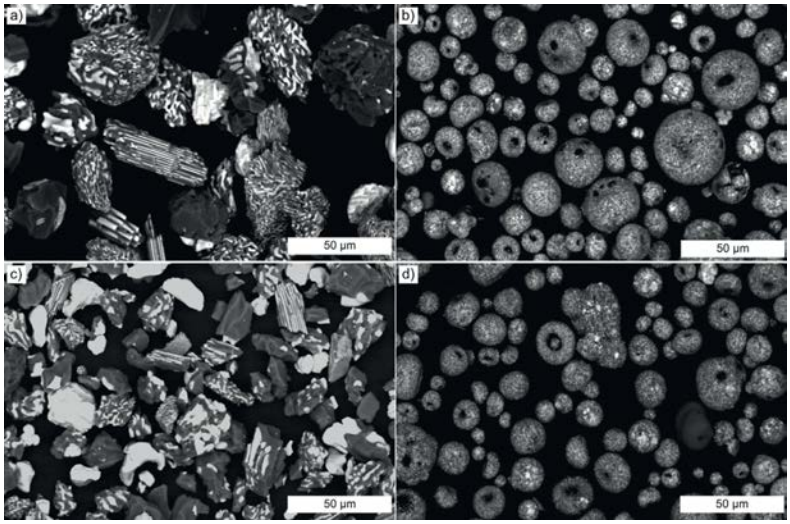

Fig. 3. Powder morphologies of a) APS F&C; b) APS A&S; c) HVOF F&C; and d) HVOF A&S powders. SEM (BSE)-images.

lapse sequence of such micrographs, failure propagation may be studied. For each coating, three samples were tested with repeatable results. More details on the testing method are presented in [29–31]. The distances between cracks were measured by selecting the two adjacent cracks next to the magistrate crack that was created in the middle of the sample where the support pin was. These two distances were measured for all samples and presented as an average of six measurements.

3. Results & discussion

3.1. The powder morphology

The powder morphologies are presented in Fig. 3. Two phases can be clearly distinguished from differing shades of grey in the images; ZrO_2 is brighter due to the greater atomic number of Zr in ZrO_2 than Al in Al_2O_3. The fused & crushed powders are of irregular shape with sharp facets and fully dense while the agglomerated & sintered powders are spherical and somewhat porous. The morphology of the particles resulting from spray drying is very variable with artefacts such as blowholes that, when large enough, can resemble a donut. [32] The blowholes can be formed during spray drying for example due to the evaporation rate of the solvent exceeding the rate of liquid/vapour diffusion through the particle, thus rupturing the particle wall. [33] Generally, in the F&C powder, most particles are a mixture of Al_2O_3 and ZrO_2 but particles consisting of only one material can be seen as well in Fig. 3a) and c). On the contrary, the nature of agglomeration and much finer size of the Al_2O_3 and ZrO_2 regions in the A&S powders enables the more homogeneous mixing of both constituents in the particles – see Fig. 3b) and d).

3.2. The coating microstructure

The cross-sectional structures of the APS-coatings, APS F&C and APS A&S, are presented in Fig. 4. Both coatings are relatively dense with 2.18 ± 0.38% and 2.03 ± 0.45% total porosity, respectively, while presenting some minor vertical quenching cracks. Presence of such intrasplat cracks is a typical result of residual stress relaxation in the ceramic coatings [34]. The gradient shades of grey coming from the different Al:Zr ratio in the individual splats indicate effective intermixing and merging of the original Al_2O_3 and ZrO_2 phases present in the feedstock powders in various contents possibly forming nanocrystalline or even amorphous splats which is common in thermal spraying of Al_2O_3-ZrO_2 coatings [17]. The elemental map of Fig. 4b) obtained by EDS is presented in Fig. 5, where the Zr- and Al-rich areas can easily be distinguished. The APS-coating sprayed with the agglomerated & sintered powder has more unmelted particles, Fig. 4d. Generally, the distinct separation of large areas of different phases in the fused & crushed powder has led to a more pronounced heterogeneous structure in the coating with Al_2O_3-rich, ZrO_2-rich and mixed regions.

Presented in Fig. 6 are the cross-section images of the F&C and A&S HVOF –coatings. Similar to their APS counterparts, also here the coating sprayed from the agglomerated & sintered powder the coating has a more homogeneous phase distribution. The coating HVOF A&S has a high density of vertical cracks – similar to both APS coatings – while the fused & crushed powder leads to a seemingly more dense structure in the coating HVOF F&C. However, the total porosities of the F&C and A&S coatings were 1.16 ± 0.35% and 0.88 ± 0.31%, respectively. In addition, due to the finer feedstock powder, both coatings exhibit a finer microstructure in comparison with the plasma-sprayed coatings.

The difference in splat sizes can also be verified from the surface images presented in Fig. 7., where the finer size of the splats can be seen in the HVOF coatings. Additionally, the amount of cracking in the F&C HVOF coating is also on the free surfaces lower than in all other coatings.

Vickers hardnesses of the coating cross-sections are plotted along with the coating porosities in the graph in Fig. 8. The hardness values reflect well the above mentioned differences in the coating microstructure. The agglomerated & sintered powders resulted in slightly more vertical cracking in the coatings and therefore a weaker structure. Low porosity and a defect-free structure can lead to higher hardnesses [2], which is also presented by the high hardness value of 917 ± 48 $HV_{0.3}$ of the seemingly dense HVOF-sprayed F&C-coating. The porosities of the coatings are on the lower end of typical porosity values of these thermal spray methods [1] and are largely a result of the spherical pores and microcracks as seen in Fig. 4 and Fig. 6. Noteworthy is the distinction between the porosities of F&C and A&S –coatings; with both spray methods the F&C coatings exhibited higher porosities, but this small difference is likely due to the darker regions in the coating cross-sections causing error in the measurement due to its visual nature.

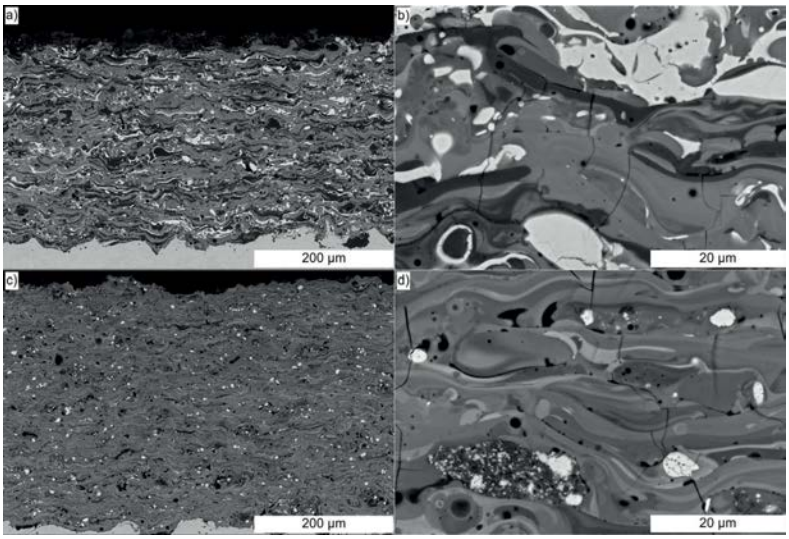

Fig. 4. APS F&C Al_2O_3-40ZrO_2 coating a) structure and b) microstructure and APS A&S Al_2O_3-40ZrO_2 coating c) structure and d) microstructure. SEM images.

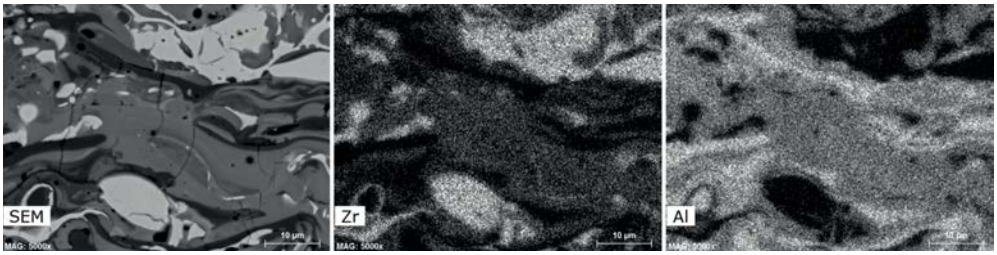

Fig. 5. EDS elemental map of APS F&C coating presenting the difference in elemental content within the coating. The light color illustrates areas rich in the element in question.

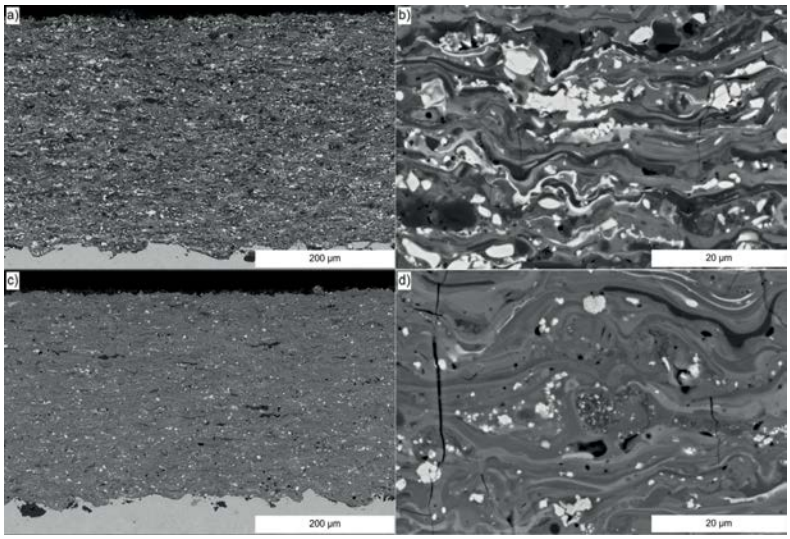

Fig. 6. HVOF F&C Al_2O_3-40ZrO_2 coating a) structure and b) microstructure and HVOF A&S Al_2O_3-40ZrO_2 coating c) structure and d) microstructure. SEM images.

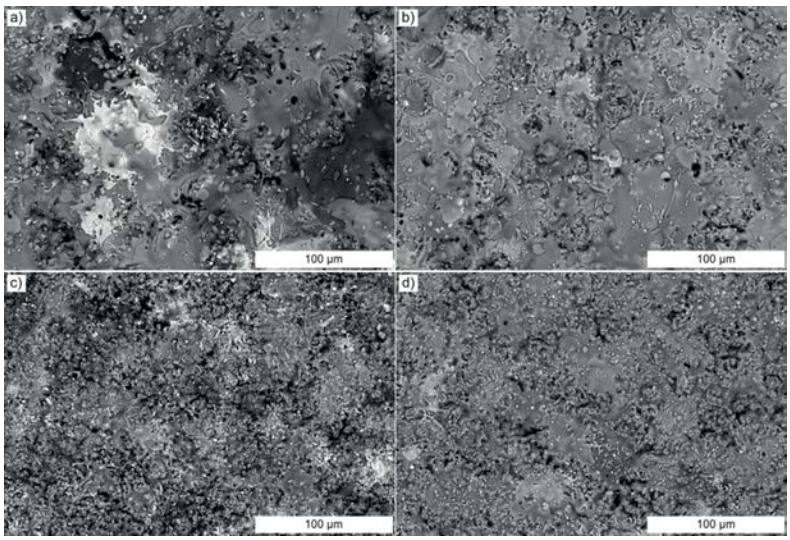

Fig. 7. Surface images of the coatings. APS a) F&C b) A&S and HVOF c) F&C and d) A&S. SEM-images.

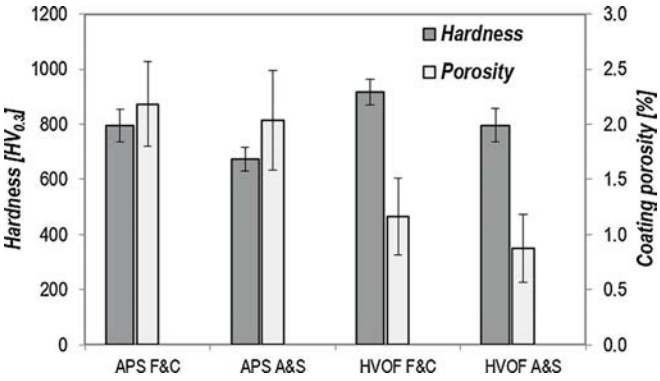

Fig. 8. Vickers hardness and porosity obtained from the coating cross-sections.

Table 2
Phase compositions of the feedstock and the coatings as calculated from the Rietveld analysis.

		APS F&C		APS A&S		HVOF F&C		HVOF A&S	
Crystallinity [%]		Feedstock 100	Coating 45	Feedstock 100	Coating 15	Feedstock 100	Coating 46	Feedstock 100	Coating 18
Phase content [mol-%]	α-Al_2O_3	64,3 ± 0,5	17,3 ± 0,5	62,0 ± 0,2	61,1 ± 0,5	63 ± 1	27,5 ± 0,5	62,0 ± 0,7	43,8 ± 0,5
	γ-Al_2O_3	–	24 ± 1	–	–	–	11 ± 1	–	–
	t-ZrO_2	1,3 ± 0,1	18 ± 1	1,13 ± 0,05	8 ± 1	1,4 ± 0,1	25 ± 1	1,11 ± 0,06	4 ± 1
	m-ZrO_2	34,4 ± 0,5	40 ± 1	36,9 ± 0,2	30 ± 1	36 ± 1	36 ± 1	36,9 ± 0,7	52 ± 1

Quantitative Rietveld refinement analysis was performed on the XRD profiles of the samples in order to determine the phase compositions of the feedstock powders and resulting coatings. The compositions extracted from the analyses are presented in Table 2. All feedstock powders were fully crystalline and exhibited similar phase compositions close to the eutectic composition 61.8 mol-% α-Al_2O_3 with the balance being mainly monoclinic ZrO_2. A graph of the XRD scans of the powders is presented in Fig. 9.

The phase composition of the coatings was more variable, their diffraction pattern fits are presented in Fig. 10. Both F&C coatings consisted of α- and γ-Al_2O_3 and monoclinic and tetragonal ZrO_2. The amounts of both α-Al_2O_3 and t-ZrO_2 were higher in the HVOF coating. The composition difference is likely due to the lower temperature of the HVOF-process leading to the temperature of the coating dropping under the transition temperature faster, which enables higher retention of the tetragonal ZrO_2. The t-ZrO_2 was found to be transformable, as investigated by calculating the c/a√2–ratio of the unit cell. The ratio was 1.02 for APS F&C and 1.019 for HVOF F&C, which are far from the ratio of non-transformable t'-ZrO_2 found to be between 1.005 [35] and 1.01 [36]. Additionally, the coatings had a crystallinity of 45–46% indicating large amounts nanocrystalline or amorphous phases.

The A&S coatings consisted of α-Al_2O_3, m-ZrO_2 and t-ZrO_2 with a crystallinity of only 15 and 18% for the APS and HVOF coatings, respectively. Hence, the coating is mainly amorphous and determination of the phase content is difficult. Moreover, due to the low amount of t-ZrO_2 we were not able to calculate the amount of t'-ZrO2 for the A&S samples. The low amount of t-ZrO_2 in the A&S coatings can be credited to the feedstock being unstabilized. Interestingly, the lower amount of

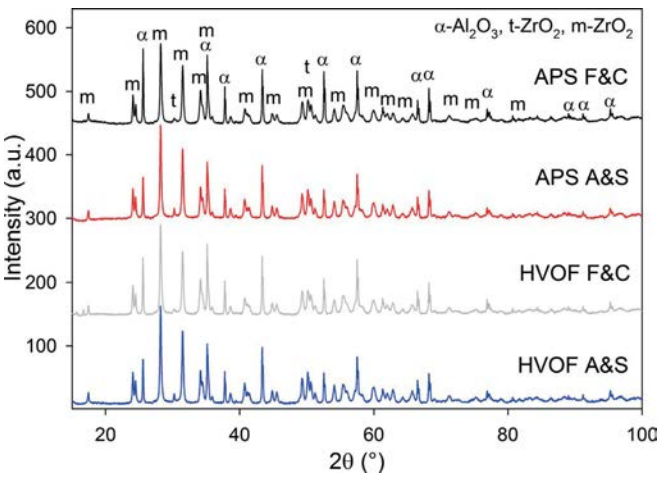

Fig. 9. XRD scans of the feedstock powders with the peaks of the different phases denoted by symbols.

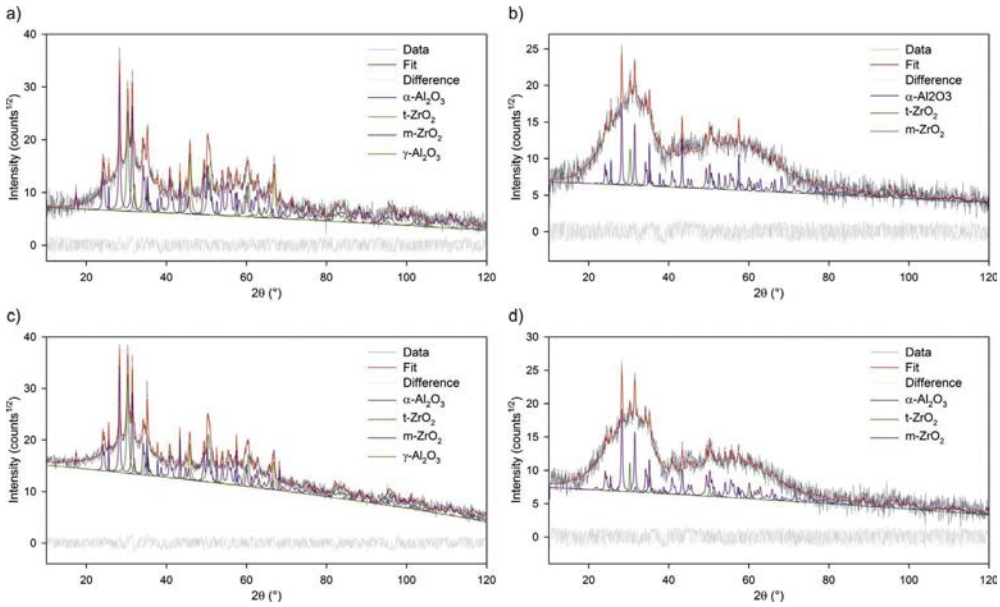

Fig. 10. Rietveld fits of the x-ray diffraction patterns of the coatings: a) APS F&C, b) APS A&S, c) HVOF F&C, d) HVOF A&S.

α-Al_2O_3 in the HVOF A&S coating as compared to APS A&S coating indicates that a higher amount of Al_2O_3 was in nanocrystalline or amorphous form, possibly stemming from a combined effect of smaller particle-size and lower process temperature. The low crystallinity in the A&S coatings is likely due to the well mixed finer primary particles of Al_2O_3 and ZrO_2, where the Al_2O_3 particles can slow the crystallization of ZrO_2 nanoparticles from amorphous ZrO_2 [37].

3.3. In-situ SEM three-point bending

During the in-situ bending experiment, evolution of the coating failure was observed [dataset] [38]. The macroscopic fracture behaviour of all the tested coatings was similar. First, several short cracks initiated above the central loading pin at the free surface of the coating, where the maximum strain was imposed. From the deflection of the sample, critical flexural strain at the coating surface was evaluated (see Fig. 11). In general, critical flexural strain of both APS samples was about 20% higher than for HVOF coatings. As the straining increased, cracks propagated in the through-thickness direction but shortly, only one crack became dominant causing localized strain relief in the surrounding material and thus retarding and then even closing the other nearby cracks. Hence, only one main through-thickness crack usually emerged above the central loading pin.

This main crack propagated almost perpendicularly to the free surface. After reaching the substrate, it diverted and propagated along the coating-substrate interface causing large-scale delamination of the coating. Straining of the partially delaminated coating could in the areas of improved mechanical anchoring lead to localized formation of short cracks originating at the coating-substrate interface and propagating towards the sample surface. This was observable especially for the HVOF A&S –coating (see Fig. 12). With further bending, secondary through-thickness cracks were also developed from the free surface (see HVOF A&S in Fig. 12d). Note that for the other samples in Fig. 12, the secondary cracking was out of observable area. Spacing between the through-thickness cracks was found to be strongly dependent on the thermal spray process, being about two-times higher for plasma spraying than for HVOF (Fig. 11) Together with higher critical flexural strain, it indicates that the coarser and looser microstructure of APS

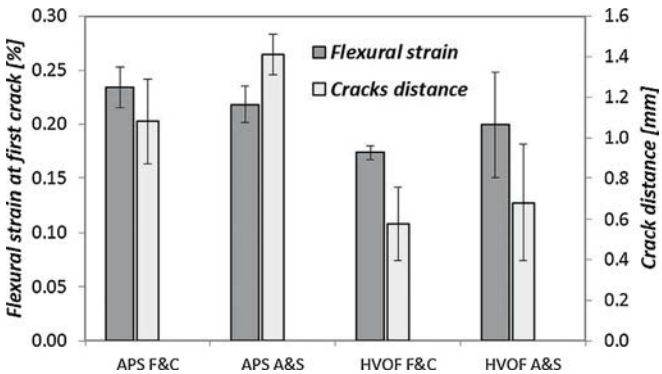

Fig. 11. Flexural strain and spacing between major through-thickness cracks as evaluated from in-situ experiment.

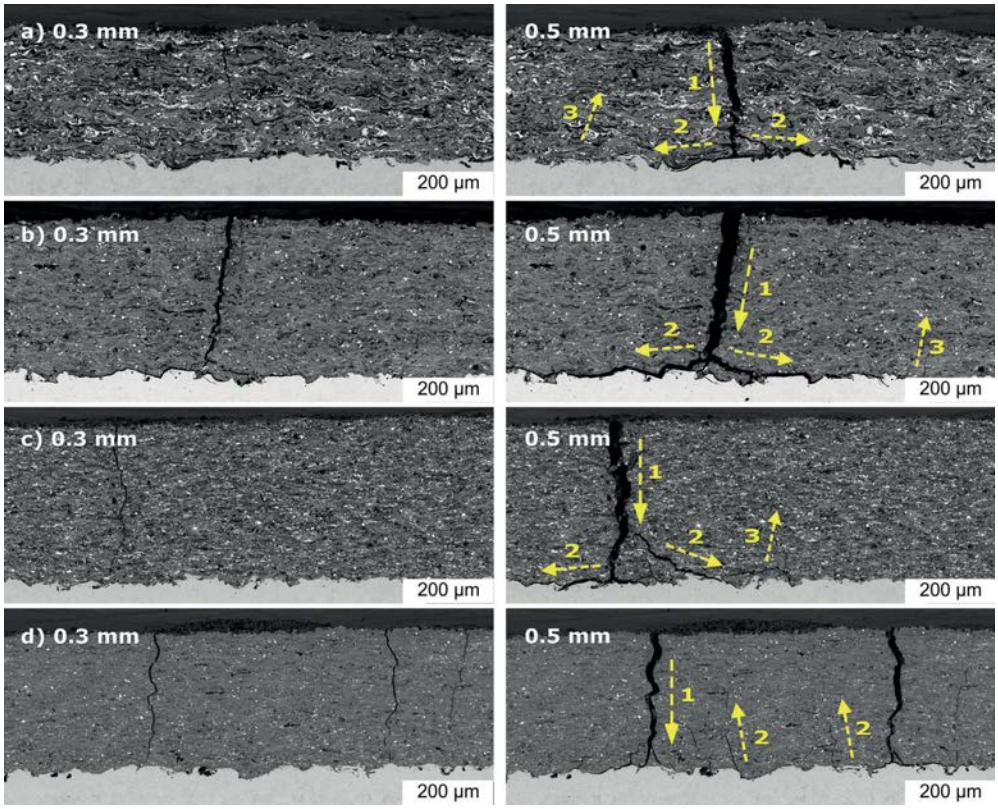

Fig. 12. Failure evolution during in-situ observation of the three-point bending of APS a) F&C, b) A&S and HVOF c) F&C, d) A&S coatings. Displacement of the central support 0.3 mm (left) and 0.5 mm (right). Arrows show the direction and propagation of the cracks. Numbers denote the order of appearance of cracks.

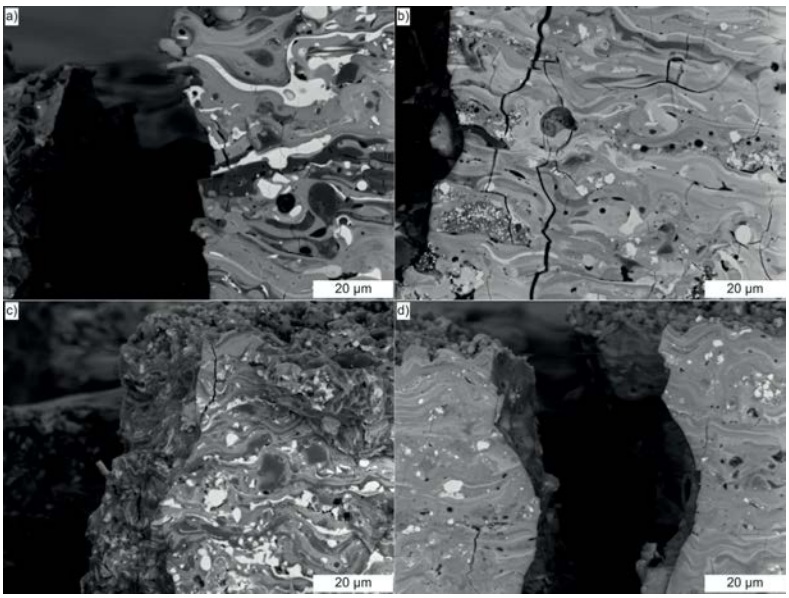

Fig. 13. Detailed SEM-images of the crack propagation after in-situ bending in a) APS F&C, b) APS A&S, c) HVOF F&C and d) HVOF A&S –coatings.

samples was more effectively accommodating the imposed straining, which thus resulted in the improved macroscopic strain-tolerance. This behaviour corresponds to earlier observations by Musalek et al. in the earlier works [39,40].

During the in-situ bending, all four tested coatings also showed excellent internal cohesion. In general, regardless of the local phase composition, cracks did not follow the splat–splat interfaces but cracking of the splats and interlinking of the original short vertical quenching cracks (see Fig. 13) were dominant micromechanisms of the crack propagation. As denoted by numbers in Fig. 12, in all cases the crack initiated at the free surface of the coating making its way towards the substrate-coating interface instantaneously (1). In both APS coatings and the HVOF F&C coating this was followed by interface opening and onset of the coating delamination (2). When suitable conditions arose (usually at a weak link in the coating and/or a peak in the substrate topography) the newly formed cracks propagated back into the coating toward the free surface (3). In the case of HVOF A&S coating the bond strength was sufficient to withstand crack propagation and the second type of cracking was suppressed. It should be noted that the coating damage was most prominent in the crack initiation area, distinguishable within about 20 µm distance from the major cracks (Fig. 13) leaving most of the surrounding coating intact.

3.4. Four-point bending

The results of the four-point bending test with acoustic emission instrumentation are presented in Fig. 14. In general, the APS-coatings showed again a higher strain tolerance when compared to the HVOF-coatings, which can be attributed to the coarser microstructure of the APS coatings and their higher internal cohesion that is able to more efficiently accommodate the imposed tensile straining. In other words, the smaller splat size of the HVOF-coatings and their denser yet partially less melted structure leads to the cracking accommodating stresses only in the near region of the crack. This is confirmed by the similar trend observed from the in-situ three-point bending, where APS coatings had a higher strain at the appearance of the first visible crack. The measured strain is higher in four-point bending than in three-point bending, since in the latter, the very first visible crack is recorded while in the four-point bending test, crossing of cumulative noise threshold is recorded as cracking. When comparing the coatings deposited with the same spray-method, the F&C-coatings has a higher strain tolerance and lower variation than the A&S coatings. This is likely a result of the more crystalline structure and hence more available slip planes of the F&C coatings. Furthermore, the variation in the results of the test correlates with coating homogeneity and the amount of glassy phase. The scatter is higher for APS- than HVOF-coatings, and for the A&S- than F&C-powders. Comparison with the scatter in the in-situ bending results reveals again similarity in the HVOF F&C coating having clearly the lowest scatter and in general, the A&S coating had vastly larger variation in test results.

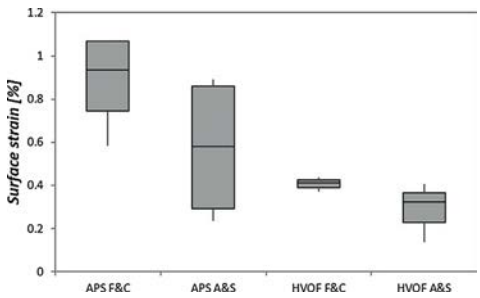

Fig. 14. Box-plot of the surface strain at the point of theoretical fracture, as measured by AE-instrumented four-point bending.

Analyses of the power spectrum densities were performed for the FFT-transformed signals. This allows us to evaluate the amplitude of the signal at different frequencies, rather than just against a time-scale [41]. Comparison between the coatings is presented in a normalized histogram with a bin size of 50 kHz and 25 kHz near the resonant frequency of the sensor at 200 kHz in Fig. 15 highlighting the characteristic frequencies recorded during bending. This enables us to compare the dynamics of the cracking in the coatings, since a more rapid crack propagation should lead to a higher frequency elastic wave in the substrate while more crack deflections and a longer crack path should lead to a lower detected frequency.

An interesting finding is that the HVOF-coatings tend to show more intensive cracking in the lower frequency range of 100–150 kHz than the APS-coatings while there is more cracking in the range 200–250 kHz in the latter. A possible explanation is that the higher melting degree and coarser microstructure of the APS coatings lead to stronger but fewer inter-splat connections and that the cracking occurs more abruptly and violently, causing a higher frequency elastic wave in the sample. On the other hand, the smaller scale microstructure and unmelted areas in the HVOF-coatings lead to a more gradual crack opening, which causes waves of lower frequencies. Similar observations were made by Driver et al. [42], who attributed lower energy acoustic emission during bending of HVOF-sprayed WC-17Co –coatings to the pre-existing cracks and their subsequent opening as opposed to well-molten structures where cracks are forced to propagate through the splats. An analysis of the acoustic wave geometry from bending YSZ thermal barrier coatings was performed by Ma et al. [20], where shorter rise time (higher frequency) was attributed to local fracture of a weak area in the coating and a longer rise time (lower frequency) was due to a slip in the coating or at the coating/substrate interface. This is analogous to the difference between ductile tearing and brittle fracture, as was also noticed earlier by Akita et al. [43] in their study of APS-sprayed Mo-coatings. They claimed that grater energy released stems from a more ductile coating, but the apparent contradiction to our findings is due to a different definition of ductility for a ceramic coating. Akita et al. defined ductility as the ability to resist microcracking, while in the current work, “tougher” behaviour means resisting catastrophic failure to greater strains since microcracks are generated already during deposition. Additionally, Tronskar et al. [44] found in impact testing of normalized ship grade steels that ductile tearing causes acoustic noise in a broader spectrum of frequencies, with the maximum peak significantly lower than in brittle fracture. This also gives assurance to our presumption that the APS coatings are more brittle due to their higher melting degree, while HVOF coatings are toughened by the pre-existing microcracks and unmelted areas. This idea is supported by the crack distances measured in the in-situ bending test (Fig. 11), where the pre-existing cracks of the HVOF-coatings led generally to smaller distances between newly formed through-thickness cracks than in the APS-coatings.

Another observation can be made of the difference between F&C and A&S coatings: there are fewer impulses in the 175–200 kHz frequency range in the A&S coatings than the F&C counterparts, while there are more impulses for the A&S coatings in the 200–225 kHz range. The difference is greater in the case of HVOF than APS, possibly due to the lower melting power of the HVOF-process emphasizing the effect of the difference in powder type. In practice, this difference is quite negligible considering the physical phenomenon and that the resonant frequency of the sensor is at 200 kHz.

4. Conclusion

In this study, APS and HVOF-sprayed Al_2O_3-40ZrO_2 coatings from eutectic F&C and A&S feedstocks were deposited and examined in regards to their behaviour in tensile loading in bending with two methods: in-situ three-point bending and macroscopic AE-instrumented

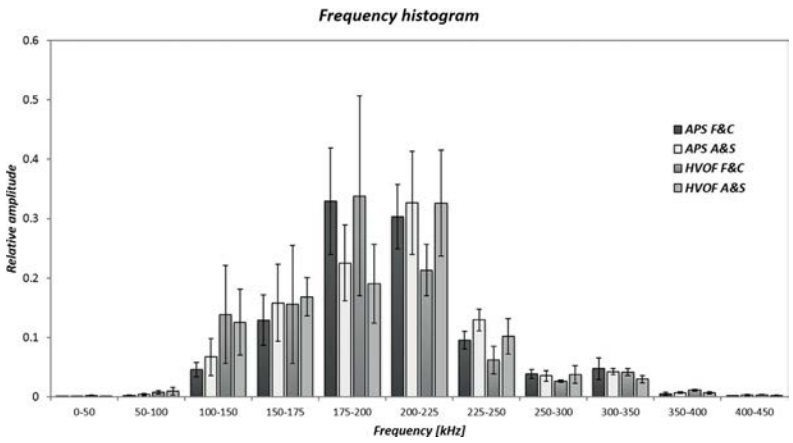

Fig. 15. A normalized histogram of the average power density spectra of the coating samples describing differences in the characteristic frequencies. Tables

four-point bending.

During in-situ bending, the cracking mechanism between different coatings did not show significant differences, except for HVOF-sprayed A&S coating that had numerous pre-existing cracks. The newly formed through thickness cracks were significantly further apart in the APS-coatings than the HVOF-coatings, indicating a greater capability of the coarser microstructure of the APS-coatings to accommodate stresses. This is also evidenced in their lower hardness values. The flexural strain from the in-situ experiment was significantly smaller than from AE, but both tests gave similar trends. The difference in detected strain is due to the difference in the method of failure detection. During the in-situ experiment, the onset of the individual cracks could be detected whereas the AE-method is sensitive to extensive coating failure, which produces acoustic energy strong enough to reach the predefined threshold energy value.

Using the F&C feedstock generally led to a higher strain tolerance, although the scatter in the case of A&S-coatings was quite high. The amorphous nature of the A&S coatings likely leads to the low strain-tolerance due to the absence of available slip planes. The variation in both tests was quite high, which was observed to be higher for coatings with a larger number of pre-existing faults. Thus, variation in these tests seems to be also a good indicator of coating quality.

The spectra of the AE-signals showed a difference in the characteristic frequency of cracking between APS and HVOF-coatings. The APS-coatings cracked more abruptly causing a higher frequency impulse, while the HVOF-coatings had more low frequency cracks probably stemming from the higher density of pre-existing cracks and unmelted particles as well as a smaller microstructural scale leading to more crack deflections. Therefore, the crack propagation in the HVOF-coatings happened more gradually.

With the help of in-situ three-point bending observations, the AE-instrumented four-point bending was validated to be a good measure of coating quality and able to detect even slight differences in toughness stemming from the coating structure. It can therefore be considered as one more method alongside the existing ones in evaluating the toughness of thermally sprayed ceramic coatings.

Further work on the topic should focus on expanding the amount and types of materials tested with four-point-bending to obtain a broader view of the toughness values in different compositions of thermally sprayed coatings.

Acknowledgements

The work was supported by DIMECC Ltd, its HYBRIDS programme and Tekes (Finnish Funding Agency for Technology and Innovation). In-situ testing was supported through grant GB14-36566G "Multidisciplinary research centre for advanced materials" (Czech Science Foundation). The authors would like to thank Mr. Mikko Kylmälahti of Tampere University of Technology for spraying the coatings.

References

[1] P. Vuoristo, Thermal Spray Coating Processes, in: S. Hashmi (Ed.), Comprehensive Materials Processing, Vol. 4 Elsevier, 2014, 2017, pp. 229–276, , http://dx.doi.org/10.1016/B978-0-08-096532-1.00407-61.
[2] L. Pawlowski, The Science and Engineering of Thermal Spray Coatings, second, John Wiley & Sons, West Sussex, England, 2008, http://dx.doi.org/10.1002/9780470754085.
[3] P.L. Fauchais, J.V.R. Heberlein, M.I. Boulos, Thermal Spray Fundamentals, Springer, U.S. Docton, M.A, 2014, http://dx.doi.org/10.1007/978-0-387-68991-3.
[4] G. Bolelli, V. Cannillo, L. Lusvarghi, T. Manfredini, Wear behaviour of thermally sprayed ceramic oxide coatings, Wear 261 (2006) 1298–1315, http://dx.doi.org/10.1016/j.wear.2006.03.023.
[5] A. Evans, Perspective on the development of high-toughness ceramics, J. Am. Ceram. Soc. (1990) 187–206, http://dx.doi.org/10.1111/j. 1151–2916.1990.tb06493.x.
[6] G.V. Srinivasan, J.F. Jue, S.Y. Kuo, A.V. Virkar, Ferroelastic domain switching in polydomain tetragonal zirconia single crystals, Am. Ceram. Soc (1989) 2098–2103, http://dx.doi.org/10.1111/j.1151-2916.1989. tb06038.x.
[7] R.A. Miller, Thermal barrier coatings for aircraft engines: history and directions, J. Therm. Spray Technol. 6 (1997) 35–42, http://dx.doi.org/10.1007/BF02646310.
[8] J.R. Kelly, I. Denry, Stabilized zirconia as a structural ceramic: an overview, Dent. Mater. 24 (2008) 289–298, http://dx.doi.org/10.1016/j.dental.2007.05.005.
[9] J. Ilavsky, C. Berndt, H. Herman, Alumina-base plasma-sprayed materials–part II: phase transformations in aluminas, J. Therm. Spray Technol. 6 (1997) 439–444, http://dx.doi.org/10.1007/s11666-997-0028-2.
[10] J. Oberste Berghaus, J.-G. Legoux, C. Moreau, F. Tarasi, T. Chráska, Mechanical and thermal transport properties of suspension thermal-sprayed alumina-zirconia composite coatings, J. Therm. Spray Technol. 17 (2007) 91–104, http://dx.doi.org/10.1007/s11666-007-9146-0.
[11] D. Chen, E.H. Jordan, M. Gell, Microstructure of suspension plasma spray and air plasma spray al2O3-ZrO2 composite coatings, J. Therm. Spray Technol. 18 (2009) 421–426, http://dx.doi.org/10.1007/s11666-009-9306-5.
[12] D. Chen, E.H. Jordan, M. Gell, Suspension plasma sprayed composite coating using amorphous powder feedstock, Appl. Surf. Sci. 255 (2009) 5935–5938, http://dx.doi.org/10.1016/j.apsusc.2009.01.038.
[13] D. Chen, E.H. Jordan, M. Gell, Solution precursor high-velocity oxy-fuel spray ceramic coatings, J. Eur. Ceram. Soc. 29 (2009) 3349–3353, http://dx.doi.org/10.1016/j.jeurceramsoc.2009.07.010.
[14] J. Chevalier, A.H. De Aza, G. Fantozzi, M. Schehl, R. Torrecillas, Extending the lifetime of ceramic orthopaedic implants, Adv. Mater. 12 (2000) 1619–1621, http://dx.doi.org/10.1002/1521-4095(200011)12:21<1619:AID-ADMA1619>3.0.CO;2-O.
[15] J. Chevalier, S. Deville, G. Fantozzi, J.F. Bartolomé, C. Pecharroman, J.S. Moya, et al., Nanostructured ceramic oxides with a slow crack growth resistance close to covalent materials, Nano Lett. 5 (2005) 1297–1301, http://dx.doi.org/10.1021/nl050492j.
[16] E. Kannisto, M.E. Cura, E. Levänen, S.P. Hannula, Mechanical properties of alumina based nanocomposites, Key Eng. Mater. 527 (2012) 101–106, http://dx.doi.org/10.4028/www.scientific.net/KEM.527.101.

[17] H.-J. Kim, Y.J. Kim, Amorphous phase formation of the pseudo-binary Al2O3–ZrO2 alloy during plasma spray processing, J. Mater. Sci 34 (1999) 29–33, http://dx.doi.org/10.1023/A:1004492919174.
[18] A.S.M. Ang, C.C. Berndt, A review of testing methods for thermal spray coatings, Int. Mater. Rev. 59 (2014) 179–223, http://dx.doi.org/10.1179/1743280414Y.0000000029.
[19] L.C. Cox, The four-point bend test as a tool for coating characterization, Surf. Coat. Technol. 36 (1988) 807–815, http://dx.doi.org/10.1016/0257-8972(88)90021-7.
[20] X.Q. Ma, S. Cho, M. Takemoto, Acoustic emission source analysis of plasma sprayed thermal barrier coatings during four-point bend tests, Surf. Coat. Technol. 139 (2001) 55–62, http://dx.doi.org/10.1016/S0257-8972(01)00995-1.
[21] L. Yang, Z.C. Zhong, J. You, Q.M. Zhang, Y.C. Zhou, W.Z. Tang, Acoustic emission evaluation of fracture characteristics in thermal barrier coatings under bending, Surf. Coat. Technol. 232 (2013) 710–718, http://dx.doi.org/10.1016/j.surfcoat.2013.06.085.
[22] E. Mayrhofer, L. Janka, W.P. Mayr, J. Norpoth, M.R. Ripoll, M. Gröschl, Cracking resistance of Cr3C2–NiCr and WC–Cr3C2–Ni thermally sprayed coatings under tensile bending stress, Surf. Coat. Technol 281 (2015) 169–175, http://dx.doi.org/10.1016/j.surfcoat.2015.09.002.
[23] E. Smazalová, Š. Houdková, The potential of AE sensing in the indentation fracture toughness measurement, in: P. Louda (Ed.), Defect and Diffusion Forum, Vol. 368 Trans Tech Publications, Zürich, Switzerland, 2016, pp. 203–206, , http://dx.doi.org/10.4028/www.scientific.net/DDF.368.203.
[24] G.R. Fischer, L.J. Manfredo, R.N. McNally, R.C. Doman, The eutectic and liquidus in the Al2O3 – ZrO2 system, J. Mater. Sci. 16 (1981) 3447–3451.
[25] H.M. Rietveld, Line profiles of neutron powder-diffraction peaks for structure refinement, Acta Crystallogr. 22 (1967) 151–152, http://dx.doi.org/10.1107/S0365110x67000234.
[26] A.A. Coelho, TOPAS Version 5 (Computer Software), (2016).
[27] M. Löhr, D. Spaltmann, S. Binkowski, E. Santner, M. Woydt, In situ acoustic emission for wear life detection of DLC coatings during slip-rolling friction, Wear 260 (2006) 469–478, http://dx.doi.org/10.1016/j.wear.2005.03.009.
[28] J. Voyer, H. Kreye, Determination of cracking resistance of thermal spray coatings during four-point bend testing using an acoustic emission technique, J. Therm. Spray Technol. 12 (2003) 416–426, http://dx.doi.org/10.1361/105996303770348285.
[29] R. Musalek, C. Taltavull, A.J. Lopez Galisteo, N. Curry, Evaluation of failure micromechanisms of advanced thermal spray coatings by in-situ experiment, Key Eng. Mater. 606 (2014) 187–190, http://dx.doi.org/10.4028/www.scientific.net/KEM.606.187.
[30] R. Musalek, M. Vilemova, J. Matejicek, U. Rey, J. Carlos, In-situ observation of ongoing microstructural changes in functionally graded thermal spray coating during mechanical loading, in: T.S. Sudarshan, P. Vuoristo, H. Koivuluoto (Eds.), Surf. Modif. Technol. XXVIII Valardocs, Tampere, Finland, 2014, pp. 571–579.
[31] R. Mušálek, O. Kovářík, J. Matějíček, In-situ observation of crack propagation in thermally sprayed coatings, Surf. Coat. Technol. 205 (2010) 1807–1811, http://dx.doi.org/10.1016/j.surfcoat.2010.03.064.
[32] P. Fauchais, G. Montavon, G. Bertrand, From powders to thermally sprayed coatings, J. Therm. Spray Technol. 19 (2010) 56–80, http://dx.doi.org/10.1007/s11666-009-9435-x.
[33] D.E. Walton, C.J. Mumford, Spray dried products – characterization of particle morphology, Trans. Inst. Chem. Eng. 77 (1999) 21–38.
[34] S. Kuroda, T.W. Clyne, The quenching stress in thermally sprayed coatings, Thin Solid Films 200 (1991) 49–66, http://dx.doi.org/10.1016/0040-6090(91)90029-W.
[35] M. Leoni, R. Jones, P. Scardi, Phase stability of scandia–yttria-stabilized zirconia TBCs, Surf. Coat. Technol. 108 (1998) 107–113, http://dx.doi.org/10.1016/S0257-8972(98)00617-3.
[36] C. Viazzi, J.-P. Bonino, F. Ansart, A. Barnabé, Structural study of metastable tetragonal YSZ powders produced via a sol–gel route, J. Alloys Compd. 452 (2008) 377–383, http://dx.doi.org/10.1016/j.jallcom.2006.10.155.
[37] B.L. Kirsch, A.E. Riley, A.F. Gross, S.H. Tolbert, Probing the effects of interfacial chemistry on the kinetics of phase transitions in amorphous and tetragonal zirconia nanocrystals, Langmuir 20 (2004) 11247–11254, http://dx.doi.org/10.1021/la048343o dataset.
[38] R. Musalek, In-situ SEM observation of crack propagation in Al2O3-ZrO2 APS and HVOF coatings, Mendeley Data v1, (2017), http://dx.doi.org/10.17632/szs2dm95vn.1.
[39] R. Musalek, J. Matejicek, M. Vilemova, O. Kovarik, Non-linear mechanical behavior of plasma sprayed alumina under mechanical and thermal loading, J. Therm. Spray Technol. 19 (2009) 422–428, http://dx.doi.org/10.1007/s11666-009-9362-x.
[40] R. Mušálek, J. Matějíček, V. Pejchal, E. Mari, a Valarezo, S. Sampath, Influence of pores and cracks morphology on mechanical behavior of thermally sprayed ceramics, in: B.R. Marple, A. Agarwal, M.M. Hyland, Y.-C. Lau, C.-J. Li, R.S. Lima, G. Montavon (Eds.), Proceedings of the International Thermal Spray Conference, DVS Media GmbH, Singapore, 2010, pp. 723–728.
[41] A. Brandt, Noise and Vibration Analysis: Signal Analysis and Experimental Procedures, 1 st, John Wiley & Sons, Inc., New Jersey United States, 2010.
[42] L.C. Driver, P.H. Shipway, D.G. Mccartney, Acoustic emission as a tool for characterising HVOF-Sprayed WC-Co coatings, in: B.R. Marple, C. Moreau (Eds.), Thermal Spray 2003: Advancing the Science And Applying the Technology, ASM InternationalOrlando, USA, 2003, pp. 801–807.
[43] K. Akita, G. Gang, S. Takahashi, H. Misawa, S. Tobe, In-situ observation and AE analysis of microscopic fracture process of thermal spray coatings.pdf, in: C. Coddet (Ed.), Proc. 15th Int. Therm. Spray Conf. ASM International, Nice, France, 1998, pp. 837–842.
[44] J.P. Tronskar, M.A. Mannan, M.O. Lai, Application of acoustic emission for measuring crack initiation toughness in instrumented charpy impact testing, J. Test. Eval. 31 (2003) 222–233, http://dx.doi.org/10.1520/JTE12420J.

PUBLICATION

II

Characterization of Powder-Precursor HVOF-Sprayed Al_2O_3-YSZ/ZrO_2 Coatings

J. Kiilakoski, J. Puranen, E. Heinonen, H. Koivuluoto and P. Vuoristo

Journal of Thermal Spray Technology 28.1 (2018), 98–107
DOI: 10.1007/s11666-018-0816-x

J Therm Spray Tech (2019) 28:98–107
https://doi.org/10.1007/s11666-018-0816-x

PEER REVIEWED

Characterization of Powder-Precursor HVOF-Sprayed Al_2O_3-YSZ/ZrO_2 Coatings

Jarkko Kiilakoski[1] · Jouni Puranen[1,2] · Esa Heinonen[3] · Heli Koivuluoto[1] · Petri Vuoristo[1]

Submitted: 25 June 2018 / in revised form: 23 November 2018 / Published online: 10 December 2018

Abstract Thermal spraying using liquid feedstock can produce coatings with very fine microstructures either by utilizing submicron particles in the form of a suspension or through in situ synthesis leading, for example, to improved tribological properties. The focus of this work was to obtain a bimodal microstructure by using simultaneous hybrid powder-precursor HVOF spraying, where nanoscale features from liquid feedstock could be combined with the robustness and efficiency of spraying with powder feedstock. The nanostructure was achieved from YSZ and ZrO_2 solution-precursors, and a conventional Al_2O_3 spray powder was responsible for the structural features in the micron scale. The microstructures of the coatings revealed some clusters of unmelted nanosized YSZ/ZrO_2 embedded in a lamellar matrix of Al_2O_3. The phase compositions consisted of γ- and α-Al_2O_3 and cubic, tetragonal and monoclinic ZrO_2. Additionally, some alloying of the constituents was found. The mechanical strength of the coatings was not optimal due to the excessive amount of the nanostructured YSZ/ZrO_2 addition. An amount of 10 vol.% or 7 wt.% 8YSZ was estimated to result in a more desired mixing of constituents that would lead to an optimized coating architecture.

Keywords Al_2O_3-ZrO_2 · ceramic matrix composite · coating · hybrid · HVOF · solution-precursor spraying

Introduction

Thermally sprayed ceramic coatings are typically used in the aerospace industry for their low thermal diffusivity and high-temperature erosion resistance. Other applications are found, e.g., in components in the process industry, such as center rolls and dewatering elements for paper machines, mechanical seals and process valves (Ref 1). In these components, combined wear- and corrosion resistance is the key factor and the main reason for choosing ceramic coatings over other material options. However, typically brittle behavior and interlamellar cracking prevent their use in many applications (Ref 2).

Al_2O_3 is a widely used ceramic material in thermal spraying due to its low cost and various favorable properties, such as resistance to abrasive and sliding wear, and high dielectric strength (Ref 3, 4). However, its tribological properties are not up to par with other ceramic coatings, such as Cr_2O_3 (Ref 5), in more demanding conditions. In a technical perspective, a vast amount of research has gone into improving the fracture toughness of Al_2O_3 with additions of ZrO_2, with the intent of strengthening the composite. This can be achieved by the well-known toughening effect of the phase transformation of tetragonal ZrO_2 to monoclinic and the following volume change as well as the ferroelastic domain switching in tetragonal ZrO_2 (Ref 6-10). An undesirable side effect of the phase change is a large volume increase, which deteriorates the

This article is an invited paper selected from presentations at the 2018 International Thermal Spray Conference, held May 7-10, 2018, in Orlando, Florida, USA, and has been expanded from the original presentation.

✉ Jarkko Kiilakoski
jarkko.kiilakoski@tut.fi

[1] Laboratory of Materials Science, Tampere University of Technology, Tampere, Finland

[2] Elcogen Oy, Vantaa, Finland

[3] Center of Microscopy and Nanotechnology, University of Oulu, Oulu, Finland

coating integrity. However, it can be countered by stabilizing the ZrO_2 to either non-transformable tetragonal or cubic phases by adding stabilizing oxides, such as MgO (resulting in MSZ, magnesia-stabilized zirconia) or Y_2O_3 (leading to YSZ, yttria-stabilized zirconia). This practice is already widely utilized in top coats of thermal barrier coatings, where the coatings resistance to catastrophic failure is critical due to immense cyclic thermo-mechanical loading (Ref 1, 11).

While improvements are usually gained in the tribological behavior of thermally sprayed Al_2O_3-YSZ coatings, no evidence of toughening has been found, though some studies claim the transformation is the cause for the improved wear behavior (Ref 12, 13). Sometimes, however, the improvement is attributed to the lower melting point and better cohesion of the coating (Ref 14). We have previously studied the effect of this phase change in conventional thermally sprayed Al_2O_3-40ZrO_2 coatings as well, but the toughening was not evident (Ref 15, 16).

Nanocrystalline structures have been achieved in thermal spraying using suspension- and solution-precursor feedstocks (Ref 13, 17-24), indicating the potential of novel processing routes in achieving the desired toughness increase. The toughening was achieved without compromising structural cohesion, for example, by increasing the crack propagation resistance when small unmelted ZrO_2 particles are preserved in the coating matrix (Ref 13). However, alloying Al_2O_3 with ZrO_2 is challenging in thermal spraying of nanoscale feedstock as the composition can easily lead to the formation of an amorphous phase during processing that deteriorates mechanical properties due to a reduction in available slip planes leading to increased brittleness (Ref 13, 25).

HVOF spraying of ceramics requires a combustible gas capable of producing a high flame temperature with oxygen to produce the energy required to melt the material. Due to the restriction of available energy combined with high velocities leading to short dwell times, the HVOF system is mainly used with low-melting ceramics, such as TiO_2 (Ref 26) or Al_2O_3 (Ref 27). For higher melting materials, such as ZrO_2, particle size is the key between achieving a coating by melting or partly melting and partly sintering the material (Ref 28).

Solution-precursor HVOF (SP-HVOF) spraying is a novel spray process, in which coating formation through in-flight nanoparticle synthesis and subsequent melting is attainable. The size of the synthesized particles in SP-HVOF is 10-500 nm (Ref 29). However, creating a thick, cohesive coating with SP-HVOF is not only tedious due to the relatively low deposition rate, but also difficult due to the necessity to melt the particles to form the coating without inducing excessive grain growth. This problem has been tackled by Joshi et al. (Ref 30) by utilizing a hybrid plasma spray, where solution and powder are being fed simultaneously into the plasma, forming a coating of micron-sized lamellae from powder particles with nano-sized particles originating from the solution in the splat boundaries. The coatings provided the best properties of both processes: The high deposition rate of traditional plasma spraying of powder feedstock, along with the high hardness and density of solution-precursor plasma-sprayed coatings. More recently, Goel et al. (Ref 31) have employed the same philosophy in depositing an Al_2O_3-YSZ coating from Al_2O_3 powder and an 8YSZ suspension with an axial plasma spray process, providing a higher wear resistance with the introduction of the suspension into the process. Similarly, Murray et al. (Ref 32) showed increased fracture toughness and lower wear rate of powder-suspension and suspension-suspension-sprayed Al_2O_3-YSZ coatings sprayed with the same system when compared to either powder- or suspension-sprayed Al_2O_3.

In this study, the feasibility of a hybrid HVOF process utilizing a powder with a second feedstock, in this case solution-precursor, is examined for Al_2O_3-YSZ/ZrO_2 composite coatings. The goal is to be able to deposit nanosized YSZ/ZrO_2 particles at the splat boundaries between the Al_2O_3 splats to bind the splats together and, thus, improve the mechanical properties of the coatings. Two separate variables were studied: the effect of the amount of YSZ (0, 20 and 40 wt.%), and the effect of stabilization of the ZrO_2. The coating microstructures were characterized by FESEM and XRD, and their mechanical properties, hardness and cavitation erosion resistance were measured.

Experimental Methods

Coating Preparation

The powder feedstock material for the alumina (Al_2O_3) component was Amperit 740.001 ($-25 + 5$ µm) (H. C. Starck GmbH, Munich, Germany). The yttria-stabilized zirconia (YSZ) solutions were manufactured by mixing a saturated water-based solution (at 20 °C) of yttrium(III)nitrate hexahydrate (Acros organics/Thermo Fisher Scientific Inc., Geel, Belgium) and a 16 wt.% zirconium acetate solution in dilute acetic acid (Sigma-Aldrich/Merck KGaA, Darmstadt, Germany) in proper ratios to achieve 8 wt.% of yttria in zirconia after pyrolysis in the flame to create stabilized tetragonal zirconia (8YSZ). One solution was prepared without adding yttria in order to examine the effect of stabilization of the zirconia.

The coatings were sprayed with a TopGun HVOF system (GTV GmbH, Luckenbach, Germany) modified for liquid feedstock spraying, using ethene as a fuel gas and

oxygen as an oxidant on 50 × 100 × 5 mm substrates of stainless steel (AISI 316) that were grit-blasted with 180-220 mesh alumina prior to deposition. The powder feedstock was fed with a commercial 9MP powder feeder (Oerlikon Metco AG, Wohlen, Switzerland), and the solution was fed with a diaphragm pump feeder made in-house, that was equipped with a closed-loop mass-flow meter to stabilize the solution flow rate. The powder and the liquid precursor were injected in the same injector where they were mixed and injected together into the combustion chamber. Atomizing of the mixture was brought about by the carrier gas of the powder. The feeding setup is explained in detail by Björklund et al. (Ref 33). The processing parameters were optimized in preliminary studies and are listed in Table 1. A schematic of the hybrid powder-precursor HVOF spray process is presented in Fig. 1.

Coating Characterization

The coatings were characterized with field emission scanning electron microscopes (FESEM) (Zeiss ULTRAplus and Zeiss Crossbeam 540, Carl Zeiss Microscopy GmbH, Jena, Germany). The FIB cross section and consequent analysis were performed with a Helios Nanolab 600 (FEI Company/Thermo Fisher Scientific Inc., Hillsboro, OR, United States). Compositional analyses of the coated surfaces were carried out using Inca x-act 350 energy-dispersive spectrometer (EDS) attached to the FESEM (ULTRAplus) and the phase analysis with x-ray diffraction (XRD, Empyrean, PANalytical, Cu-Kα radiation, The Netherlands).

Mechanical Characterization

The coating hardness was determined from ten indentations on the coating cross section using a Vickers hardness tester (MMT-X7, Matsuzawa Co., Ltd., Akita, Japan) with a load of 300 gf ($HV_{0.3}$). The cavitation erosion test was performed with an ultrasonic transducer (VCX-750, Sonics and Materials Inc., Newtown, CT, USA), according to the ASTM G32-10 standard for indirect cavitation erosion. The vibration tip, made of a Ti-6Al-4V alloy, was vibrating at a frequency of 20 kHz with an amplitude of 50 µm at a distance of 500 µm from the surface. The sample surfaces were ground flat and polished with a polishing cloth and diamond suspension (3 µm). The samples were cleaned in an ultrasonic bath with ethanol and weighed after drying. Samples were attached on a stationary sample holder, and the head of the ultrasonic transducer was placed at a distance of 0.5 mm. Samples were weighed after 15, 30, 60 and 90 min. One sample per coating was tested. The long duration and high impact frequency of the test lend credibility to sufficient statistical certainty. Cavitation resistance of the coatings was calculated as the reciprocal of the mean depth of erosion per hour, which in turn is derived from the theoretical volume loss (presuming a fully dense coating) and the area of the vibrating tip.

Results and Discussion

Microstructural Characterization

The cross sections of the coatings are presented in Fig. 2 and in higher magnification in Fig. 3. The coatings adhered well to the substrate, and in all hybrid coatings bimodality was achieved with in situ synthesized YSZ/ZrO_2 particles of < 200 nm embedded between the well-melted Al_2O_3 splats. The coating structures seemingly have some apparent porosity; however, it is likely stemming from pullouts, i.e., the removal of poorly bonded particles or agglomerates during the sample preparation. According to the cross-sectional images, the synthesized nanoparticles obtained a round morphology indicating partially molten state, but a majority of the nanoparticles were not well

Table 1 Processing parameters of the coatings

Sample name	A	A20Y	A40Y	A40Z
Material chemical composition, wt.%	Al_2O_3	Al_2O_3-20YSZ	Al_2O_3-40YSZ	Al_2O_3-40ZrO_2
C_2H_4, slpm	97			
O_2, slpm	232			
O_2/C_2H_4-ratio	2.38			
Powder feed rate, g/min	12	16	12	12
Solution feed rate, g/min	…	22	44	44
Standoff distance, mm	100			
Relative surface speed, m/min	51			
Offset, mm/pass	4			
Passes, number	28	10	10	20
Coating thickness, µm	180	170	134	250

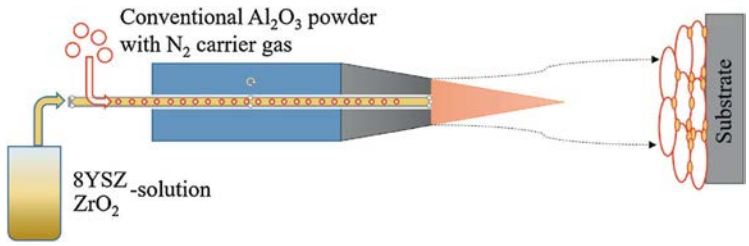

Fig. 1 A schematic of the hybrid powder-precursor HVOF process

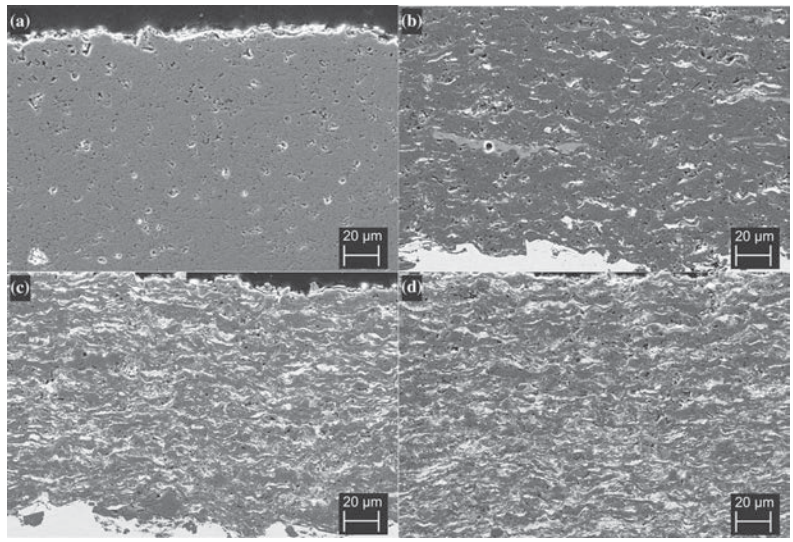

Fig. 2 Cross-sectional micrographs of the coatings. (a) A, (b) A20Y, (c) A40Y, (d) A40Z. FESEM (SE) images

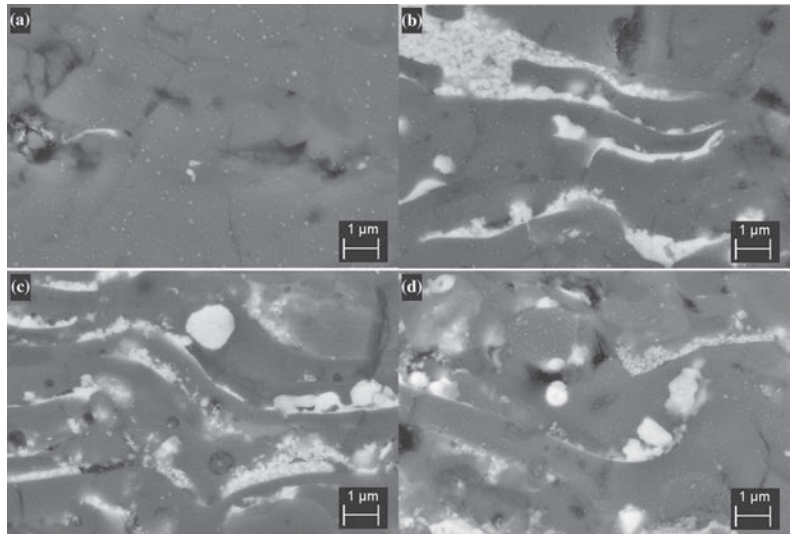

Fig. 3 Cross-sectional micrographs of the coatings. (a) A, (b) A20Y, (c) A40Y, (d) A40Z. FESEM (SE) images. The artifacts on the cross sections arise from residue in sample preparation

integrated to the alumina splats, as presented in Fig. 4(a). In addition, some mixed-phase areas were found, shown as the light gray areas in Fig. 4(b). This indicates the possibility of strengthening the traditional powder-sprayed coating structure by interlocking the microscale splats, as the nanosized ceramics (with a very large surface area) enhance the diffusion of atoms in splat-nanoparticle interface (Ref 34). Additionally, since it has been shown that reducing the primary particle size to the nanoscale can lead to significant reductions in the sintering temperature in stabilized ZrO_2 (Ref 35), some amount of sintering and enhanced diffusion could occur during spraying. Therefore, in optimal conditions, the sintered YSZ could be chemically bonded by diffusion/mixed phase with surrounding Al_2O_3 splats, leading to an extremely coherent structure. Some amount of unmelted nanoparticles can potentially also improve the toughness and wear resistance of the coating when the nanostructured zones are well embedded in the coating and act as crack arresters (Ref 36).

The EDS analyses of the coatings are presented in Table 2. The amount of ZrO_2 was about half of the nominal amount from the feedstock. The low deposition efficiency of ZrO_2 in comparison with Al_2O_3 can be attributed to its higher melting point as well as small particle size, leading to particles drifting along with the gas flow away from the substrate due to the high stagnation pressure zone near the surface slowing the particles down (bow-shock effect) and drag along the surface (Ref 37-39). Further optimization of the process parameters should improve this aspect along with decreasing the amount of unmelted YSZ/ZrO_2 particles.

The EDS map of the coating A40Y is presented in Fig. 5. As expected from the contrast in the FESEM images, the bright areas consist of YSZ and darker areas of Al_2O_3. A mixed-phase area exists with a grayish color that can be verified from the EDS map, consisting of oxides of both aluminum and zirconium. In order to confirm that the mixed color did not arise from a brighter layer of zirconia under a darker layer alumina, FIB-FESEM studies were carried out. The sample was inspected from a FIB-milled cross section, where a light gray area was located, and the sample was subsequently milled from that plane on two more times, 2 μm at a time, as displayed in Fig. 6. It was ensured that the mixed-phase splat was indeed continuous also in the third dimension and not an artifact from the penetration depth of the electrons.

The x-ray diffraction patterns are presented in Fig. 7. As expected, the ZrO_2 in the stabilized Al_2O_3-YSZ coatings was in the tetragonal form. A40Z consisted also of monoclinic and cubic ZrO_2, which was unexpected since the stable phase of ZrO_2 in room temperature is monoclinic. The occurrence of all the phases of ZrO_2 in the unstabilized coating can be explained either by their metastability or by the size dependence of the phase transformations: For example, cubic ZrO_2 stays stable in room temperature with crystallite sizes < 2 nm (Ref 40, 41). Al_2O_3 was in all cases as α- and γ-phases, as is typical in HVOF spraying of Al_2O_3, where the core of some particles of the feedstock-powder presumably does not melt and stays as α-phase. Interestingly, amorphous compounds, which are a common product of thermal spraying Al_2O_3-ZrO_2 mixtures from powder (Ref 16, 25), were not found in significant quantities.

Mechanical Properties

Coating hardnesses were decreased by the addition of YSZ/ZrO_2 in Al_2O_3, as presented in Table 3. However, the reduction in hardness was moderate in the case of A20Y, indicating the possibility to achieve a dense structure even

Table 2 Coating composition as calculated from EDS analyses

wt.%	Al_2O_3	ZrO_2	Y_2O_3
A	100.0	0.0	0.0
A20Y	90.0	9.9	0.1
A40Y	73.3	26.0	0.8
A40Z	69.9	30.0	0.0

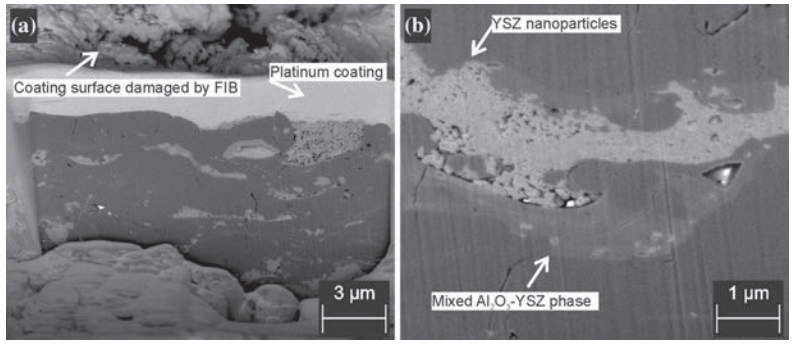

Fig. 4 FIB-milled cross section of (a) A40Y showing mixed phase and unmelted ZrO_2 particles in splat boundaries and (b) signs of diffusion of YSZ in Al_2O_3. The white regions are severely charged areas. FESEM (BSE) images

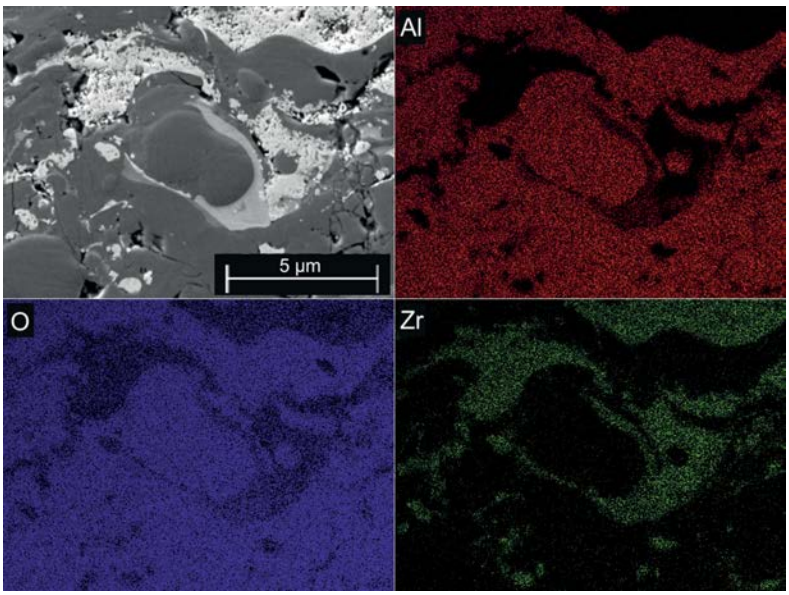

Fig. 5 EDS map of A40Y visualizing the elemental distribution in the coating

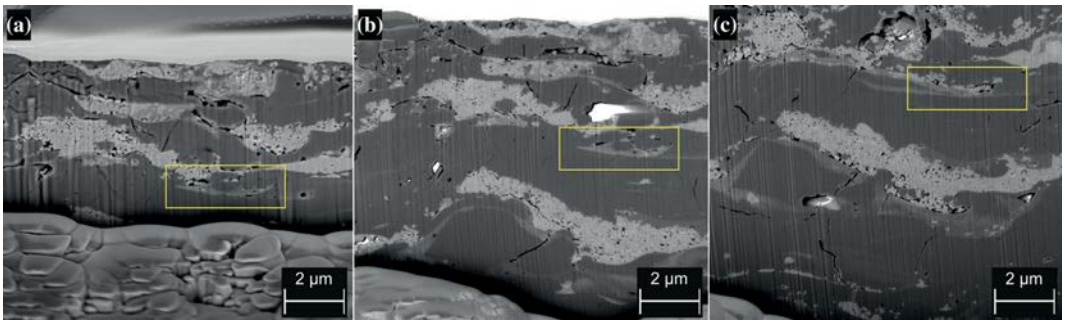

Fig. 6 The cross section of A40Y FIB-milled to (a) 0 µm, (b) 2 µm and (c) 4 µm depth from the reference plane. The box indicates the same detail of a mixed-phase region of Al_2O_3 and YSZ. The white regions are severely charged areas. FESEM images

with the addition of nanoparticles, as also evidenced by Goel et al. (Ref 31). The coatings with 40 wt.% nominal addition of YSZ/ZrO_2 underwent a more severe reduction in hardness, as could be predicted from the large clusters of nanoparticles between the splats as seen in all hybrid coatings in the cross sections in Fig. 3 and in detail for A40Y in Fig. 4; the cohesion of the coatings was reduced as compared to the reference.

Cavitation erosion resistance is typically a good measure of the cohesion of thermally sprayed coatings, and it is able to reveal weak links in the microscale (Ref 15, 42). The experiment revealed structural weakness in the hybrid powder-precursor-sprayed coatings: Similarly to the hardness values, a reduction in cavitation resistance was observed with increasing amounts of YSZ/ZrO_2, as can be observed in Fig. 8. However, this time the reduction is significant, dropping to less than half with 20 wt.% YSZ and to less than a quarter with 40 wt.% YSZ and ZrO_2 additions as compared to pure Al_2O_3. This is supported by Fig. 9, where surface images of A40Y are presented as-sprayed and after the test. Clearly, there are vast amounts of YSZ nanoparticles on top of the surface (Fig. 9a), like was seen between the splats as well (Fig. 4a), that impair the cohesion of the coating, which is most exposed under fatiguing conditions. These particles were removed during the experiment, as can be seen from their lesser amount in Fig. 9(b), where mainly larger well-melted splats are visible. The cavitation erosion resistance is typically favored

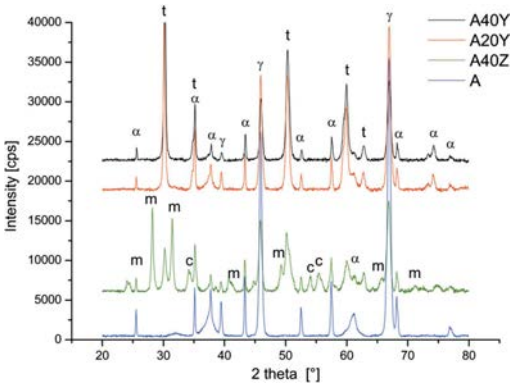

Fig. 7 The XRD patterns of the coatings. Symbols: t = tetragonal ZrO_2, m = monoclinic ZrO_2, c = cubic ZrO_2, α = α-Al_2O_3, γ = γ-Al_2O_3

Table 3 The Vickers hardnesses of the coatings along with the 95% confidence intervals (CI)

Coating	Mean hardness ($HV_{0.3}$)	95% CI
A	1090	75
A20Y	1032	92
A40Y	869	49
A40Z	823	81

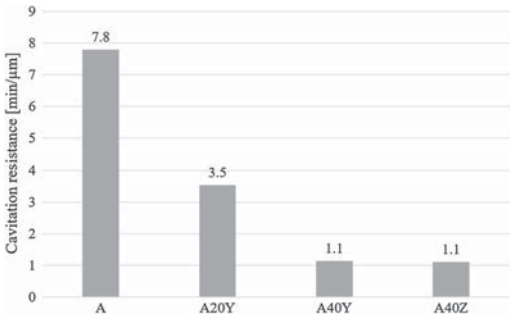

Fig. 8 The cavitation resistance of the coatings, i.e., the time in minutes it takes to remove one µm of material

by good cohesion and small splat size of the formed coating, while nonintegrated particles are readily attacked and act as concentration sites for the erosion (Ref 15, 42). The hybrid HVOF-sprayed coatings aimed to achieve these beneficial qualities but missed the goal as the nanoparticles were not successfully embedded in the coating and an insufficient amount of mixed-phase regions were created to strengthen the coating. These results are contradictory to, for example, the results of Murray et al. (Ref 32) who were able to increase the wear resistance in dry-sliding ball-on-flat test of the reference Al_2O_3 coating by the addition of YSZ suspension. The test conditions were 30 min with a 6.3-mm-diameter alumina ball, a load of 10 N and a sliding speed of 10 mm/s. In their case, however, the major difference was that an axial-feed plasma-spray system was used, which has enough power to melt the YSZ particles from the suspension and there was no detrimental nonintegrated particles embedded in the coating. Additionally, the scale in their test is some orders of magnitude larger since the cavitating bubbles, being a few tens of microns, mainly nucleate on surface asperities and cavities of similar size (Ref 43). The tests measure, thus, somewhat different features.

Tailoring Possibilities of the Coating Architecture

In order to evaluate the next steps to optimize the coating architecture, calculations were performed on black/white histograms of a cross-sectional image (as visualized in Fig. 10) of the pure Al_2O_3 coating to obtain the amount of horizontal vacancies between the lamellae. These vacancies could be filled with the nanosized YSZ/ZrO_2 particles or the Al_2O_3-YSZ/ZrO_2 mixed phase in order to increase the structural integrity of the coating. Theoretically, packing the interlamellar vacancies with a sufficient amount of nanoparticles while avoiding overpacking would lead to the densest achievable coating with optimal properties, as pictured in Fig. 10(b). Five vertical areas of the image were selected, and the area fraction of interlamellar vacancies to lamellae is calculated from a black/white histogram, Fig. 10(c). By selecting narrow, vertical areas from regions with few vertical cracks, we aim to isolate the horizontal vacancies between the lamellae, which are desirable to be filled. An average of 10 vol.% of horizontal vacancies/splat boundaries was determined, which translates to a theoretically optimal mixture of 7 wt.% of the 8YSZ solution and 93 wt.% Al_2O_3 powder. This is not far from the actual amount obtained from A20Y due to the lower deposition efficiency of YSZ. Hence, a coating with this or lower ratio should be manufactured and evaluated in the next phase of the study, in order to create a distinct enough difference to A20Y.

Drawing from the results of this study, future research should steer itself toward lower melting feedstock or additives in the solution, such as citric acid or acetic acid, to increase the exothermic nature of the synthesis reaction (Ref 44). By combining solution and powder feedstock in situ, it is possible to combine oxides into coatings jointly with other oxides, hard metals or metals of virtually any combination without the limitations of powder or

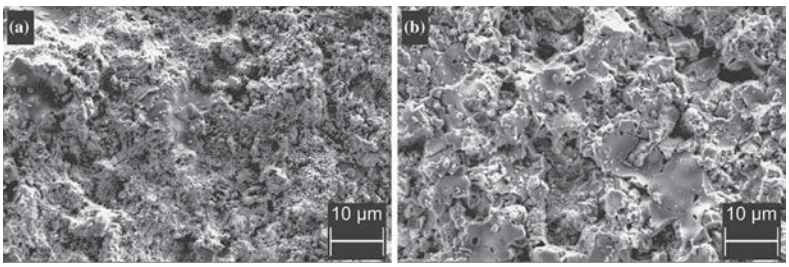

Fig. 9 FESEM images of the surfaces of the A40Y coating (a) as-sprayed showing nanoparticles on the surface of the coating and (b) after cavitation erosion, when there is no evidence of nanoparticles left on the larger splats

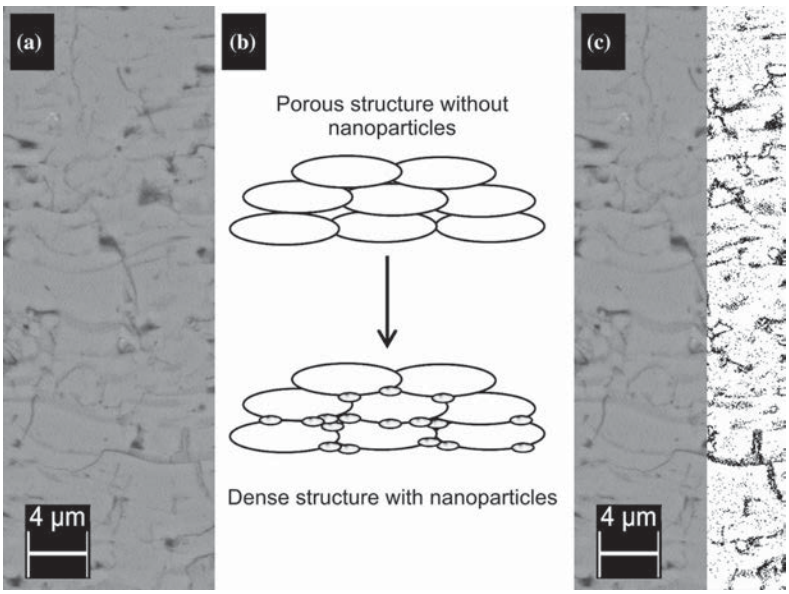

Fig. 10 (a) A portion of a FESEM cross section of coating A used to calculate the amount of vacancies between the Al_2O_3 lamellae. (b) Visualization of the theory of packing the empty areas with nanoparticles. (c) An example of the slicing procedure done to perform calculations of the amount of vacancies

suspension preparation, thereby obtaining novel functional properties for thermally sprayed coatings.

Conclusions

Preliminary results on the characterization of coatings prepared via a hybrid powder-precursor HVOF spray process were presented in this study. The coatings were manufactured from a solution of zirconium acetate and yttrium nitrate hexahydrate, and a commercial powder feedstock of Al_2O_3. Microscopic characterization techniques were used to investigate the formed microstructures, and cavitation erosion was utilized to evaluate the cohesion and structural integrity of the coating.

The coating structures were macroscopically dense and bimodal, with nanosized YSZ/ZrO_2 particles and agglomerates thereof occupying the interlamellar regions between the Al_2O_3 splats, along with some mixed phase of Al_2O_3-YSZ/ZrO_2. However, the addition of YSZ/ZrO_2 lowered the hardness of the coating slightly. The cause was determined to be the areas with agglomerates of unmelted YSZ/ZrO_2 that were also found to weaken the coating in cavitation erosion, which tests the structural integrity and cohesion of the coating through fatigue from microscopic impacts. Thus, the desired improvement in mechanical properties was not achieved yet. The role of Y_2O_3 in stabilizing t-ZrO_2 as compared to unstabilized ZrO_2 had no effect on the hardness or cavitation resistance of the coating with the current achieved microstructure.

The usability of the novel hybrid powder-precursor HVOF process has been successfully demonstrated, and with further process optimization the composition is believed to provide interesting results. The results implicate that by reducing the amount of solution-precursor-synthesized YSZ/ZrO_2, the coating cohesiveness would be

sufficient to bring out the toughening effect of the added nanostructured phase. Based on the calculations of vacancies between splats in the Al_2O_3 coating, an optimal feedstock mixing ratio would be 7 wt.% of 8YSZ solution of the total feed presuming identical deposition efficiencies of the two feedstocks. Further studies are recommended to optimize the relationship between the feedstock and deposition parameters. Additionally, by utilizing different feedstocks with lower melting points than YSZ or ZrO_2, it is foreseen to be possible to produce interesting nano-microcomposite coatings of various compositions with relative ease and reproducibility bringing material tailoring of thermally sprayed coatings to new levels.

Acknowledgments The authors gratefully acknowledge the financial support from the graduate school of the President of Tampere University of Technology and Business Finland (Finnish innovation funding, trade, investment and travel promotion organization), its "Ductile and Damage Tolerant Ceramic Coatings" project and the participating companies. The authors would like to thank colleagues from Tampere University of Technology: Mr. Mikko Kylmälahti for spraying the coatings and M.Sc. Jarmo Laakso and Dr. Mari Honkanen for the electron microscopy.

References

1. P. Vuoristo, Thermal Spray Coating Processes, *Comprehensive Materials Processing: Films and Coatings: Technology and Recent Development*, Vol 4, S. Hashmi, Ed., Elsevier, Amsterdam, 2014, p 229-276
2. L. Pawlowski, *The Science and Engineering of Thermal Spray Coatings*, 2nd ed., Wiley, West Sussex, 2008
3. J. Ilavsky, C. Berndt, and H. Herman, Alumina-Base Plasma-Sprayed Materials—Part II: Phase Transformations in Aluminas, *J. Therm. Spray Technol.*, 1997, **6**(4), p 439-444
4. P.L. Fauchais, J.V.R. Heberlein, and M.I. Boulos, *Thermal Spray Fundamentals*, Springer, Boston, 2014
5. G. Bolelli, V. Cannillo, L. Lusvarghi, and T. Manfredini, Wear Behaviour of Thermally Sprayed Ceramic Oxide Coatings, *Wear*, 2006, **261**(11-12), p 1298-1315
6. J. Chevalier, S. Deville, G. Fantozzi, J.F. Bartolomé, C. Pecharroman, J.S. Moya, L.A. Diaz, and R. Torrecillas, Nanostructured Ceramic Oxides with a Slow Crack Growth Resistance Close to Covalent Materials, *Nano Lett.*, 2005, **5**(7), p 1297-1301
7. J. Chevalier, A.H. De Aza, G. Fantozzi, M. Schehl, and R. Torrecillas, Extending the Lifetime of Ceramic Orthopaedic Implants, *Adv. Mater.*, 2000, **12**(21), p 1619-1621
8. E. Kannisto, M.E. Cura, E. Levänen, and S.P. Hannula, Mechanical Properties of Alumina Based Nanocomposites, *Key Eng. Mater.*, 2012, **527**, p 101-106
9. A. Evans, Perspective on the Development of High-Toughness Ceramics, *J. Am. Ceram. Soc.*, 1990, **73**(2), p 187-206
10. G.V. Srinivasan, J.F. Jue, S.Y. Kuo, and A.V. Virkar, Ferroelastic Domain Switching in Polydomain Tetragonal Zirconia Single Crystals, *J. Am. Ceram. Soc.*, 1989, **72**(11), p 2098-2103
11. R.A. Miller, Thermal Barrier Coatings for Aircraft Engines: History and Directions, *J. Therm. Spray Technol.*, 1997, **6**(1), p 35-42
12. G. Perumal, M. Geetha, R. Asokamani, and N. Alagumurthi, Wear Studies on Plasma Sprayed Al_2O_3-40wt% 8YSZ Composite Ceramic Coating on Ti-6Al-4V Alloy Used for Biomedical Applications, *Wear*, 2014, **311**(1-2), p 101-113
13. J. Oberste Berghaus, J.-G. Legoux, C. Moreau, F. Tarasi, and T. Chráska, Mechanical and Thermal Transport Properties of Suspension Thermal-Sprayed Alumina-Zirconia Composite Coatings, *J. Therm. Spray Technol.*, 2007, **17**(1), p 91-104
14. Y. Bai, F.L. Yu, S.W. Lee, H. Chen, and J.F. Yang, Characterization of the Near-Eutectic Al_2O_3-40 wt% ZrO_2 Composite Coating Fabricated by Atmospheric Plasma Spray. Part II: Microstructure and Mechanical Properties of Nanocomposite Coating, *Mater. Manuf. Process.*, 2012, **27**(1), p 58-64
15. J. Kiilakoski, F. Lukac, H. Koivuluoto, and P. Vuoristo, Cavitation Wear Characteristics of Al_2O_3-ZrO_2-Ceramic Coatings Deposited by APS and HVOF-Processes, in *Proceedings of the ITSC 2017*, June 7-9, 2017 (Düsseldorf, Germany), DVS Media GmbH (2017), pp. 928-933
16. J. Kiilakoski, R. Musalek, F. Lukac, H. Koivuluoto, and P. Vuoristo, Evaluating the Toughness of APS and HVOF-Sprayed Al_2O_3-ZrO_2-Coatings by In-Situ- and Macroscopic Bending, *J. Eur. Ceram. Soc.*, 2018, **38**(4), p 1908-1918
17. D. Chen, E.H. Jordan, and M. Gell, Suspension Plasma Sprayed Composite Coating Using Amorphous Powder Feedstock, *Appl. Surf. Sci.*, 2009, **255**(11), p 5935-5938
18. D. Chen, E.H. Jordan, and M. Gell, Microstructure of Suspension Plasma Spray and Air Plasma Spray Al_2O_3-ZrO_2 Composite Coatings, *J. Therm. Spray Technol.*, 2009, **18**(3), p 421-426
19. D. Chen, E.H. Jordan, and M. Gell, Solution Precursor High-Velocity Oxy-Fuel Spray Ceramic Coatings, *J. Eur. Ceram. Soc.*, 2009, **29**(16), p 3349-3353
20. G. Darut, H. Ageorges, A. Denoirjean, G. Montavon, and P. Fauchais, Effect of the Structural Scale of Plasma-Sprayed Alumina Coatings on Their Friction Coefficients, *J. Therm. Spray Technol.*, 2008, **17**(5-6), p 788-795
21. F.-L. Toma, L.-M. Berger, T. Naumann, and S. Langner, Microstructures of Nanostructured Ceramic Coatings Obtained by Suspension Thermal Spraying, *Surf. Coat. Technol.*, 2008, **202**(18), p 4343-4348
22. A. Killinger, M. Kuhn, and R. Gadow, High-Velocity Suspension Flame Spraying (HVSFS), a New Approach for Spraying Nanoparticles with Hypersonic Speed, *Surf. Coat. Technol.*, 2006, **201**(5), p 1922-1929
23. S. Govindarajan, R.O. Dusane, and S.V. Joshi, In Situ Particle Generation and Splat Formation During Solution Precursor Plasma Spraying of Yttria-Stabilized Zirconia Coatings, *J. Am. Ceram. Soc.*, 2011, **94**(12), p 4191-4199
24. J. Tikkanen, K.A. Gross, C.C. Berndt, V. Pitkänen, J. Keskinen, S. Raghu, M. Rajala, and J. Karthikeyan, Characteristics of the Liquid Flame Spray Process, *Surf. Coat. Technol.*, 1997, **90**(3), p 210-216
25. H.-J. Kim and Y.J. Kim, Amorphous Phase Formation of the Pseudo-Binary Al_2O_3-ZrO_2 Alloy During Plasma Spray Processing, *J. Mater. Sci.*, 1999, **34**(1), p 29-33
26. R.S. Lima and B.R. Marple, From APS to HVOF Spraying of Conventional and Nanostructured Titania Feedstock Powders: A Study on the Enhancement of the Mechanical Properties, *Surf. Coat. Technol.*, 2006, **200**(11), p 3428-3437
27. C.C. Stahr, S. Saaro, L.M. Berger, J. Dubský, K. Neufuss, and M. Herrmann, Dependence of the Stabilization of α-Alumina on the Spray Process, *J. Therm. Spray Technol.*, 2007, **16**(5-6), p 822-830

28. T.A. Dobbins, R. Knight, and M.J. Mayo, HVOF Thermal Spray Deposited Y_2O_3-Stabilized ZrO_2 Coatings for Thermal Barrier Applications, *J. Therm. Spray Technol.*, 2003, **12**(2), p 214-225
29. J. Puranen, J. Laakso, M. Honkanen, S. Heinonen, M. Kylmälahti, S. Lugowski, T.W. Coyle, O. Kesler, and P. Vuoristo, High Temperature Oxidation Tests for the High Velocity Solution Precursor Flame Sprayed Manganese-Cobalt Oxide Spinel Protective Coatings on SOFC Interconnector Steel, *Int. J. Hydrog. Energy*, 2015, **40**(18), p 6216-6227
30. S.V. Joshi, G. Sivakumar, T. Raghuveer, and R.O. Dusane, Hybrid Plasma-Sprayed Thermal Barrier Coatings Using Powder and Solution Precursor Feedstock, *J. Therm. Spray Technol.*, 2014, **23**(4), p 616-624
31. S. Goel, S. Björklund, U. Wiklund, and S. V. Joshi, Hybrid Powder-Suspension Al_2O_3-ZrO_2 Coatings by Axial Plasma Spraying: Processing, Characteristics & Tribological Behaviour, in *Proceedings of the ITSC 2017*, June 7-9, 2017 (Düsseldorf, Germany), DVS Media GmbH (2017), pp. 374-379
32. J.W. Murray, A. Leva, S. Joshi, and T. Hussain, Microstructure and Wear Behaviour of Powder and Suspension Hybrid Al_2O_3-YSZ Coatings, *Ceram. Int.*, 2018, **44**(7), p 8498-8504
33. S. Björklund, S. Goel, and S. Joshi, Function-Dependent Coating Architectures by Hybrid Powder-Suspension Plasma Spraying: Injector Design, Processing and Concept Validation, *Mater. Des.*, 2018, **142**, p 56-65
34. M.J. Mayo, Processing of Nanocrystalline Ceramics from Ultrafine Particles, *Int. Mater. Rev.*, 1996, **41**(3), p 85-115
35. W.H. Rhodes, Agglomerate and Particle Size Effects on Sintering Yttria-Stabilized Zirconia, *J. Am. Ceram. Soc.*, 1981, **64**(1), p 19-22
36. R.S. Lima and B.R. Marple, Enhanced Ductility in Thermally Sprayed Titania Coating Synthesized Using a Nanostructured Feedstock, *Mater. Sci. Eng. A*, 2005, **395**(1-2), p 269-280
37. C. Qiu and Y. Chen, Manufacturing Process of Nanostructured Alumina Coatings by Suspension Plasma Spraying, *J. Therm. Spray Technol.*, 2009, **18**(2), p 272-283
38. K. Vanevery, M.J.M. Krane, R.W. Trice, H. Wang, W. Porter, M. Besser, D. Sordelet, J. Ilavsky, and J. Almer, Column Formation in Suspension Plasma-Sprayed Coatings and Resultant Thermal Properties, *J. Therm. Spray Technol.*, 2011, **20**(4), p 817-828
39. B. Samareh and A. Dolatabadi, A Three-Dimensional Analysis of the Cold Spray Process: The Effects of Substrate Location and Shape, *J. Therm. Spray Technol.*, 2007, **16**(5-6), p 634-642
40. E. Nouri, M. Shahmiri, H. Rezaie, and F. Talayian, The Effect of Alumina Content on the Structural Properties of ZrO_2-Al_2O_3 Unstabilized Composite Nanopowders, *Int. J. Ind. Chem.*, 2012, **3**(1), p 17
41. S. Tsunekawa, S. Ito, Y. Kawazoe, and J.T. Wang, Critical Size of the Phase Transition from Cubic to Tetragonal in Pure Zirconia Nanoparticles, *Nano Lett.*, 2003, **3**(7), p 871-875
42. V. Matikainen, K. Niemi, H. Koivuluoto, and P. Vuoristo, Abrasion, Erosion and Cavitation Erosion Wear Properties of Thermally Sprayed Alumina Based Coatings, *Coatings*, 2014, **4**(1), p 18-36
43. C.E. Brennen, *Cavitation and Bubble Dynamics. Oxford Engineering Science Series*, 1st ed., Oxford University Press Inc, New York, 1995
44. A.E. Danks, S.R. Hall, and Z. Schnepp, The Evolution of 'Sol-Gel' Chemistry as a Technique for Materials Synthesis, *Mater. Horiz. R. Soc. Chem.*, 2016, **3**(2), p 91-112

PUBLICATION

III

Characterization of High-Velocity Single Particle Impacts on Plasma-Sprayed Ceramic Coatings

J. Kiilakoski, M. Lindroos, M. Apostol, H. Koivuluoto, V.-T. Kuokkala and P. Vuoristo

Journal of Thermal Spray Technology 25.6 (2016), 1127–1137
DOI: 10.1007/s11666-016-0428-2

Characterization of High-Velocity Single Particle Impacts on Plasma-Sprayed Ceramic Coatings

Jarkko Kiilakoski, Matti Lindroos, Marian Apostol, Heli Koivuluoto, Veli-Tapani Kuokkala, and Petri Vuoristo

High-velocity impact wear can have a significant effect on the lifetime of thermally sprayed coatings in multiple applications, e.g., in the process and paper industries. Plasma-sprayed oxide coatings, such as Cr_2O_3- and TiO_2-based coatings, are often used in these industries in wear and corrosion applications. An experimental impact study was performed on thermally sprayed ceramic coatings using the High-Velocity Particle Impactor (HVPI) at oblique angles to investigate the damage, failure, and deformation of the coated structures. The impact site was characterized by profilometry, optical microscopy, and scanning electron microscopy (SEM). Furthermore, the connection between the microstructural details and impact behavior was studied in order to reveal the damage and failure characteristics at a more comprehensive level. Differences in the fracture behavior were found between the thermally sprayed Cr_2O_3 and TiO_2 coatings, and a concept of critical impact energy is presented here. The superior cohesion of the TiO_2 coating inhibited interlamellar cracking while the Cr_2O_3 coating suffered greater damage at high impact energies. The HVPI experiment has proven to be able to produce valuable information about the deformation behavior of coatings under high strain rates and could be utilized further in the development of wear-resistant coatings.

Keywords electron microscopy, fracture, impact wear, thermal spray coatings, wear testing

Introduction

Thermal spraying means depositing a thick coating (from tens of micrometers up to some millimeters) by propelling molten or semi-molten material onto a substrate, where it flattens and solidifies, forming a coating. The coating is formed of splats that have cooled rapidly, in excess of 10^6 K/s for ceramics (Ref 1). The cooling leads to a varying microstructure with several phases, pores, and inclusions of unmolten particles (Ref 1, 2). Thermally sprayed ceramic coatings such as Al_2O_3, Cr_2O_3, ZrO_2-$8Y_2O_3$, and TiO_2 are widely used in applications requiring a surface resistant to corrosion and wear (Ref 3-5). Such applications can be found for example in process and paper industries, where ceramic coatings are used against adhesive wear and for their low thermal conductivity (Ref 2, 5). The coatings are most commonly deposited by Atmospheric Plasma Spraying (APS) or High-Velocity Oxy-Fuel (HVOF) spraying. Other beneficial qualities of thermally sprayed ceramic coatings can be high hardness, low friction, resistance to low-angle erosion, electrical insulation, and semiconductivity.

Thermally sprayed ceramic coatings often exhibit microcracking in the direction perpendicular to the substrate, stemming from their brittleness and, as a result, inability to accommodate residual stresses during cooling. This leads to their limited use in applications, which require impact resistance and where ductility is often considered beneficial (Ref 5). Plasma-sprayed Cr_2O_3 coatings are, however, widely used against adhesive and abrasive wear, as well as against corrosion when sealed, whereas TiO_2 coatings are used or researched for their solid-lubrication, electrical conductivity, and photocatalytic properties (Ref 6-8). APS Cr_2O_3 coatings usually have a hardness between 1000 and 1300 $HV_{0.3}$ (Ref 6, 9), while TiO_2 coatings typically have a hardness of around 800 $HV_{0.3}$ sprayed both with APS and HVOF (Ref 10).

The brittleness of ceramic coatings is evidenced by their low ability to resist crack growth, which is indicative of the amount of energy needed to break the material (Ref 11, 12). Due to the large amount of defects in plasma-sprayed coatings, their mechanical properties are often poorer than those of the corresponding bulk materials. For example, the elastic moduli of oxide coatings are estimated to be only 20-40% of those of their bulk counterparts (Ref 5). These properties are in the first place not only related to the feedstock material and the final microstructure of the coatings, but they can also be influenced for example by optimizing the feedstock man-

Jarkko Kiilakoski, Matti Lindroos, Marian Apostol, Heli Koivuluoto, Veli-Tapani Kuokkala, Petri Vuoristo, Department of Materials Science, Tampere University of Technology, P.O. Box 589, 33101 Tampere, Finland. Contact e-mail: jarkko.kiilakoski@tut.fi.

ufacturing and spray processes. New spray methods and coatings with nanoscale features provide promising new routes for achieving toughness in ceramic coatings (Ref 13).

The wear of thermally sprayed ceramic coatings is largely dependent on the composition of the coating, interlamellar strength, and the porosity and density of microcracks in the microstructure (Ref 14, 15). Additionally, residual stresses may play a certain role in applications where outside stress is imposed on the coating (Ref 16, 17). The stresses can add up or reduce depending on their sign which can accelerate failure. The stresses for plasma-sprayed ceramic coatings have usually been thought of as being tensile (Ref 17-19), although polishing of the coating can induce slight compressive stresses (Ref 17).

Research on the erosion resistance of plasma-sprayed Al_2O_3 and TiO_2 coatings has shown that they have sufficient resistance against scratching by low-angle erosion due to their high hardness and stiffness, but with right angle impacts the wear rates were increased even fivefold (Ref 20). Indeed, Matikainen et al. (Ref 21) found that for Al_2O_3 and Al_2O_3-TiO_2 coatings sprayed with HVOF and APS spray processes, the erosion wear rate with a 30° angle was between 25 and 50% of the wear rate with an angle of 90°. The mechanism of material removal by small particles was mainly brittle fracture, preceded by plastic deformation, while for larger particles with the impact angle of 90°, brittle fracture occurred at the interface between the lamellae. Westergård et al. (Ref 22) noted from eroded surfaces of plasma-sprayed Al_2O_3, Al_2O_3-13TiO_2, and Cr_2O_3 that during erosion cracking in the coating follows the path of weak sites in the coating. This suggests that erosive wear resistance is a good measure of the cohesion of the coating (Ref 23).

Supporting the above, Takeuchi et al. (Ref 24) found that the erosion resistance of plasma-sprayed TiO_2 is superior to that of Cr_2O_3 at the impact angle of 60°. They also performed a drop test of a steel ball on the coatings at a 45° angle and observed the TiO_2 coating to endure twice as many impacts as the Cr_2O_3 coating. Sparks et al. (Ref 25) have studied the effect of erodents of different shapes and velocities on a silica glass ceramic bulk material in a dry erosion test. They used angular and blocky silica sands of particle sizes 125-150 μm with a gas blast erosion rig. They found that in the tests at low velocities (44 m/s) with rounded particles, a transition in the erosion wear rate took place between the impact angles of 45° and 60°. In higher angles and velocities, the wear of the ceramic was characterized by lateral cracking and flake formation, whereas below the transition point plastic deformation preceded the fracture. To the best of our knowledge, similar studies have not been performed on wear-resistant ceramic coatings, which would reveal the connection between deformation, critical loading conditions, and failure mechanisms. However, it must be recognized that these coatings may not provide the best wear resistance when erosion is the prevailing loading mode. In such applications, cermets such as tungsten and chromium carbides are often preferred due to the possibility of adjusting the amount of hard phase favorable against erosion. (Ref 20).

High-velocity single impact studies have been performed at Tampere Wear Center (TWC) on various materials with the High-Velocity Particle Impactor (HVPI). The test setup has been successfully used for studying impacts in a controlled way for materials such as steels (Ref 26, 27), hybrids (Ref 28, 29), thermally sprayed MMC coatings (Ref 30), and rubbers (Ref 31). Waudby et al. (Ref 30) characterized the high-velocity impacts with various impact velocities on thermally sprayed cermet coatings and concluded that the erosion mechanism is mostly cracking, indicating brittle behavior of the coatings. They also determined the critical level of impact energy above which coating delamination and significant plastic deformation of the substrate were evident. Below this impact energy, the coating cracked and deformed but still stayed somewhat intact and on the substrate, providing protection against further impacts.

In the present study, high-velocity single impact experiments were performed to elucidate the wear characteristics and deformation behavior of two wear-resistant ceramic coatings, i.e., atmospheric plasma-sprayed Cr_2O_3 and TiO_2, in low-angle impacts. These coatings were chosen for their different microstructural characteristics, which are presumed to result in different types of wear behavior. Electron microscopy and profilometry were used to analyze the failure mechanisms and microstructures of the coatings before and after the impact tests.

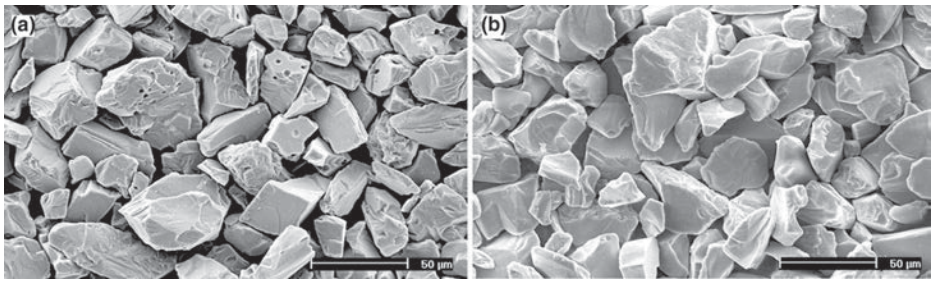

Fig. 1 Powder morphologies of the (a) Cr_2O_3 and (b) TiO_2 powders. SEM images

Materials and Methods

Materials

Conventional chromia (dichromium trioxide, Cr_2O_3) (H.C. Starck, Amperit 704.001) and titania (titanium dioxide, TiO_2) (H.C. Starck, Amperit 782.1) were chosen as coating materials. Both powders were fused and crushed with a nominal powder size of $-45+22$ μm. The powder morphologies are presented in Fig. 1. The coatings were sprayed on low carbon steel (AISI 5120) plates, which were grit-blasted with alumina (grit 36) before spraying. The coatings were produced by using the atmospheric plasma spray (APS) process consisting of an Oerlikon Metco F4 MB atmospheric plasma gun and a Plasma Technik A-3000S 4/2 plasma spray system. The spray parameters are presented in Table 1. The TiO_2 coating was sprayed with less power due to its lower melting point (~1857°C vs. ~2330°C for Cr_2O_3) (Ref 11). Both coatings were ground with grit 600 and 1200 SiC-papers to thicknesses of 120 μm for TiO_2 and 320 μm for Cr_2O_3 and polished with 3 μm and 1 μm diamond suspensions. In the case of microscopic examination of crack paths, the two thicknesses are not believed to have a significant effect.

High-Velocity Single Impact Experiment

The experimental setup of the High-Velocity Particle Impactor is illustrated in Fig. 2(a). In the method, compressed air is used to accelerate the projectile in a smooth bore barrel to a predefined impact velocity, which is measured with a chronograph placed in front of the sample. The material of the spherical projectiles of two different sizes used in the present study is chromium steel. The impact events are recorded with a high-speed camera (NAC, Memrecam fx K5) typically with a 50 μs interframe rate to calculate the exit velocities of the projectiles after the impact. An example of overlaid and processed high-speed camera images is presented in Fig. 2(b) and the used test parameters in Table 2.

The incident velocities, v_{inci}, were measured with a ballistic chronograph placed in front of the target assembly, and the initial kinetic energies, E_{inci}, were calculated. The exit velocity v_{exit}, the distance traveled by the projectile in a certain time increment ($\Delta s/\Delta t$), and thus reflected kinetic energy E_{refl} were determined by image analysis from the high-speed images (Fig. 2b). The fraction of energy dissipated E_d during the incident was calculated as

$$E_d = E_{inci} - E_{refl} = \frac{1}{2} m_p (v_{inci} - v_{exit})^2 \qquad \text{Eq 1}$$

where m_p is the mass of the projectile.

Table 1 Spray parameters used for the APS ceramic coatings

	Cr_2O_3	TiO_2
Current (A)	630	600
Power (kW)	46.2	43.2
Ar/H_2 (slpm)	38/13	47/12
Powder feed (g/min)	53	50
Spray distance (mm)	110	
Surface speed (m/min)	87	

Characterization Methods

The microstructures of the powders and coatings as well as the impact craters were investigated by Scanning Electron Microscope (SEM) Philips XL30 equipped with Energy Dispersive x-ray (EDX) microanalyzer. Microhardnesses of the coatings were measured as averages of ten indentations with a microhardness tester Matsuzawa MMT-X7 using loads from 100 gf ($HV_{0.1}$) to 1000 gf (HV_1). In addition, Vickers indentations were also done with loads ranging from 2000 gf (HV_2) up to 30,000 gf (HV_{30}). The indents were studied with SEM. The amount of cracks in the coating resulting from the impact was determined with optical image analysis (ImageJ) from SEM (BSE)-images from the surface of the impact sites. The surface topologies of the impact craters were analyzed using a Wyko NT-1100 optical profilometer. A special Matlab code was developed to analyze the profilometer data, while Minitab 15 (Minitab Inc.) was used for the statistical analysis of the energy dissipation behavior.

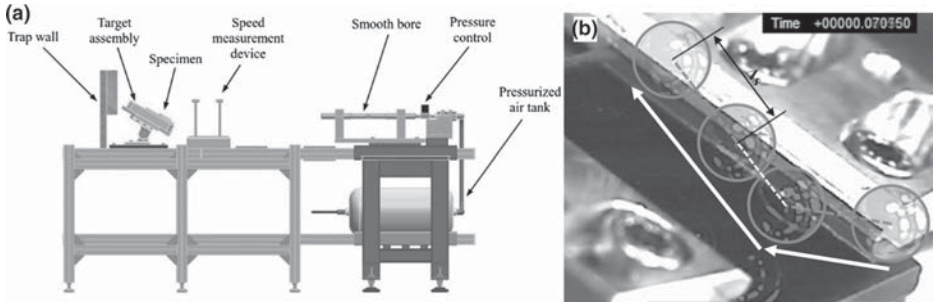

Fig. 2 (a) A schematic drawing of the HVPI setup (Ref 32) and (b) four overlaid high-speed images presenting a 30° impact incident; outlines of the projectiles are shown for clarity

Table 2 Test parameters and the measured impact velocities in the HVPI single impact experiments

	Impact angle, °	Diameter of the projectile, mm	Mass of the projectile, g	Incident velocity of the projectile, m/s
Cr_2O_3 coating	15	9	2.9	34.7 ± 0.5
		5	0.51	48.0 ± 0.0
	30	9	2.9	34.3 ± 0.5
		5	0.51	47.3 ± 0.5
TiO_2 coating	15	9	2.9	35.0 ± 0.0
		5	0.51	47.7 ± 0.5
	30	9	2.9	35.0 ± 0.0
		5	0.51	47.3 ± 0.5

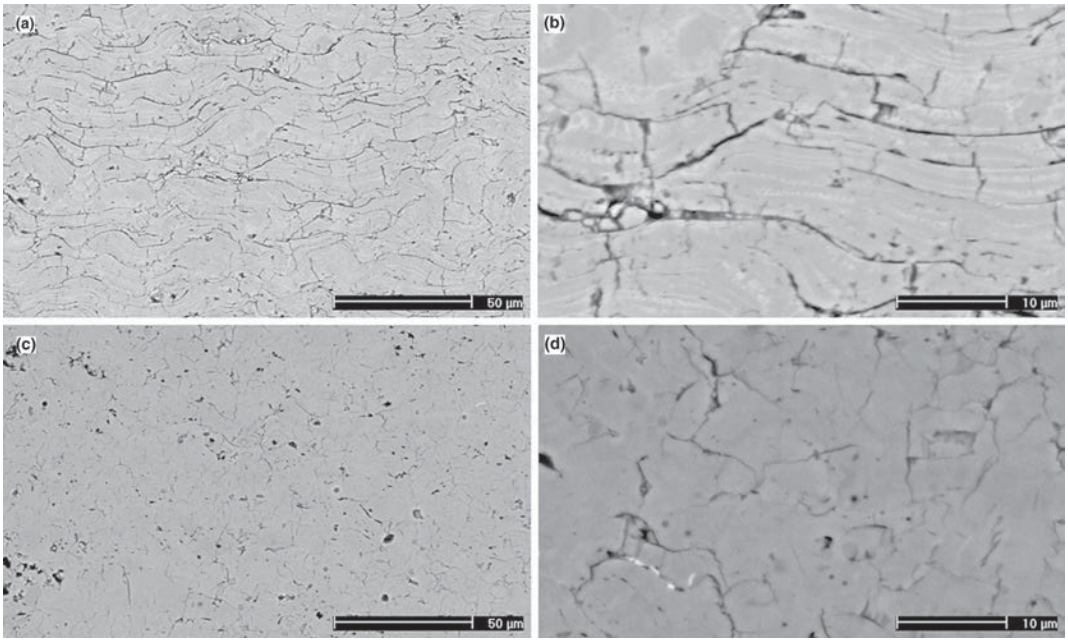

Fig. 3 Microstructures of the plasma-sprayed Cr_2O_3 (a and b) and TiO_2 (c and d) coatings. SEM BSE images

Results and Discussion

Microstructures

Figure 3 presents the original microstructures of the plasma-sprayed Cr_2O_3 (a,b) and TiO_2 (c,d) coatings. Both coatings exhibit both lateral and horizontal cracks stemming from the tensile residual stresses, which are typical for plasma-sprayed ceramic coatings (Ref 5, 33). In the TiO_2-coating, some horizontal microcracks are present, but in general the lamellae seem to be bonded better with no pronounced interfaces. A small amount of voids and pullouts is present in both coatings.

The extensive interlamellar cracking observed in the Cr_2O_3 coating is often attributed to its high melting point and high tendency to form gaseous phases during spraying. (Ref 34) This vapor readily condensates on the sample surface, weakening the bond between the already sprayed and subsequent lamellae, thus leading to poor cohesion. The intra-splat cracks are due to the rapid quenching of the splats and the inability of the ceramic splats to deform. Since TiO_2 is a less refractory ceramic, the coatings formed from it are often less porous, as is the case here as well.

High-Velocity Single Impact Experiments

The results of the HVPI tests are presented in Table 3, where the impact angle, ball diameter, and exit velocity are presented along with the incident and dissipated energies. Additionally, the amount of cracking was determined with optical image analysis from the SEM images of the impact craters. As seen in Table 3, the energy dissipation depends heavily on the test conditions for both materials. In all cases except for the one with the greatest initial energy (9 mm ball, 30° impact angle), the

Table 3 Results of the HVPI tests

	Angle, °	D_{ball}, mm	V_{exit}, m/s	E_{inci}, J	E_d, J	E_d, %	Amount of cracks, %
Cr_2O_3	15	9	30.2 ± 0.7	1.74 ± 0.06	0.42 ± 0.03	24.2 ± 1.9	0.5
		5	41.2 ± 1.3	0.59 ± 0.00	0.15 ± 0.03	26.2 ± 4.5	0.125
	30	9	27.4 ± 0.3	1.71 ± 0.06	0.62 ± 0.06	36.2 ± 2.6	1.6
		5	35.7 ± 0.5	0.57 ± 0.01	0.25 ± 0.02	43.0 ± 2.6	0.2
TiO_2	15	9	29.9 ± 0.1	1.78 ± 0.00	0.48 ± 0.01	27.2 ± 0.7	0.6
		5	40.6 ± 1.1	0.58 ± 0.01	0.16 ± 0.01	27.5 ± 2.7	0.4
	30	9	28.9 ± 0.2	1.78 ± 0.00	0.56 ± 0.02	31.6 ± 1.1	0.9
		5	33.7 ± 0.6	0.57 ± 0.01	0.28 ± 0.02	49.2 ± 2.4	0.9

'Angle' is the impact angle of the projectile, d_{ball} is the diameter of the projectile, v_{exit} is the velocity of the projectile after the impact, and E_d is the dissipated energy. E_d (%) is the ratio of dissipated energy to incident energy

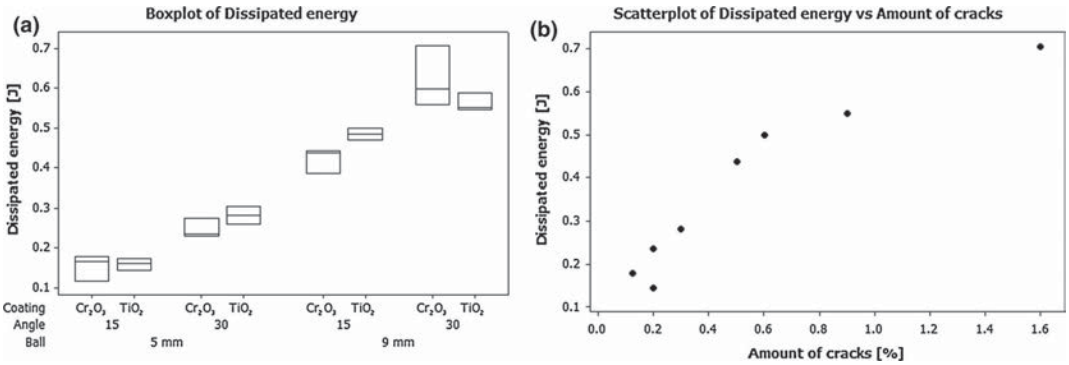

Fig. 4 (a) Dissipated energies at 15° and 30° impact angles with two projectile sizes for both coatings. (b) Relationship between dissipated energy and amount of deformation-induced cracks in the microstructure

TiO_2 coating dissipated more energy than the Cr_2O_3 coating. This correlates very well with the amount of cracks found on the surface of the samples. The percentage of energy dissipation is, interestingly enough, quite similar at the 15° angle for both projectile sizes. However, at 30°, the smaller projectile loses approximately 50% more of its initial energy than the larger projectile.

Figure 4(a) presents the dissipated energy for both impact angles and projectile sizes. In the boxplot, the outline of the boxes represents the range of results and the line in the middle the median. From these results, it is clear that there is a change in the relative amount of energy dissipation with the strongest impact for the Cr_2O_3-coating, as described above. Figure 4(b) shows the relationship between the measured energy dissipation and the identified percentage of deformation-induced cracks in the microstructure. The increase in the amount of cracks indicates that a reasonable part of the energy is consumed in the fracturing process. Since increase in the amount of impact energy that the coating absorbs increases the amount of cracking, it seems plausible that the main mechanism of energy dissipation is indeed cracking.

When examining more closely the SEM images in Fig. 5, extensive cracking in the bottom of the crater of the impact can be observed. Similar behavior has been reported for example by Waudby et al. (Ref 30). Adhesion of varying extent between the coating and the projectile was a common denominator for all impacts, as implied by the small amount of iron on the bottom of all craters. The Cr_2O_3 coating showed less absorbed energy during the impacts when smaller projectile size and lower impact angles were used. This indicates that the Cr_2O_3 coating is capable of reflecting the impact energy without severe cracking, i.e., higher hardness/strength allows better storage of elastic energy instead of cracking or failure. However, quite the opposite happens when the coating is no longer able to withstand the deformation and cracking prevails: the fracture process consumes more energy, which can be seen as pronounced energy dissipation at 30° impacts and larger particle sizes. Lindroos et al. (Ref 26) found that for steels the percentage of dissipated energy at the 30° impact angle is double compared to 15°, suggesting a strong correspondence to the test conditions as also witnessed here to a lesser extent. In the present case, the incident energy with 9-mm projectiles is high enough to cause cracking, which is especially evident at the higher impact angle. This also indicates that the observed behavior relates to a certain critical limit before more severe failure occurs, similarly as observed by Sparks et al. in (Ref 25). On the other hand, TiO_2 generally shows slightly higher energy dissipation into the coating/substrate-system as well as cracking but not a distinctive

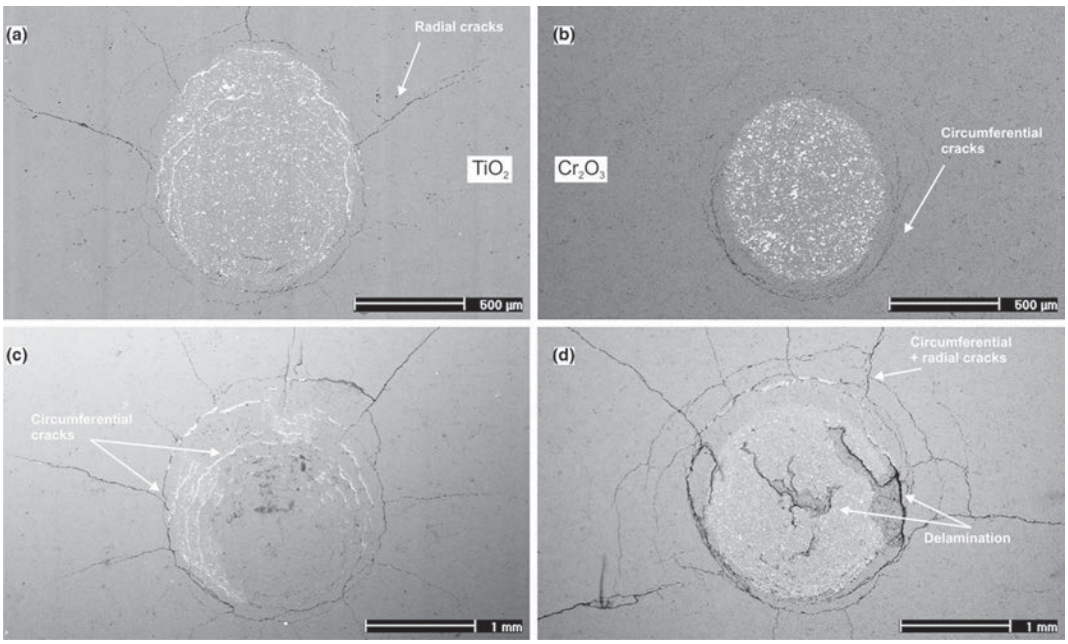

Fig. 5 Surface of the impact craters: (a) TiO_2, 5 mm, 15°; (b) Cr_2O_3, 5 mm, 15°; (c) TiO_2, 9 mm, 30°; and (d) Cr_2O_3, 9 mm, 30°. SEM BSE images

transition to severe cracking, probably due to its better structural cohesion, as seen in the cross section in Fig. 3.

2D-profiles of the impact craters as shown in Fig. 5 are presented in Fig. 6. The difference in the depth of the craters between the two coatings is noticeable. With the 5-mm projectile, the maximum depths of the craters in the Cr_2O_3 and TiO_2 coatings are 10 and 35 µm, respectively. This is in good agreement with what can be seen in Fig. 5(a) and (b), where the damage in Cr_2O_3 is very limited in comparison to TiO_2. However, with the larger projectile, the maximum depths are from 100 µm (Cr_2O_3) to 85 µm (TiO_2). This can partly be attributed to the extensive delamination in the middle of the crater in the Cr_2O_3 coating. Nevertheless, the result could be expected based on the amount of cracking visible in Fig. 5(d). Also the shape of the crater in the Cr_2O_3 with the larger projectile is similar to that of the craters in both TiO_2 impact sites, while the smaller projectile creates a crater with a shape of a dent without a clear crater lip.

The cross sections of the impact craters with the lighter impacts (5-mm projectile and 15° angle) are presented in Fig. 7. It is clear from Fig. 7(a) that the Cr_2O_3-coating stayed largely intact, although a slight dent and cohesive cracking occurred directly under the impact site. The TiO_2-coating (Fig. 7b), on the contrary, suffered severe damage in the form of vertical (circumferential) cracking and delamination at the substrate-coating interface.

Figure 8 presents the cross sections of the impact craters created by the highest impact energies (9-mm projectile and 30° angle). Both coatings exhibit delamination from the substrate and circumferential cracking that is also seen in Fig. 5(c) and (d). Heavy interlamellar cracking can also be seen on the exit side of the impact crater, probably created by the plastic deformation of the substrate clearly visible in Fig. 8. Differing from the TiO_2 coating (Fig. 8c and d), in the Cr_2O_3 coating (Fig. 8a and b), heavy decohesion occurs within the coating in the center of the crater. The largest of these cracks seems to be almost perpendicular to the impact direction of 30°. The TiO_2 coating does not exhibit such behavior; instead, the coating has detached from the substrate but internally it remains essentially intact. No significant difference between the two different impact incidents can be observed for the TiO_2-coating, and the failure mode seems to be essentially the same, as evidenced by Figs. 7(b) and 8(b). The effect of residual stresses on the cracking is yet to be determined; however, it is believed to be negligible considering the high-energy impact in comparison with intralamellar cohesion of the coatings.

When comparing the behavior of the interfacial cracks in Fig. 8(c) and (d), it seems that in the Cr_2O_3 coating sufficiently far from the crater the cracks transform from an interfacial crack into an interlamellar crack. This phenomenon may be explained with the well-known equation (Ref 11, 35) for fracture toughness, i.e.,

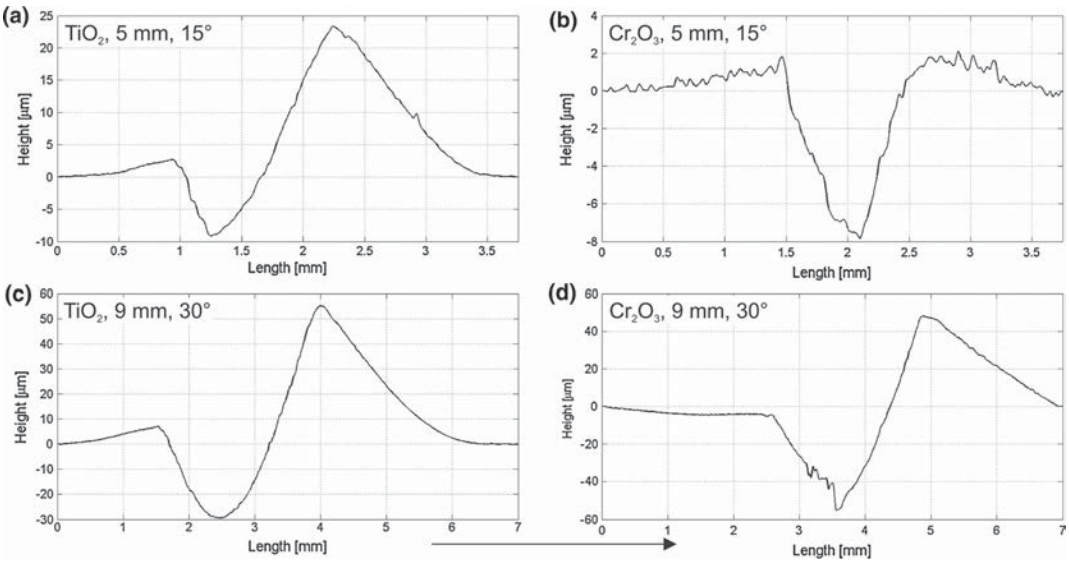

Fig. 6 2D-profiles of four impact craters: (a) TiO_2, 5 mm, 15°; (b) Cr_2O_3, 5 mm, 15°; (c) TiO_2, 9 mm, 30°; and (d) Cr_2O_3, 9 mm, 30°. The arrow shows the impact direction

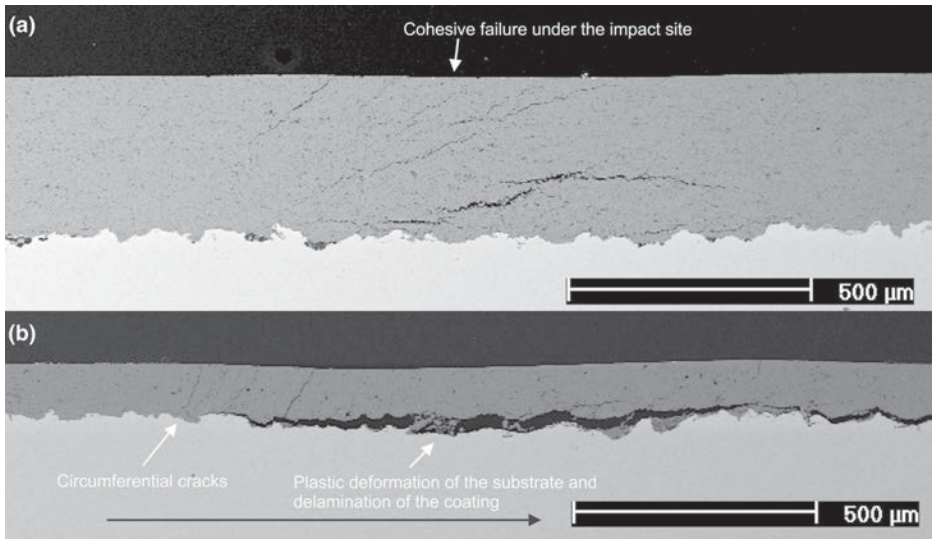

Fig. 7 SEM images of the cross sections of the impact craters created by the 5-mm projectile at a 15° angle in (a) Cr_2O_3-coating and (b) TiO_2-coating. Impact direction in both images is left-to-right as also shown by the arrow

$$\sigma_f \sqrt{\pi c_{crit}} \geq \sqrt{2\gamma Y} = K_{IC} \qquad \text{Eq 2}$$

where σ_f is the stress at fracture, c_{crit} is the critical crack length, γ is the intrinsic surface energy of the material, and Y is Young's modulus. In Eq 2, the stress intensity factor on the left hand side has to overcome the critical stress intensity factor, K_{IC}, which is a function of Young's modulus and the surface energy required when creating two new surfaces as the crack propagates. In fact, for purely brittle solids, 2γ is the limit that the toughness of

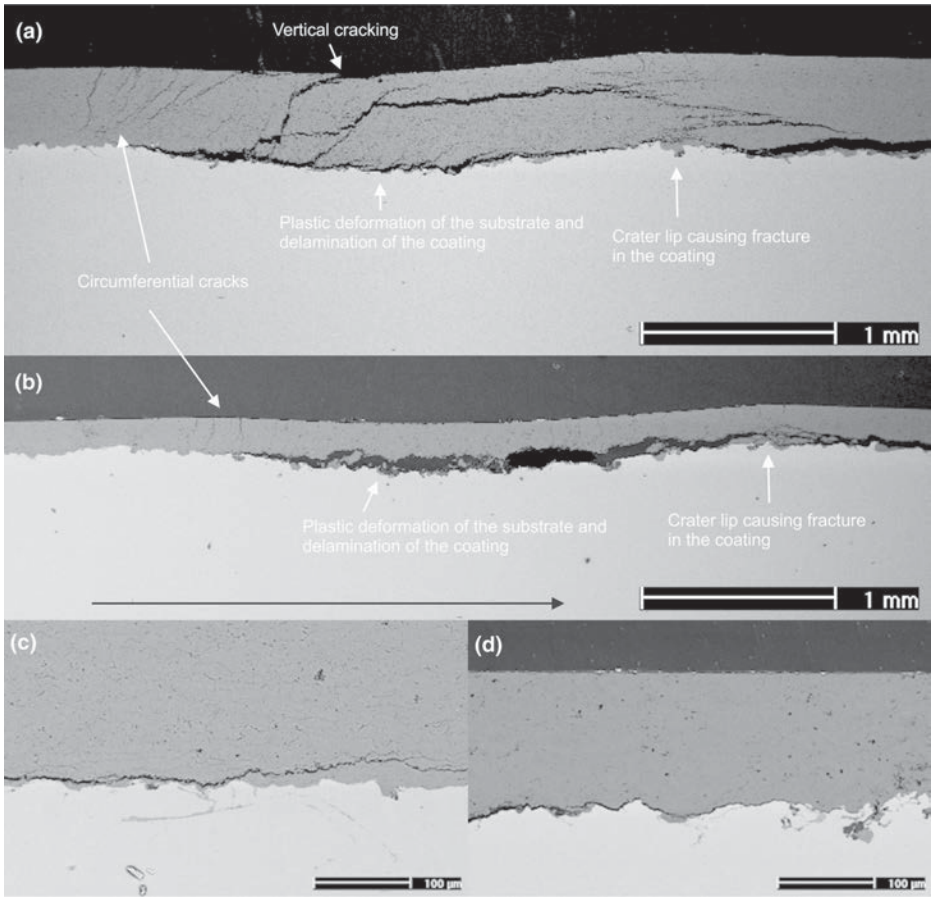

Fig. 8 SEM-images of the cross sections of the impact craters created by the 9-mm projectile at a 30° angle in (a, c) Cr_2O_3-coating and (b, d) TiO_2-coating. Impact direction in all images is left-to-right as also shown by the arrow

the material (G_c) approaches (Ref 11). Disregarding possible local differences in the elastic modulus within the Cr_2O_3-coating, it seems that the energy required to create the new surfaces (γ) is lower between the lamellae than at the interface. This phenomenon only appears as the energy of the crack diminishes, possibly due to the elastic waves that propagate on the substrate surface postimpact and make the interface a more favorable crack path. In the practical applications of thermal-sprayed ceramic coatings, metallic interlayers (bond coats) are often used between the ceramic coating and the substrate to improve the adhesion between the coating and the substrate (Ref 2). The situation would be more complex and likely the crack path would look somewhat different if a bond coat was applied, but we can definitely compare the two impact incidents in both materials. While the aforementioned inspection of the crack path is valid for the Cr_2O_3 coating, this behavior cannot be seen in the TiO_2 coating. Instead, the crack in the latter case simply terminates at the interface. This leads to a conclusion that the cohesion of the TiO_2 coating is apparently higher, i.e., the energy required to break an interlamellar bond is higher than the one required to break the adhesion between the coating and the substrate.

Vickers Indentations

Both coatings were indented on the surface with a Vickers indenter using loads from 100 grams to 30 kg. The hardness values were determined from the indents made with loads under 1000 grams and are plotted in Fig. 9. The hardness of Cr_2O_3 is higher than that of TiO_2 at all loads, especially at the smaller ones: $HV_{0.1} = 1311 \pm 101$ for Cr_2O_3 and 905 ± 72 for TiO_2 leads to a difference of 406 $HV_{0.1}$ in hardness. With the 1000-gram load, for example, the difference is only 286 HV_1 (1115 ± 92 vs. 830 ± 35).

Hence, the measured hardness of the Cr_2O_3-coating is higher but the difference decreases when using heavier loads in the measurement, which indicates that cohesion of the coating, not the material property, is the determining factor of coating hardness with high loads.

Both coatings were tested also at higher indentation loads. As Fig. 10 shows, while the indentation at 2 kg is still quite well defined in both coatings, when using a 30 kg load the Cr_2O_3 coating is severely damaged and the indentation cannot any more be measured (in fact, the behavior changes already between 3 and 5 kg). The TiO_2 coating shows mainly deformation accompanied by radial cracks. Naturally, the moderate thickness of the TiO_2-coating affects the shape of the indentation, but the ability of the ceramic coating to deform without large-scale brittle failure is nevertheless noteworthy.

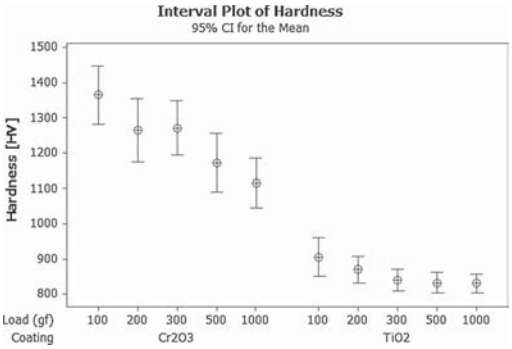

Fig. 9 Vickers hardness values measured for the Cr_2O_3 and TiO_2-coatings with different loads

Similar behavior of the coatings under indentation with different loads further confirms that there indeed seems to be a threshold for a ceramic coating below which the hardness of the coating affects the impact energy absorbance more than the cohesion. Above this limit the structure of the coating seems to collapse, at least in the case of Cr_2O_3. However, further examinations are needed to more deeply understand this behavior. Some attempts have already been made for using the Weibull distribution in characterizing Vickers indentations with different loads on thermally sprayed ceramic coatings by Lima et al. (Ref 36), and a concept of brittleness as well as a threshold value for bulk ceramics have been suggested by Quinn et al. (Ref 37). Similar investigations would be beneficial for more materials and coatings manufactured with different coating methods. Both lower and higher impact energies should be used to verify that the threshold for the Cr_2O_3-coating indeed exists, as well as to possibly find such a threshold for TiO_2-coatings, too. A larger test

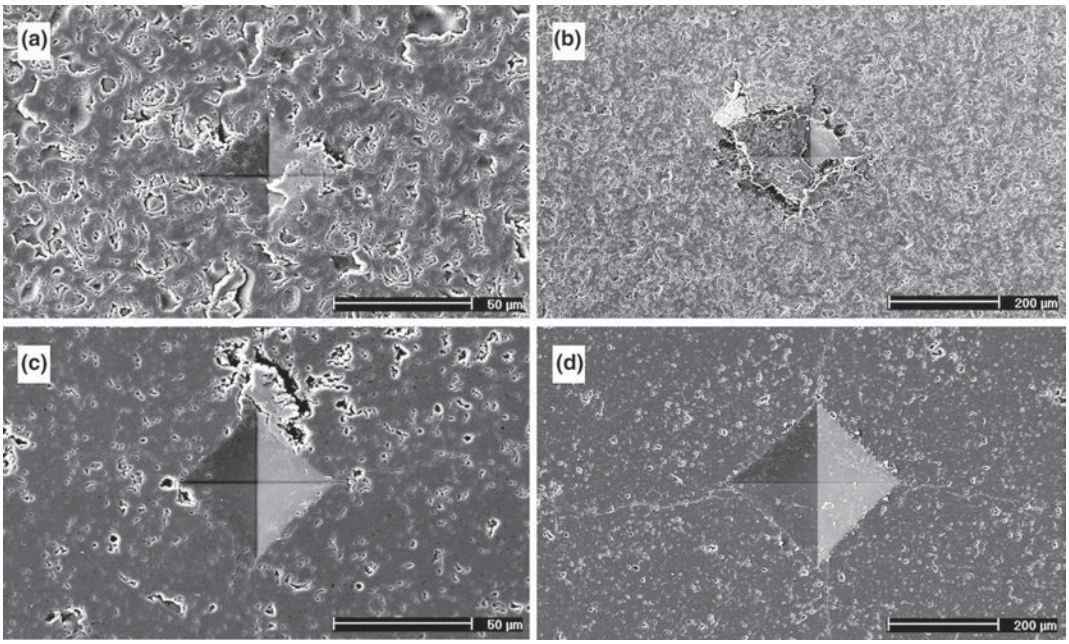

Fig. 10 SEM images of Vickers indentations in the Cr_2O_3-coating with (a) HV_2 and (b) HV_{30}, and in the TiO_2-coating with (c) HV_2 and d) HV_{30}

matrix would also give more statistical significance to the findings.

Conclusions

Two plasma-sprayed ceramic coatings, Cr_2O_3 and TiO_2, were studied under high-velocity single impacts as well as with Vickers indentation experiments to characterize their deformation and failure mechanisms. The following observations and conclusions were made:

The hardness of the coating seems to be able to deter the impacting projectile when the kinetic energy of the projectile is small, but with higher impact energies the cohesion of the coating becomes the determining factor.

The Cr_2O_3-coating, with lower cohesion but higher hardness, is damaged less with small impact energies.

The TiO_2-coating stayed largely intact with higher impact energies even with high degree of deformation of the substrate.

The energy dissipation mechanism of thermally sprayed ceramic coatings in high-velocity impacts is mainly fracturing.

The HVPI method proved a valuable experimental technique for the research of thermally sprayed ceramic coatings.

Acknowledgments

The work has been done within FIMECC Ltd and its HYBRIDS and BSA programmes. The authors gratefully acknowledge the financial support from Tekes (Finnish Funding Agency for Technology and Innovation) and the participating companies. The authors would like to thank Mr. Mikko Kylmälahti of Tampere University of Technology for spraying the coatings.

References

1. R.C. Tucker Jr., Introduction to Thermal Spray Technology, ASM. Handbook, C.M. Cotell, J.A. Sprague, F.A. Smidt Jr., Eds., *ASM Handbook, Volume 5A*, *Thermal Spray Technology*, R.C. Tucker Jr., Ed., ASM International, 2013, p 3-28
2. P. Vuoristo, Thermal Spray Coating Processes, *Comprehensive Materials Processing*, S. Hashmi, G.F. Batalha, C.J. Van Tyne, B. Yilbas, Eds., Elsevier, 2014, p 229-276
3. H. Nakahira, Blast-furnace Tuyere Having Excellent Thermal Shock Resistance and High Durability, US3977660 A, 1976
4. G. Di Girolamo, E. Serra, Thermally Sprayed Nanostructured Coatings for Anti-wear and TBC Applications: State-of-the-art and Future Perspectives, *Anti-Abrasive Nanocoatings,* M. Aliofkhazraei, Ed., Woodhead Publishing Limited, 2015, p 513-541
5. L. Pawlowski, Applications of Coatings, *The Science and Engineering of Thermal Spray Coatings*, 2nd ed., John Wiley & Sons, 2008, p 543-596
6. E. Leivo, M. Vippola, P. Sorsa, P. Vuoristo, and T. Mäntylä, Wear and Corrosion Properties of Plasma Sprayed Al_2O_3 and Cr_2O_3 Coatings Sealed by Aluminum Phosphates, *J. Therm. Spray Technol.*, 1997, **2**(6), p 205-210
7. L.M. Berger, Titanium Oxide—New Opportunities for An Established Coating Material, *Thermal Spray 2004: Advances in Technology and Application, on CD-ROM, May 10-12, 2004 (Osaka, Japan)*, DVS-German Welding Society, 2004
8. F. Toma, L. Berger, and C. Stahr, Microstructures and Functional Properties of Suspension-Sprayed Al_2O_3 and TiO_2 Coatings: An Overview, *J. Therm. Spray Technol.*, 2010, **1-2**(19), p 262-274
9. L.M. Berger, D.S. Saaro, D. Carl, C. Stahr, B.T. Fh-iws, and D. Sven, Development of Ceramic Coatings in the Cr_2O_3-TiO_2 System, *Therm. Spray Bull.*, 2009, **1**, p 64-77
10. A. Ibrahim, R.S. Lima, C.C. Berndt, and B.R. Marple, Fatigue and Mechanical Properties of Nanostructured and Conventional Titania (TiO_2) Thermal Spray Coatings, *Surf. Coat. Technol.*, 2007, **16-17**(201), p 7589-7596
11. M.W. Barsoum, *Fundamentals Of Ceramics*, 2nd ed., IOP Publishing, 2002, p 356-399
12. Y.X. Wang and S. Zhang, Toward Hard Yet Tough Ceramic Coatings, *Surf. Coat. Technol.*, 2014, **258**, p 1-16
13. P. Fauchais, G. Montavon, R.S. Lima, and B.R. Marple, Engineering a New Class of Thermal Spray Nano-Based Microstructures from Agglomerated Nanostructured Particles, Suspensions and Solutions: An Invited Review, *J. Phys. D Appl. Phys.*, 2011, **9**(44), p 1-53
14. L. Erickson, H. Hawthorne, and T. Troczynski, Correlations Between Microstructural Parameters, Micromechanical Properties and Wear Resistance of Plasma Sprayed Ceramic Coatings, *Wear*, 2001, **1-12**(250), p 569-575
15. R.S. Lima and B.R. Marple, From APS to HVOF Spraying of Conventional and Nanostructured Titania Feedstock Powders: A Study on the Enhancement of the Mechanical Properties, *Surf. Coat. Technol.*, 2006, **11**(200), p 3428-3437
16. J. Matejicek, S. Sampath, and J. Dubsky, X-ray Residual Stress Measurement in Metallic and Ceramic Plasma Sprayed Coatings, *J. Therm. Spray Technol.*, 1998, **4**(7), p 489-496
17. G. Bolelli, L. Lusvarghi, T. Varis, E. Turunen, M. Leoni, P. Scardi, C.L. Azanza-Ricardo, and M. Barletta, Residual Stresses in HVOF-Sprayed Ceramic Coatings, *Surf. Coat. Technol.*, 2008, **19**(202), p 4810-4819
18. A. Ang and C. Berndt, A Review of Testing Methods for Thermal Spray Coatings, *Int. Mater. Rev.*, 2014, **4**(59), p 179-223
19. J. Pina, A. Dias, and J.L. Lebrun, Study by X-ray Diffraction and Mechanical Analysis of the Residual Stress Generation During Thermal Spraying, *Mater. Sci. Eng., A*, 2003, **1-2**(347), p 21-31
20. I. Kleis, P. Kulu, Erosion Resistance of Powder Materials and Coatings, *Solid Particle Erosion: Occurrence, Prediction and Control*, Springer, 2008, p 129-168
21. V. Matikainen, K. Niemi, H. Koivuluoto, and P. Vuoristo, Abrasion, Erosion and Cavitation Erosion Wear Properties of Thermally Sprayed Alumina Based Coatings, *Coatings*, 2014, **1**(4), p 18-36
22. R. Westergård, N. Axén, U. Wiklund, and S. Hogmark, An Evaluation of Plasma Sprayed Ceramic Coatings by Erosion, Abrasion and Bend Testing, *Wear*, 2000, **1-2**(246), p 12-19
23. L.C. Erickson, R. Westergård, U. Wiklund, N. Axén, H.M. Hawthorne, and S. Hogmark, Cohesion in Plasma-Sprayed Coatings—A Comparison Between Evaluation Methods, *Wear*, 1998, **1**(214), p 30-37
24. J. Takeuchi, H. Nakahira, J. Nagai, Physical Properties of Some Oxide Coatings by Low Pressure Plasma Spraying, *2nd Plasma Technik Symposium, Vol. 2*, S. Blum-Sandmeier, H. Eschnauer, P. Huber, A. Nicoll, Eds., June 5-7, 1991 (Lucerne, Switzerland), Plasma Technik AG, 1991
25. A.J. Sparks and I.M. Hutchings, Transitions in the Erosive Wear Behaviour of a Glass Ceramic, *Wear*, 1991, **1-2**(149), p 99-110

26. M. Lindroos, M. Apostol, V. Kuokkala, A. Laukkanen, K. Valtonen, K. Holmberg, and O. Oja, Experimental Study on the Behavior of Wear Resistant Steels Under High Velocity Single Particle Impacts, *Int. J. Impact Eng*, 2015, **78**, p 114-127
27. M. Lindroos, M. Apostol, V. Heino, K. Valtonen, A. Laukkanen, K. Holmberg, and V.-T. Kuokkala, The Deformation, Strain Hardening, and Wear Behavior of Chromium-Alloyed Hadfield Steel in Abrasive and Impact Conditions, *Tribol. Lett.*, 2015, **57**, p 1-11
28. E. Sarlin, M. Apostol, M. Lindroos, V.-T. Kuokkala, J. Vuorinen, T. Lepistö, and M. Vippola, Impact Properties of Novel Corrosion Resistant Hybrid Structures, *Compos. Struct.*, 2014, **108**, p 886-893
29. E. Sarlin, M. Lindroos, M. Apostol, V.T. Kuokkala, J. Vuorinen, T. Lepistö, and M. Vippola, The Effect of Test Parameters on the Impact Resistance of a Stainless Steel/Rubber/Composite Hybrid Structure, *Compos. Struct.*, 2014, **113**, p 469-475
30. R. Waudby, T. Varis, T. Suhonen, K. Holmberg, M. Apostol, M. Lindroos, V. Kuokkala, High Velocity Impact Testing of Thermal Spray Hard Carbide Coatings on Steel Substrates, *Proceedings of 5th World Tribology Congress WTC 2013*, September 8-13, 2013 (Torino, Italy), Politecnico di Torino, 2013
31. W. Molnar, S. Nugent, M. Lindroos, M. Apostol, and M. Varga, Ballistic and Numerical Simulation of Impacting Goods on Conveyor Belt Rubber, *Polym. Test.*, 2015, **42**, p 1-7
32. M. Apostol, V. Kuokkala, A. Laukkanen, K. Holmberg, R. Waudby, M. Lindroos, High Velocity Particle Impactor—Modeling and Experimental Verification of Impact Wear Tests, *Proceedings of 5th World Tribology Congress WTC 2013*, September 8-13, 2013 (Torino, Italy), Politecnico di Torino, 2013
33. S. Kuroda and T.W. Clyne, The Quenching Stress in Thermally Sprayed Coatings, *Thin Solid Films*, 1991, **1**(200), p 49-66
34. J. Leitner, K. Voleník, K. Neufuss, and B. Kolman, Vaporization of Components from Alloy Powder Particles in a Plasma Flow, *Czech J. Phys.*, 2006, **2**(56), p 1391-1400
35. C.B. Carter and M.G. Norton, *Fracturing: Brittleness, Ceramic Materials: Science and Engineering*, LLC, Springer Science + Business Media, 2007, p 325-339
36. R. Lima and B. Marple, High Weibull Modulus HVOF Titania Coatings, *J. Therm. Spray Technol.*, 2003, **2**(12), p 240-249
37. J.B. Quinn and G.D.G. Quinn, Indentation Brittleness of Ceramics: A Fresh Approach, *J. Mater. Sci.*, 1997, **16**(32), p 4331-4346

PUBLICATION

IV

Characterizing the micro-impact fatigue behavior of APS and HVOF-sprayed ceramic coatings

J. Kiilakoski, C. Langlade, H. Koivuluoto and P. Vuoristo

Surface and Coatings Technology 371.(2018), 245–254
DOI: 10.1016/j.surfcoat.2018.10.097

Surface & Coatings Technology 371 (2019) 245–254

Contents lists available at ScienceDirect

Surface & Coatings Technology

journal homepage: www.elsevier.com/locate/surfcoat

Characterizing the micro-impact fatigue behavior of APS and HVOF-sprayed ceramic coatings

J. Kiilakoski[a,*], C. Langlade[b], H. Koivuluoto[a], P. Vuoristo[a]

[a] Laboratory of Materials Science, Tampere University of Technology, P.O. Box 589, FI-33101 Tampere, Finland
[b] Université de Bourgogne Franche Comté, Laboratory ICB-LERMPS UMR CNRS 6303, site UTBM, 90010 Belfort Cedex, France

ARTICLE INFO

Keywords:
Thermal spray
Ceramic coating
Impact test
Fracture
Surface fatigue
Characterization

ABSTRACT

The fatigue life of thermally sprayed Al_2O_3- and Cr_2O_3-based coatings has been studied under low-energy (0.7–5 mJ) impact conditions. A threshold impact energy and amount of repetitions the coatings can endure with said energy before catastrophic failure was obtained. The catastrophic failure was determined to occur when the fracture mode of the coating switched from brittle cone cracking to quasi-plastic radial cracking. The results are examined relative to the microstructural features along with other properties of the coatings - hardness and cavitation resistance. The experiment provided a new approach for a straightforward comparison of the micro-scale impact fatigue life of thermally sprayed coatings unachievable with previous methods.

1. Introduction

Thermal spraying is a common line-of-sight method to produce coatings of a multitude of materials on large surfaces. Often, these coatings are required to exhibit good tribological and chemical resistance. Such applications are found in the process industry e.g. in center press rolls and dewatering elements for paper machines, mechanical seals and process valves. For the demand of such environments demand, coatings deposited from ceramic feedstock are typically the most suitable solution due to their excellent wear properties and chemical inertness. [1,2] However, the main drawback with these coatings is their brittleness [3], which often hinders their usability in applications where impact resistance and ductility are beneficial. Hence, the failure mechanism in ceramic coatings is typically brittle fracture with zero to little plastic deformation. [2] Significant efforts have been put on the improvement of the toughness of ceramic coatings through material processing by incorporating another ceramic phase [4,5], a metallic phase [6] or novel spray processing methods [7–10]. Despite the improvements in fracture toughness, the development of damage during fatigue has a multitude of variables and is not yet fully understood.

As is the case with coatings, the main issue also with traditional ceramics when considering mechanical properties is brittleness. Ceramics cannot relieve stress in their structure, making them sensitive to existing cracks and flaws that dictate the strength of the material. [11] The growth of the crack or flaw under stress is essential to the lifetime of the component: when it reaches a critical size, which is determined by fracture toughness, the component fails. [11–13] The lifetime of the component can be determined by fatiguing tests, such as spherical indentation, where the flaw is intentionally grown until the component fails. The phenomenon of fatiguing under spherical indentation occurs by an initiation and propagation of a tensile-driven "brittle" cone-crack followed by shear-driven "quasi-plastic" radial cracking along with deeply penetrating secondary cone cracks with higher number of repetitions or increasing load. [14–16] To combat the initiation of cracking, Lee et al. [15] have found that in silicon nitride with different microstructures, higher toughness leads to suppression of cone cracking and less strength degradation with increasing indentation loads. They concluded that the quasi-plastic fracture mode is less deleterious to component strength. In another study on the same topic, Kim et al. [16] have studied the transition between the two modes in a fatigue test extensively in soda-lime glass, porcelain and silicon nitride, and observed some degradation in the inert strength of the material during propagation of the cone crack, but severe degradation when radial cracking had commenced. While components in some applications can sustain their ability to function even with cone cracks, radial cracking typically leads to catastrophic failure [16,17]. Therefore, extrapolation of strength values measured from low amount of repetitions was deemed dangerous. Similar deduction was suggested by Quinn et al. [18] for the Vickers indentation experiment, where the increasing load led to declining hardness value until a "brittleness threshold" was reached. They confirmed the results with eight different ceramics. We

* Corresponding author.
E-mail address: jarkko.kiilakoski@tut.fi (J. Kiilakoski).

https://doi.org/10.1016/j.surfcoat.2018.10.097
Received 25 July 2018; Received in revised form 4 October 2018; Accepted 30 October 2018
Available online 02 November 2018

measured similar results previously on thermally sprayed Cr_2O_3 and TiO_2 –coatings [19], where hardness values lowered with increasing load until the Cr_2O_3 coating catastrophically failed and the TiO_2 coating started to conform to the substrate.

However, limited amount of fatigue testing by indentation has been performed on thermally sprayed ceramic coatings. Ahmed et al. [20] investigated the rolling contact fatigue of thermally sprayed hard metal and ceramic coatings and determined the failure modes as: abrasion, delamination, bulk failure and spalling. From these failure modes, abrasion and bulk failure seem unlikely for ceramic coatings under an indenter due to the fixed site of analysis and the higher susceptibility to damage of the coating in relation to the substrate. Therefore, the probable failure modes are delamination and spalling. These failure modes were defined by the authors as stemming from stress concentrations due to coating defects and subsurface crack initiation and propagation, which would suggest the “quasi-plastic” mode of failure. Vackel et al. [21] investigated the effect of thermal history, microstructure and residual stresses of HVOF-sprayed WC-CoCr coatings on a component lifetime in a bending fatigue test. They determined that higher hardness and compressive stresses were advantageous to the fatigue life of the system. In a similar test, Ibrahim et al. [22] confirmed that compressive residual stresses and a higher elastic modulus are desired for fatigue life improvement. Due to these properties, they found an improvement of HVOF-sprayed over APS-sprayed TiO_2.

Impact fatigue of coatings is, however, quite different from the mentioned circumstances since the Hertzian contact is highly localized and mainly compressive under the indent with some additional shear. [23] On the topic of hertzian impacts, Musalek et al. [24] used spherical indentation to observe changes in the microstructure of an alumina coating sprayed with a water-stabilized plasma system after a single indentation. They discovered cracking, closing of existing cracks, debonding and sliding on the splat interfaces, which would suggest a “quasi-plastic” behavior as previously defined. Other considerations for coatings are the lower initiation loads for cone cracks for thin coatings (thickness smaller than the diameter of the indenting sphere) [17] and that segregate phases on grain boundaries lead to high compressive stresses on the boundaries, which in turn emphasizes “brittle” fracture mode [25]. The consequence of these considerations is that the lack of compressive stresses at the splat boundaries lead to a preference to shearing under indentation, and the low thickness of the coating can further lower the initiation threshold of conical cracking. Therefore, it is logical to turn attention towards measuring the onset of the quasi-plastic regime, when catastrophic failure occurs.

To study this phenomenon, one suitable measure would be impact fatigue resistance under controlled conditions and a small enough scale. Such equipment has been utilized to study the phase-transformation in metals [26,27] and damage behavior of thin hard coatings [28]. In these studies the precisely controllable impact energy and location has allowed for meticulous examination of the impacts leading to models of critical stress levels for the materials as well as studying of the microstructural changes during a fatiguing at a controlled time. The micro-impact fatigue experiment in question would potentially give a new method of studying the development of fracturing in thermally sprayed ceramic coatings as well, where it has not yet been applied.

The objective of this study is to find the impact energy limits where selected plasma- and HVOF-sprayed ceramic coatings have their transformation from brittle to quasi-plastic cracking leading to catastrophic failure. This is achieved by exploring their mechanical response when subjected to a repeated number of impacts with different loads, followed by different number of impacts with a constant load. These results are then compared with other measured mechanical properties of the coatings.

2. Experimental methods

Thermally sprayed Al_2O_3- and Cr_2O_3-based ceramic coatings on 1.0841 steel substrates were examined in this study. The coatings were sprayed with two methods: atmospheric plasma-spray (APS, F4 torch, Oerlikon Metco AG, Winterthur, Switzerland) and high-velocity oxy-fuel spray (HVOF, TopGun, GTV Gmbh, Luckenbach, Germany) from feedstock powders provided by three different manufacturers (H.C. Starck GmbH, Munich, Germany; Ceram GmbH, Albbruck-Birndorf, Germany and Millidyne Oy, Tampere, Finland). The target coating thickness was 250–300 µm, which was approximated by measuring with a Surfix easy-coating thickness gauge (Phynix GmbH & Co. KG, Neuss, Germany). The deposition parameters have been optimized in previous studies with the aim of achieving a dense microstructure and high hardness for wear applications. The information on the powders and the coating deposition parameters can be found in Tables 1 & 2.

Table 1
Processing parameters of the APS-coatings.

Sample name	APS-Al_2O_3	APS-Al_2O_3-40ZrO_2	APS-Cr_2O_3
Powder manufacturer	H.C. Starck	Ceram	H.C. Starck
Material chemical composition [wt%]	Al_2O_3	Al_2O_3-40ZrO_2	Cr_2O_3
Powder manufacturing method	Fused & crushed (F&C)		
Powder size distribution [µm]	−45 + 22	−45 + 20	−45 + 22
Ar [slpm]	41	41	38
H_2 [slpm]	14	13	13
Current [A]	610	610	630
Voltage [V]	74	70	73
Powder feed rate [g/min]	39	45	51
Standoff distance [mm]	110	140	110
Relative surface speed [m/min]	96	87	107
Offset [mm/pass]	6	7	6
Passes [number]	60	36	74
Coating thickness [µm]	~300	~300	~421

The coating cross-sections were prepared by grinding up to P1200 grit paper and consequently polishing up to a ¼-µm diamond slurry. The coating hardnesses were determined from ten indentations on the cross-section using a Vickers hardness tester (MMT-X7, Matsuzawa, Akita, Japan) with a load of 300 gf ($HV_{0.3}$) and the coating microstructures were characterized with a scanning electron microscope (XL30, FEI Company/Thermo Fisher Scientific Inc., Hillsboro, OR, United States).

The micro-impact fatigue experiments were performed with an in-house –made apparatus at Université de Technologie de Belfort-Montbéliard (Sevenans, France) of which a schematic is presented in Fig. 1. The input parameters are excitation time of the electromagnet that accelerates the indenter in milliseconds and the amount of repetitions. The distance between the sample and the indenter was kept constant at 0.7 mm and the velocity of the indenter was measured, as well as the load induced on the sample. The velocity and load measurements were performed for the first and last five repetitions, as well as once in the middle of the set for five repetitions. In the first set of experiments, a 2 mm diameter ZrO_2-ball indenter was used with repetitions of 1000 and the excitation time was increased from 0.7 ms to 1.1 ms with 0.1 ms increments (corresponding roughly to loads of 100 to 600 N or impact energies of 0.7 to 5 mJ). In the second set, fixed excitation times were used for each sample based on their perceived damage while varying the repetitions from 100 to 1000 in order to find the energy/repetition amount the sample can endure. For further examination, the impact energy values were chosen over load values due to the effect of substrate thickness and properties, such as acoustic impedance, on the measured load. This enables simpler comparison between coatings on various substrates without additional variables in the future. In all fatigue tests, the frequency of the impacts was 10 Hz. More details of the test can be found e.g. in [26,28,29]. Before the experiments, the coating surfaces were ground with P600 and P1200 SiC-papers and polished with a 3 µm diamond slurry to achieve as similar a surface topography as possible. The coating thicknesses were

Table 2
Processing parameters of the HVOF-coatings.

Sample name	HVOF-Al_2O_3	HVOF-Al_2O_3-40ZrO_2	HVOF-Cr_2O_3	HVOF-Cr_2O_3-3TiO_2	HVOF-Cr_2O_3-5TiO_2
Powder manufacturer	H.C. Starck	Ceram	Saint-Gobain	Millidyne	Millidyne
Material chemical composition [wt%]	Al_2O_3	Al_2O_3-40ZrO_2	Cr_2O_3	Cr_2O_3-3TiO_2	Cr_2O_3-5TiO_2
Powder manufacturing method	Fused & crushed			Agglomerated & sintered	
Powder size distribution [μm]	−20 + 5	−25 + 5	−15 + 5	−30 + 10	−25 + 8
C_2H_4 [slpm]	93	90	137	127	130
O_2 [slpm]	270	257	288	275	308
O_2/C_2H_4-ratio	2.9	2.9	2.1	2.2	2.37
Powder feed rate [g/min]	40	30	20	25	15
Standoff distance [mm]	150	150	150	150	170
Relative surface speed [m/min]	179	179	179	179	80
Offset [mm/pass]	3	3	3	3	3
Passes [number]	24	36	60	60	60
Coating thickness [μm]	~250	~330	~200	~220	~240

measured to ensure no more than 50 μm of coating was removed during the preparation. The impact craters were examined with an optical microscope as well as an optical profilometer (Infinitefocus G5, Alicona Imaging GmbH, Austria) to obtain their volume loss after the experiment.

Additionally, the cavitation erosion resistance of the coatings was measured to compare another mechanical property with the micro-impact fatigue test. The cavitation erosion was performed with an ultrasonic transducer (VCX-750, Sonics & Materials, Newtown, USA), according to the ASTM G32-10 standard for indirect cavitation erosion. The vibration tip was an alloy of Ti-6Al-4V. The sample surfaces were ground flat and polished with a polishing cloth and diamond suspension (3 μm). Samples were cleaned in an ultrasonic bath with ethanol and weighed after drying. Samples were attached on a stationary sample holder and the head of the ultrasonic transducer was placed at a distance of 0.5 mm. Samples were weighed after 15, 30, 60 and 90 min. The cavitation resistance of the coatings was calculated as the reciprocal of the mean-depth of erosion per hour, which in turn is derived from the theoretical volume loss (presuming a fully dense coating) and the area of the vibrating tip.

3. Results & discussion

The micrographs of the cross-sections of the coatings are presented in Fig. 2. All coatings were of good quality with a high melting degree and some intrinsic porosity. The thicknesses were roughly 300 μm for all coatings. The APS-coatings exhibited larger micro features due to the larger feedstock particle size whereas the structure of the HVOF-samples was finer throughout. The APS Al_2O_3 and Cr_2O_3-coatings are representative of typical APS-coatings by having clear borders between lamellas as well as intralamellar cracking. In HVOF-sprayed Cr_2O_3-3TiO_2 and Cr_2O_3-5TiO_2, metallic lamellae from particles reduced during spraying are visible as lighter, homogeneous splats. When comparing the Al_2O_3-40ZrO_2-coatings, the melting degree of the lighter Zr-rich phase is clearly higher in the APS- than the HVOF-sample along with more of the light grey mixed Al_2O_3-ZrO_2-phase.

3.1. Micro-impact fatigue with constant repetitions and varying impact energies

The samples were subdued to 1000 impacts with differing excitation times of the impactor, leading to differing impact energies. Optical micrographs of the impact sites on the samples after the first experiment are presented in Figs. 3 and 4. All samples were relatively unaffected by 1000 impacts of the shortest excitation time of 0.7 ms (ca. 1.3 J energy input). From some samples, even distinguishing the impact site proved impossible, indicating the absence of cone cracks. These appeared with 0.8 ms (ca. 2 J) for the rest of the coatings, but the first differences were found with 0.9 ms (ca. 3 J) when the HVOF-Cr_2O_3-sample shattered indicating heavy radial cracking. This was followed by similar catastrophic failure of the HVOF-Cr_2O_3-3TiO_2-sample at 1.0 ms (ca. 4 J). With this impact energy, also all of the other coatings exhibited prominent rings of cracks around the craters that could be interpreted as failure, albeit vastly milder than with the two coatings mentioned above. The harshest conditions (1.1 ms/ca. 4.5–5 J) produced similar craters as the previous ones, only slightly larger. Altogether the crater development is very similar to what has been reported for traditional bulk ceramics [16], where ring cracks appeared already after one impact and radial cracking commenced only after a large amount of repetitions.

The test gives a seemingly large variation of impact energies with the same excitation time. However, since the energy was only calculated form 15 repetitions out of 1000 in each case, it is believed that over the whole test the energies are averaged to essentially similar values for each coating. For the concurrently ran load measurements the variation was significantly smaller but as outlined in section 2, utilizing the load values are not desirable due to differences in substrate properties. From the optical micrographs the following conclusions can

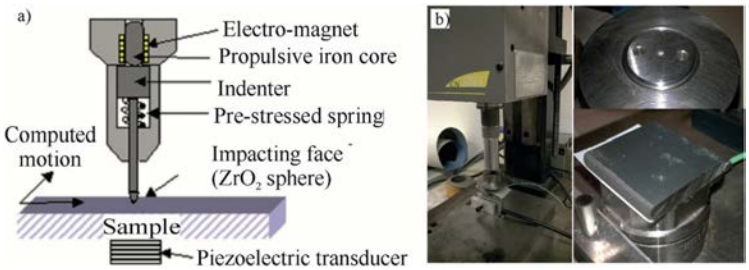

Fig. 1. a) A schematic presentation of the micro-impact fatigue test apparatus. Modified from [13]. b) Images of the test setup, the impacting ball and the sample attached to the load cell.

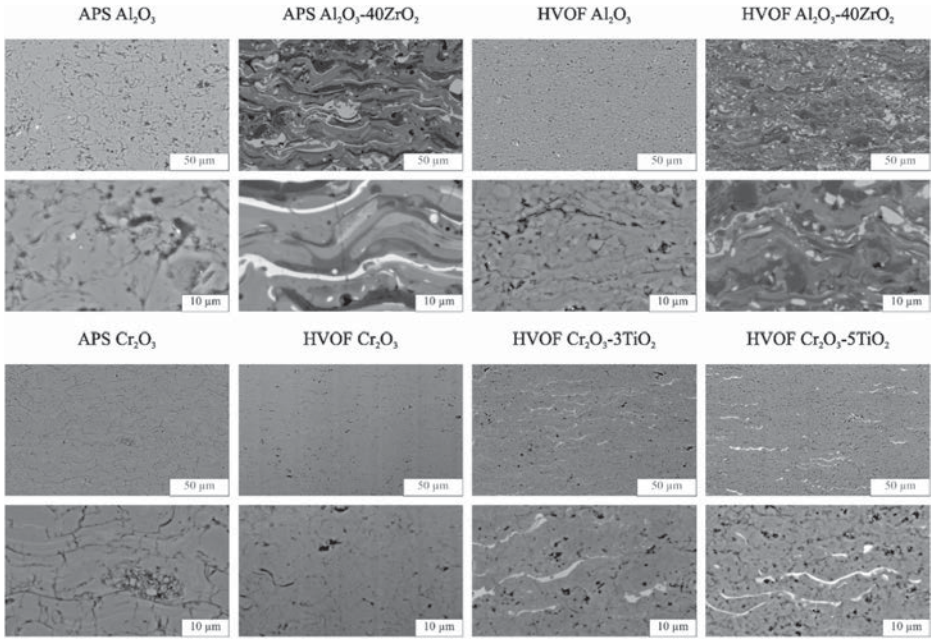

Fig. 2. Cross-sections of the coatings tested in the study. SEM (BSE)-images.

be drawn: 1) The Cr_2O_3-based HVOF coatings are very resistant to impact fatigue on small loads, in fact in many cases no cone cracking appeared on the coatings. 2) When the impacting energy reaches a critical level the HVOF Cr_2O_3 coating fails catastrophically. This is likely due to the high internal stresses stemming from the considerably higher deposition temperature [30]. However, adding TiO_2 increases the resistance of the coating to this behavior by lowering the melting point of the ceramic composite mixture. 3) Plasma-sprayed coatings and HVOF-sprayed Al_2O_3-based coatings exhibit a more gradual propagation of cone cracking, i.e. development of damage, as a function of impact energy. This is possibly due to lower internal stresses stemming from lower heat loads to the substrate. 4) It is very challenging to determine the exact point where the radial cracking and therefore failure commence visually, since a visible cone crack crater already exist in

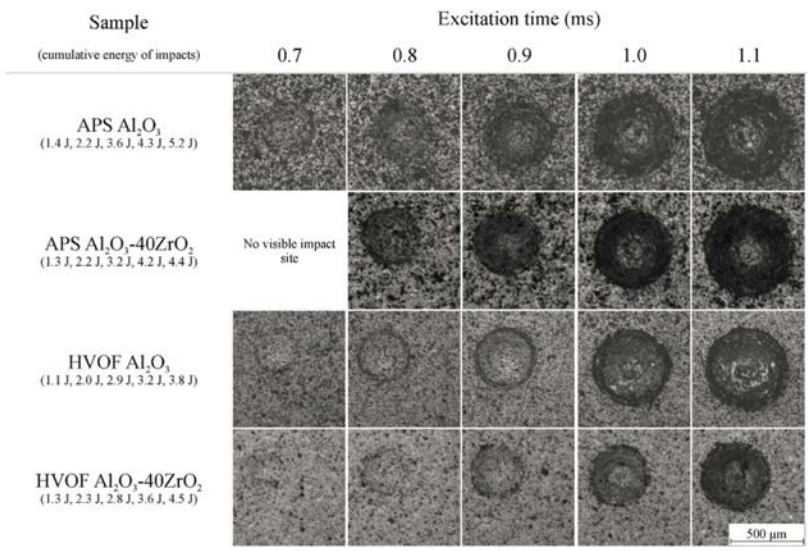

Fig. 3. Optical micrographs of the impact craters of the Al_2O_3-based coatings after the micro-impact fatigue experiment with fixed amount of repetitions. The scale bar is the same for all images.

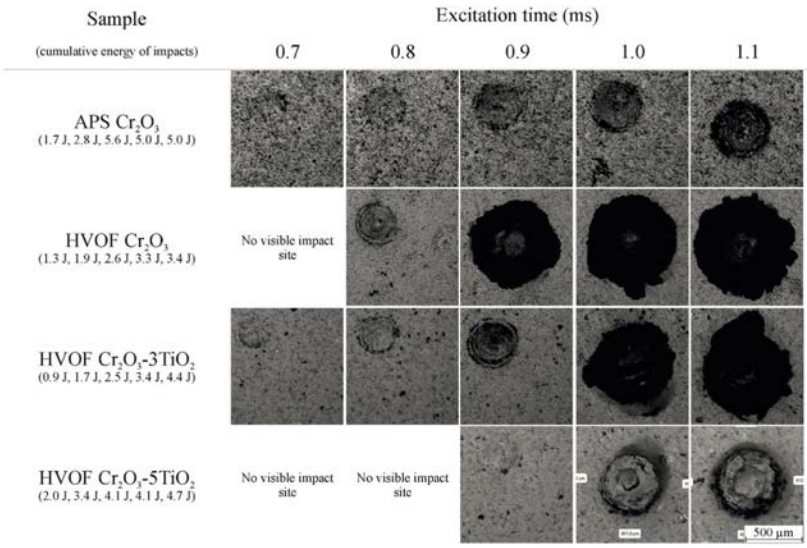

Fig. 4. Optical micrographs of the impact craters of the Cr_2O_3-based coatings after the micro-impact fatigue experiment with fixed amount of repetitions. The scale bar is the same for all images.

most cases even at small loads and its propagation and the appearance of radial cracking is very gradual.

The visual method of observing the failure is very subjective due to the difficulty of determining the exact point of failure and, therefore, efforts were put forth to find a way to determine failure numerically. For this reason, the volumes of the craters were measured and are presented in Table 3. Clearly, there are large differences in crater volumes between the coatings and the enlargement of the crater can be determined as a function of impact energy. The outlier of the group is HVOF Cr_2O_3-5TiO_2 where the crater was smaller with the 1.1 ms impact than 1.0 ms, seen as a negative change in normalized volume in Table 3. This is deemed to be a result of the debris from the crater remaining somewhat attached to the coating (as seen in Fig. 4) distorting the measurement. Despite the seemingly gradual increase in the volume of the crater in the optical micrographs, there seems to exist one greater increase in the measured volume with each coating. Hence, the volume values were normalized to the largest measured crater volume (V_{max}) of each coating, and their increase/decrease was evaluated as percentage points [pp] with the increase in excitation time, Eq. (1).

$$\Delta V\,[pp] = \frac{V_n - V_{n-1}}{V_{max}} \times 100 \tag{1}$$

Comparing the change in normalized volume and the optical micrographs it was observed than typically an increase in normalized volume of 15 pp. of more coincided with also the visual point of catastrophic failure in those cases where visual determination was possible. This is of course an arbitrary value, but seems to correlate well in all cases and will be useful when estimating the performance of the coating whose failure method was more gradual and difficult to distinguish visually. The idea is analogous to the sudden drop in inert strength as measured for bulk ceramics as a function of load cycles [16,25]. The crater volumes and the relative changes are presented in Fig. 5.

Table 3
Crater volumes and incremental volume changes to the previous crater. The points of failure are in bold.

Sample	Attribute	Excitation time [ms]				
		0.7	0.8	0.9	1	1.1
APS-Al_2O_3	Crater volume [$\mu m^3 \times 10^{-3}$]	120	295	616	1179	2149
	Volume change [pp]	–	8.1	14.9	**26.2**	45.1
APS-Al_2O_3-40ZrO_2	Crater volume [$\mu m^3 \times 10^{-3}$]	37	229	518	1432	2629
	Volume change [pp]	–	7.3	11.0	**34.8**	45.5
HVOF-Al_2O_3	Crater volume [$\mu m^3 \times 10^{-3}$]	19	71	189	558	953
	Volume change [pp]	–	5.5	12.4	38.7	41.4
HVOF-Al_2O_3-40ZrO_2	Crater volume [$\mu m^3 \times 10^{-3}$]	18	54	121	319	769
	Volume change [pp]	–	−4.7	8.7	**25.7**	58.6
APS-Cr_2O_3	Crater volume [$\mu m^3 \times 10^{-3}$]	50	106	207	403	764
	Volume change [pp]	–	7.4	13.2	**25.7**	47.3
HVOF-Cr_2O_3	Crater volume [$\mu m^3 \times 10^{-3}$]	49	83	12,730	17,284	24,035
	Volume change [pp]	–	0.1	**52.6**	18.9	28.1
HVOF-Cr_2O_3-3TiO_2	Crater volume [$\mu m^3 \times 10^{-3}$]	8	40	266	8503	16,069
	Volume change [pp]	–	0.2	1.4	**51.3**	47.1
HVOF-Cr_2O_3-5TiO_2	Crater volume [$\mu m^3 \times 10^{-3}$]	–	–	79	95	76
	Volume change [pp]	–	–	–	**17.1**	−20.2

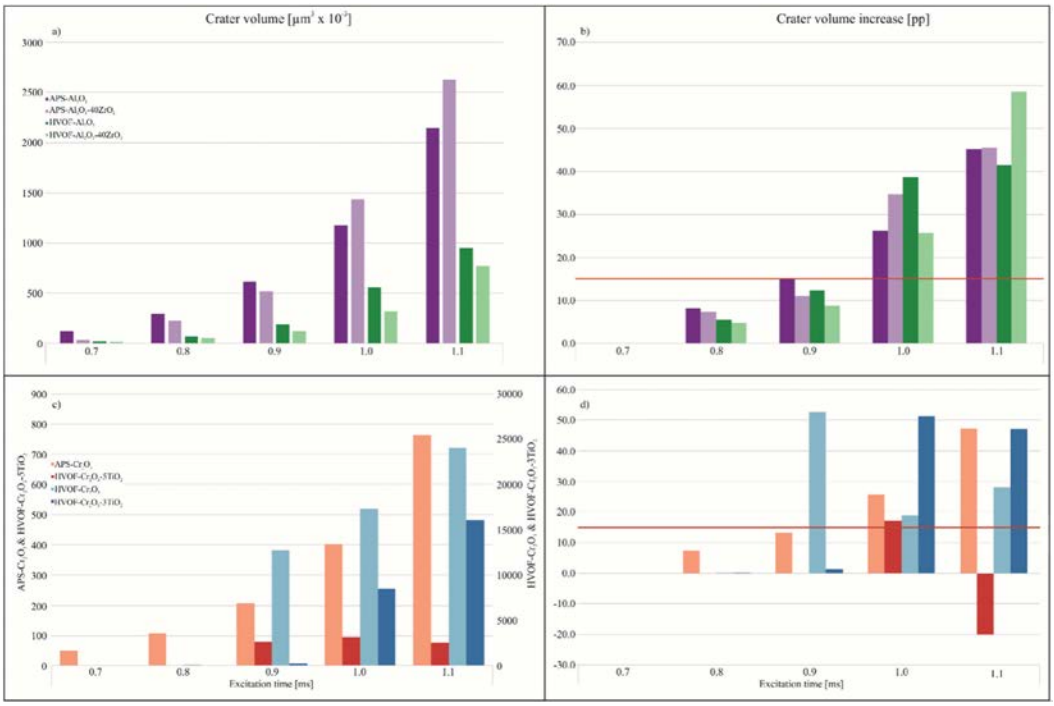

Fig. 5. Graphs of the measured crater volumes for a) Al_2O_3-based samples, b) Cr_2O_3-based samples and the changes in normalized crater volume for c) Al_2O_3-based samples d) Cr_2O_3-based samples. Constant repetitions, variable excitation time.

3.2. Micro-impact fatigue with constant impact energy and varying repetitions

The second set of experiments was conducted with the excitation time determined in the previous step to lead to failure for each coating separately, while the repetitions were increased as follows: 100, 200, 400, 600, and 800. Note that this excitation time was chosen based on the visual inspection of the optical images only, before measurement of the crater volumes. Hence, the excitation times are higher with samples APS Cr_2O_3, HVOF Al_2O_3, HVOF Al_2O_3-40ZrO_2 and HVOF Cr_2O_3-5TiO_2 than the final ones determined from the crater volumes. Since from the micrographs there was some uncertainty which excitation time lead to failure the higher one was chosen to ensure catastrophic failure is achieved during the 1000 impacts. Optical micrographs of the samples after the second experiment are presented in Figs. 6 and 7.

All samples demonstrate visual markings of cone cracking already with 100 repetitions with the chosen excitation times. HVOF-samples Cr_2O_3, Cr_2O_3-3TiO_2 and Cr_2O_3-5TiO_2 exhibited a clear point of failure at 400, 800 and 400 repetitions, respectively. The Cr_2O_3-sample endured by far the highest temperatures during spraying, probably leading to the most compressive stress profile in comparison, leading to it being the first to fail. The Cr_2O_3-3TiO_2 and Cr_2O_3-5TiO_2 were more similar, due to the different impact energies utilized, but likely the 5TiO_2-alloyed sample failed first also due to higher compressive stresses due to a higher (stoichiometric) flame temperature. For the Al_2O_3-based samples and APS Cr_2O_3, the damage development between increasing repetitions was very gradual and the point of failure was again difficult to distinguish. Therefore, the same approach as the first set was utilized and the volume losses and changes in normalized volume loss were measured and are presented in Table 4. The last values with 1000 repetitions are from Table 3, highlighting the variation between the tests in some coatings. Unlike with the first experiment, here negative values of volume change were recorded in multiple occasions with increasing repetitions. This can arise from the relatively small difference in total impact energy, and variation from the difference with the sample distance from the impactor due to unevenness of the samples. The crater volumes and changes in volume are visualized in Fig. 8.

Since different excitation times were used for the samples, a comparison of cumulative impact energies is a viable way to compare the ability of the samples to resist micro-impact fatigue. This is calculated by multiplying the incoming impact energy by the amount of repetitions that lead to failure. This way, both the used excitation time and repetition amount are accounted for in the comparison. Since the durability can only be determined to the accuracy of 100 or 200 repetitions, the range of energies between the last stage of no failure and after failure is given. The samples are presented in order of least resistance to micro-impact fatigue based on these values in Fig. 9.

From the second experimental set, the following conclusions can be drawn; 1) It seems to be irrelevant whether Al_2O_3 or Cr_2O_3 is the base constituent of the coating material. 2) The spray parameter requirements, such as flame temperature, placed by the material have a large effect on the microstructure through residual stresses generated by the thermal history of the sample [30] and hence the fatigue life of the coating. Typically compressive stresses in the coatings are advantageous to tensile fatigue tests [21,22,31], but when the stresses area excessive they become deleterious. 3) Alloying phases can change the behavior greatly: addition of TiO_2 into Cr_2O_3 and ZrO_2 into Al_2O_3 increases fatigue resistance. This effect is either due to their lower hardness [11,32] that are more malleable or to lowering the melting point of the materials and therefore assisting the deposition.

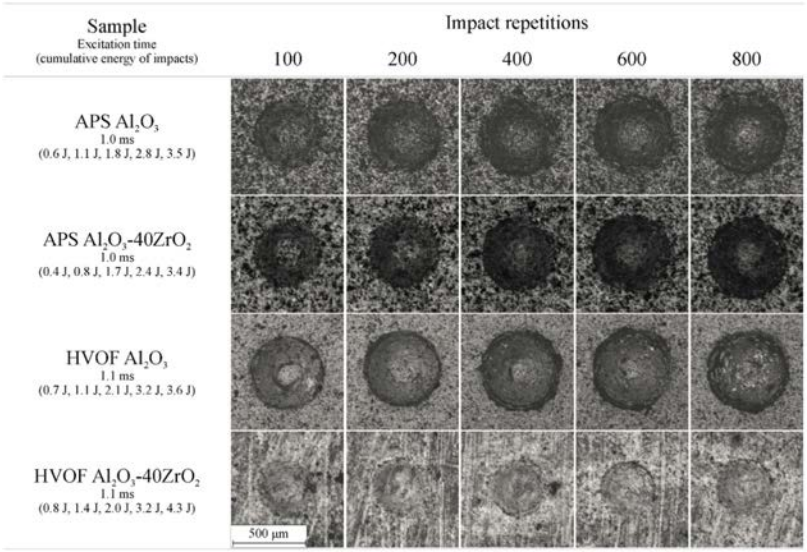

Fig. 6. Optical micrographs of the impact craters of the Al_2O_3-based coatings after the micro-impact fatigue experiment with fixed excitation time and varying repetitions.

3.3. Hardness and cavitation erosion resistance

To investigate the significance of the results further, the hardness values and cavitation erosion resistance values of the coatings are compared and presented in Fig. 10. Vickers hardness value is typically indicative of the crack propagation resistance and structural integrity of the coating [22] in a scale of some tens of micrometers when indented from the cross-section, while cavitation erosion resistance is thought to be a good measure of the coating cohesion and resistance to repeated impacts in a scale of about 10 µm [33]. Generally, HVOF-sprayed samples have a higher hardness and cavitation erosion resistance. The reason for the difference in hardness lies in a finer microstructure, lower porosity [34] and ability to deflect the propagating crack due to unmelted/nanostructured zones [35]. The difference in cavitation erosion resistance stems from the fine microstructure being able to deflect cavitating bubbles better [33].

The order of the samples is kept the same to underline that there is no clear connection between either hardness or cavitation resistance and the results of the micro-impact fatigue experiment. The Cr_2O_3-based coatings are harder (1150–1600 $HV_{0.3}$) than Al_2O_3-based

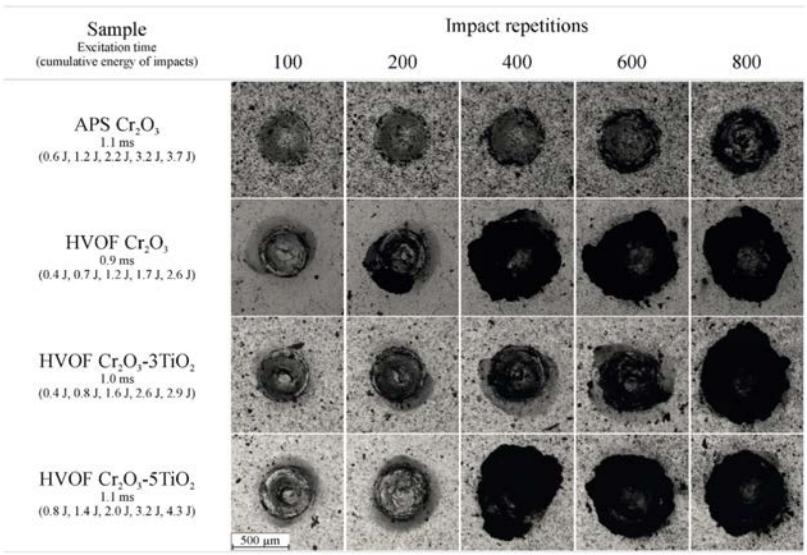

Fig. 7. Optical micrographs of the impact craters of the Cr_2O_3-based coatings after the micro-impact fatigue experiment with fixed excitation time and varying repetitions.

Table 4
Crater volumes and incremental volume changes to the previous crater. The points of failure are in bold.

Sample	Attribute	Repetitions					
		100	200	400	600	800	1000
APS-Al_2O_3	Crater volume [$\mu m^3 \times 10^{-3}$]	526	755	978	1096	1297	1179
	Volume change [pp]	–	**17.6**	17.2	9.1	15.5	−9.1
APS-Al_2O_3-40ZrO_2	Crater volume [$\mu m^3 \times 10^{-3}$]	603	684	881	897	1331	1432
	Volume change [pp]	–	5.7	13.8	1.1	**30.3**	7.1
HVOF-Al_2O_3	Crater volume [$\mu m^3 \times 10^{-3}$]	586	629	784	725	758	953
	Volume change [pp]	–	4.5	**16.3**	−6.2	3.5	20.4
HVOF-Al_2O_3-40ZrO_2	Crater volume [$\mu m^3 \times 10^{-3}$]	199	175	146	192	225	769
	Volume change [pp]	–	−3.1	−3.8	6.0	4.4	**70.7**
APS-Cr_2O_3	Crater volume [$\mu m^3 \times 10^{-3}$]	506	615	678	889	882	764
	Volume change [pp]	–	12.2	7.2	**23.7**	−0.8	−13.2
HVOF-Cr_2O_3	Crater volume [$\mu m^3 \times 10^{-3}$]	336	1697	10,183	10,591	9430	12,730
	Volume change [pp]	–	10.7	**66.7**	3.2	−9.1	25.9
HVOF-Cr_2O_3-3TiO_2	Crater volume [$\mu m^3 \times 10^{-3}$]	650	850	1148	1751	15,823	8503
	Volume change [pp]	–	1.3	1.9	3.8	**88.9**	−46.3
HVOF-Cr_2O_3-5TiO_2	Crater volume [$\mu m^3 \times 10^{-3}$]	288	139	9729	10,209	8548	76
	Volume change [pp]	–	−1.5	**93.9**	4.7	−16.3	−83.0

coatings (800–1050 $HV_{0.3}$) as is typically the case [3,36]. Within the same material, utilizing HVOF-spray instead of APS provided higher hardnesses for the reasons outlined in the previous paragraph. Alloying led to no significant change in hardness for the materials. Based on hardness values, no connection with impact-fatigue behavior exists. In fact, the three hardest coatings, Cr_2O_3, Cr_2O_3-5TiO_2 and Cr_2O_3-3TiO_2 are quite different in their micro-impact fatigue resistance.

Cavitation erosion resistance is more of a function of the spray method, and consequently the APS-coatings perform poorly in this experiment. This is likely due to the larger globular pores [34] that readily act as bubble nucleation sites where erosion initiates rapidly [33]. The Cr_2O_3-based coatings are more resistant to cavitation than Al_2O_3-coatings, but alloying with ZrO_2 improves the performance of Al_2O_3-coatings to equal or higher levels. The finest feedstock size, $-15 + 5$ µm, of the HVOF Cr_2O_3-coating leads to the finest microstructure and again to the highest cavitation erosion resistance. The connection to hardness exists in that microhardness is more influenced by the material property and cavitation resistance is a combination of material choice with the scale and quality of the microstructure. As presented in Fig. 10, neither of these properties correlate with the repeating micro-impact fatigue

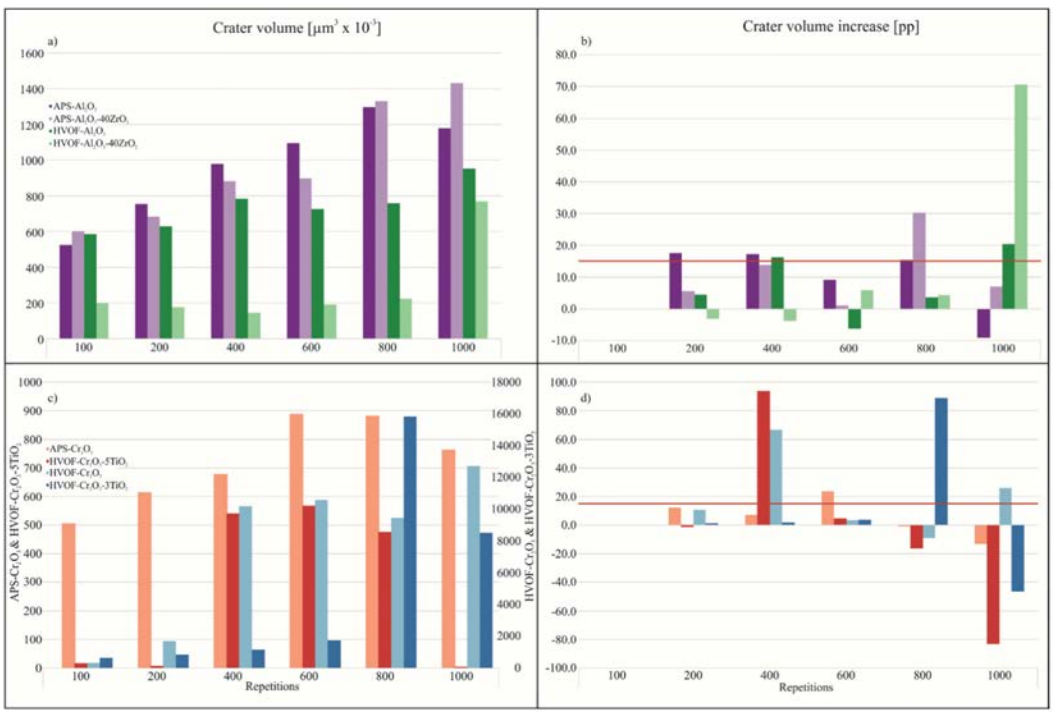

Fig. 8. Graphs of the measured crater volumes for a) Al_2O_3-based sample, c) Cr_2O_3-based samples and the changes in normalized crater volume for b) Al_2O_3-based samples d) Cr_2O_3-based samples. Constant excitation time, variable repetitions.

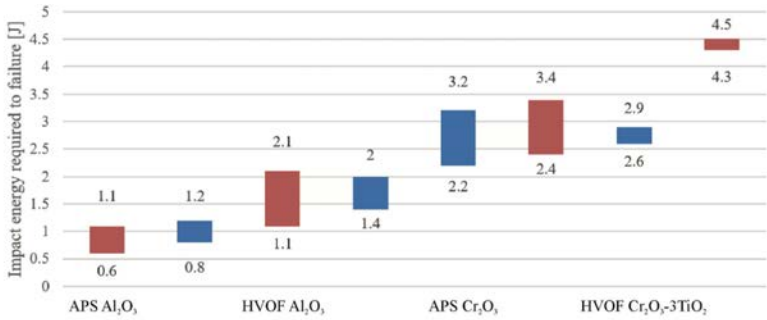

	HVOF Cr_2O_3		HVOF Cr_2O_3-5TiO_2		APS Al_2O_3-40ZrO_2		HVOF Al_2O_3-40ZrO_2	
Excit. Time (ms)	1	0.9	1.1	1.1	1.1	1	1	1.1
Repetititons	200	400	400	400	600	800	800	1000

Fig. 9. The cumulative impact energies required for failure in the second experimental set. Red bars indicate Al_2O_3-based samples and blue Cr_2O_3-based samples. In the table the excitation time and repetitions to failure are given. (For interpretation of the references to colour in this figure legend, the reader is referred to the web version of this article.)

experiment, highlighting the new information obtainable from the experiment.

4. Conclusion

The characteristics of micro-impact fatigue on thermally sprayed ceramic coatings were outlined in this study. Plasma- and HVOF-sprayed Al_2O_3, Al_2O_3-40ZrO_2 and Cr_2O_3 coatings and HVOF-sprayed Cr_2O_3-3TiO_2 and Cr_2O_3-5TiO_2 coatings were examined through an in-house made impact tester, where a 2 mm ZrO_2 sphere was fatiguing the coating surface with a frequency of 10 Hz and impact energies of 1.1–5.2 mJ. Two experimental set-ups were used. First, 1000 impacts were inflicted with varying energies. Second, based on the failure limit of the coating the impact energy was kept constant while the impact number was varied. The resulting impact craters were examined by optical microscopy and optical profilometry to determine the volume losses.

For all Al_2O_3-based coatings, aside from APS Al_2O_3-40ZrO_2, a cone crack was visible even with the lowest impact energies and it propagated quite gradually with increasing impact energies. The Cr_2O_3-based coatings were quite resistant to cone cracking but in the HVOF-sprayed samples the propagation was rapid and radial cracking leading to catastrophic failure appeared rapidly and clearly. Coinciding with this point of failure it was noticed that the normalized volume increment of the craters was 15 percentage points or more, an arbitrary number that gave good agreement with all coatings. This number is specific for the experiment, but the implication is that by following the evolution of damage in a ceramic coating an outlier in the trend can indicate that a limit of damage tolerance has been reached.

The coating material was deemed to be of little significance to the endurance of the coating. Rather, microstructural integrity and the residual stress state were extremely important, as evidenced by the positive effect of alloying of the base material in order to bring the composite melting temperature lower and to add a second phase to

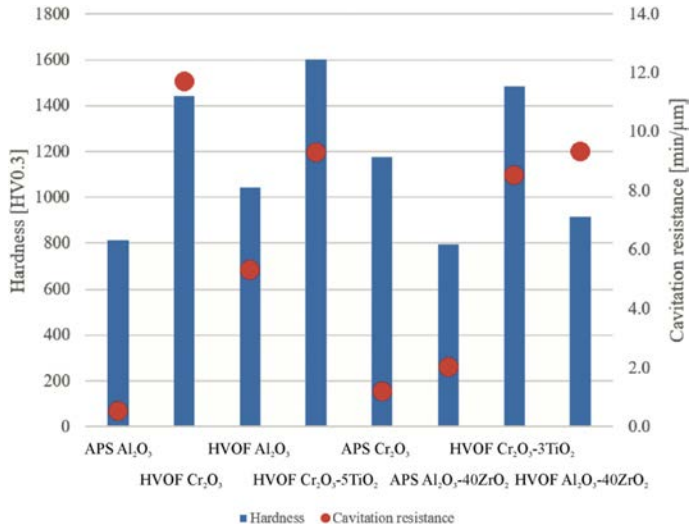

Fig. 10. Cavitation resistance and hardness of the coatings.

disperse the energy of cracking. Resistance to micro-impact fatigue was found not to correlate neither with coating microhardness nor cavitation erosion resistance, both of which are typically good indicators of structural cohesion and integrity. Therefore, the test gives a new approach into the research of the impact properties and fatigue life of thermally sprayed ceramic coatings. Further studies should focus on the relationship between micro-impact fatigue resistance and the thermal history and residual stress state of the coatings.

Acknowledgements

This work was supported by the graduate school of the President of Tampere University of Technology; and Business Finland (Finnish innovation funding, trade, investment, and travel promotion organization), its “Ductile & Damage Tolerant Ceramic Coatings”-project and the participating companies. The authors are grateful to Mr. Mikko Kylmälahti from Tampere University of Technology and Mr. Veli-Pekka Tarkiainen from Valmet Technologies Inc. (Jyväskylä, Finland) for spraying the coatings.

References

[1] P. Vuoristo, Thermal spray coating processes, in: S. Hashmi (Ed.), Compr. Mater. Process. Film. Coatings Technol. Recent Dev. Vol. 4 Elsevier, 2014, pp. 229–276, , https://doi.org/10.1016/B978-0-08-096532-1.00407-6.
[2] L. Pawlowski, The Science and Engineering of Thermal Spray Coatings, Second Ed, John Wiley & Sons, West Sussex, England, 2008, https://doi.org/10.1002/9780470754085.
[3] G. Bolelli, V. Cannillo, L. Lusvarghi, T. Manfredini, Wear behaviour of thermally sprayed ceramic oxide coatings, Wear 261 (2006) 1298–1315, https://doi.org/10.1016/j.wear.2006.03.023.
[4] E. Turunen, A. Hirvonen, T. Varis, T. Fält, S.-P. Hannula, T. Sekino, K. Niihara, Application of HVOF techniques for spraying of ceramic coatings, AZo J. Mater. Online. 3 (2007) 1–8, https://doi.org/10.2240/azojomo0260.
[5] E. Turunen, T. Varis, J. Keskinen, T. Fält, S.P. Hannula, Improved mechanical properties by nanoreinforced ceramic composite HVOF coatings, Adv. Sci. Tech. 45 (2006) 1240–1245, https://doi.org/10.4028/www.scientific.net/AST.45.1240.
[6] S.P. Hannula, E. Turunen, J. Keskinen, T. Varis, T. Fält, T.E. Gustafsson, R. Nowak, Development of nanostructured Al_2O_3-Ni HVOF coatings, Key Eng. Mater. 317–318 (2006) 539–544.
[7] D. Chen, E.H. Jordan, M. Gell, X. Ma, Dense TiO_2 coating using the solution precursor plasma spray process, J. Am. Ceram. Soc. 91 (2008) 865–872, https://doi.org/10.1111/j.1551-2916.2007.02225.x.
[8] J.W. Murray, A. Leva, S. Joshi, T. Hussain, Microstructure and wear behaviour of powder and suspension hybrid Al_2O_3–YSZ coatings, Ceram. Int. 44 (2018) 8498–8504, https://doi.org/10.1016/j.ceramint.2018.02.048.
[9] F.-L. Toma, L.-M. Berger, T. Naumann, S. Langner, Microstructures of nanostructured ceramic coatings obtained by suspension thermal spraying, Surf. Coat. Technol. 202 (2008) 4343–4348, https://doi.org/10.1016/j.surfcoat.2008.04.007.
[10] G. Bolelli, V. Cannillo, R. Gadow, A. Killinger, L. Lusvarghi, J. Rauch, Properties of high velocity suspension flame sprayed (HVSFS) TiO_2 coatings, Surf. Coat. Technol. 203 (2009) 1722–1732, https://doi.org/10.1016/j.surfcoat.2009.01.006.
[11] M.W. Barsoum, Fundamentals of Ceramics, 2nd ed., IOP Publishing, London, 2002.
[12] B.R. Lawn, Fracture and deformation in brittle solids: a perspective on the issue of scale, J. Mater. Res. 19 (2004) 22–29, https://doi.org/10.1557/jmr.2004.19.1.22.
[13] A. Evans, Perspective on the development of high-toughness ceramics, J. Am. Ceram. Soc. 73 (1990) 187–206, https://doi.org/10.1111/j.1151-2916.1990.tb06493.x.
[14] B. Lawn, R. Wilshaw, Indentation fracture: principles and applications, J. Mater. Sci. 10 (1975) 1049–1081, https://doi.org/10.1007/BF00823224.
[15] S.K. Lee, S. Wuttiphan, B.R. Lawn, Role of microstructure in Hertzian contact damage in silicon nitride, J. Am. Ceram. Soc. 80 (1997) 2367–2381, https://doi.org/10.1111/j.1151-2916.1997.tb03129.x.
[16] D.K. Kim, Y.G. Jung, I.M. Peterson, B.R. Lawn, Cyclic fatigue of intrinsically brittle ceramics in contact with spheres, Acta Mater. 47 (1999) 4711–4725, https://doi.org/10.1016/S1359-6454(99)00246-3.
[17] L. Ceseracciu, M. Anglada, E. Jiménez-Piqué, Influence of the elastic mismatch on the Hertzian cone crack path in ceramic bilayers, J. Eur. Ceram. Soc. 31 (2011) 1951–1955, https://doi.org/10.1016/j.jeurceramsoc.2011.04.032.
[18] J.B. Quinn, G.D.G. Quinn, Indentation brittleness of ceramics: a fresh approach, J. Mater. Sci. 2 (1997) 4331–4346, https://doi.org/10.1023/A:1018671823059.
[19] J. Kiilakoski, M. Lindroos, M. Apostol, H. Koivuluoto, V.-T. Kuokkala, P. Vuoristo, Characterization of high-velocity single particle impacts on plasma-sprayed ceramic coatings, J. Therm. Spray Technol. 25 (2016) 1127–1137, https://doi.org/10.1007/s11666-016-0428-2.
[20] R. Ahmed, M. Hadfield, Mechanisms of fatigue failure in thermal spray coatings, J. Therm. Spray Technol. 11 (2002) 333–349, https://doi.org/10.1361/105996302770348727.
[21] A. Vackel, S. Sampath, Fatigue behavior of thermal sprayed WC-CoCr-steel systems: role of process and deposition parameters, Surf. Coat. Technol. 315 (2017) 408–416, https://doi.org/10.1016/j.surfcoat.2017.02.062.
[22] A. Ibrahim, R.S. Lima, C.C. Berndt, B.R. Marple, Fatigue and mechanical properties of nanostructured and conventional titania (TiO_2) thermal spray coatings, Surf. Coat. Technol. 201 (2007) 7589–7596, https://doi.org/10.1016/j.surfcoat.2007.02.025.
[23] B.R. Lawn, Indentation of ceramics with spheres: a century after Hertz, J. Am. Ceram. Soc. 81 (2005) 1977–1994, https://doi.org/10.1111/j.1151-2916.1998.tb02580.x.
[24] R. Musalek, J. Matejicek, M. Vilemova, O. Kovarik, Non-linear mechanical behavior of plasma sprayed alumina under mechanical and thermal loading, J. Therm. Spray Technol. 19 (2010) 422–428, https://doi.org/10.1007/s11666-009-9362-x.
[25] J.H. Kim, S. Lee, K.S. Lee, D.K. Kim, The effect of grain boundary phase on contact damage resistance of alumina ceramics, J. Mater. Sci. 39 (2004) 7023–7030, https://doi.org/10.1023/B:JMSC.0000047547.09325.3d.
[26] A.C. Sekkal, C. Langlade, A.B. Vannes, A micro/macro impact test at controlled energy for erosion and phase-transformation simulation, Tribol. Lett. 15 (2003) 263–274, https://doi.org/10.1023/A:1024996621189.
[27] A.C. Sekkal, C. Langlade, A.B. Vannes, Tribologically transformed structure of titanium alloy ($TiAl_6V_4$) in surface fatigue induced by repeated impacts, Mater. Sci. Eng. A 393 (2005) 140–146, https://doi.org/10.1016/j.msea.2004.10.008.
[28] F. Ledrappier, C. Langlade, Y. Gachon, B. Vannes, Blistering and spalling of thin hard coatings submitted to repeated impacts, Surf. Coat. Technol. 202 (2008) 1789–1796, https://doi.org/10.1016/j.surfcoat.2007.07.107.
[29] G. Kermouche, C. Langlade, Mechanical nano-structuration of a C45 steel under repeated normal impacts, IOP Conf. Ser. Mater. Sci. Eng. 63 (2014) 012019, , https://doi.org/10.1088/1757-899X/63/1/012019.
[30] S. Kuroda, T.W. Clyne, The quenching stress in thermally sprayed coatings, Thin Solid Films 200 (1991) 49–66, https://doi.org/10.1016/0040-6090(91)90029-W.
[31] R.T.R. McGrann, D.J. Greving, J.R. Shadley, E.F. Rybicki, B.E. Bodger, D.A. Somerville, The effect of residual stress in HVOF tungsten carbide coatings on the fatigue life in bending of thermal spray coated aluminum, J. Therm. Spray Technol. 7 (1998) 546–552, https://doi.org/10.1361/105996398770350774.
[32] T. Varis, J. Knuuttila, T. Suhonen, U. Kanerva, J. Silvonen, J. Leivo, E. Turunen, Improving the properties of HVOF-sprayed Cr_2O_3 by nanocomposite powders, in: E. Lugscheider (Ed.), ITSC 2008 - Therm. Spray Crossing Borders, DVS-Verlag GmbH, Düsseldorf, Germany, Maastricht, the Netherlands, 2008, pp. 452–455.
[33] J. Kiilakoski, F. Lukac, H. Koivuluoto, P. Vuoristo, Cavitation wear characteristics of Al_2O_3-ZrO_2-ceramic coatings deposited by APS and HVOF processes, Proc. ITSC 2017, DVS Media GmbH, Düsseldorf, Germany, Düsseldorf, Germany, 2017, pp. 928–933.
[34] A. Kulkarni, J. Gutleber, S. Sampath, A. Goland, W.B. Lindquist, H. Herman, a.J. Allen, B. Dowd, Studies of the microstructure and properties of dense ceramic coatings produced by high-velocity oxygen-fuel combustion spraying, Mater. Sci. Eng. A 369 (2004) 124–137, https://doi.org/10.1016/j.msea.2003.10.295.
[35] R.S. Lima, B.R. Marple, Enhanced ductility in thermally sprayed titania coating synthesized using a nanostructured feedstock, Mater. Sci. Eng. A 395 (2005) 269–280, https://doi.org/10.1016/j.msea.2004.12.039.
[36] Y. Xie, H.M. Hawthorne, The damage mechanisms of several plasma-sprayed ceramic coatings in controlled scratching, Wear 233–235 (1999) 293–305, https://doi.org/10.1016/S0043-1648(99)00211-2.

PUBLICATION

V

Process Parameter Impact on Suspension-HVOF-Sprayed Cr_2O_3 Coatings

J. Kiilakoski, R. Trache, S. Björklund, S. Joshi and P. Vuoristo

Journal of Thermal Spray Technology (2019), 1–12
DOI: 10.1007/s11666-019-00940-7

J Therm Spray Tech
https://doi.org/10.1007/s11666-019-00940-7

PEER REVIEWED

Process Parameter Impact on Suspension-HVOF-Sprayed Cr_2O_3 Coatings

Jarkko Kiilakoski[1] · Richard Trache[2] · Stefan Björklund[3] · Shrikant Joshi[3] · Petri Vuoristo[1]

Submitted: 9 July 2019 / in revised form: 6 September 2019

Abstract Chromium oxide (Cr_2O_3) is commonly used as an atmospheric plasma-sprayed (APS) coating from powder feedstock in applications requiring resistance to sliding wear and corrosion, as well as amenability to texturing, e.g., in anilox rolls. Recently, high-velocity oxy-fuel spray methods involving suspension feedstock have been considered an extremely promising alternative to produce denser and more homogeneous chromium oxide coatings with lower as-sprayed surface roughness, higher hardness and potentially superior wear performance compared to conventional APS-sprayed coatings. In this study, the impact of process parameters namely auxiliary air cleaning nozzles and a transverse air curtain on suspension high-velocity oxy-fuel-sprayed Cr_2O_3 suspensions is presented. The produced coatings are characterized for their microstructure, mechanical properties and wear resistance by cavitation erosion. The results reveal the importance of optimized air nozzles and air curtain to achieve a vastly improved coating structure and performance.

Keywords Cr_2O_3 · influence of spray parameters · mechanical properties · SHVOF · suspension spraying

✉ Jarkko Kiilakoski
jarkko.kiilakoski@saint-gobain.com

[1] Materials Science and Environmental Engineering, Tampere University, Korkeakoulunkatu 6, 33720 Tampere, Finland

[2] Treibacher Industrie AG, Althofen, Austria

[3] Production Technology, University West, Trollhättan, Sweden

Introduction

Thermally sprayed chromium oxide coatings are known to exhibit a very high hardness of up to 1900-2000 HV_{5N} (Ref 1) and possess good adhesive and abrasion wear resistance (Ref 2) in conjunction with excellent corrosion properties (Ref 3). Chromium oxide coatings are commonly used in applications such as anilox rolls and doctor blades in the paper making industry (Ref 4), pump sleeves and feeding screws (Ref 3, 5, 6) where their wear and corrosion resistance is beneficial. Chromium oxide has traditionally been processed by atmospheric plasma spray (APS) (Ref 6, 7), but other methods like high-power atmospheric plasma spray (Ref 7), detonation gun spraying (Ref 8) or HVOF spraying (Ref 9, 10) have also been explored. One of the greatest challenges in spraying Cr_2O_3 is its high volatility at high temperatures encountered during spraying, leading to formation of gaseous species according to (Ref 11-13)

$$Cr_2O_3(s) + 3/2O_2(g) = 2CrO_3(g) \quad (1)$$

in a dry atmosphere or

$$Cr_2O_3(s) + 2H_2O(g) + 3/2O_2(g) = 2CrO_2(OH)_2(g) \quad (2)$$

in a moist atmosphere. Although the above gaseous species cannot be verified from samples of thermally sprayed Cr_2O_3 coatings, Cr(VI)has been detected therein (Ref 14). The vaporization also lowers significantly the deposition efficiency (DE) and can adversely influence coating quality. To hinder vaporization, among other benefits, specific additives, such as TiO_2 or Al_2O_3, are commonly used with Cr_2O_3. (Ref 1, 15, 16) Additionally, with conventional APS processes, the reducing hydrogen-containing atmosphere can lead to further reduction of the chromia to Cr, CrO and Cr_3O_4. (Ref 5, 17) The lower temperature and a less reducing atmosphere

Published online: 31 October 2019

of gas-fuel HVOF torches could be beneficial in removing the problem of unwanted reactions during spraying of Cr_2O_3.

Thermal spraying with suspension feedstock is increasingly emerging as an attractive extension of the traditional thermal spray coating methods. In suspension spraying, the feedstock consists of fine particles suspended in an aqueous or organic solvent. The technique is used with both plasma and HVOF spray processes and aims to achieve finer, even nanosized microstructures, thereby altering the properties of the coating significantly. Indeed, one of the main advantages is the injection of fine particles directly into the flame, circumventing the problems of poor flowability associated with fine powder feedstock. (Ref 18-20). Suspensions have been utilized mainly for spraying materials such as TiO_2 (Ref 21-23), Cr_2O_3 (Ref 23-25), YSZ (Ref 26-28), hydroxyapatite (Ref 29, 30) and Al_2O_3 (Ref 31-34). However, the majority of suspension spraying development has focused on the improvement in YSZ coating properties, where the results have already led to the commercial application of thermal barrier coatings by suspension plasma spraying (SPS). The previous works on Cr_2O_3 suspensions have had a strong emphasis on the development of the suspensions of both pure Cr_2O_3 and its mixtures with TiO_2. (Ref 23-25)

Currently, suspension spraying technology has matured to the point of emergence of various commercially available sources for feedstock. However, knowledge on the spraying of these feedstocks and functional performance of the resulting coatings, particularly for wear applications, is scarce and needs to be comprehensively explored. Especially in the case of Cr_2O_3, the underlying problems of volatility and reduction reactions during spraying still exist and need to be tackled systematically in order to establish economical feasibility, technical capability and reproducibility of the process. In this study, we reveal the path of parameter screening used for optimizing S-HVOF spraying of Cr_2O_3 suspension. In the process, the impact of spray parameters varied, i.e., oxygen/fuel ratio, suspension feed rate and spray distance on coating properties is also established. Additionally, different auxiliary air cooling/cleaning systems attached to the S-HVOF spray process were evaluated to enhance the removal of unmelted fine particles during coating (Ref 1). The coatings are characterized based on their cross-sectional microstructures, Vickers microhardness and surface roughness. The best coatings from the final optimization were also subjected to cavitation erosion tests to determine their structural integrity.

Experimental Methods

Coating Deposition

The coatings were deposited on stainless steel (AISI 316) substrates with a TopGun HVOF system (GTV GmbH, Luckenbach, Germany) using ethene as the combustion gas. The spray torch was modified for liquid feedstock spraying by an in-house made injector with an internally mixing two-fluid atomizing nozzle and a conical combustion chamber, where the suspension was injected axially. Nitrogen was used as the atomizing gas for the suspension. The process parameters are presented in Table 1 and a schematic presentation of the suspension injector in Fig. 1. A commercially available suspension feedstock was used in this study (AuerCoat® Cr_2O_3 Suspension, Treibacher Industrie AG, Althofen, Austria). The solid content in the suspension was 40 wt.% of Cr_2O_3 (> 99% purity) in water, and the size of the particles was d_{10} = 0.2-0.8 µm, d_{50} = 2-5 µm and d_{90} = 5-10 µm. The suspension was fed with an in-house made pressure-vessel-type feeder connected to a closed-loop mass flowmeter for the liquid. A suspension feed rate of up to 53 g/min was used, corresponding to a solid feed rate of 21 g/min. Flat substrate specimens grit-blasted with 180-220 mesh alumina were affixed on a plane during spraying and air cooling was utilized. The investigated parameters were as follows: spray distance, airflow through air cooling nozzles, air pressure of an air curtain, amount of suspension feed and the amount of total combustion gas flow (given in Tables 2 and 3). The substrate temperature was monitored with an infrared thermal camera (TI300, Fluke Co., Everett, WA, USA), and it was ensured that the temperature of the sample did not rise above 250 °C. A new spray pass was started when the temperature dropped to 200 °C. A pair of Silvent 209L (Silvent AB, Borås, Sweden) air cooling nozzles ("1." in Fig. 2), one preceding and one following the spray torch,

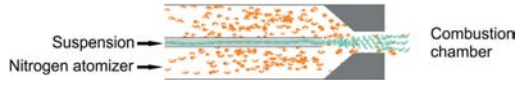

Fig. 1 A schematic illustration of the internally mixing two-fluid atomizing nozzle of the suspension injector

Table 1 Fixed process parameters during process parameter impact studies

Chamber type, mm	Suspension injector diameter, mm	Ethene flow, slpm	Oxygen flow, slpm	Step, mm	Surface speed, m/min	Atomizer gas, slpm
135, conical	0.8	88	213	3	57	4.5

Table 2 Summary of varied process parameters and corresponding hardness and roughness results

Parameter	Susp. Feed, g/min	Spray distance, mm	Passes	Flow rate of air nozzles, slpm	Pass thickness, µm/pass	Hardness [$HV_{0.3}$]	S_a, µm
H-110-0-0	53	110	20	...	5	957 ± 60	2.5
H-100-0-0	53	100	20	...	4	1060 ± 45	2.2
H-90-0-0	53	90	20	...	5	1141 ± 106	4.0
H-80-0-0	53	80	20	...	5	1396 ± 132	7.3
H-80-400-0	50	80	20	400	6	1416 ± 67	2.9
H-90-400-0	50	90	20	400	6	1368 ± 143	1.3
H-80-600-0	50	80	20	600	7	752 ± 91	14.0
H-90-600-0	50	90	20	600	5	1380 ± 23	3.8
L-80-600-0	23	80	12	600	2	1444 ± 57 $HV_{0.05}$	3.6
L-90-600-0	23	90	12	600	2	903 ± 391 $HV_{0.05}$	3.0

Specimen nomenclature specifies suspension feed: H/L (High/Low)-spray distance–air nozzle flow-air curtain pressure

Table 3 Summary of varied process parameters used with the evaluation of the transverse air curtain and corresponding hardness and roughness results

Parameter	Ethene flow, slpm	Oxygen flow, slpm	Susp. Feed, g/min	SD, mm	Passes	Pass thickness, µm/pass	Air curtain pressure, MPa	Hardness [$HV_{0.3}$]	S_a, µm
H-90-400-2	88	213	47	90	20	6	0.2	1358 ± 44	3.4
H-90-400-4	88	213	50	90	20	6	0.4	1351 ± 47	1.9
H-90-400-7	88	213	50	90	20	6	0.7	1495 ± 71	1.8
H-90-400-7 (g)	120	275	40	90	20	4	0.7	1335 ± 66	2.4
L-90-400-4	88	213	20	90	40	2	0.4	1277 ± 88	1.8

Specimen nomenclature specifies suspension feed: H/L (High/Low)-spray distance–air nozzle flow—transverse air curtain pressure, (g) = alternate gas parameters

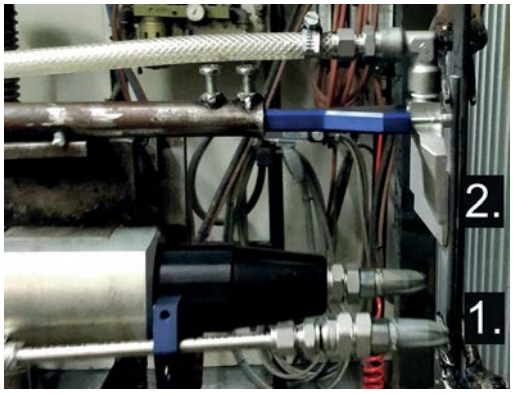

Fig. 2 Auxiliary cooling systems utilized in the study. 1. Air nozzles parallel to the spray plume. 2. Air curtain transverse to the spray plume

were used, and a Silvent 973 air curtain nozzle ("2." in Fig. 2) was also transversely mounted at a distance of about 70 mm from the nozzle exit.

Coating Characterization

The coating cross sections were characterized with a scanning electron microscope (SEM) (IT500, JEOL Ltd., Tokyo, Japan) with a 15 kV accelerating voltage, and the cross-sectional microhardness values were averaged from five indentations made with a Vickers microhardness tester (MMT-X7,Matsuzawa Co., Ltd., Akita, Japan) at a load of 300 grams. Surface roughness values (S_a) of the specimens were measured with an InfiniteFocus G5 (Alicona Imaging GmbH, Austria) optical profilometer over an area profile of 1.62×1.62 mm^2. Cavitation erosion tests were performed with an ultrasonic transducer (VCX-750, Sonics and Materials Inc., Newtown, CT, USA), according to the ASTM G32-10 standard for indirect cavitation erosion. The vibration tip, made of a Ti-6Al-4 V alloy, was placed at a distance of 0.5 mm from the sample surface and vibrated at a frequency of 20 kHz with an amplitude of 50 µm. The coated samples were cleaned in an ultrasonic bath with ethanol and weighed after drying. Samples were periodically weighed after 15, 30, 60 and 90 min of testing. The sample surfaces were tested as-sprayed. The length of the cavitation test

along with the periodic intermittent weight measurements increases the statistical validity of the test, and, hence, only one sample per coating was tested. The mean depth of erosion (MDE) was calculated following the equation

$$\mathrm{MDE}\left[\frac{\mu\mathrm{m}}{\mathrm{min}}\right] = \frac{1000\left[\frac{\mu\mathrm{m}}{\mathrm{m}}\right] * \mathrm{SER}\left[\frac{\mathrm{mm}^3}{\mathrm{h}}\right]}{60\left[\frac{\mathrm{min}}{\mathrm{h}}\right] * A\left[\mathrm{mm}^2\right]},$$

where SER is the volume loss per hour calculated from the last three measuring points (1 h) to remove the effects of the bubble incubation stage and surface roughness and A is the surface area of the vibrating tip. The coatings were presumed to be fully dense Cr_2O_3 when volume loss was calculated from mass loss for simplicity. Cavitation resistance of the coatings was then calculated as the reciprocal of the mean depth of erosion.

Results and Discussion

Influence of Spray Distance

The starting parameters for the initial investigation of the coatings originated from our previous experience with liquid feedstock HVOF spraying and from the spray parameters used by Toma et al. (Ref 23). The parameters are presented in

Table 1. To assess the role of gun-to-substrate standoff distance on coating quality, specimens were first sprayed at four spray distances of 80, 90, 100 and 110 mm. From the cross sections of the resulting set of coatings shown in Fig. 3, it is evident that all the coatings have visible interfaces between successive spray passes, which could be attributable to the presence of some microporosity, dust or vaporized and condensed Cr_2O_3. This is likely to diminish the structural integrity of the coating. All the coatings also exhibited cracking, either in the vertical or horizontal directions or both, suggesting excessive thermal loading from the relatively short spray distance. Regardless, the coating hardness values measured in the range 950–1400 HV0.3 were comparable to the value of 1400 $HV_{0.3}$ obtained by Toma et al. (Ref 23). The deposition rates were also reasonable at roughly 5 µm per pass, which is consistent with our experience with HVOF spraying of Cr_2O_3 powders. The as-deposited coating surfaces were found to be increasingly uneven (higher S_a) when moving to shorter spray distances, as seen in the surface morphology images in Fig. 3 and also quantified by the roughness values in Table 2. This phenomenon is speculated to arise from the higher surface temperature trapping more fine particles that are not directly deposited, but are traveling perpendicular to the surface away from the torch, as explained in detail by VanEvery et al. (Ref 27) and Fauchais et al. (Ref 1). This leads to greater deposition on surface asperities of the substrate for shorter spray distances. As a suitable compromise between hardness and roughness, spray distances of 80 and 90 mm were chosen for the ensuing parametric studies. Additionally, it became clear that cleaning the surface of unmelted/condensated fine chromia particles between the coating layers could be beneficial in reducing interpass porosity. Therefore, air nozzles were mounted on both sides of the torch (see arrangement 1 in Fig. 2).

Influence of the Airflow of Air Cooling Nozzles

The flow in the air nozzles could be adjusted between 0 and 600 slpm with an accuracy of 50 slpm. By manually determining flow rates that would be high enough without apparently interfering with the spray plume, the flow rates to be investigated were chosen to be 400 and 600 slpm. Apart from the spray distances of 80 and 90 mm chosen based on the preceding set of experiments, only the suspension feed was varied for a couple of runs, roughly halving it to 23 g/min to assess the corresponding influence on coating quality. In all the coatings, there was still fine particulate dust visible at the spray pass interfaces, as seen in the exemplary cross-sectional micrographs from coatings in Fig. 4. Some horizontal and treelike cracks were seen in the coatings at the spray distance of 80 mm (see Fig. 4c), regardless of the airflow in the nozzles. This suggests that 90 mm is the more suitable spray distance, as it keeps the temperature of the substrate/coating system better under control with milder heat cycling. In particular, H-90-400-0 and H-90-600-0 exhibited no cracking and their cross sections seemed quite coherent. The hardness of both coatings was around 1350–1400 $HV_{0.3}$. It is also evident that 600 slpm airflow is excessive with 80 mm spray distance (coating H-80-600-0), as the airflow appears to promote column formation by the fine particles (Fig. 5c, left), due to the higher airflow promoting deviation of the trajectory of the still molten fines, leading to a slightly cauliflower-like surface structure often associated with a columnar structure (Ref 27). This apparently increases the measured pass thickness and, coupled with crack formation from the dissimilar thermal history of the coating layers, leads to subpar hardness of less than 800 $HV_{0.3}$ (as compared to the ca. 1400 $HV_{0.3}$ for H-80-0-0 and H-80-400-0). The additional 10 mm distance between the air nozzles and the substrate seems to make a significant difference between H-80-600-0 and H-90-600-0, as is evident from Figs. 4c and 5c.

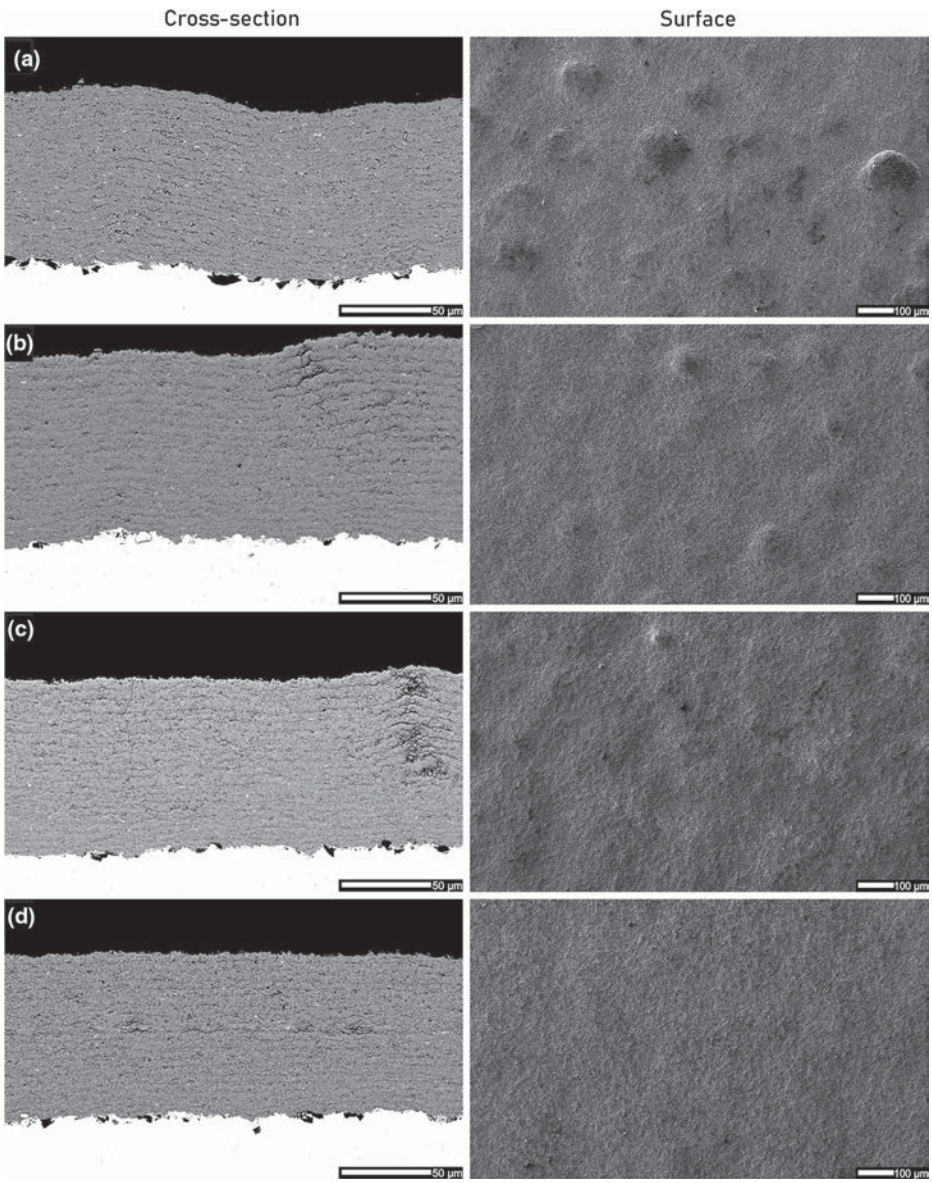

Fig. 3 SEM (SE) images of the cross sections and surface morphologies of coatings deposited with varying spraying distance: (a) 80 mm (H-80-0-0), (b) 90 mm (H-90-0-0), (c) 100 mm (H-100-0-0), (d) 110 mm (H 110-0-0)

Influence of the Suspension Feed Rate

One set of experiments involved keeping the 600 slpm air nozzle flow rate, but reducing the suspension feed rate by approximately a factor of two (to 23 g/min, coatings L-80/90-600-0). As expected, the corresponding deposition rate dropped to 2 µm/pass. Although these coating runs were interrupted, they clearly revealed that the longer spray distance of 90 mm led to a significant drop in hardness while at a spray distance of 80 mm the coating exhibited promising

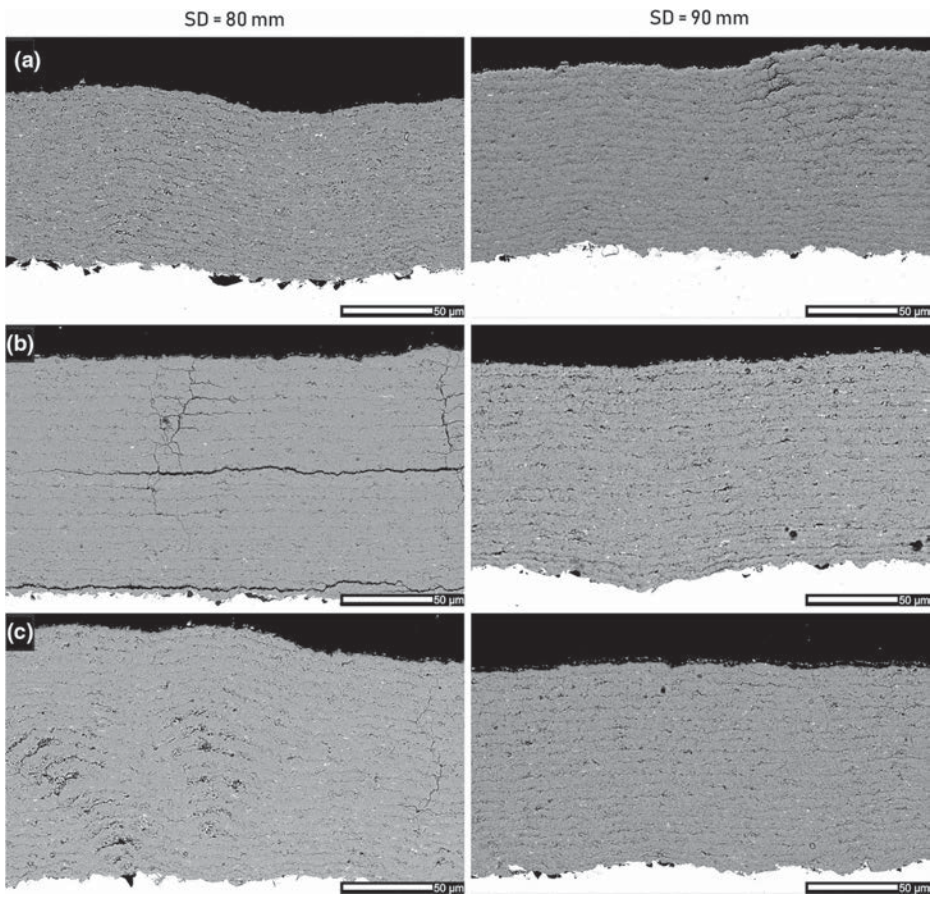

Fig. 4 Cross-sectional SEM (SE) images of microstructures of coatings showing the evolution in structure when an air cooling nozzle was used: (a) 0 slpm (H-80/90-0-0), (b) 400 slpm (H-80/90-400-0), (c) 600 slpm (H-80/90-600-0)

hardness. This difference could possibly be attributed to higher degree of atomization of the suspension followed by a more pronounced scattering of droplets in the flame when compared to the higher feed rate. This would lead to the smaller droplets losing their momentum with the longer spray distance combined with the strong stagnation zone from the air nozzle flow. Due to the inconclusive results, the lower feed rate was decided to be also investigated in the following step while maintaining the flow rate through the air nozzle at 400 slpm.

Influence of the Air Pressure, the Transverse Air Curtain and Fuel Gas Flow

The pressure for the air curtain was chosen to be 0.2, 0.4 and 0.7 MPa to facilitate removal of fine particles without affecting melting of the particles excessively. Even with 0.2 MPa of transverse air curtain pressure, an improvement was seen in the coating microstructure as less pronounced interpass porosity and a more homogeneous surface topography, which is shown in Fig. 6.

With increasing air curtain pressure, the surface roughness of the coatings was generally found to be lower while the hardness values remained the same or slightly increased, as given in Table 3. At the same time, the thickness per pass was essentially unaltered. The beneficial effect of the air curtain was seemingly achieved with 0.4 MPa pressure, as can be seen in the images for SD = 90 mm in Fig. 6. It is pertinent to note that the surface and cross-section images do not show additional improvement when the pressure was further increased from 0.4 to 0.7 MPa. The surface roughness did not improve either when the air curtain pressure

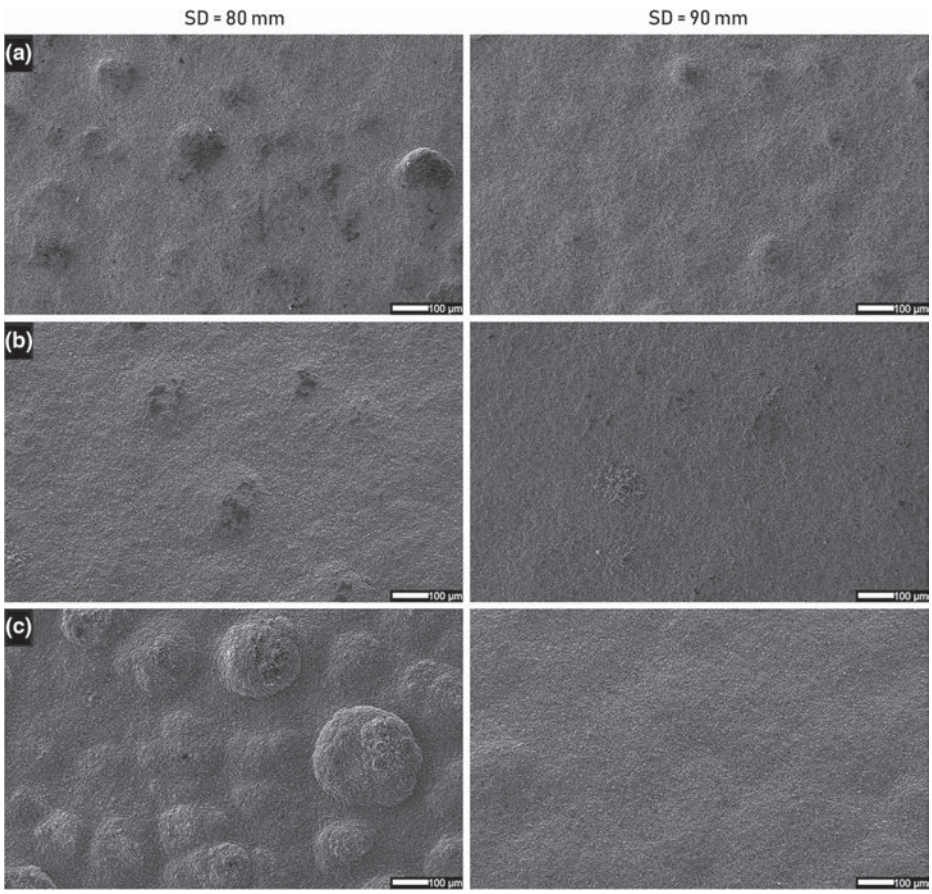

Fig. 5 Surface morphology SEM (SE) images of microstructures of coatings showing the evolution in structure when an air cooling nozzle was used: (a) 0 slpm (H-80/90-0-0), (b) 400 slpm (H-80/90-400-0), (c) 600 slpm (H-80/90-600-0)

was increased from 0.4 to 0.7 MPa. Therefore, an air curtain pressure of 0.4 MPa was used to investigate the effect of a lower feed rate of 20 g/min (coating L-90-400-4), which led to the deposition rate being halved while the hardness lowered slightly and the roughness remained the same.

The higher air curtain pressure of 0.7 MPa was chosen when evaluating the effect of higher gas flow of the fuel and oxygen in H-90-400-7(g). The choice was made to ensure that the curtain is powerful enough even with the increased density of the flame of the torch. The increased flame velocity led to a lower deposition rate, through a combination of a lower suspension feed and likely either less melting of the feedstock due to the shorter dwell time or a reduction in the velocity of the particles prior to impact due to a stronger stagnation zone close to the surface. This stagnation can lead to a reduction in perpendicular velocity for small particles to almost zero, while the radial velocity can reach 100 m/s (Ref 35), easily leading to off-normal impact and consequent deposition of the particles. (Ref 36) The shorter dwell time may in insufficient time to melt the particle thoroughly, even though the higher total gas flow often leads to an increase in particle temperature. (Ref 37) However, the temperature is always measured from the surface of the particle, and the convection and conduction of the heat inside the particle takes time. (Ref 38) An increase of 80 slpm, in an example of a DJ-2600 Hybrid, of gas flow would increase the particle velocity by 70 m/s and its temperature by 30 °C. (Ref 37) Therefore, it is likely that the reduction in the dwell time has more influence than the increase in temperature.

The hardness was lower and the roughness higher when compared with H-90-400-7.

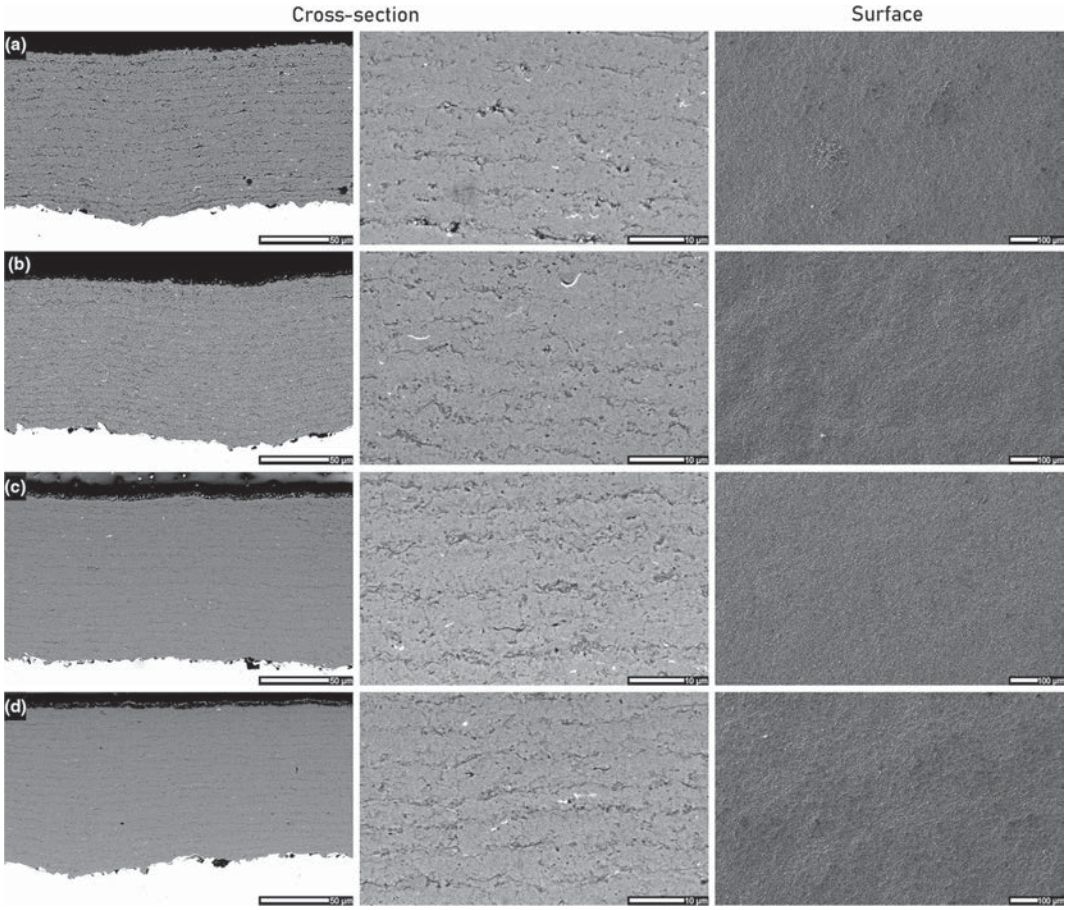

Fig. 6 Cross-sectional SEM (SE) images of microstructures of coatings with SD = 90 showcasing the effect of transverse air curtain pressure: (a) 0 bar (H-90-400-0), (b) 2 bar (H-90-400-2), (c) 4 bar (H-90-400-4), (d) 7 bar (H-90-400-7)

Physical Characterization of the Coatings

Microhardness and Roughness

The hardness and as-sprayed roughness values of all the coatings are summarized in Fig. 7. It can be said that, generally, the hardness of the coating increases with shortening of spray distance, while the roughness increases. The addition of the air nozzles improved one or both of these properties while increasing the reliability and homogeneity with the exception of H-80-600-0, where the airflow was seemingly causing too much turbulence at this short spray distance.

By addition of a transverse air curtain, the coating structure was found to become more homogeneous, eliminating the variability in hardness values of the coatings already with a 0.2 MPa curtain pressure (coating H-90-400-2). This would indicate effective removal of fine particles that end up as defects in the coating, thereby compromising the structure. At 0.4 and 0.7 MPa transverse air curtain pressure, both the hardness variability and surface roughness were improved. Higher combustion gas flow led to slightly lower hardness and higher roughness as did the lower feed rate of suspension.

Integrity and Cohesion of Coatings as Studied by Cavitation Erosion

In the final stage of the study, the cohesion of the coatings in the H-90 series of spray runs was evaluated by cavitation erosion experiments. The coatings deposited with a spray

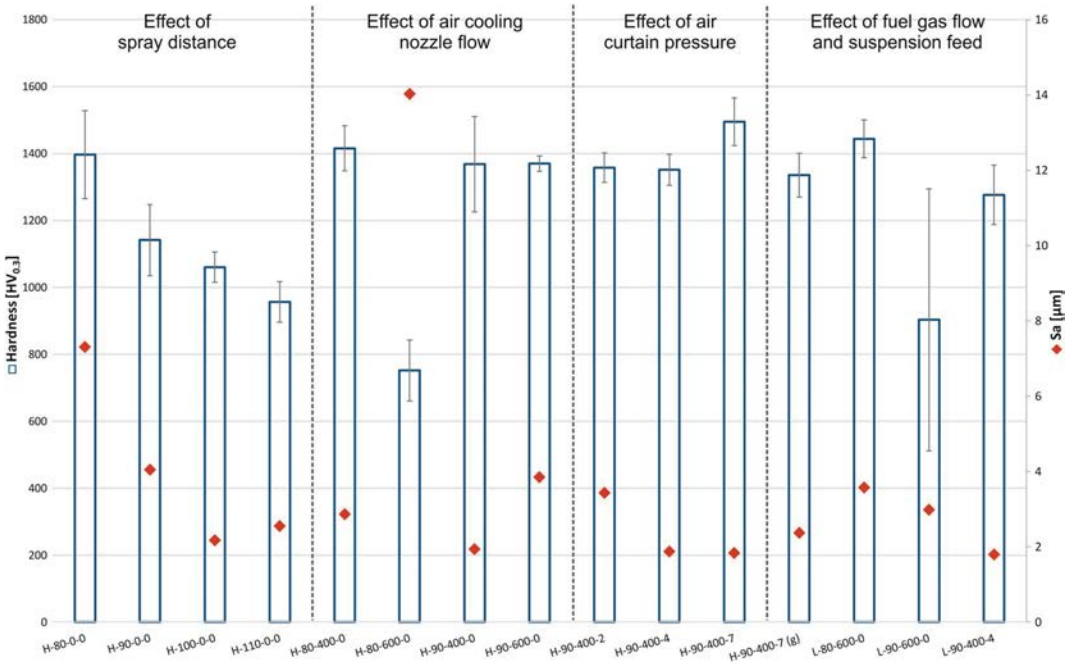

Fig. 7 Vickers hardness with its standard deviation and roughness values of all investigated coatings

distance of 90 mm were selected from previous examinations based on the *prima facie* promising overall quality of coatings (microstructure, hardness and surface roughness). Past studies have shown that cavitation erosion is a good indicator of the structural cohesion of a ceramic coating and the cavitation erosion resistance is hindered by poor splat-to-splat adherence (Ref 39, 40). This makes it ideal for testing the effect of fine particle removal from splat boundaries. The results from the cavitation erosion tests are presented in Fig. 8.

It is seen that the use of an air curtain with moderate pressures is advisable: with 0.2 and 0.4 MPa air curtain pressure, the cavitation resistance is increased, indicating improved cohesion likely due to a lower amount of poorly bonded fine particles at the splat boundaries. Increasing the air curtain pressure to 0.7 MPa decreased the cavitation resistance slightly, probably due to a decrease in the particle velocities and temperature leading to less impact energy and bonding between splats. Interestingly, higher combustion gas flows that would normally increase bonding, led to even less cohesion of the coating. This derives possibly from an increase in the amount of defects, which the higher surface roughness would indicate as well. Surface images of H-90-400-7 and H-90-400-7(g) are presented in Fig. 9 before (a) and after cavitation erosion (b). In the as-sprayed surfaces, no clear

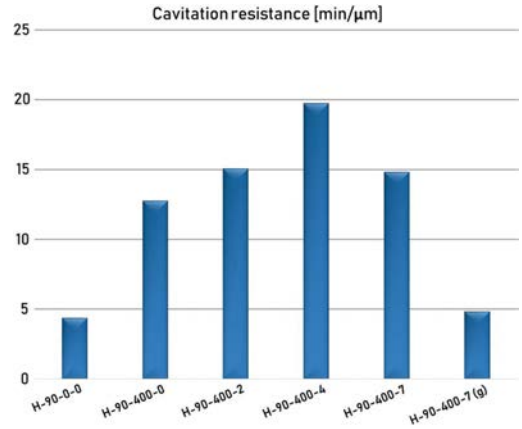

Fig. 8 Cavitation erosion resistance of coatings with 90 mm spray distance and 400 slpm air nozzle flow

difference in the amount of dust or unmelted particles can be seen. However, in H-90-400-7(g), a larger amount of protrusions are found—such as pointed by the white arrow—that likely cause the higher surface roughness. These, in unison with weak splat interfaces, provide low-energy pathways

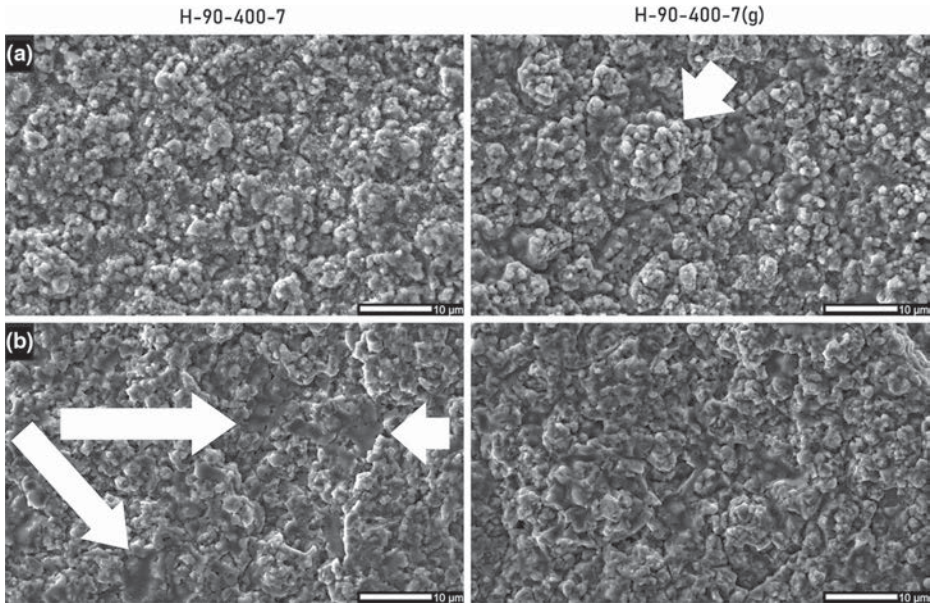

Fig. 9 Surface images (SEM) of coating H-90-400-7 and H-90-400-7(g) (a) as-sprayed and (b) after cavitation erosion. White arrows point to a protrusion in H-90-400-7(g) in (a) and to well-melted splats in H-90-400-7 revealed by cavitation erosion in (b)

to crack propagation in the coating. (Ref 41) Indeed, in Fig. 9b), large areas of well-melted splats can be seen in H-90-400-7 (white arrows), while such regions are sparse in H-90-400-7(g). This lends credibility to the idea of cooling/slowing of the particles during spraying, leading to less cohesion and a lower melting degree. It is believed that the majority cause of the weakening of the structure is due to the formation of the more pronounced stagnation zone due to the short spray distance, which affect the trajectory and velocity of the particles (Ref 36), and in a smaller part unmelted dine particles.

Conclusions

In this study, the effect of process parameters during SHVOF spraying of a Cr_2O_3 suspension on coating quality was investigated. The evaluated parameters were as follows: spray distance, flow rate of auxiliary air cooling nozzles for surface cleaning, pressure of a transverse air curtain for the removal of fine particles and excess heat load, total combustion gas flow and suspension feed rate. Other parameters were kept constant. All coatings were deposited with good efficiency, but the quality varied drastically. The need for auxiliary systems became clear, as fine unmelted particles were deposited on the splat interfaces, i.e., between passes of the torch. The coatings were evaluated by their microstructure, hardness, surface roughness and cavitation erosion resistance.

The conclusions can be summarized based on the parameters as follows:

- *Spray distance* While a longer spray distance produced a smoother, cleaner coating, the hardness values were superior with shorter spray distances. A distance of 90 mm was found to be optimal.
- *Air cooling nozzles* The benefit of the surface cleaning effect of the nozzles was clear in improving the coating cohesion. However, too much airflow could cause too much turbulence at the surface, leading to higher surface roughness and lower hardness. An airflow of 400 slpm was sufficient in this study.
- *Air curtain* An improvement was seen immediately with even the lightest air curtain pressure of 0.2 MPa, visibly reducing the amount of defects between spray passes. The reduction in heat load on the samples also reduced the roughness of the coatings. While all pressure levels improved the coating, the optimal structure and cavitation erosion resistance were found with 0.4 MPa.
- *Fuel gas flow* The higher fuel gas flow led to a stronger stagnation zone close to the sample surface, decreasing the velocity and deflecting the trajectory of the particles which decreased the hardness and cavitation resistance

and increased the surface roughness. Additionally, the shorter dwell time led to less melting of the particles, causing a lower deposition rate.

- *Suspension feed rate* Lowering of the suspension feed rate by half did not bring about any improvements in the coating structure, but led to a reduction in deposition rate.

The optimization path in this work gives encouragement in the development of high-performance oxide coatings from suspension feedstock. After optimization, the coatings have good mechanical properties with a decent deposition rate, with still room to improve. Further studies should be directed toward optimizing the amount of suspension feed as well as gas flow parameters of the torch, along with different combustion chamber geometries and the effect of air curtain pressure on particle velocity, temperature and trajectory.

Acknowledgments The authors gratefully acknowledge the financial support from 'the graduate school of the President of Tampere University of Technology', the 'K.F. and Maria Dunderberg Foundation' and Business Finland (Finnish innovation funding, trade, investment and travel promotion organization), its ''Ductile and Damage Tolerant Ceramic Coatings'' project and the participating companies. The authors would like to thank Mr. Anssi Metsähonkala of Tampere University for manufacturing the coatings.

References

1. P.L. Fauchais, J.V.R. Heberlein, and M.I. Boulos, Overview of Thermal Spray, *Thermal Spray Fundamentals: From Powder to Part*, P.L. Fauchais, J.V. Heberlein, and M.I. Boulos, Ed., Springer, New York, 2014, p 17-72
2. S. Usmani and K.N. Tandon, Evaluation of Thermally Sprayed Coatings under Reciprocating Lubricated Wear Conditions, *J. Therm. Spray Technol.*, 1992, **1**(3), p 249-255
3. P. Vuoristo, Thermal Spray Coating Processing, *Comprehensive Materials Processing Volume 4: Films and Coatings: Technology and Recent Development*, 1st ed., S. Hashmi, Ed., Elsevier, Oxford, 2014, p 229-276
4. J.R. Davis, ASM Handbook, Volume 5A: Thermal Spray Technology. in R.C.J. Tucker ed., (Materials Park, OH, USA), ASM International, 2013.
5. L. Pawlowski, Technology of Thermally Sprayed Anilox Rolls: State of Art, Problems, and Perspectives, *J. Therm. Spray Technol.*, 1996, **5**(3), p 317-334
6. F. Rastegar and A.E. Craft, Piston Ring Coatings for High Horsepower Diesel Engines, *Surf. Coatings Technol.*, 1993, **61**(1–3), p 36-42
7. T. Morishita, Coatings by 250 kW Plasma Jet Spray System. in *Proceedings of the 2nd Plasma Technik Symposium*, ed. by S. Blum-Sandmeier, H. Eschnauer, P. Huber, and A. Nicoll, Eds., (Luzern, Switzerland), Plasma Technik AG, Wohlen, 1992, pp. 137–142.
8. K. Niemi, P. Vuoristo, and T. Mäntylä, Chromium Oxide Coatings Deposited by Plasma Spraying and Detonation Gun Spraying. in *Proceedings of the 2nd Plasma Technik Symposium*, ed. by S. Blum-Sandmeier, H. Eschnauer, P. Huber, and A. Nicoll, Eds., (Luzern, Switzerland), Plasma Technik AG, Wohlen, 1991, pp. 311–322.
9. G. Bolelli, L. Lusvarghi, T. Manfredini, F. Pighetti Mantini, R. Polini, E. Turunen, T. Varis, and S.-P. Hannula, Comparison Between Plasma- and HVOF-Sprayed Ceramic Coatings: Part I, : Microstructure and Mechanical Properties, *Int. J. Surf. Sci. Eng.*, 2007, **1**(1), p 38-61
10. T. Varis, J. Knuuttila, T. Suhonen, U. Kanerva, J. Silvonen, J. Leivo, and E. Turunen, Improving the Properties of HVOF-Sprayed Cr2O3 by Nanocomposite Powders, *Thermal Spray 2008: Crossing Borders, on CD-ROM*, E. Lugscheider, Ed., DVS-Verlag GmbH, Düsseldorf, 2008, p 452-455
11. N. Jacobson, D. Myers, E. Opila, and E. Copland, Interactions of Water Vapor with Oxides at Elevated Temperatures, *J. Phys. Chem. Solids*, 2005, **66**(2–4), p 471-478
12. D. Caplan and M. Cohen, The Volatilization of Chromium Oxide, *J. Electrochem. Soc.*, 1961, **108**(5), p 438-442
13. G.R. Holcomb, Calculation of Reactive-Evaporation Rates of Chromia, *Oxid. Met.*, 2008, **69**(3–4), p 163-180
14. M. Harju, M. Järn, P. Dahlsten, J.P. Nikkanen, J.B. Rosenholm, and T. Mäntylä, Influence of Long-Term Aqueous Exposure on Surface Properties of Plasma-Sprayed Oxides Cr2O3 and Cr2O3-25 Wt.% TiO2, *J. Colloid Interface Sci.*, 2008, **326**(2), p 403-410
15. L.-M. Berger, F.-L. Toma, S. Scheitz, R. Trache, and T. Börner, Thermisch Gespritzte Schichten Im System Al_2O_3–Cr_2O_3–TiO_2—Ein Update, *Materwiss. Werksttech.*, 2014, **45**(6), p 465-475
16. S.H. Yu and H. Wallar, Chromia Spray Powders. (United States), United States Patent and Trademark Office, 2006, p. 5.
17. M. Vippola, J. Vuorinen, P. Vuoristo, T. Lepistö, and T. Mäntylä, Thermal Analysis of Plasma Sprayed Oxide Coatings Sealed with Aluminium Phosphate, *J. Eur. Ceram. Soc.*, 2002, **22**(12), p 1937-1946
18. F.-L. Toma, A. Potthoff, L.-M. Berger, and C. Leyens, Demands, Potentials, and Economic Aspects of Thermal Spraying with Suspensions: A Critical Review, *J. Therm. Spray Technol.*, 2015, **24**(7), p 1143-1152
19. P. Fauchais, M. Vardelle, A. Vardelle, and S. Goutier, What Do We Know, What Are the Current Limitations of Suspension Plasma Spraying?, *J. Therm. Spray Technol.*, 2015, **24**(7), p 1120-1129
20. A. Killinger, P. Müller, and R. Gadow, What Do We Know, What Are the Current Limitations of Suspension HVOF Spraying?, *J. Therm. Spray Technol.*, 2015, **24**(7), p 1130-1142
21. G. Bolelli, V. Cannillo, L. Lusvarghi, and R. Gadow, Deposition of TiO2 Coatings: Comparison Between High Velocity Suspension Flame Spraying (HVSFS), Atmospheric Plasma Spraying and HVOF-Spraying, *Thermal Spray 2009: Expanding Thermal Spray Performance to New Markets and Applications*, B.R. Marple, M.M. Hyland, Y.-C. Lau, C.-J. Li, R.S. Lima, and G. Montavon, Ed., Springer, Las Vegas, 2010, p 207-212
22. F.-L. Toma, L.-M. Berger, I. Shakhverdova, B. Leupolt, A. Potthoff, K. Oelschlägel, T. Meissner, J.A.I. Gomez, and Y. de Miguel, Parameters Influencing the Photocatalytic Activity of Suspension-Sprayed TiO2 Coatings, *J. Therm. Spray Technol.*, 2014, **23**(7), p 1037-1053
23. F.L. Toma, A. Potthoff, and M. Barbosa, Microstructural Characteristics and Performances of Cr2O3 and Cr2O3-15%TiO2 S-HVOF Coatings Obtained from Water-Based Suspensions, *J. Therm. Spray Technol.*, 2018, **27**(3), p 344-357

24. R. Gadow, A. Killinger, and J. Rauch, New Results in High Velocity Suspension Flame Spraying (HVSFS), *Surf. Coat. Technol.*, 2008, **202**(18), p 4329-4336
25. J. Rauch, G. Bolelli, A. Killinger, R. Gadow, V. Cannillo, and L. Lusvarghi, Advances in High Velocity Suspension Flame Spraying (HVSFS), *Surf. Coat. Technol.*, 2009, **203**(15), p 2131-2138
26. A. Killinger, M. Kuhn, and R. Gadow, High-Velocity Suspension Flame Spraying (HVSFS), A New Approach for Spraying Nanoparticles with Hypersonic Speed, *Surf. Coat. Technol.*, 2006, **201**(5), p 1922-1929
27. K. VanEvery, M.J.M. Krane, R.W. Trice, H. Wang, W. Porter, M. Besser, D. Sordelet, J. Ilavsky, and J. Almer, Column Formation in Suspension Plasma-Sprayed Coatings and Resultant Thermal Properties, *J. Therm. Spray Technol.*, 2011, **20**(4), p 817-828
28. M. Marr, J. Kuhn, C. Metcalfe, J. Harris, and O. Kesler, Electrochemical Performance of Solid Oxide Fuel Cells Having Electrolytes Made by Suspension and Solution Precursor Plasma Spraying, *J. Power Sour.*, 2014, **245**, p 398-405
29. N. Stiegler, D. Bellucci, G. Bolelli, V. Cannillo, R. Gadow, A. Killinger, L. Lusvarghi, and A. Sola, High-Velocity Suspension Flame Sprayed (HVSFS) Hydroxyapatite Coatings for Biomedical Applications, *J. Therm. Spray Technol.*, 2012, **21**(2), p 275-287
30. G. Bolelli, D. Bellucci, V. Cannillo, R. Gadow, A. Killinger, L. Lusvarghi, P. Müller, and A. Sola, Comparison between Suspension Plasma Sprayed and High Velocity Suspension Flame Sprayed Bioactive Coatings, *Surf. Coat. Technol.*, 2015, **280**, p 232-249
31. J. Kiilakoski, A. Lutoschkin, M. Plachetta, M. Apostol, H. Koivuluoto, P. Müller, A. Killinger, P. Vuoristo, Fracture Characteristics of High-Velocity Suspension Flame-Sprayed Aluminum Oxide Coatings. in *Proceedings of the International Thermal Spray Conference*, (May 10–12, 2016 (Shanghai, China)), DVS Media GmbH, Düsseldorf, Germany, 2016, pp. 466–471.
32. F.-L. Toma, S. Langner, M.M. Barbosa, L. Berger, C. Rödel, A. Potthoff, Influence of the Suspension Characteristics and Spraying Parameters on the Properties of Dense Suspension-HVOF Sprayed Al2O3 Coatings. in *Thermal Spray 2011: Proceedings of the International Thermal Spray Conference*, ed. by B.R. Marple, A. Agarwal, M.M. Hyland, Y.-C. Lau, C.-J. Li, R.S. Lima, A. McDonald, (September 27-29, 2011 (Hamburg, Germany)), Springer, n.d., pp. 421–426.
33. G. Bolelli, J. Rauch, V. Cannillo, A. Killinger, L. Lusvarghi, and R. Gadow, Microstructural and Tribological Investigation of High-Velocity Suspension Flame Sprayed (HVSFS) Al2O3 Coatings, *J. Therm. Spray Technol.*, 2009, **18**(1), p 35-49
34. S. Goel, S. Björklund, N. Curry, U. Wiklund, and S. Joshi, Axial Suspension Plasma Spraying of Al2O3 Coatings for Superior Tribological Properties, *Surf. Coat. Technol.*, 2017, **315**, p 80-87
35. M. Li and P.D. Christofides, Computational Study of Particle In-Flight Behavior in the HVOF Thermal Spray Process, *Chem. Eng. Sci.*, 2006, **61**(19), p 6540-6552
36. B. Samareh and A. Dolatabadi, A Three-Dimensional Analysis of the Cold Spray Process: The Effects of Substrate Location and Shape, *J. Therm. Spray Technol.*, 2007, **16**(5–6), p 634-642
37. T. Varis, T. Suhonen, A. Ghabchi, A. Valarezo, S. Sampath, X. Liu, and S.P. Hannula, Formation Mechanisms, Structure, and Properties of HVOF-Sprayed WC-CoCr Coatings: an Approach toward Process Maps, *J. Therm. Spray Technol.*, 2014, **23**(6), p 1009-1018
38. L. Pawlowski, *The Science and Engineering of Thermal Spray Coatings*, 2nd ed., Wiley, West Sussex, 2008
39. J. Kiilakoski, F. Lukac, H. Koivuluoto, P. Vuoristo, Cavitation Wear Characteristics of Al_2O_3-ZrO_2 -Ceramic Coatings Deposited by APS and HVOF –Processes. in *Proceedings of the ITSC 2017*, (Düsseldorf, Germany), DVS Media GmbH, Düsseldorf, Germany, 2017, pp. 928–933.
40. V. Matikainen, K. Niemi, H. Koivuluoto, and P. Vuoristo, Abrasion Erosion and Cavitation Erosion Wear Properties of Thermally Sprayed Alumina Based Coatings, *Coatings*, 2014, **4**(1), p 18-36
41. V. Matikainen, S. Rubio Peregrina, N. Ojala, H. Koivuluoto, J. Schubert, and P. Vuoristo Houdková, Erosion Wear Performance of WC-10Co4Cr and Cr_3C_2–25NiCr Coatings Sprayed with High-Velocity Thermal Spray Processes, *Surf. Coat. Technol.*, 2019, **370**, p 196-212